Molecular pathology and computational image analyses in gynecologic malignancies

Edited by
Sandra Orsulic and Umberto Malapelle

About Frontiers

Frontiers is more than just an open access publisher of scholarly articles: it is a pioneering approach to the world of academia, radically improving the way scholarly research is managed. The grand vision of Frontiers is a world where all people have an equal opportunity to seek, share and generate knowledge. Frontiers provides immediate and permanent online open access to all its publications, but this alone is not enough to realize our grand goals.

Frontiers journal series

The Frontiers journal series is a multi-tier and interdisciplinary set of open-access, online journals, promising a paradigm shift from the current review, selection and dissemination processes in academic publishing. All Frontiers journals are driven by researchers for researchers; therefore, they constitute a service to the scholarly community. At the same time, the *Frontiers journal series* operates on a revolutionary invention, the tiered publishing system, initially addressing specific communities of scholars, and gradually climbing up to broader public understanding, thus serving the interests of the lay society, too.

Dedication to quality

Each Frontiers article is a landmark of the highest quality, thanks to genuinely collaborative interactions between authors and review editors, who include some of the world's best academicians. Research must be certified by peers before entering a stream of knowledge that may eventually reach the public – and shape society; therefore, Frontiers only applies the most rigorous and unbiased reviews. Frontiers revolutionizes research publishing by freely delivering the most outstanding research, evaluated with no bias from both the academic and social point of view. By applying the most advanced information technologies, Frontiers is catapulting scholarly publishing into a new generation.

What are Frontiers Research Topics?

Frontiers Research Topics are very popular trademarks of the *Frontiers journals series*: they are collections of at least ten articles, all centered on a particular subject. With their unique mix of varied contributions from Original Research to Review Articles, Frontiers Research Topics unify the most influential researchers, the latest key findings and historical advances in a hot research area.

Find out more on how to host your own Frontiers Research Topic or contribute to one as an author by contacting the Frontiers editorial office: frontiersin.org/about/contact

Molecular pathology and computational image analyses in gynecologic malignancies

Topic editors

Sandra Orsulic — University of California, Los Angeles, United States
Umberto Malapelle — University of Naples Federico II, Italy

Table of
contents

Editorial: Molecular pathology and computational image analyses in gynecologic malignancies

Umberto Malapelle[1*†] and Sandra Orsulic[2,3,4*†]

[1]Department of Public Health, University of Naples Federico II, Naples, Italy, [2]United State (US) Department of Veterans Affairs, Greater Los Angeles Healthcare System, Los Angeles, CA, United States, [3]Department of Obstetrics and Gynecology, David Geffen School of Medicine, University of California Los Angeles, Los Angeles, CA, United States, [4]Jonsson Comprehensive Cancer Center, University of California Los Angeles, Los Angeles, CA, United States

Editorial on the Research Topic
Molecular pathology and computational image analyses in gynecologic malignancies

Gynecological malignancies represent an important public health problem due to high cancer-related mortality. Despite improvements in diagnosis and treatment, gynecological malignancies account for about 40% of all cancer incidence and more than 30% of all cancer-related mortality in women worldwide (1, 2). Recent advances in molecular pathology, digital pathology, and computational imaging are paving way for new approaches to the diagnosis and prediction of clinical outcomes in gynecological malignancies (Orsulic et al.; 3–7). The continuously increasing capacity to store and analyze digital data enables applications of new technologies, such as artificial intelligence- and deep learning-assisted image analyses to generate thousands of image features and other non-biased continuous quantifiable variables that can be readily integrated with other -omic platforms (8). Future clinical application of such features combined with improvements in molecular pathology may be an arrow in the quiver of pathologists in diagnosis and guiding patient treatment and management decisions.

In this Research Topic of Frontiers in Oncology, we attempt to address some major advances in molecular and computational pathology in gynecological malignancies.

Endometrial cancer is the most common gynecological cancer in developed countries. Ovarian preservation treatment (OPT) is an option for patients of child-bearing age and with early-stage endometrial cancer, however, the benefits need to be carefully assessed against the risk of cancer progression. In order to assist radiologists in assessing the depth of myometrial invasion and selecting eligible patients for OPT, Yan et al. developed and validated a radiomics nomogram based on multi-parametric magnetic resonance imaging

and the least absolute shrinkage and selection operator algorithm. Molecular analyses are a useful tool in the characterization and classification of recently identified malignancies, such as mesonephric-like adenocarcinoma (MLA), a rare and aggressive neoplasm that mostly arises in the uterine corpus. Ma et al. analyzed molecular alterations in four MLA cases and identified several immunohistochemical markers as well as recurrent mutations in PIK3CA, KRAS, and PTEN, which not only support the classification of these malignancies as Müllerian in origin with mesonephric differentiation but also provides important leads for targeted therapies.

Cervical cancer is the leading cause of gynecological tumor-related mortality worldwide and the second most common malignancy in women. Human papilloma virus (HPV) infection and integration within the human genome is the primary cause of cervical cancer. Integration can disrupt the function of nearby genes, including oncogenes and tumor suppressor genes, and cause genomic rearrangements and instability (9). However, the potential intra-tumoral heterogeneity in integration sites has not been explored. Using an optimized dual-color fluorescence *in situ* hybridization (FISH) method to detect HPV integration sites in formalin-fixed, paraffin-embedded cervical cancer samples, Xiong et al. showed that cervical cancer may comprise subpopulations of cells with distinct integration sites that are otherwise indistinguishable by cell and nuclear morphology. Beyond diagnosis, molecular testing may be adopted for prognostic and predictive purposes in cervical cancer patients. Ma et al. showed that the upregulation of *CD27*, *TNF*, *TNFRSF12A*, *TNFRSF13C*, and *TNFRSF9* and the downregulation of *EDA* mRNA expression levels may serve as prognostic biomarkers of cervical cancer because they are associated with the immunotherapy response of these patients. In addition to molecular tools, cervical cancer patients may benefit, in particular in the field of screening and early diagnosis, from artificial intelligence-based medical tools. As summarized by Hou et al., clinical application of artificial intelligence may reduce turn-around time and the need for professional and technical personnel as well as eliminate human bias in evaluating subjective variables.

Ovarian cancer is a complex gynecological malignancy with a high mortality rate. To shed light on the molecular heterogeneity of this disease, Chen et al. explored a novel molecular phenotyping method for ovarian cancer subtypes based on metabolic genes through a comprehensive analysis of genomic data. The authors identified three different molecular subtypes (C1, C2, and C3) of ovarian carcinomas, which improved our understanding of the molecular characteristics of human ovarian cancer and uncovered new potential therapeutic targets. Wang et al. reviewed the role of the glyoxalase system as a marker for diagnosis and a novel target for antitumor therapy in breast, ovarian, endometrial, and cervical cancers. Although research in the past two decades has revealed that the fallopian tube is the likely precursor tissue for most epithelial ovarian cancers, the cell-intrinsic and microenvironmental conditions that lead to epithelial cell transformation into serous tubal intraepithelial carcinoma (STIC) are unknown. Wu et al. used computational image analyses to identify potential morphometric and topologic differences in fallopian tubes with and without STIC lesions. They showed that STIC lesions were accompanied by global stromal alterations and age-associated reorganization of tubal secretory and ciliated cells, which may provide a favorable microenvironment for cancer initiation. Another poorly understood aspect of ovarian cancer is metastasis outside of the peritoneal cavity. Brain metastases are rare in ovarian cancer, possibly because patients succumb to the peritoneal disease before the cancer has a chance to metastasize to other parts of the body. Using a spatially-oriented single-cell proteomics platform, Pejovic et al. identified cell populations that are shared between primary low-grade serous ovarian carcinomas and brain metastases, suggesting that cells predetermined for brain metastasis may exist in the early stages of cancer development. They also identified several brain metastasis-specific oncogenic and immunosuppressive pathways that could be used for targeted therapy.

Overall, this Research Topic has highlighted some major advances in molecular and computational pathology in gynecological malignancies. Ongoing research is warranted to improve the clinical outcome of these patients.

Author contributions

All listed authors have made a substantial, direct, and intellectual contribution to the work and approved it for publication.

Funding

Conflict of interest

UM has received personal fees as consultant and/or speaker bureau from Boehringer Ingelheim, Roche, MSD, Amgen, Thermo Fisher Scientifics, Eli Lilly, Diaceutics, GSK, Merck and AstraZeneca, unrelated to the current work.

The remaining author declares that the research was conducted in the absence of any commercial or financial relationships that could be construed as a potential conflict of interest.

Publisher's note

All claims expressed in this article are solely those of the authors and do not necessarily represent those of their affiliated organizations, or those of the publisher, the editors and the reviewers. Any product that may be evaluated in this article, or claim that may be made by its manufacturer, is not guaranteed or endorsed by the publisher.

References

1. Siegel RL, Miller KD, Fuchs HE, Jemal A. Cancer statistics, 2022. *CA Cancer J Clin* (2022) 72:7. doi: 10.3322/caac.21708

2. Sung H, Ferlay J, Siegel RL, Laversanne M, Soerjomataram I, Jemal A, et al. Global cancer statistics 2020: GLOBOCAN estimates of incidence and mortality worldwide for 36 cancers in 185 countries. *CA Cancer J Clin* (2021) 71:209. doi: 10.3322/caac.21660

3. Libera L, Sahnane N, Pepe F, Pisapia P, De Luca C, Russo G, et al. Critical aspects of microsatellite instability testing in endometrial cancer: A comparison study. *Hum Pathol* (2022) 128:134. doi: 10.1016/j.humpath.2022.07.014

4. Malapelle U, Parente P, Pepe F, De Luca C, Pisapia P, Sgariglia R, et al. Evaluation of micro satellite instability and mismatch repair status in different solid tumors: A multicenter analysis in a real world setting. *Cells* (2021) 10:1878. doi: 10.3390/cells10081878

5. Oaknin A, Gilbert L, Tinker AV, Brown J, Mathews C, Press J, et al. Safety and antitumor activity of dostarlimab in patients with advanced or recurrent DNA mismatch repair deficient/microsatellite instability-high (dMMR/MSI-h) or proficient/stable (MMRp/MSS) endometrial cancer: Interim results from GARNET-a phase I, single-arm study. *J Immunother Cancer* (2022) 10:e003777. doi: 10.1136/jitc-2021-003777

6. Spriggs DR, Longo DL. Progress in BRCA-mutated ovarian cancer. *N Engl J Med* (2018) 379:2567. doi: 10.1056/NEJMe1812644

7. González-Martín A, Pothuri B, Vergote I, DePont Christensen R, Graybill W, Mirza MR, et al. Niraparib in patients with newly diagnosed advanced ovarian cancer. *N Engl J Med* (2019) 381:2391. doi: 10.1056/NEJMoa1910962

8. Xu Y, Liu X, Cao X, Huang C, Liu E, Qian S, et al. Artificial intelligence: A powerful paradigm for scientific research. *Innovation* (2021) 2:100179. doi: 10.1016/j.xinn.2021.100179

9. Hu Z, Zhu D, Wang W, Li W, Jia W, Zeng X, et al. Genome-wide profiling of HPV integration in cervical cancer identifies clustered genomic hot spots and a potential microhomology-mediated integration mechanism. *Nat Genet* (2015) 47:158. doi: 10.1038/ng.3178

MRI-Based Radiomics Nomogram for Selecting Ovarian Preservation Treatment in Patients With Early-Stage Endometrial Cancer

Bi Cong Yan[1,2†], Xiao Liang Ma[1†], Ying Li[1†], Shao Feng Duan[3], Guo Fu Zhang[4] and Jin Wei Qiang[1*]

[1] Department of Radiology, Jinshan Hospital, Fudan University, Shanghai, China, [2] Department of Diagnostic and Interventional Radiology, Shanghai Jiao Tong University Affiliated Sixth People's Hospital, Shanghai, China, [3] Precision Health Institution, GE Healthcare, Shanghai, China, [4] Department of Radiology, Obstetrics & Gynecology Hospital, Fudan University, Shanghai, China

Background: Ovarian preservation treatment (OPT) was recommended in young women with early-stage endometrial cancer [superficial myometrial invasion (MI) and grades (G) 1/2-endometrioid adenocarcinoma (EEC)]. A radiomics nomogram was developed to assist radiologists in assessing the depth of MI and in selecting eligible patients for OPT.

Methods: From February 2014 to May 2021, 209 G 1/2-EEC patients younger than 45 years (mean 39 ± 4.3 years) were included. Of them, 104 retrospective patients were enrolled in the primary group, and 105 prospective patients were enrolled in the validation group. The radiomics features were extracted based on multi-parametric magnetic resonance imaging, and the least absolute shrinkage and selection operator algorithm was applied to reduce the dimensionality of the data and select the radiomics features that correlated with the depth of MI in G 1/2-EEC patients. A radiomics nomogram for evaluating the depth of MI was developed by combing the selected radiomics features with the cancer antigen 125 and tumor size. Receiver operating characteristic (ROC) curves were used to evaluate the diagnostic performance of the radiomics nomogram and of radiologists without and with the aid of the radiomics nomogram. The net reclassification index (NRI) and total integrated discrimination index (IDI) based on the total included patients to assess the clinical benefit of radiologists with the radiomics nomogram were calculated.

Results: In the primary group, for evaluating the depth of MI, the AUCs were 0.96 for the radiomics nomogram; 0.80 and 0.86 for radiologists 1 and 2 without the aid of the nomogram, respectively; and 0.98 and 0.98 for radiologists 1 and 2 with the aid of the nomogram, respectively. In the validation group, the AUCs were 0.88 for the radiomics nomogram; 0.82 and 0.83 for radiologists 1 and 2 without the aid of the nomogram, respectively; and 0.94 and 0.94 for radiologists 1 and 2 with the aid of the nomogram, respectively. The yielded NRI and IDI values were 0.29 and 0.43 for radiologist 1 and 0.23 and 0.37 for radiologist 2, respectively.

Conclusions: The radiomics nomogram outperformed radiologists and could help radiologists in assessing the depth of MI and selecting eligible OPTs in G 1/2-EEC patients.

Keywords: radiomics, nomogram, endometrial cancer, myometrial invasion, ovarian preservation

INTRODUCTION

Endometrial cancer (EC) is the most common gynecological cancer in developed countries (1). Approximately 11% of EC patients are diagnosed before the age of 50, and 5% are diagnosed before the age of 40 (2). Staging surgery (including hysterectomy and bilateral salpingo-oophorectomy [BSO]) is the primary treatment for EC. Adequate preoperative staging and triage are essential for determining the surgical procedures and adjuvant therapy.

However, BSO results in the abrupt disruption of hormone levels, with short-term intense menopausal symptoms that can compromise one's quality of life and lead to osteoporosis, metabolic syndrome, and cardiovascular disease (3, 4). Studies have suggested that BSO and ovarian preservation treatment (OPT) have similar mortality in young women with early-stage EC and that OPT does not decrease the overall survival of these patients (5–7). Furthermore, young patients with early-stage EC are more likely to die from cardiovascular diseases than from EC (5). Thus, the decision to preserve the ovaries in young EC patients is critical. More recently, studies recommended that OPT can be considered for patients younger than 45 years with early-stage EC [grade 1 and 2 (G 1/2) endometrioid adenocarcinoma (EEC), and myometrial invasion (MI) < 50%] and without ovarian mass (8–10).

Dilatation and curettage (D&C) and magnetic resonance imaging (MRI) are two recommended ways to preoperatively evaluate the tumor grade and EC staging (11, 12). Radiomics is an emerging technology that correlates image-based features with clinically relevant oncological outcomes. Studies suggest that quantitative radiomics or texture features may be useful for evaluating the deep myometrial invasion (DMI), with a similar accuracy of 84.8% compared with the subjective interpretation by experienced radiologists (13, 14). Moreover, tumor size or volume as determined on MRI is also useful for evaluating the depth of MI (11, 15). The radiomics nomogram includes a numerical probability of important clinical tumor diagnostic information and is considered a useful tool for quantifying tumor risk factors (16–18).

Therefore, in this study, we developed an MRI radiomics nomogram to assist radiologists in selecting eligible candidates for OPT by assessing DMI in G 1/2-EEC patients younger than 45 years.

MATERIALS AND METHODS

Patients

The Institutional Review Board approved this study (approval number 2020-10). Informed consent was obtained.

From February 2014 to September 2019, the electronic medical records of a total of 135 consecutive histopathologically proven EC patients under 45 years of age were reviewed.

Potential candidates for this study met the following criteria: 1) premenopausal patients younger than 45 years; 2) patients who underwent total hysterectomy with BSO and were histopathologically diagnosed with G1/2 and early-stage (International Federation of Gynecology and Obstetrics [FIGO] stages I–II) EEC; 3) patients without other or previous malignancies in the reproductive system, without family history of breast cancer, ovarian cancer, or Lynch syndrome; and 4) patients who underwent MRI scanning with sequences of T2-weighted imaging (T2WI), contrast-enhanced T1-weighted imaging (CE-T1WI), diffusion-weighted imaging (DWI), and apparent diffusion coefficient (ADC) maps. The exclusion criteria were as follows: 1) receiving anticancer treatment before surgery (n = 1); 2) absence of preoperative pelvic MRI (n = 9); 3) poor imaging quality due to artifacts or tumor invisible on MRI (n = 3); 4) no total hysterectomy performed (n = 5); 5) patients diagnosed with G3 EEC or non-EEC, or having a history of other cancer (n = 1); or 6) without serum cancer antigen 125 (CA125) information (n = 12). Furthermore, from September 2019 to May 2021, another 105 eligible EEC out of 109 patients were prospectively enrolled and formed the validation group. **Figure 1** shows the workflow of this study.

General clinical information, including age and tumor size (tumor maximum diameter measured retrospectively on T2WI), and CA125 from preoperative information, ER (estrogen receptor), PR (progesterone receptor), Ki67, and CK7 from postoperative pathology were collected. The univariate and multivariate logistic regression analyses were performed to analyze the predictive factors for DMI in G 1/2-EECs for OPT. The tumor stage was determined according to the 2014 FIGO staging system based on the final pathologic reports.

Imaging

All enrolled patients received pelvic MRI within 30 days before surgery. The mean interval between MRI and surgery was 20 days (range, 5–26 days). MRI was performed using 1.5-T scanners (Avanto, Siemens, Erlangen, Germany) with an eight-channel pelvic phased-array coil. The patients lay supine and breathed freely during acquisition. The following sequences were obtained with a field of view (FOV) of 360 × 280 mm; axial T1WI (time of repetition [TR]/time of echo [TE] = 761/10 ms, matrix = 256 × 256, thickness = 4 mm); axial T2WI (TR/TE = 4,000/98, matrix = 256 × 256, thickness = 4 mm) with and without fat saturation (FS), coronal T2WI (FOV 400 mm, TR/TE = 3849/83 ms, matrix 320 × 256, thickness = 4 mm, slice gap = 1 mm), and sagittal T2WI (FOV 270 mm, TR/TE = 4,490/83 ms, matrix 320 × 256, thickness = 4 mm, slice gap = 1 mm); axial DWI (TR/TE =
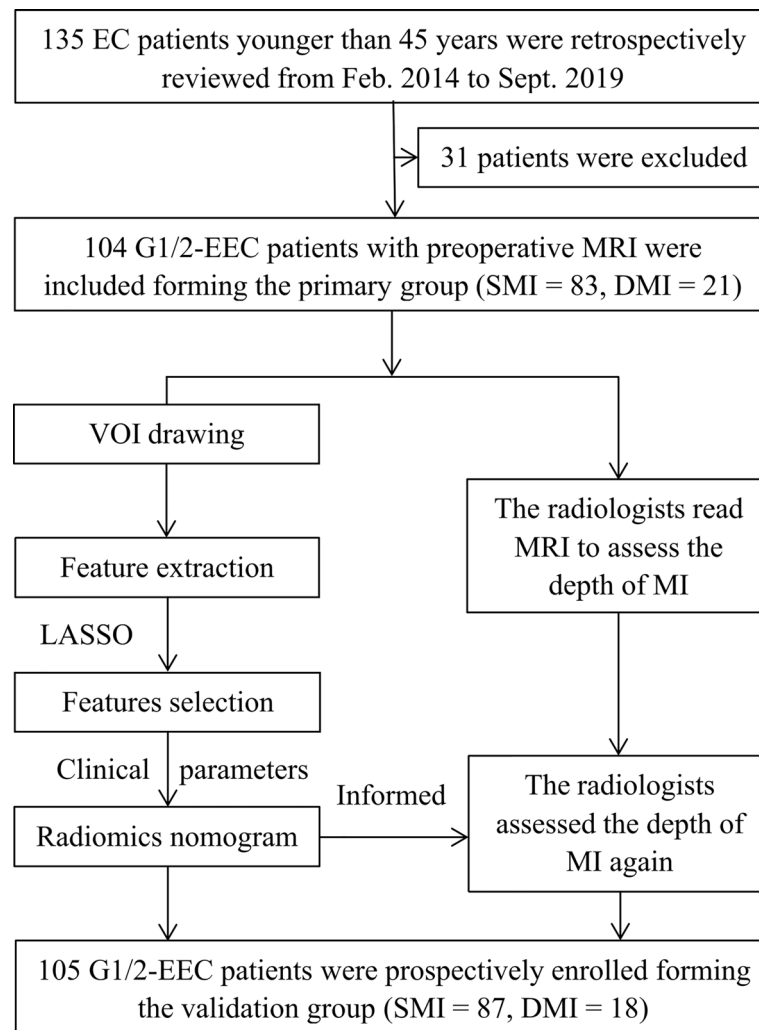
FIGURE 1 | The workflow of this study. G 1/2, grade 1 and 2; DMI, deep myometrial invasion; EC, endometrial cancer; EEC, endometrioid adenocarcinoma; SMI, superficial myometrial invasion; MI, myometrial invasion; LASSO, least absolute shrinkage and selection operator.

4,000/100 ms, b = 0, 1,000 s/mm^2, matrix = 128 × 128, thickness = 5 mm); and axial CE-T1WI with FS (TR/TE = 196/2.9 ms, matrix = 128 × 128, thickness = 4 mm) and sagittal CE-T1WI with FS (FOV 400 mm, TR/TE = 439/10 ms, thickness = 4 mm, matrix 320 × 256). CE-T1WI with FS was performed at the arterial phase (30–40 s), venous phase (75–90 s), and delayed phase (120–180 s) after the intravenous administration of gadopentetate dimeglumine (0.5 mmol/ml, GE Healthcare, Shanghai, China) at a dose of 0.2 mmol/kg of body weight and a rate of 2 to 3 ml/s. An ADC map was automatically generated based on DWI (b = 0 and b = 1000 s/mm^2).

Radiomics Feature Extraction

The patients' images were first imported into MITK Workbench software (http://mitk.org/wiki/The_Medical_Imaging_Interaction_Toolkit_ (MITK)). The multisequence images from axial DWI, ADC map, and CE-T1WI-FS (delay phase) were subsequently aligned to axial T2WI images. Regions of interest (ROIs) were manually drawn by radiologist 1 (with 5 years of MRI experience in gynecological imaging) along the tumor margin on each T2WI slice and automatically matched to T1WI, DWI (1,000 s/mm^2), ADC map, and CE sequences. After tumor segmentation, a 3D volume of interest (VOI) was obtained by resampling the image with sitkBSpline interpolator. The radiomics features were extracted using Pyradiomics (https://pypi.org/project/pyradiomics/). Imaging preprocessing was performed to ensure comparability of MRI gray values, and a fixed bin width of 1 was used to compute textural features. All radiomics feature implementations followed the IBSI recommendation (https://arxiv.org/abs/1612.07003).

Feature Selection

One month later, 50 patients were randomly chosen, and tumors were drawn by radiologist 1 repeatedly and by radiologist 2 (with

10 years of MRI experience in gynecological imaging) independently. The interclass and intraclass correlation coefficients (ICCs) of the extracted features were calculated to assess the reproducibility of radiomics features. We devised a three-step procedure for dimensionality reduction and selection of robust features (19). Firstly, features with both interclass and intraclass ICCs larger than 0.75 were considered robust and reproducible (20). Secondly, Pearson's correlation was used to identify redundant features and the feature was selected for subsequent investigation. If two features had a Pearson correlation coefficient > 0.9 (21), the feature with the larger mean absolute coefficient was removed. Thirdly, the least absolute shrinkage and selection operator (LASSO) was used to select nonzero coefficient features associated with DMI in G 1/2-EEC patients with 10-fold cross-validation by the penalty parameter to avoid overfitting. The process of feature selection using the LASSO algorithm is shown in **Figure 2**. A radiomics signature was generated *via* a linear combination of selected features weighted by their respective coefficients.

Radiomics Nomogram Development, Validation, and Diagnostic Performance

Based on the data of the primary group, the radiomics nomogram was developed using multivariable logistic regression by combining the radscore with the clinical parameters (CA125 and tumor size) selected and referred to other studies (22–24). The nomogram was then validated in the validation group.

All the MRI sequences (axial, sagittal, and/or coronal) were reviewed independently by the two radiologists who were available for preoperative clinical information, but blind to the results of surgical histopathology. MI was evaluated as the absence or superficial myometrial invasion (SMI) (MI < 50%) and DMI (MI ≥ 50%). To investigate the clinical application of the radiomics nomogram, after a period of 60 days, all cases were

repeatedly reviewed by the same radiologists referring to the nomogram's prediction possibility for DMI of each patient, the diagnoses were made, and the radiologists were named with the aid of nomogram.

To evaluate DMI in G 1/2-EEC for OPT, the diagnostic performances of the radiomics nomogram and the radiologists without and with the aid of the nomogram were assessed using receiver operating characteristic (ROC) curves in the primary and validation groups. The net reclassification index (NRI) and total integrated discrimination index (IDI) based on the whole data set of the radiologists without and with the aid of the nomogram were compared. Calibration curves were plotted using the Hosmer–Lemeshow (H-L) test to evaluate the calibration performance, which measured how close the prediction value generated by the nomogram was to the observed outcome. A significant result indicated a disagreement between the prediction value and the observed outcome of the nomogram.

Statistical Analysis

The sample size for this study in the validation group was calculated as the following: if the study achieves 99% diagnostic performance (β = 0.01, α = 0.05) with mean nomogram scores of 0.6 and 0.1 in SMI and DMI patients, respectively, 115 samples are needed. If the study achieves 85%–95% diagnostic performance, 70 samples are needed. We included 105 patients finally.

All statistical analyses were performed using R software (Version 4.0.2; http://www.r-project.org). Student's t-test was used to compare quantitative variables (age, tumor size, and CA125), and the Mann–Whitney U test, chi-squared test, or Fisher's exact test was used to compare qualitative variables. The DeLong test was used to compare the diagnostic performance of the radiomics nomogram, the radiologists without and with the aid of the nomogram. The "rms" package, "pROC" package, "dca. R" package, and "PredictABEL" package were used for the

FIGURE 2 | The top 13 radiomics features associated with DMI in G 1/2-EEC patients younger than 45 years were identified using the least absolute shrinkage and selection operator (LASSO) method in the primary group. **(A)** The parameter lambda (λ) is chosen using 10-fold cross-validation. **(B)** LASSO coefficient profiles of the selected features. A vertical line is plotted at the optimal value, resulting in 13 features with nonzero coefficients. EEC, endometrioid adenocarcinoma; DMI, deep myometrial invasion.

analyses. The R code is supplied in the **Supplement Material**. A p value < 0.05 was considered statistically significant.

RESULTS

Finally, 209 G 1/2-EEC patients (mean 39 ± 4.3 years; range 25–45 years) were retrospectively included in the primary group. The clinicopathological characteristics of the included G 1/2-EEC patients are summarized in **Table 1**. The 209 EEC patients included 155 G1 and 54 G2 patients. The multivariate logistic regression analysis showed that the predictive factors for DMI in G 1/2-EEC were ER (with 0.75 of OR), PR (with 1.26 of OR), and CA125 (with 1.01 of OR), which are shown in **Table 2**.

Feature Selection and Model Building

A total of 358 radiomics features, including 14 shape features, 72 first-order features, and 272 texture features, were extracted from the T2WI, DWI, ADC, and CE-T1WI sequences. Features with either interobserver or intraobserver ICC < 0.75 were removed, leaving 191 features. Based on the primary group, features with Pearson correlation coefficients > 0.9 were removed, leaving 160 features. After LASSO analysis, 13 radiomics features were finally included to form the radiomics signature. The 13 radiomics features including ADC_firstorder_Minimum and other features for assessing the depth of MI are shown in **Figure 3A**. The radscore calculation is shown in the following:

Radscore = 0.20192 + 0.05968×T2WI_firstorder_10P + -0.05049 × T2WI_firstorder_RobustMAD + 0.06464 × DWI_glcm_Id + -0.06397 × DWI_glszm_ZP + -0.0279 × CE_firstorder_Minimum + -0.02266 × CE_firstorder_Range + 0.16195 × CE_firstorder_Skewness + -0.12198 × CE_firstorder_TotalEnergy + 0.13675 × CE_glrlm_LRHGLE + -0.06215 × CE_glszm_LAE + 0.07236 × CE_glszm_SAHGLE + 0.00689 × ADC_firstorder_Minimum + 0.06399 × ADC_glcm_Contras

The co-occurrence network of the connection of each radiomics feature and clinical information are shown in **Figure 3B**. An MRI radiomics nomogram was further developed by incorporating the 13 radiomics features with CA125 and tumor size by linear regression to assess DMI in G 1/2-EEC in the primary group and is shown in **Figure 4**. Moreover, the calibration curves of the nomogram in the primary and validation groups are as shown in **Figure 5**.

The Reason for Misjudgment

In the 209 EEC patients, 27 patients had adenomyosis, 70 patients had leiomyoma, and 22 patients had both adenomyosis and leiomyoma at the final pathological diagnosis. The misjudgment reasons and cases for the radiomics nomogram and radiologists are exhibited in **Table 3**. The radiomics nomogram misjudged the depth of MI mostly due to the small tumor size, which indicated that the drawing of ROI might influence the diagnostic performance (**Figure 6**).

TABLE 1 | Clinicopathologic characteristics of the included grade 1/2 EEC patients.

	Primary group			Validation group		
	SMI (n = 83)	DMI (n = 21)	P value	SMI (n = 87)	DMI (n = 18)	p value
Age (year)	39.9 ± 4.6	41.4 ± 2.7	0.051	38.0 ± 4.2	42.3 ± 2.8	<0.001
CA125 (U/ml)	25.0 ± 20.3	47.9 ± 18.7	<0.001	16.4 ± 9.1	40.0 ± 29.3	0.003
Tumor size (mm)	44.9 ± 16.5	41.8 ± 16.4	0.437	46.5 ± 17.1	42.6 ± 10.7	0.220
Radscore	0.12 ± 0.2	0.52 ± 0.2	<0.001	0.17 ± 0.2	0.35 ± 0.2	0.006
ER (+/-)	53/30	6/15	0.008	59/28	7/11	0.041
CK7 (+/-)	50/33	10/11	0.685	76/11	12/6	0.069
PR (+/-)	41/42	15/6	0.118	63/24	9/9	0.113
Ki67 (+/-)	5/78	4/17	0.144	17/70	4/14	1.000
P53 (+/-)	40/43	12/9	0.625	63/24	8/10	0.042
Radiologist 1			<0.001			<0.001
SMI	78 (94.0%)	7 (33.3%)		85 (97.7%)	6 (33.3%)	
DMI	5 (6.0%)	14 (66.7%)		2 (2.3%)	12 (66.7%)	
Rad 1 + nomogram			<0.001			<0.001
SMI	83 (94.0%)	7 (33.3%)		86 (98.9%)	2 (11.1%)	
DMI	5 (6.0%)	14 (66.7%)		1 (1.1%)	16 (88.9%)	
Radiologist 2			<0.001			<0.001
SMI	79 (95.2%)	5 (23.8%)		86 (98.9%)	6 (33.3%)	
DMI	4 (4.8%)	16 (76.2%)		1 (1.1%)	12 (66.7%)	
Rad 2 + nomogram			<0.001			<0.001
SMI	83 (100%)	1 (4.8%)		87 (100%)	2 (11.1%)	
DMI	0 (0%)	20 (95.2%)		0 (0.0%)	16 (88.9%)	
Tumor grade			0.017			0.141
Grade 1	64 (77.1%)	10 (47.6%)		70 (80.5%)	11 (61.1%)	
Grade 2	19 (22.9%)	11 (52.4%)		17 (19.5%)	7 (38.9%)	

Continuous variables are presented as the mean ± standard deviation.
+/-, positive/negative; CA125, cancer antigen 125; DMI, deep myometrial invasion; EEC, endometrioid adenocarcinoma; FIGO, International Federation of Obstetrics and Gynecology; SD, standard deviation; SMI, superficial myometrial invasion; Rad, radiologist.

TABLE 2 | The univariate and multivariate logistic regression analyses for independent predictive factors of DMI in patients for ovarian preservation.

Variables	Univariate analysis			Multivariate analysis		
	Odds ratio	95% CI	p-value	Odds ratio	95% CI	p-value
Age	1.01	1.00–1.03	0.141	1.01	0.99–1.02	0.274
CA125	1.01	1.00–1.01	<0.001	1.01	1.00–1.01	<0.001
Tumor size (mm)	1.00	0.99–1.00	0.435	1.00	1.00–1.00	0.706
ER	0.79	0.68–0.92	0.003	0.75	0.62–0.90	0.002
PR	1.15	0.99–1.35	0.072	1.26	1.06–1.50	0.011
CK7	0.95	0.81–1.11	0.518	1.06	0.86–1.30	0.586
Ki67	1.30	0.99–1.71	0.059	1.25	0.97–1.59	0.082
P53	1.06	0.91–1.24	0.469	1.04	0.88–1.25	0.629

CA125, cancer antigen 125; ER, estrogen receptor; PR, progesterone receptor.
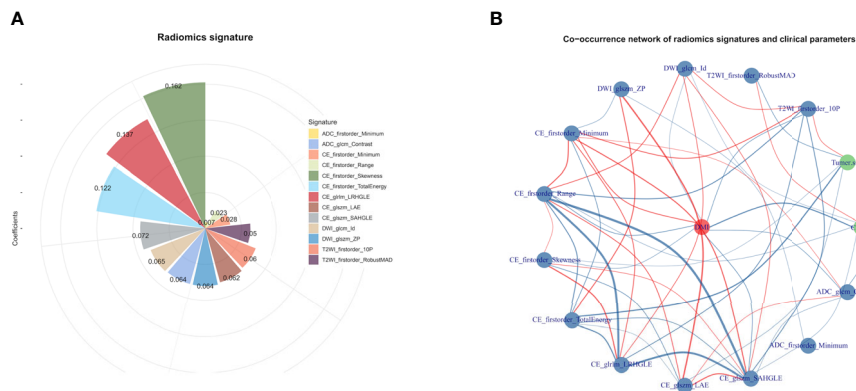
FIGURE 3 | (A) The selected features for DMI in G 1/2-EEC patients for ovarian preservation. The chart shows that the features contribute to the radiomics signature with their coefficients obtained from linear regression. **(B)** The co-occurrence matrix plots the correlations of the patients for DMI (red spot), clinical parameters (CA125 and tumor size), and radiomics features. The blue line indicates a negative correlation, and the red line indicates a positive correlation (p < 0.05).
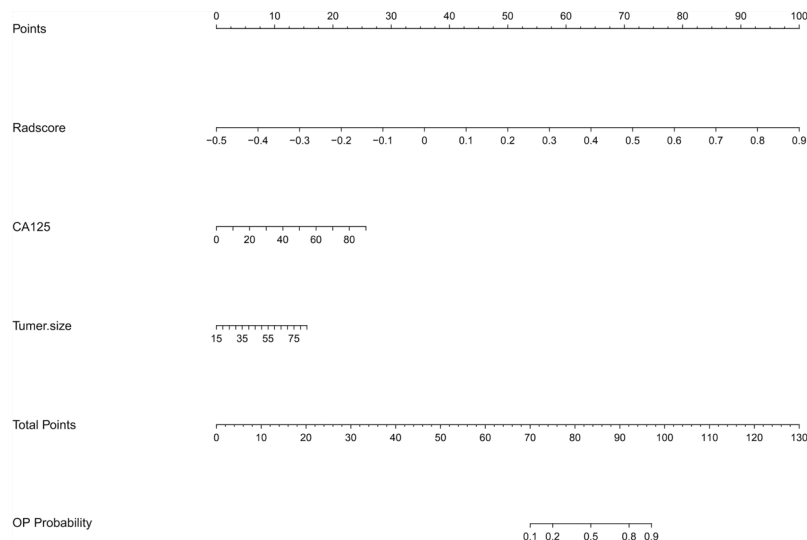
FIGURE 4 | The radiomics nomogram incorporating the selected radiomics features with clinical parameters (CA125 and tumor size) in the primary group. To use the nomogram, locating the margin according to the patient information, drawing a line straight up to the point axis to obtain the score associated with the margin, and repeating for the radscore. By summing the scores of each point and locating it on the total points and drawing a line straight down to the bottom axis, the estimated probability of DMI in G 1/2-EEC patients for ovarian preservation can be determined.
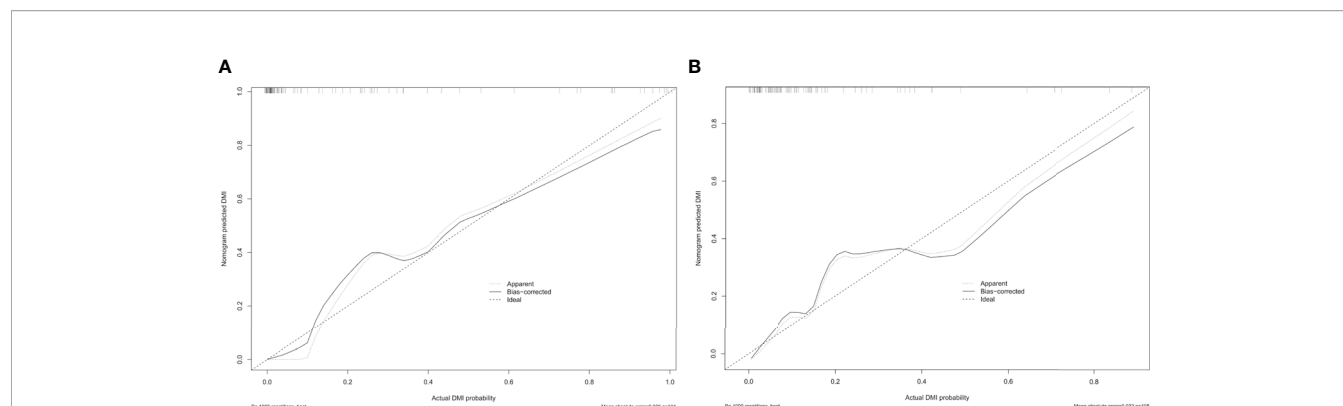
FIGURE 5 | The calibration curve of the radiomics nomogram for predicting DMI in G 1/2-EEC patients, **(A)** in the primary group (p = 0.987) and **(B)** in the validation group (p = 0.437), which indicates the agreement between the prediction value and the observed outcome of the radiomics nomogram.

Diagnostic Performance Assessment

The AUC, sensitivity, specificity, accuracy, and negative and positive predictive values (NPV and PPV) for the radiologists without and with the aid of the nomogram in the primary and validation groups for identifying DMI in G 1/2-EEC patients for OPT are shown in **Table 4** and **Figure 7**. For identifying DMI in G 1/2-EEC, ROC curve analyses showed that the AUCs were 0.92 and 0.70 for the radiomics signature; were 0.96 and 0.88 for the radiomics nomogram in the primary and validation groups, respectively; were 0.80, 0.86, 0.98, and 0.98 for radiologists 1 and 2 without and with the nomogram aid in the primary group; and were 0.82, 0.83, 0.94, and 0.94 in the validation group, respectively. The DeLong test showed that the AUCs of the radiomics nomogram were higher than that of radiologist 1 (p = 0.009), but not in the primary group of radiologist 2 (p = 0.061) and radiologists 1 and 2 in the validation group (p = 0.405 and 0.450, respectively). The AUC of the radiologists with the aid of the nomogram was higher than those of radiologists 1 and 2 alone in the primary (p < 0.001 and p = 0.009) and validation groups (p = 0.023 and 0.021). The AUCs of each selected clinical characteristic and radiomics feature are shown in the **Supplementary Table**.

The reclassification measures of discrimination confirmed that the radiologists with the aid of the nomogram performed better than the radiologists alone based on the whole data, with an NRI of 0.29 (95% CI: 0.15–0.43) and an IDI of 0.43 (95% CI: 0.32–0.54) for radiologist 1 and with an NRI of 0.23 (95% CI: 0.10–0.36) and an IDI of 0.37 (95% CI: 0.26–0.47) for radiologist

2 (both p < 0.01) (**Figure 8**). These results indicated that 37–43 patients per 100 patients would have an accurate assessment of DMI using the MRI radiomics nomogram.

DISCUSSION

In this study, a radiomics nomogram was developed by combining multiparametric MRI radiomics features and clinical information to assess the depth of MI in G1/2-EEC patients to select eligible OPT patients. The radiomics nomogram could aid radiologists in making decisions in selecting eligible OPT patients by assessing MI. NRI and IDI analyses showed a better clinical usefulness in the radiologists with the aid of the nomogram than in the radiologists alone for individually identifying MI in choosing eligible OPT patients.

In addition to the immediate consequences of hot flashes and vaginal atrophy, BSO causes surgical menopause in young women, which results in a number of long-term sequelae, including an increased risk of cardiovascular disease, osteoporosis, hip fracture, and cognitive dysfunction (25, 26). A meta-analysis showed that the relative risk of cardiovascular disease was 2.62 in women who underwent BSO (25). In young women, BSO alone tended to increase the risk of myocardial infarction with a relative risk of 1.6 (27). A prospective, population-based cohort study found that women who underwent prophylactic BSO before the age of 45 had a 67% increase in mortality, mainly in women who had not received

TABLE 3 | The certain cases of misjudgment with the reason in the radiomics nomogram and radiologists.

	Misjudgment	Adenomyosis	Leiomyoma	Cornua uteri	Small tumor size
Radiomics nomogram	SMI	2	2	2	15
	DMI	1	4	0	0
Radiologist 1	SMI	2	1	3	0
	DMI	6	6	1	0
Radiologist 2	SMI	2	1	2	0
	DMI	5	5	1	0

DMI, deep myometrial invasion; SMI, superficial myometrial invasion.
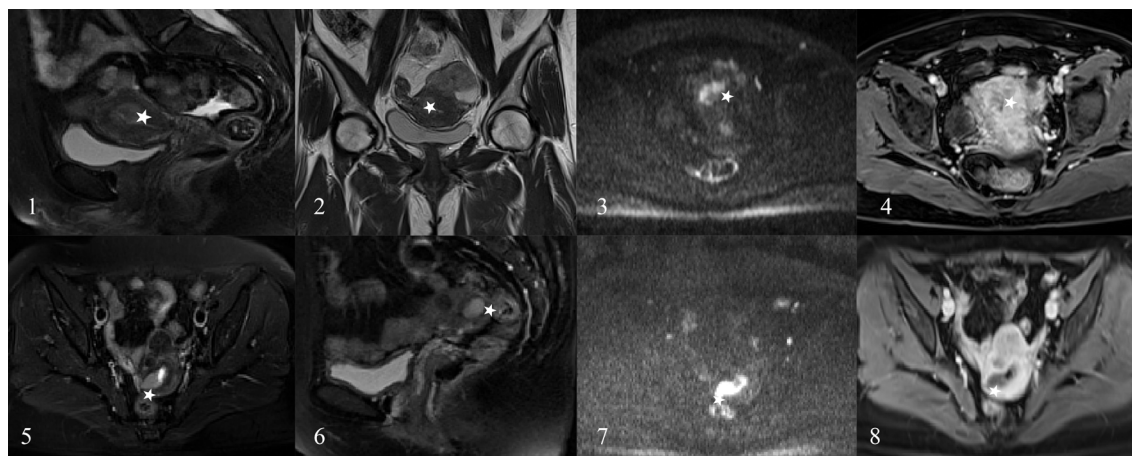
FIGURE 6 | The EC patients misjudged by radiologists. A 45-year-old woman (images 1 to 4) and a 43-year-old woman (images 5 to 8) who were diagnosed as the DMI by radiologists (stars) and diagnosed as superficial myometrial invasion (SMI) by the radiomics nomogram and proven the SMI by pathology.

TABLE 4 | The diagnostic performance of the radiologists without and with the aid of the nomogram in the primary and validation groups.

Model	AUC (95% CI)	p value[c]	SEN	SPE	ACC	NPV	PPV
Primary group							
Radiomics nomogram	0.96 (0.92–0.99)	0.009[a] 0.061[b]	100%	83.15%	86.5%	1.00	0.60
Radiologist 1	0.80 (0.70–0.91)		66.7%	94.0%	88.5%	0.92	0.74
Radiologist 1 + nomogram	0.98 (0.93–1.00)	<0.001[c]	95.2%	100%	99.0%	0.99	1.00
Radiologist 2	0.86 (0.76–0.95)		76.2%	95.2%	91.3%	0.94	0.80
Radiologist 2 + nomogram	0.98 (0.93–1.00)	0.009[c]	95.2%	100%	99.0%	0.99	1.00
Validation group							
Radiomics nomogram	0.88 (0.80–0.96)	0.405[a] 0.450[b]	72.2%	89.6%	86.7%	0.94	0.59
Radiologist 1	0.82 (0.71–0.93)		66.7%	97.7%	92.4%	0.93	0.86
Radiologist 1 + nomogram	0.94 (0.86–1.00)	0.023[c]	88.9%	98.8%	97.1%	0.98	0.94
Radiologist 2	0.83 (0.72–0.94)		66.7%	98.8%	93.3%	0.93	0.92
Radiologist 2 + nomogram	0.94 (0.87–1.00)	0.021[c]	88.9%	100%	98.1%	0.98	1.00

ACC, accuracy; AUC, area under the curve; CI, confidence interval; SEN, sensitivity; SPE, specificity; NPV, negative predictive value; PPV, positive predictive value.
[a]vs. radiologist 1.
[b]vs. radiologist 2.
[c]Without vs. with the aid of the nomogram.

estrogen treatment (28). Ovarian conservation had no effect on either cancer-specific or overall survival (6, 7). Therefore, to avoid the adverse consequences of BSO, there is a strong rationale for OPT in young early-stage EC patients.

Early-stage EC patients younger than 45 are recommended to receive OPT. The assessment of the depth of MI may be a challenge when 1) the tumor involves the uterine cornu; 2) the uterine anatomy is distorted by leiomyomas or adenomyosis; 3) a large endometrial tumor distends and thins the myometrium; and 4) the endometrial tumor is relatively isointense to the myometrium on T2WI. In these clinical scenarios, radiologists have difficulty assessing MI properly and should be aware of

possible tumor overstaging (29). Under these circumstances, radiomics nomograms may be a particularly useful tool to improve the delineation of tumor margins and to avoid overestimation of tumor extent, as shown in this study.

Recently, a computerized deep-learning model was developed to automatically evaluate the depth of MI in EC patients, with a sensitivity of 66.6% and a specificity of 87.5%. The results showed a better and more time-efficient performance in the deep learning model than the radiologists (14). In contrast, our radiomics nomogram model combined MRI-based radiomics features and the clinical characteristics (tumor size and CA125) to yield a high accuracy in assessing the DMI of early-stage EC
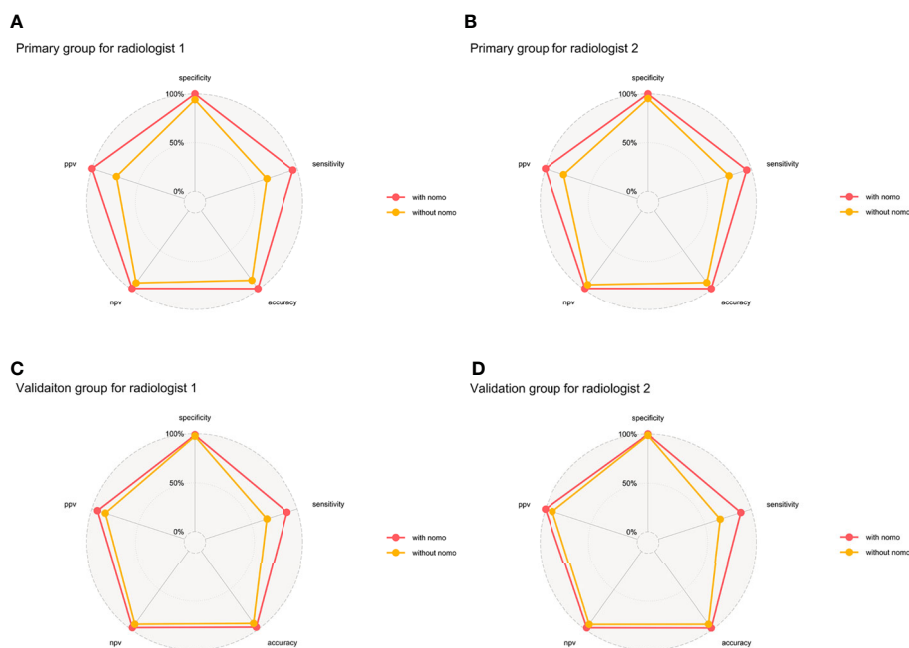
FIGURE 7 | Binary diagnosis of the two radiologists without and with the aid of a nomogram. **(A, B)** are for the primary group; **(C, D)** are for the validation group. PPV, positive predictive value; NPV, negative predictive value.
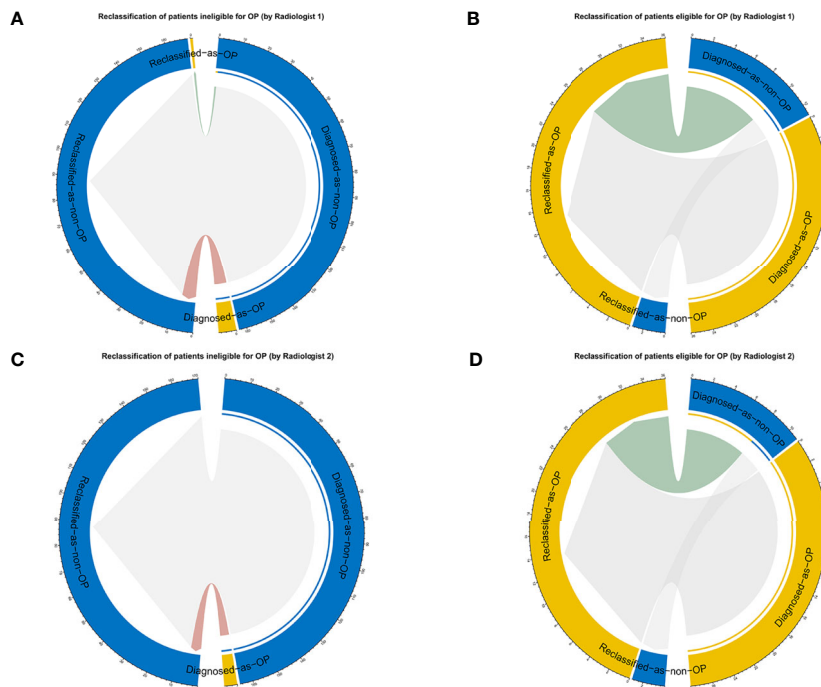
FIGURE 8 | The reclassification results are shown as circle plots. Reclassification of patients for different groups (**A, B** for radiologist 1, and **C, D** for radiologist 2). Groups were illustrated according to the molder of the radiologists with the aid of a nomogram. OP, ovarian preservation.

patients. The radiomics nomogram could generate a certain possibility of DMI for each patient to help radiologists assess the depth of MI.

Some studies have suggested that MRI-based texture analysis could be helpful in determining the depth of MI in EC patients (13, 30). Ytre-Hauge et al. obtained an accuracy of 78% for DMI detection, which was significantly higher than that of the radiologists reading (accuracy of 70%) in the same population (30). A recent study used MRI radiomics-powered machine learning to help radiologists evaluate the presence of DMI, yielding an accuracy of 86% and an AUC of 0.92 and increasing the radiologists' performance from 82% to 100% ($p = 0.48$). However, this study included only 54 patients and extracted features only from T2WI (31).

In our study, the multiparametric MRI radiomics nomogram was generated, which contributed to good diagnostic performance by unraveling more comprehensive information about tumor heterogeneity. The difference between our study and previous studies was that our nomogram was used to offer the radiologists a certain possibility of DMI and gave them a hint of the depth of MI. When radiologists face specific perplexing clinical scenarios, this radiomics nomogram could help them obtain a more confident diagnosis. Furthermore, the reclassification framework was used to provide an outcome prediction analysis of clinical decision-making. The clinical benefits were significantly improved, with IDIs of 0.43 and 0.37 in radiologists 1 and 2, respectively, which indicated that 37–43 out of 100 patients would be reclassified correctly from the radiomics-aided radiologists' prediction compared to the radiologists alone.

There were some limitations in our study. First, we did not include high-order wavelet features because previous studies suggested that wavelet features were not stable and lacked reasonable clinical interpretation (32). Second, this was a single-center scanner study; therefore, our results should be validated on data from multiple centers and from different scanners prior to clinical implementation. Third, the deep-learning based features were not investigated although some studies of other cancers showed a good performance (33–35). Last, the imbalance of the DMI and SMI datasets was not balanced by using any techniques such as the synthetic minority oversampling technique; however, we tried to select robust and reproducible features with a stable diagnostic performance.

In conclusion, the multiparametric MRI-based radiomics nomogram outperformed the radiologists in assessing the depth of MI in G 1/2-EEC patients younger than 45 years and for selecting eligible OPT patients. It could help radiologists significantly improve the predictive performance of MI status.

DATA AVAILABILITY STATEMENT

The raw data supporting the conclusions of this article will be made available by the authors, without undue reservation.

ETHICS STATEMENT

The studies involving human participants were reviewed and approved by the ethics committee of Obstetrics & Gynecology Hospital, Fudan University. The patients/participants provided their written informed consent to participate in this study.

AUTHOR CONTRIBUTIONS

The study supervisor is JQ. The authors responsible for the study concept, design, and implementation are BY and XM. YL contributed to the data analysis and performed the statistical analysis. SD helped in giving the R code. BY, XM, and GZ contributed to the data acquisition. BY and YL conducted the ROI drawing. BY was the major contributor and contributed to writing the first draft. JQ revised and edited the manuscript. All authors contributed to the article and approved the submitted version.

FUNDING

SUPPLEMENTARY MATERIAL

The Supplementary Material for this article can be found online at: https://www.frontiersin.org/articles/10.3389/fonc.2021.730281/full#supplementary-material

REFERENCES

1. Siegel RL, Miller KD, Fuchs HE, Jemal A. Cancer Statistics, 2021. *CA Cancer J Clin* (2021) 71:7–33. doi: 10.3322/caac.21654:10.3322/caac.21654
2. Lee NK, Cheung MK, Shin JY, Husain A, Teng NN, Berek JS, et al. Prognostic Factors for Uterine Cancer in Reproductive-Aged Women. *Obstet Gynecol* (2007) 109:655–62. doi: 10.1097/01.AOG.0000255980.88205.15
3. Moeini A, Machida H, Takiuchi T, Blake EA, Hom MS, Miki T, et al. Association of Nonalcoholic Fatty Liver Disease and Venous Thromboembolism in Women With Endometrial Cancer. *Clin Appl Thromb Hemost* (2017) 23:1018–27. doi: 10.1177/1076029616665925
4. Matsuo K, Gualtieri MR, Cahoon SS, Jung CE, Paulson RJ, Shoupe D, et al. Surgical Menopause and Increased Risk of Nonalcoholic Fatty Liver Disease in Endometrial Cancer. *Menopause* (2016) 23:189–96. doi: 10.1097/GME.0000000000000500
5. Matsuo K, Machida H, Shoupe D, Melamed A, Muderspach LI, Roman LD, et al. Ovarian Conservation and Overall Survival in Young Women With Early-Stage Low-Grade Endometrial Cancer. *Obstet Gynecol* (2016) 128:761–70. doi: 10.1097/AOG.0000000000001647
6. Wright JD, Jorge S, Tergas AI, Hou JY, Burke WM, Huang Y, et al. Utilization and Outcomes of Ovarian Conservation in Premenopausal Women With Endometrial Cancer. *Obstet Gynecol* (2016) 127:101–8. doi: 10.1097/AOG.0000000000001181

7. Wright JD, Buck AM, Shah M, Burke WM, Schiff PB, Herzog TJ. Safety of Ovarian Preservation in Premenopausal Women With Endometrial Cancer. *J Clin Oncol* (2009) 27:1214–9. doi: 10.1200/JCO.2008.19.8150

8. Baiocchi G, Clemente AG, Mantoan H, da Costa WL Jr, Bovolim G, Guimaraes APG, et al. Adnexal Involvement in Endometrial Cancer: Prognostic Factors and Implications for Ovarian Preservation. *Ann Surg Oncol* (2020) 27:2822–6. doi: 10.1245/s10434-020-08261-8

9. Matsuo K, Cripe JC, Kurnit KC, Kaneda M, Garneau AS, Glaser GE, et al. Recurrence, Death, and Secondary Malignancy After Ovarian Conservation for Young Women With Early-Stage Low-Grade Endometrial Cancer. *Gynecol Oncol* (2019) 155:39–50. doi: 10.1016/j.ygyno.2019.08.007

10. Kinjyo Y, Kudaka W, Ooyama T, Inamine M, Nagai Y, Aoki Y. Ovarian Preservation in Young Women With Endometrial Cancer of Endometrioid Histology. *Acta Obstet Gynecol Scand* (2015) 94:430–4. doi: 10.1111/aogs.12588

11. Nougaret S, Reinhold C, Alsharif SS, Addley H, Arceneau J, Molinari N, et al. Endometrial Cancer: Combined MR Volumetry and Diffusion-Weighted Imaging for Assessment of Myometrial and Lymphovascular Invasion and Tumor Grade. *Radiology* (2015) 276:797–808. doi: 10.1148/radiol.15141212

12. Lin G, Ng KK, Chang CJ, Wang JJ, Ho KC, Yen TC, et al. Myometrial Invasion in Endometrial Cancer: Diagnostic Accuracy of Diffusion-Weighted 3.0-T MR Imaging–Initial Experience. *Radiology* (2009) 250:784–92. doi: 10.1148/radiol.2503080874

13. Ueno Y, Forghani B, Forghani R, Dohan A, Zeng XZ, Chamming's F, et al. Endometrial Carcinoma: MR Imaging-Based Texture Model for Preoperative Risk Stratification-A Preliminary Analysis. *Radiology* (2017) 284:748–57. doi: 10.1148/radiol.2017161950

14. Chen X, Wang Y, Shen M, Yang B, Zhou Q, Yi Y, et al. Deep Learning for the Determination of Myometrial Invasion Depth and Automatic Lesion Identification in Endometrial Cancer MR Imaging: A Preliminary Study in a Single Institution. *Eur Radiol* (2020) 30:4985–94. doi: 10.1007/s00330-020-06870-1

15. Todo Y, Watari H, Okamoto K, Hareyama H, Minobe S, Kato H, et al. Tumor Volume Successively Reflects the State of Disease Progression in Endometrial Cancer. *Gynecol Oncol* (2013) 129:472–7. doi: 10.1016/j.ygyno.2013.02.034

16. Tang XR, Li YQ, Liang SB, Jiang W, Liu F, Ge WX, et al. Development and Validation of a Gene Expression-Based Signature to Predict Distant Metastasis in Locoregionally Advanced Nasopharyngeal Carcinoma: A Retrospective, Multicentre, Cohort Study. *Lancet Oncol* (2018) 19:382–93. doi: 10.1016/S1470-2045(18)30080-9

17. Zhang Y, Chen W, Yue X, Shen J, Gao C, Pang P, et al. Development of a Novel, Multi-Parametric, MRI-Based Radiomic Nomogram for Differentiating Between Clinically Significant and Insignificant Prostate Cancer. *Front Oncol* (2020) 10:888. doi: 10.3389/fonc.2020.00888

18. Yan BC, Li Y, Ma FH, Zhang GF, Feng F, Sun MH, et al. Radiologists With MRI-Based Radiomics Aids to Predict the Pelvic Lymph Node Metastasis in Endometrial Cancer: A Multicenter Study. *Eur Radiol* (2021) 31:411–22. doi: 10.1007/s00330-020-07099-8

19. Xie CY, Hu YH, Ho JW, Han LJ, Yang H, Wen J, et al. Using Genomics Feature Selection Method in Radiomics Pipeline Improves Prognostication Performance in Locally Advanced Esophageal Squamous Cell Carcinoma-A Pilot Study. *Cancers (Basel)* (2021) 13:2145. doi: 10.3390/cancers13092145

20. Koo TK, Li MY. A Guideline of Selecting and Reporting Intraclass Correlation Coefficients for Reliability Research. *J Chiropr Med* (2016) 15:155–63. doi: 10.1016/j.jcm.2016.02.012

21. Mukaka MM. Statistics Corner: A Guide to Appropriate Use of Correlation Coefficient in Medical Research. *Malawi Med J* (2012) 24:69–71.

22. Sahin H, Sarioglu FC, Bagci M, Karadeniz T, Uluer H, Sanci M. Preoperative Magnetic Resonance Volumetry in Predicting Myometrial Invasion, Lymphovascular Space Invasion, and Tumor Grade: Is it Valuable in International Federation of Gynecology and Obstetrics Stage I Endometrial Cancer? *Int J Gynecol Cancer* (2018) 28:666–74. doi: 10.1097/IGC.0000000000001208

23. Fasmer KE, Bjørnerud A, Ytre-Hauge S, Grüner R, Tangen IL, Werner HM, et al. Preoperative Quantitative Dynamic Contrast-Enhanced MRI and Diffusion-Weighted Imaging Predict Aggressive Disease in Endometrial Cancer. *Acta Radiol* (2018) 59:1010–7. doi: 10.1177/0284185117740932

24. Modarres-Gilani M, Vaezi M, Shariat M, Zamani N, Nourizadeh R. The Prognostic Role of Preoperative Serum CA125 Levels in Patients With Advanced Endometrial Carcinoma. *Cancer Biomark* (2017) 20:135–41. doi: 10.3233/CBM-160529

25. Atsma F, Bartelink MLEL, Grobbee DE, van der Schouw YT. Postmenopausal Status and Early Menopause as Independent Risk Factors for Cardiovascular Disease: A Meta-Analysis. *Menopause-the J North Am Menopause Society* (2006) 13:265–79. doi: 10.1097/01.gme.0000218683.97338.ea

26. Rocca WA, Bower JH, Maraganore DM, Ahlskog JE, Grossardt BR, de Andrade M, et al. Increased Risk of Cognitive Impairment or Dementia in Women Who Underwent Oophorectomy Before Menopause. *Neurology* (2007) 69:1074–83. doi: 10.1212/01.wnl.0000276984.19542.e6

27. Falkeborn M, Schairer C, Naessen T, Persson I. Risk of Myocardial Infarction After Oophorectomy and Hysterectomy. *J Clin Epidemiol* (2000) 53:832–7. doi: 10.1016/s0895-4356(00)00187-6

28. Rocca WA, Grossardt BR, de Andrade M, Malkasian GD, Melton LJ. Survival Patterns After Oophorectomy in Premenopausal Women: A Population-Based Cohort Study. *Lancet Oncol* (2006) 7:821–8. doi: 10.1016/S1470-2045(06)70869-5

29. Nougaret S, Horta M, Sala E, Lakhman Y, Thomassin-Naggara I, Kido A, et al. Endometrial Cancer MRI Staging: Updated Guidelines of the European Society of Urogenital Radiology. *Eur Radiol* (2019) 29:792–805. doi: 10.1007/s00330-018-5515-y

30. Ytre-Hauge S, Dybvik JA, Lundervold A, Salvesen ØO, Krakstad C, Fasmer KE, et al. Preoperative Tumor Texture Analysis on MRI Predicts High-Risk Disease and Reduced Survival in Endometrial Cancer. *J Magn Reson Imaging* (2018) 48:1637–47. doi: 10.1002/jmri.26184

31. Stanzione A, Cuocolo R, Del Grosso R, Nardiello A, Romeo V, Travaglino A, et al. Deep Myometrial Infiltration of Endometrial Cancer on MRI: A Radiomics-Powered Machine Learning Pilot Study. *Acad Radiol* (2021) 28:737–44. doi: 10.1016/j.acra.2020.02.028

32. Fiset S, Welch ML, Weiss J, Pintilie M, Conway JL, Milosevic M, et al. Repeatability and Reproducibility of MRI-Based Radiomic Features in Cervical Cancer. *Radiother Oncol* (2019) 135:107–14. doi: 10.1016/j.radonc.2019.03.001

33. Liu F, Liu D, Wang K, Xie X, Su L, Kuang M, et al. Deep Learning Radiomics Based on Contrast-Enhanced Ultrasound Might Optimize Curative Treatments for Very-Early or Early-Stage Hepatocellular Carcinoma Patients. *Liver Cancer* (2020) 9:397–413. doi: 10.1159/000505694

34. Cheng NM, Yao J, Cai J, Ye X, Zhao S, Zhao K, et al. Deep Learning for Fully Automated Prediction of Overall Survival in Patients With Oropharyngeal Cancer Using FDG-PET Imaging. *Clin Cancer Res* (2021) 27:3948–59. doi: 10.1158/1078-0432

35. Jiang Y, Jin C, Yu H, Wu J, Chen C, Yuan Q, et al. Development and Validation of a Deep Learning CT Signature to Predict Survival and Chemotherapy Benefit in Gastric Cancer: A Multicenter, Retrospective Study. *Ann Surg* (2020). doi: 10.1097/SLA.0000000000003778

Detection of HPV and Human Chromosome Sites by Dual-Color Fluorescence *In Situ* Hybridization Reveals Recurrent HPV Integration Sites and Heterogeneity in Cervical Cancer

Jinfeng Xiong[1†], Jing Cheng[2†], Hui Shen[1], Ci Ren[1], Liming Wang[1], Chun Gao[1], Tong Zhu[1], Xiaomin Li[1], Wencheng Ding[1], Da Zhu[1*] and Hui Wang[1*]

[1] Department of Obstetrics and Gynecology, Tongji Hospital, Tongji Medical College, Huazhong University of Science and Technology, Wuhan, China, [2] Department of Obstetrics and Gynecology, Zhongnan Hospital, Wuhan University, Wuhan, China

Human papillomavirus (HPV) integration in the human genome is suggested to be an important cause of cervical cancer. With the development of sequencing technologies, an increasing number of integration "hotspots" have been identified. However, this HPV integration information was derived from analysis of whole cervical cancer tissue, and we know very little about the integration in different cancer cell subgroups or individual cancer cells. This study optimized the preparation of probes and provided a dual-color fluorescence *in situ* hybridization (FISH) method to detect HPV integration sites in paraffin-embedded cervical cancer samples. We used both HPV probes and site-specific probes: 3p14 (*FHIT*), 8q24 (*MYC*), 13q22 (*KLF5/KLF12*), 3q28 (*TP63*), and 5p15 (*TERT*). We detected HPV signals in 75 of the 96 cases of cervical cancer; 62 cases showed punctate signals, and 13 cases showed diffuse punctate signals. We identified 3p14 as a high-frequency HPV integration site in 4 cervical cancer cases. HPV integration at 8p14 occurred in 2 cases of cervical cancer. In the same cervical cancer tissue of sample No.1321, two distinct subgroups of cells were observed based on the HPV probe but showed no difference in cell and nucleus morphology. Our study provides a new method to investigate the frequent HPV integration sites in cervical cancer and reports the heterogeneity within cervical cancer from the perspective of HPV integration.

Keywords: human papillomavirus, HPV integration, FISH, cervical cancer, site-specific

INTRODUCTION

Cervical cancer remains the leading cause of gynecological tumor-related mortality worldwide and the second most common malignancy in women, with 570,000 women diagnosed with cervical cancer and 311,000 dying from the disease each year (1, 2).

Most HPV infections are cleared by the immune system, but in some cases, the infection persists. Persistent infection with high-risk HPV leads to cervical intraepithelial neoplasia (CIN), which occasionally develops into cervical cancer (3). High-risk HPV types include 16, 18, 31, 33, 58 and other subtypes. HPV16 and 18 infection is common and can be detected in approximately 70% of cervical cancer cases. After infection, the virus can remain in the episome or integrate into the human genome, and the two patterns may coexist (4).

Recent studies have suggested that the integration of HPV in the human genome is an important cause of cervical cancer. Integration can preserve the upstream regulatory region (URR) of the virus. This HPV replication initiation region in the human genome is not stable but activates the cell's DNA replication and other systems, which is an important "trigger" for cancer (5). The integration of HPV DNA into the human genome causes various genetic changes, such as oncogene amplification, inactivation of tumor suppressor genes, chromosomal rearrangement, and genomic instability. Integration can occur near key genes, leading to increased instability near integration sites in the human cell genome, resulting in local chromatin structural and functional changes and even the formation of new virus-human gene fusion transcripts in response to URRs of the virus (6, 7). In 2015, whole-genome sequencing and high-throughput virus capture sequencing methods identified up to 3,667 HPV integration breakpoints in cervical neoplasms (8). Frequent integration has been reported in genes associated with tumor progression, such as the oncogene MYC. It has been reported that loss of function of the tumor suppressor gene RAD51B after HPV DNA insertion affects DNA repair pathways and genomic instability in tumors (9).

Increasing research on HPV integration has led to the recognition of HPV integration status as a potential biomarker for the prediction of diagnosis, progression, and survival and even as a biomarker for cancer screening (10). With the development of high-throughput sequencing technologies (e.g., whole-genome sequencing, transcriptome sequencing, HIVID, etc.), an increasing number of integration "hotspots" have been identified (8, 9). However, this HPV integration information was derived from analyses of the whole cervical cancer tissue, and we know very little about the integration in different cancer cell subgroups or individual cancer cells. To visually display the more refined HPV integration at the single tumor cell level, this study optimized the preparation of probes and provided a dual-color FISH method to verify the HPV integration sites in paraffin-embedded cervical cancer samples. By preserving the original morphology and spatial structure of tumor tissue, we provide a new method to investigate the relationship between HPV integration and cervical carcinogenesis.

MATERIALS AND METHODS

Tissue Material

Formalin-fixed and paraffin wax-embedded cervical cancer samples were selected from the Department of Pathology, Tongji Hospital, Wuhan, China. All the samples were reviewed and confirmed independently by two pathologists, and cases with discrepancies were discussed until a consensus was reached. Samples with poor morphology or too many lymphocytes were excluded.

Clinical characteristics were obtained from patient charts. The TNM staging system, which is based on surgical and pathological reports, was used in this study to evaluate cervical cancer patients. We collected a total of 96 samples: 93 squamous cell carcinoma (SCC) samples, 3 adenocarcinoma (AD) samples. The study was approved by the hospital's ethics committee.

Probe Selection and Labeling Procedures

Bacterial artificial chromosome (BAC) plasmids for 8q24 (RP11-1145O20), 3p14 (RP11-191B8), 3q28 (RP11-373I6), 5p15 (RP11-326E20) and 13q22 (RP11-179I20) were purchased from Life Technologies (California, America). The whole-genome plasmid of HPV types 16 and 18 was a gift from Haraud zur Hausen. The probes were labeled by standard nick translation with biotin- or digoxigenin-dUTPs. The biotin-labeled HPV probes and digoxigenin-labeled BAC probes were then coprecipitated with human Cot-1 DNA and salmon sperm DNA. Pelleted probes were then dissolved in a hybridization buffer composed of 50% formamide, 2×SSC, and 10% dextran sulfate. The detailed protocol and parameters of HPV-BAC dual-color probes are provided in the **Supplementary Material**.

Tissue Pretreatment

Four-micrometer thick paraffin wax tissue sections were dewaxed, dehydrated with 100% ethanol for 3 min twice before air drying, and pretreated with 3% H_2O_2 for 10 min at room temperature. The slides were incubated in 1 M NaSCN for 20 min at 80°C, followed by digestion with 4 mg/ml pepsin (1:3000, Sigma) in 0.02 M HCl for 12 min at 37°C. The slides were rinsed 2 times in 2× SSC, postfixed in 4% formaldehyde for 10 min at room temperature, and dehydrated in an ascending ethanol series.

Probes and target DNA were denatured simultaneously for 7 min at 90°C before hybridization overnight at 37°C. After hybridization, the preparations were washed stringently in 50% formamide (3 × 5 min) and 2× SSC at 43°C.

Probe Detection

The biotin- and digoxigenin-labeled probes were detected consecutively using the dual-color tyramide signal amplification (TSA) procedure. The biotin-labeled probe was detected by streptavidin-HRP (1:100, Perkin Elmer). Then, the first amplification reaction was carried out under a coverslip by applying 50 μl of Cy3-tyramide (1:50, Perkin Elmer) for 20 min at room temperature. Thereafter, the slides were soaked in blocking reagent (Perkin Elmer) for 15 min at room temperature to block the remaining peroxidase activity. Subsequently, the digoxigenin-labeled probe was detected by anti-digoxigenin-HRP (1:200,

Roche), followed by TSA amplification using FITC-tyramide (1:50, Perkin Elmer). Finally, the slides were washed in 4× SSC, dehydrated in an ascending ethanol series, and mounted in Vectashield (Vector Laboratories).

Microscopic Imaging and Evaluation of FISH Results

Images were recorded with a fluorescence microscope (Olympus BX53) equipped with FITC, TRITC, and DAPI bandpass filters. A minimum of 100 nuclei in each sample were observed for HPV integration site evaluation. Among the cells containing HPV signals, the ratio of cells with colocalized HPV probe signals and BAC probe signals was calculated. Samples with a ratio greater than 60% were evaluated for HPV integration in a specific site.

Control

HPV and BAC probe hybridization on HPV-positive cell lines (SiHa, HeLa and CaSki) was used as a control for HPV integration site detection. On sample tissue sections, BAC probes were also used as a control for effective hybridization.

RESULTS

HPV Integration in Cervical Cancer Cell Lines and Cervical Cancer Tissues Can Be Detected by Dual-Color Fluorescence *In Situ* Hybridization

HPV16/18 probes were hybridized in SiHa and CaSki cells, two smaller HPV signals were observed in SiHa cells with only two

copies of HPV16 (**Figure 1A**), and 7 to 8 signals of different sizes were observed in dots and clumps in CaSki cells with 500 HPV16/18 copies (**Figure 1D**). We observed that with the increase in HPV integrated copy number in cells, the fluorescence intensity and area of the HPV signal also increased, but the relationship was not linear. The results of hybridization in SiHa cells prove that our HPV probe has sufficient sensitivity.

In previous studies, only HPV probes were used to study the presence and amount of HPV integration. To further study the integration sites of HPV, we explored the simultaneous hybridization of HPV probes and BAC plasmid probes into cervical cancer cells. Since previous studies suggested that two HPV16 copies of SiHa were integrated near the KLF5 gene at 13q22, our experiment showed that the HPV signal and the BAC plasmid probe targeting the 13q22 (RP11-315L12) signal were colocalized, as expected (**Figures 1A–C**). Chromosomal site probes can be used to indicate whether HPV is integrated at the site and can be used as a control for whether hybridization is successful. The results from SiHa cells confirmed the credibility of our dual-color probe.

We further explored the application of dual-color probes in paraffin sections of cervical cancer to prepare for possible clinical application. The *in situ* hybridization methods (including experimental procedures and various parameters) in cultured cells and paraffin sections are completely different. Through a review of the literature and experiments (11–13), we confirmed that both the sodium bisulfite and sodium thiocyanide methods are feasible. We found that the sodium bisulfite method was milder and preserved the nucleus well, but it often failed in aged
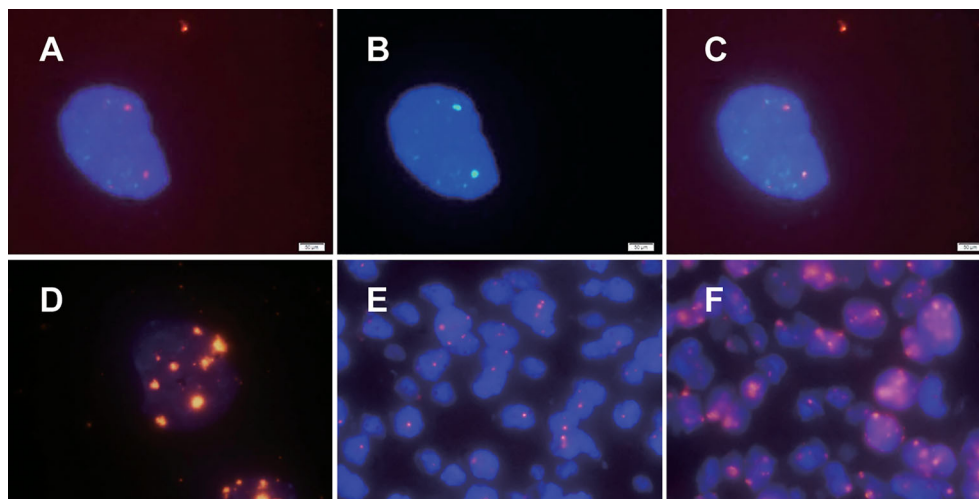
FIGURE 1 | HPV signal patterns in cervical cancer cell lines and cervical cancer paraffin sections detected by dual-color FISH. The fluorescence intensity and area of the HPV signal were observed to increase with increasing HPV integrated copy number in cells, but the relationship was not linear. HPV signals in SiHa and CaSki cells are illustrated in **(A, D)**, respectively. **(B)** The specific chromosomal site (Bacterial artificial chromosome, BAC) probe targeting the 13q22 in SiHa. As shown in **(C)**, the HPV signal and the specific chromosomal site probe targeting the 13q22 (RP11-315L12) signal were colocalized. There were two main types of HPV signals in paraffin specimens of cervical cancer: punctate signals and diffuse-punctate signals. The punctate signals indicate integrated HPV **(E)**, while diffuse signals indicate the presence of episomal HPV at the same time **(F)**.

paraffin sections. The sodium thiocyanide method is not easy to use, but the treatment is more complete, and it also has a higher success rate of hybridization for aged paraffin sections. To study the integration sites of HPV, we used the sodium thiocyanide method in this study. There were two main types of HPV signals in cervical cancer paraffin sections: punctate signals and diffuse-punctate signals. The punctate signal suggests integrated HPV (**Figure 1E**), and the diffuse signal suggests the presence of episomal HPV at the same time (**Figure 1F**).

Integration of HPV at Human Chromosomal Loci in Cervical Cancer Tissues

We detected HPV signals in 75 cases of cervical cancer; 62 cases showed punctate signals, and 13 cases showed diffuse punctate signals (**Table 1**). We did not observe a simple diffuse signal in cervical cancer, which is consistent with the findings that HPV is generally integrated in cervical cancer in previous studies (12, 14).

Our criteria for determining HPV integration were as follows: when the percentage was greater than 60% (cells showing colocalized HPV signals and chromosomal locus probe signals/cells containing HPV signals), we concluded that HPV was integrated at this site (**Figures 2A–C**); otherwise, there was no integration at this site (**Figures 2D–F**). Based on a review of the literature on HPV integration sites and genomic alterations in cervical cancer (8, 15), we prepared probes targeting five regions of the human chromosome: 3p14 containing *FHIT*, 8q24 containing *MYC*, 13q22 containing *KLF5/KLF12*, 3q28 containing *TP63*, and 5p15 containing *TERT*. We detected 3p14 as a high-frequency HPV integration site in 4 cervical cancers. HPV integration at 8p14 occurred in 2 cases of cervical cancer. We found HPV integration in one patient each at 5p15 and 13q22. We did not detect HPV integration at 3q28, although 3q28 shows the greatest copy number amplification in cervical cancer and is associated with CIN progression (16) (**Table 1**).

HPV Signaling Suggests Clonality and Heterogeneity in Cervical Cancer Tissue

In contrast to PCR or high-throughput sequencing methods, the FISH method can detect HPV integration without destroying tissue morphology. Using an HPV probe as a guide, we observed major differences (both clonality and heterogeneity) in cancer cells within cervical cancer. For example, in sample No. 1321, two groups of cancer cells in the same cervical cancer tissue showed no difference in cell and nucleus morphology after HE staining and were pathologically identified as the same type of cells (**Figures 3A–C**). However, two distinct subgroups of cells were observed by the HPV probe. Every cell in the a group showed HPV integration, the HPV signal area was large, and the intensity was high, suggesting intense HPV integration. In the b group, some of the cells showed HPV integration, the HPV signal area was small, and the intensity was low, suggesting low integration (**Figures 3D–F**).

DISCUSSION

Currently, many studies have suggested that HPV integration plays an important role in the development of cervical cancer, but our knowledge of HPV integration is still insufficient. The reasons are as follows: First, HPV integration sites in the human genome are numerous and scattered, and different studies have reported different integration hotspots (6, 8, 17–20). Previous studies have detected high-frequency HPV integration sites and attempted to explain the relationship between HPV integration and the progression of cervical cancer by using high-frequency HPV integration sites. There is no conclusion yet regarding whether HPV integration is the driver of cervical cancer or the consequence of human cell genome instability during cervical cancer development (21). Second, the HPV sequence is not completely integrated into the human cell genome; only fragments are integrated (14). The integrated fragments are different in different samples and different at different sites in the same sample (8). Previous studies suggested that integrated HPV breaks in the E2 region and retains the viral oncogenes E6 and E7 (21), but the results of high-throughput sequencing suggest that this is not always the case (8). It is still unclear whether every integrated HPV fragment has a role. To elucidate the relationship between HPV integration and cervical cancer and the carcinogenic mechanism of HPV integration, we must be able to truly and accurately detect HPV integration.

Previous studies on HPV integration mainly include PCR, high-throughput sequencing, and *in situ* hybridization, each of which has advantages and disadvantages. PCR technology includes DIPS-PCR, APOT-PCR and others, which use specially designed primers to amplify HPV-human fusion fragments (22, 23). Considering the different specificities of primers, PCR can indeed detect some HPV-human fusion fragments, but some will be missed. High-throughput sequencing technologies, including WGS, RNA-seq, and HIVID, are more efficient and comprehensive in detecting HPV-human fusion fragments (8, 9). High-throughput sequencing technology provides an overall picture of HPV integration in a given tissue. There is a lack of information on differences in HPV integration in the tissue, and validation by other techniques (PCR, FISH) is required.

Previous studies on HPV integration using FISH techniques mainly investigated the association between HPV integration and CIN progression (12, 24). At present, there are few studies on the simultaneous detection of HPV integration and a specific chromosomal locus in cervical cancer paraffin specimens. The main obstacle is the preparation of FISH probes. The specific chromosomal site probe was nick translated from the BAC clones. The BAC was sufficiently long, and even if HPV integration led to the loss of some chromosomal fragments, the chromosomal site-specific probes still showed signals, such as at 3p14. Therefore, regardless of whether the DNA copy number at the integration site increases or decreases, we can effectively detect the HPV integration site with colocalization of two colors.

The advantage of paraffin specimens over primary cultured cancer cells is that paraffin specimens are easier to obtain and

TABLE 1 | Detailed information on HPV integration sites detected by FISH.

Sample ID	Pathology	Stage	HPV16/18		HPV integration	Chromosomal site				
			Punctate	Diffuse		8q24	3p14	3q28	5p15	3q22
1005	SCC	II	▲			2%			2%	
1007	SCC	II	▲			9%		17%	5%	
1009	SCC	I	▲			19%	17%	47%	11%	10%
1011	SCC	II	▲			7%		6%	2%	10%
1013	SCC	I	▲		3p14	3%	**88%**	7%	24%	4%
1015	SCC	I	▲		5p15			6%	**99%**	9%
1017	SCC	II	▲			2%				5%
1023	SCC	I	▲			9%				
1025	SCC	II	▲			4%	3%	28%	26%	8%
1053	SCC	I	▲				3%	13%	6%	5%
1055	SCC	I	▲				2%		11%	7%
1071	SCC	I	▲					5%		2%
1073	SCC	I	▲	▲				7%	3%	13%
1075	SCC	II	▲	▲		10%	11%	11%	2%	5%
1083	SCC	I	▲	▲		19%	22%	6%	15%	6%
1087	SCC	II	▲					10%		6%
1095	SCC	I	▲							4%
1097	SCC	I	▲					3%	7%	4%
1101	SCC	II	▲			4%			5%	
1103	SCC	I	▲	▲		10%	11%	8%	24%	
1111	SCC	I	▲	▲		11%	6%	10%	8%	3%
1117	SCC	II	▲				6%			
1123	SCC	I	▲					14%		4%
1135	AD	I	▲							
1141	SCC	I	▲						8%	3%
1142	SCC	I	▲			8%		27%	6%	
1143	SCC	II	▲			7%				
1151	SCC	II	▲		3p14		**67%**	16%	16%	
1162	SCC	I	▲			3%	4%			2%
1166	SCC	II	▲					4%	13%	11%
1168	SCC	II	▲					13%		
1169	SCC	I	▲	▲				12%	9%	
1173	SCC	II	▲		13q22			10%	13%	**83%**
1174	SCC	I	▲					7%	14%	8%
1175	SCC	II	▲						8%	
1293	SCC	III	▲		8q24	**100%**	8%		14%	18%
1295	SCC	I	▲	▲		6%	6%	21%	8%	18%
1297	SCC	I	▲				13%		12%	
1299	SCC	I	▲	▲		2%	5%	6%		9%
1301	SCC	I	▲				2%	4%	14%	10%
1303	SCC	III	▲	▲		2%	11%	12%	5%	26%
1305	SCC	II	▲			15%	3%		13%	
1307	SCC	I	▲							5%
1309	SCC	I	▲	▲				3%	14%	7%
1311	SCC	I	▲			9%			6%	23%
1313	AD	II	▲			10%		35%		12%
1317	SCC	II	▲				7%	5%	7%	
1319	SCC	I	▲					4%	10%	6%
1321	SCC	I	▲			5%		20%	27%	5%
1325	SCC	II	▲		3p14		**71%**	14%	11%	9%
1329	SCC	I	▲			6%	26%	1%	3%	5%
1331	SCC	II	▲				3%	26%	8%	5%
1335	SCC	I	▲				5%	15%	5%	4%
1339	SCC	II	▲				4%	13%	2%	20%
1342	SCC	I	▲		8q24	**67%**	3%		16%	
1343	SCC	I	▲			20%	13%	29%	14%	8%
1344	SCC	I	▲				4%	2%	3%	9%
1345	SCC	I	▲					8%	3%	5%
1346	SCC	III	▲	▲		12%	16%	5%	20%	17%
1347	SCC	I	▲	▲		27%		7%	6%	24%
1348	SCC	I	▲					2%	9%	16%

(Continued)

TABLE 1 | Continued

Sample ID	Pathology	Stage	HPV16/18		HPV integration	Chromosomal site				
			Punctate	Diffuse		8q24	3p14	3q28	5p15	3q22
1351	SCC	I	▲				4%		19%	2%
1352	SCC	I	▲							7%
1353	SCC	II	▲						5%	
1356	SCC	IV	▲					6%	12%	11%
1357	SCC	III	▲				3%	5%	18%	7%
1360	SCC	I	▲				6%	1%	7%	17%
1361	SCC	II	▲			6%	7%	2%	2%	10%
1362	SCC	II	▲				3%		17%	
1363	SCC	II	▲			4%	7%	9%	15%	17%
1364	SCC	II	▲				9%		5%	3%
1365	SCC	I	▲						14%	
1366	SCC	II	▲				5%			6%
1367	SCC	I	▲		3p14		**82%**	3%	9%	4%
1368	SCC	I	▲				2%		23%	2%

SCC, squamous cell carcinoma; AD, adenocarcinoma. The bold values indicate ratio more than 60%.

▲ *HPV16 positive and/or HPV18 positive.*
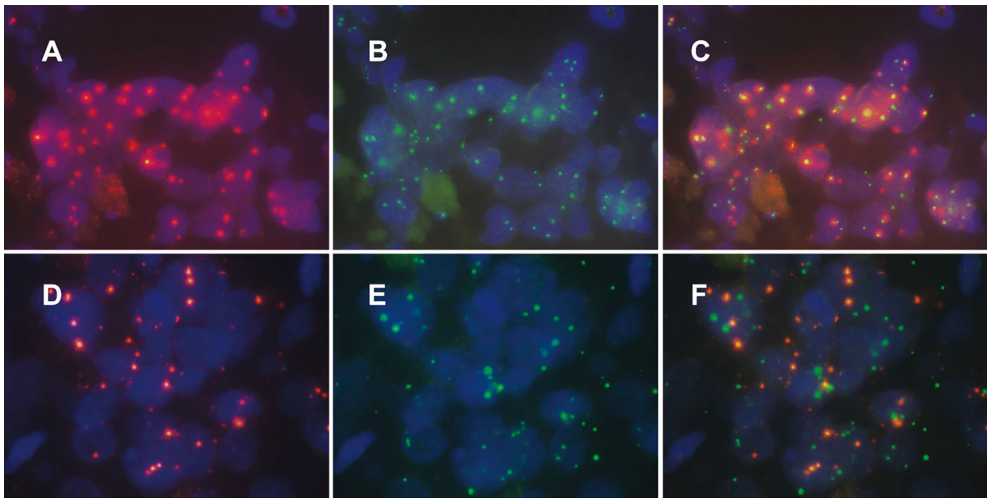
FIGURE 2 | Patterns of human specific chromosomal site probe signals and HPV signals in cervical cancer tissue. Among the cells containing HPV signals, the ratio of cells with colocalized HPV probe signals and specific chromosomal site probe signals was calculated. Samples with a ratio greater than 60% were evaluated for HPV integration in a specific site **(A–C)**; otherwise, we evaluate that HPV was not integrated at this site **(D–F)**.

retrospectively analyzed, can preserve the morphology of cervical cancer tissue, and can be applied clinically. To simultaneously detect integrated HPV and a specific chromosomal site, our dual-color FISH technique needs to address the following two key points: probe nick translation and hybridization process. The formula of the dual-color probe, time of nick translation, and dose of human COT-1 DNA were optimized through repeated trials in this study. We provide the detailed protocol in the **Supplementary Material** to help more researchers use this method. *In situ* hybridization of paraffin sections is an improvement over previous research techniques (11, 12).

No HPV16/18 signal was detected in 21 cervical cancer specimens, the possible reasons for not detecting HPV16/18 signals in some samples are as follows: (1) There was no HPV integration in this sample. (2) As 80% of cervical cancers are infected by HPV16/18, we selected HPV16/18 probe. However, a few samples may not be HPV16/18 integrated but integrated by other subtypes. (3) Considering the intra-tumoral heterogeneity of cervical cancer tissues, some tumor cell clones in the same tissue have HPV integration but some clones do not. The tumor cell population at the paraffin sections we examined may happened to be with no HPV integration.

We used a threshold value for identifying an HPV integration site: in cells containing HPV signals, the ratio of cells with colocalized HPV signals and chromosomal site-specific signals is more than 60%, which is interpreted as HPV integration at a specific site. The application of FISH in fusion gene research could be used as a reference, since fusion gene and HPV
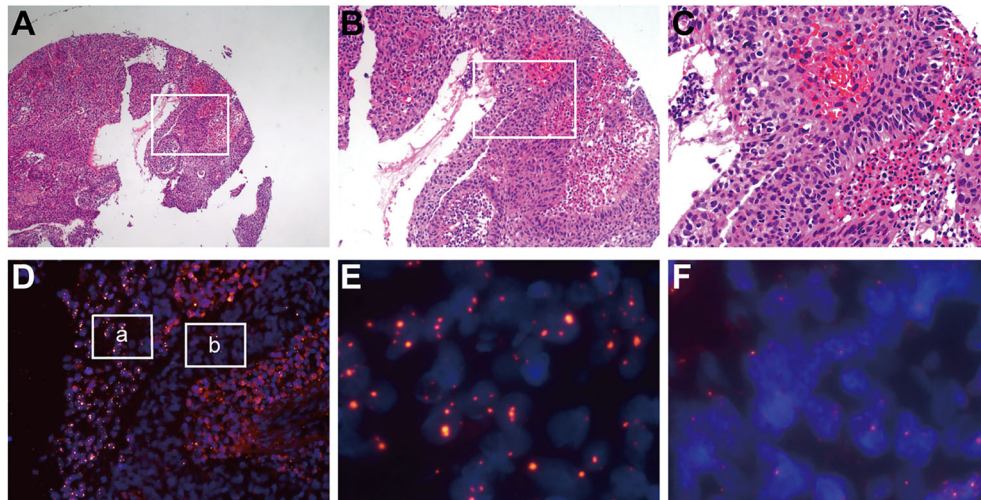
FIGURE 3 | HPV signaling suggests clonality and heterogeneity in cervical cancer tissue. In sample No. 1321, two groups of cancer cells in the same cervical cancer tissue showed no difference in cell and nuclear morphology after HE staining and were pathologically identified as the same type of cells **(A–C)**, which were distinguished significantly by HPV probes **(D)**. Every cell in the "a" group **(E)** showed HPV integration, the HPV signal area was large, and the intensity was high, suggesting intense HPV integration. In the "b" group **(F)**, some of the cells showed HPV integration, the HPV signal area was small, and the intensity was low, suggesting a low integration.

integration have similarities. Tomlins used FISH to evaluate the TMPRSS2:ETV1 fusion gene in paraffin sections of prostate cancer and found that, fusion signals were observed in an average of 31% of the 100 cancer cells in the positive case (Supporting Online Material page 3) (25). Therefore, the cut-off value of 60% in this study is a relatively strict standard. Considering that we are the first to evaluate HPV integration using the ratio of cells with colocalization signals, the threshold of this ratio is worthy of further study.

Our selection of five candidate chromosomal sites is based on a review of HPV integration in cervical cancer research (8, 15). *FHIT* is a tumor suppressor at 3p14, which is significant copy number loss in cervical cancer, as loss of its activity results in replication stress and DNA damage. *MYC* is an oncogene, and it has been suggested that *MYC* activation is associated with HPV integration at 8q24. *KLF5* is a transcriptional activator at 13q22 and may play a role in cell proliferation. Telomerase expression plays a role in cellular senescence, and deregulation of telomerase expression is found in somatic cells. 3q28 is significant copy number gain in cervical cancer, amplification and overexpression of *TP63* at 3q28 is a biomarker of progression from CIN to cervical cancer. In our study, 3p14 and 8q24 were two high-frequency sites of HPV integration. Future studies may be able to reclassify cervical cancer at the molecular level from the perspective of HPV integration.

Moreover, the integrated HPV signal can be used as a guide for the discovery of cervical cancer cell subgroups with different integrated viral loads. These subgroups may reveal the origin, metastasis, and recurrence of cervical cancer. This finding suggests that previous PCR and high-throughput sequencing methods for detecting HPV integration sites in entire cervical cancer tissue cannot accurately reveal the characteristics of different subgroups of cancer cells. This limitation may be why previous studies often report many integration sites, but they cannot determine whether these integration sites are the initiating factors before carcinogenesis or the consequence of genome instability after carcinogenesis.

In clinical applications, high-throughput sequencing technologies such as WGS and HIVID can be combined with FISH to detect HPV integration after cervical cancer tissues are obtained by surgery. On the one hand, FISH can be used to verify sequencing results. Since the determination of HPV integration sites by sequencing is based on the similarity of base sequences, sequencing reads with low specificity or containing repetitive sequences will lead to sequence alignment errors, which can be verified by FISH. On the other hand, FISH can be used to detect whether the cancer cells containing a specific HPV integration site are the majority or the minority, which can be indirectly shown by the abundance of the human-virus fusion sequence in the sequencing results, while it can be intuitively observed by FISH. If cancer cells containing a specific HPV integration site are the majority in the tissue, HPV integration at this site may be the key factor promoting cervical cancer. If they are the minority, HPV integration at this site may be a consequence of genome instability in cancer cells.

In conclusion, our study provides a method for the detection of HPV integration sites in paraffin-embedded cervical cancer samples using dual-color FISH and reports the heterogeneity within cervical cancer from the perspective of HPV integration. Our study provides new methods and ideas for research on HPV integration in cervical carcinogenesis.

DATA AVAILABILITY STATEMENT

The original contributions presented in the study are included in the article/**Supplementary Material**. Further inquiries can be directed to the corresponding authors.

ETHICS STATEMENT

The studies involving human participants were reviewed and approved by Ethics Committee of Tongji Hospital. The patients/participants provided their written informed consent to participate in this study.

AUTHOR CONTRIBUTIONS

HW and DZ designed and supervised the research together with JX. DZ and HS provided technical support. DZ, JX, CR, LW, and WD performed the experiments. CG, TZ, and XL obtained specimens. JC collected clinical data. HW, DZ, JX, and HS provided analysis and interpretation of data. The manuscript was drafted by DZ and JX. All authors contributed to the article and approved the submitted version.

SUPPLEMENTARY MATERIAL

The Supplementary Material for this article can be found online at: https://www.frontiersin.org/articles/10.3389/fonc.2021.734758/full#supplementary-material.

REFERENCES

1. Ferlay J, Soerjomataram I, Dikshit R, Eser S, Mathers C, Rebelo M, et al. Cancer Incidence and Mortality Worldwide: Sources, Methods and Major Patterns in GLOBOCAN 2012. *Int J Cancer* (2015) 136:E359–86. doi: 10.1002/ijc.29210

2. Bray F, Ferlay J, Soerjomataram I, Siegel RL, Torre LA, Jemal A. Global Cancer Statistics 2018: GLOBOCAN Estimates of Incidence and Mortality Worldwide for 36 Cancers in 185 Countries. *CA Cancer J Clin* (2018) 68:394–424. doi: 10.3322/caac.21492

3. Crosbie EJ, Einstein MH, Franceschi S, Kitchener HC. Human Papillomavirus and Cervical Cancer. *Lancet* (2013) 382:889–99. doi: 10.1016/S0140-6736(13)60022-7

4. Oyervides-Munoz MA, Perez-Maya AA, Rodriguez-Gutierrez HF, Gomez-Macias GS, Fajardo-Ramirez OR, Trevino V, et al. Understanding the HPV Integration and its Progression to Cervical Cancer. *Infect Genet Evol* (2018) 61:134–44. doi: 10.1016/j.meegid.2018.03.003

5. Kadaja M, Isok-Paas H, Laos T, Ustav E, Ustav M. Mechanism of Genomic Instability in Cells Infected With the High-Risk Human Papillomaviruses. *PloS Pathog* (2009) 5:e1000397. doi: 10.1371/journal.ppat.1000397

6. Kraus I, Driesch C, Vinokurova S, Hovig E, Schneider A, von Knebel Doeberitz M, et al. The Majority of Viral-Cellular Fusion Transcripts in Cervical Carcinomas Cotranscribe Cellular Sequences of Known or Predicted Genes. *Cancer Res* (2008) 68:2514–22. doi: 10.1158/0008-5472.CAN-07-2776

7. Lu X, Lin Q, Lin M, Duan P, Ye L, Chen J, et al. Multiple-Integrations of HPV16 Genome and Altered Transcription of Viral Oncogenes and Cellular Genes Are Associated With the Development of Cervical Cancer. *PloS One* (2014) 9:e97588. doi: 10.1371/journal.pone.0097588

8. Hu Z, Zhu D, Wang W, Li W, Jia W, Zeng X, et al. Genome-Wide Profiling of HPV Integration in Cervical Cancer Identifies Clustered Genomic Hot Spots and a Potential Microhomology-Mediated Integration Mechanism. *Nat Genet* (2015) 47:158–63. doi: 10.1038/ng.3178

9. Ojesina AI, Lichtenstein L, Freeman SS, Pedamallu CS, Imaz-Rosshandler I, Pugh TJ, et al. Landscape of Genomic Alterations in Cervical Carcinomas. *Nature* (2014) 506:371–5. doi: 10.1038/nature12881

10. Liu L, Ying C, Zhao Z, Sui L, Zhang X, Qian C, et al. Identification of Reliable Biomarkers of Human Papillomavirus 16 Methylation in Cervical Lesions Based on Integration Status Using High-Resolution Melting Analysis. *Clin Epigenet* (2018) 10:10. doi: 10.1186/s13148-018-0445-8

11. Hopman AH, Kamps MA, Smedts F, Speel EJ, Herrington CS, Ramaekers FC. HPV *In Situ* Hybridization: Impact of Different Protocols on the Detection of Integrated HPV. *Int J Cancer* (2005) 115:419–28. doi: 10.1002/ijc.20862

12. Hopman AHN, Smedts F, Dignef W, Ummelen M, Sonke G, Mravunac M, et al. Transition of High-Grade Cervical Intraepithelial Neoplasia to Micro-Invasive Carcinoma Is Characterized by Integration of HPV 16/18 and Numerical Chromosome Abnormalities. *J Pathol* (2004) 202:23–33. doi: 10.1002/path.1490

13. Algeciras-Schimnich A, Policht F, Sitailo S, Song M, Morrison L, Sokolova I. Evaluation of Quantity and Staining Pattern of Human Papillomavirus (HPV)-Infected Epithelial Cells in Thin-Layer Cervical Specimens Using Optimized HPV-CARD Assay. *Cancer Cytopathol* (2007) 111:330–8. doi: 10.1002/cncr.22946

14. Pett M, Coleman N. Integration of High-Risk Human Papillomavirus: A Key Event in Cervical Carcinogenesis? *J Pathol* (2007) 212:356–67. doi: 10.1002/path.2192

15. Wentzensen N, Vinokurova S, von Knebel Doeberitz M. Systematic Review of Genomic Integration Sites of Human Papillomavirus Genomes in Epithelial Dysplasia and Invasive Cancer of the Female Lower Genital Tract. *Cancer Res* (2004) 64:3878–84. doi: 10.1158/0008-5472.CAN-04-0009

16. Zhu D, Jiang XH, Jiang YH, Ding WC, Zhang CL, Shen H, et al. Amplification and Overexpression of TP63 and MYC as Biomarkers for Transition of Cervical Intraepithelial Neoplasia to Cervical Cancer. *Int J Gynecol Cancer* (2014) 24:643–8. doi: 10.1097/IGC.0000000000000122

17. Melsheimer P, Vinokurova S, Wentzensen N, Bastert G, von Knebel Doeberitz M. DNA Aneuploidy and Integration of Human Papillomavirus Type 16 E6/E7 Oncogenes in Intraepithelial Neoplasia and Invasive Squamous Cell Carcinoma of the Cervix Uteri. *Clin Cancer Res* (2004) 10:3059–63. doi: 10.1158/1078-0432.CCR-03-0565

18. Schmitz M, Driesch C, Beer-Grondke K, Jansen L, Runnebaum IB, Durst M. Loss of Gene Function as a Consequence of Human Papillomavirus DNA Integration. *Int J Cancer* (2012) 131(5):E593–602. doi: 10.1002/ijc.27433

19. Schmitz M, Driesch C, Jansen L, Runnebaum IB, Durst M. Non-Random Integration of the HPV Genome in Cervical Cancer. *PloS One* (2012) 7:e39632. doi: 10.1371/journal.pone.0039632

20. Das P, Thomas A, Mahantshetty U, Shrivastava SK, Deodhar K, Mulherkar R. HPV Genotyping and Site of Viral Integration in Cervical Cancers in Indian Women. *PloS One* (2012) 7:e41012. doi: 10.1371/journal.pone.0041012

21. Woodman CB, Collins SI, Young LS. The Natural History of Cervical HPV Infection: Unresolved Issues. *Nat Rev Cancer* (2007) 7:11–22. doi: 10.1038/nrc2050

22. Luft F, Klaes R, Nees M, Durst M, Heilmann V, Melsheimer P, et al. Detection of Integrated Papillomavirus Sequences by Ligation-Mediated PCR (DIPS-PCR) and Molecular Characterization in Cervical Cancer Cells. *Int J Cancer* (2001) 92:9–17. doi: 10.1002/1097-0215(200102)9999:9999<::AID-IJC1144>3.0.CO;2-L

23. Klaes R, Woerner SM, Ridder R, Wentzensen N, Duerst M, Schneider A, et al. Detection of High-Risk Cervical Intraepithelial Neoplasia and Cervical Cancer by Amplification of Transcripts Derived From Integrated Papillomavirus Oncogenes. *Cancer Res* (1999) 59:6132–6.

24. Van Tine BA, Kappes JC, Banerjee NS, Knops J, Lai L, Steenbergen RD, et al. Clonal Selection for Transcriptionally Active Viral Oncogenes During Progression to Cancer. *J Virol* (2004) 78:11172–86. doi: 10.1128/JVI.78.20.11172-11186.2004

25. Tomlins SA, Rhodes DR, Perner S, Dhanasekaran SM, Mehra R, Sun XW, et al. Recurrent Fusion of TMPRSS2 and ETS Transcription Factor Genes in Prostate Cancer. *Science* (2005) 310:644–8. doi: 10.1126/science.1117679

Conflict of Interest: The authors declare that the research was conducted in the absence of any commercial or financial relationships that could be construed as a potential conflict of interest.

Check for updates

Artificial Intelligence in Cervical Cancer Screening and Diagnosis

Xin Hou [1], Guangyang Shen [1], Liqiang Zhou [2], Yinuo Li [1], Tian Wang [1] and Xiangyi Ma [1*]

[1] Department of Obstetrics and Gynecology, Tongji Medical College, Tongji Hospital, Huazhong University of Science and Technology, Wuhan, China, [2] Cancer Centre and Center of Reproduction, Development and Aging, Faculty of Health Sciences, University of Macau, Macau, Macau SAR, China

Cervical cancer remains a leading cause of cancer death in women, seriously threatening their physical and mental health. It is an easily preventable cancer with early screening and diagnosis. Although technical advancements have significantly improved the early diagnosis of cervical cancer, accurate diagnosis remains difficult owing to various factors. In recent years, artificial intelligence (AI)-based medical diagnostic applications have been on the rise and have excellent applicability in the screening and diagnosis of cervical cancer. Their benefits include reduced time consumption, reduced need for professional and technical personnel, and no bias owing to subjective factors. We, thus, aimed to discuss how AI can be used in cervical cancer screening and diagnosis, particularly to improve the accuracy of early diagnosis. The application and challenges of using AI in the diagnosis and treatment of cervical cancer are also discussed.

Keywords: cervical cancer, cervical intraepithelial neoplasia (CIN), artificial intelligence, deep learning, cytology, colposcopy, early screening and diagnosis

1 INTRODUCTION

Cervical cancer is one of the most common malignancies in women, with 604,000 new cases and 342,000 deaths in 2020 (1). It is the only cancer that can be eliminated *via* primary prevention strategies comprising a fully effective 9-valent human papillomavirus (HPV) vaccine, early detection, and timely treatment (2).

Almost all cases of cervical cancer are caused by persistent infection of the cervical epithelium with one of the 15 genotypes of the carcinogenic HPV. The four major steps in the development of cervical cancer are as follows: infection of the metaplastic epithelium at the cervical transformation zone, persistent HPV infection, progression of persistently infected epithelium to cervical precancer, and invasion through the basement membrane of the epithelium (3). The HPV vaccines can protect girls and young woman against infection with the HPV virus. But HPV vaccine coverage rate is very low at present (even in some developed countries) (2, 4) and the beneficiaries are limited to young women aged <26 in terms of 9-valent HPV vaccines. According to American Cancer Society, vaccinated women are also recommended that be screened the same as unvaccinated women because it is impossible to avoid risk completely (5). Hence, routine screening for cervical cancer is still important to women. Approximately 30% of cervical intraepithelial neoplasia (CIN) grade 3 lesions develop into invasive cancers within 30 years. Slow progression offers many opportunities for the detection and treatment of these lesions (6). Screening and treatment of precancerous lesions in women is a cost-effective way to prevent cervical cancer (7). Ideally, screening strategies should be

able to detect early lesions that may develop into cervical cancer, while avoiding the detection of transient HPV infections and benign abnormalities that can lead to overtreatment and other hazards associated with screening (5). With the continuous improvement of screening techniques, there has been an increase in the detection rate of cervical cancer and a decrease in the mortality rate; however, most deaths occur in low- and middle-income countries (8). Despite new developments in effective screening programs, many of these cannot be implemented or maintained because of weak health infrastructure (9, 10). Moreover, the accuracy of manual screening is not always 100% (11), resulting in some related lesions that cannot be timely diagnosed. Thus, developing a more accurate and economical cervical cancer screening method is the main challenge for the early diagnosis of cervical cancer.

In recent years, AI has been increasingly applied in the diagnosis of various diseases, such as the classification of skin tumors (12, 13), diagnosis and classification of retinal diseases (14), and imaging diagnosis of tumors (15), and has shown promising application value. AI can automatically recognize images, extract features, learn classification, and process data using complex algorithms. The application of AI in the early screening and diagnosis of cervical cancer is conducive to addressing limited human resources and improving diagnostic accuracy.

This article aimed to introduce recent AI technologies and demonstrate their utility and potential for the screening and early diagnosis of cervical cancer. This review also discusses the current challenges and proposes future research directions.

2 METHODS FOR CERVICAL CANCER SCREENING AND DIAGNOSIS

The latest World Health Organization guidelines recommend the following three screening methods for the early detection of cervical cancer: HPV testing, cytology (including traditional pap smear and liquid-based cytology smear), and visual inspection with acetic acid (VIA) (16). We focused on the first two methods because VIA is only used when the first two are not available. HPV testing and cytology uses brushed exfoliated cells from the cervix as test samples. HPV testing detects high-risk types of HPV infection in the cervix, whereas cytological examination uses a microscope to identify cells taken from the cervix for possible cervical cancer or precancerous lesions (17). **Figure 1** shows the evolution of cervical cancer screening methods. However, colposcopy-guided biopsy remains as the gold standard for cervical cancer diagnosis, followed by staging according to the clinical examination and imaging results.

2.1 Introduction to Cytology
A conventional Pap smear (CPS) is a manual screening procedure used to identify and classify exfoliated cervical cells under a microscope according to the color and characteristics of the nucleus and cytoplasm (18). Liquid-based cytology (LBC) can improve preparation techniques (19). The LBC specimen is better fixed in glass slides, easier to preserve and perform artificial removal, and has a more uniform sample distribution than CPS (20).

Cytology results are described according to the Bethesda system (TBS) (21). Cervical cells are grouped into specific categories according to their abnormal changes about nuclear size, degree of dyeing etc (22). Abnormal epithelial cells include atypical squamous cells and atypical glandular cells. The TBS nomenclature details are listed in **Table 1**.

2.2 Introduction to Colposcopy
Colposcopy is defined as the use of a specific instrument to magnify the fully exposed cervix by 5 to 40 times for a real-time visual assessment of the cervix, especially the transformation area, for the detection of CIN or squamous intraepithelial lesion (SIL) and invasive cancer (23). A colposcopy-guided biopsy of the suspected site is performed to determine whether further treatment, such as conization or cryotherapy, is needed, which is important in patients with high-grade CIN or more severe disease (24).

2.3 Procedures for Early Screening and Diagnosis of Cervical Cancer
According to the latest recommendations of the American Cancer Society on cervical cancer screening, women with a cervix aged ≥25 years are recommended to undergo cervical cancer screening. For women between the ages of 25 and 65,

FIGURE 1 | Evolution of cervical cancer screening methods. The figure shows major milestones in the evolution of cervical cancer screening. The main screening methods for cervical cancer are HPV testing and TCT (cytology) nowadays.
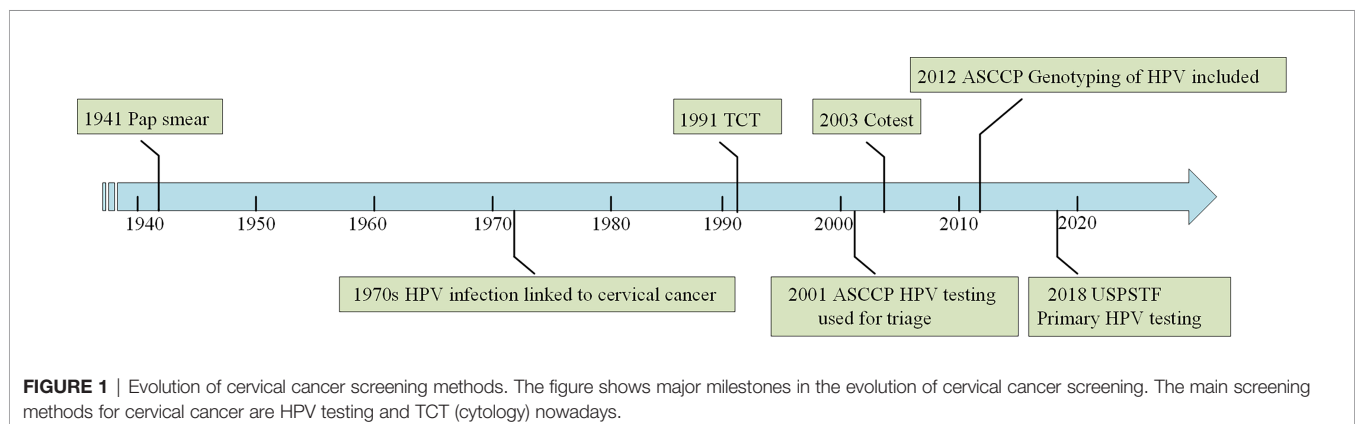
TABLE 1 | The Bethesda system.

Cell types	Classification
Normal	
Atypical squamous cells (ASC)	(1) atypical squamous cells of uncertain significance (ASC-US)
	(2) Highly squamous intraepithelial disease (ASC-H) cannot be ruled out;
	(3) Low-grade squamous intraepithelial lesions (LSILs, equivalent to CIN1);
	(4) Highly squamous intraepithelial lesions (HSILs), including CIN2 CIN3 and carcinoma in situ (CIS);
	(5) Squamous cell carcinoma (SCC)
Atypical glandular cells (AGC)	(1) Atypical glandular cells, not otherwise specified (AGC-NOS); (specify endocervical, endometrial, or not otherwise specified)
	(2) Atypical glandular cells, favor neoplastic; (specify endocervical or endometrial)
	(3) Endocervical adenocarcinoma in situ (AIS);
	(4) adenocarcinoma (specify endocervical, endometrial, extrauterine, or not otherwise specified).

primary HPV test should be performed every five years (5). If a primary HPV test is not available, co-testing (HPV testing in combination with cytology) or cytology evaluation can be performed every three years. Colposcopy or recommended screening methods can be performed based on the results (25), which are shown in the **Figure 2**.

Referral colposcopy further determines the presence of CIN and identifies or excludes invasive carcinoma (4). Patients with a high suspicion of invasive cancer should undergo colposcopy-guided biopsy, the gold standard for the diagnosis of cervical cancer and plays a key role in the early detection of cervical cancer (26).

3 APPLICATIONS OF AI IN EARLY SCREENING OF CERVICAL CANCER

3.1 HPV Typing and Detection

Continuous high-risk HPV infection can lead to cervical cancer (27). HPV testing can detect HPV infection and help screen

high-risk populations. Genotyping of HPV will make it easier to assess the risk of women with positive cervical smear results and HPV DNA-positive results (28), thus making it more conducive for cervical cancer screening and management. AI learning technology uses research related to HPV testing to improve accuracy and diversify the use of HPV testing in cervical cancer screening. These studies are summarized in **Table 2**.

Different types of HPV are associated with different types of lesions. For example, cervical adenocarcinomas are usually associated with HPV 18 type and tend to shed fewer cells; thus, they are difficult to detect by cytology (32). Having high-risk HPV types (e.g., 16, 18, and 31) contributes to a greater risk of developing cervical malignancies (11). Therefore, distinguishing among the specific types of HPV will make it easier to classify and manage HPV-infected women. Based on the additional genotyping information provided by Onclarity, Wong et al. derived a decision system with 94.32% specificity of the best classifier. The system highlighted the patients who are at high risk of developing CIN2/3+, demonstrated that some infections involving multiple HPV types carry additional risks, and identified
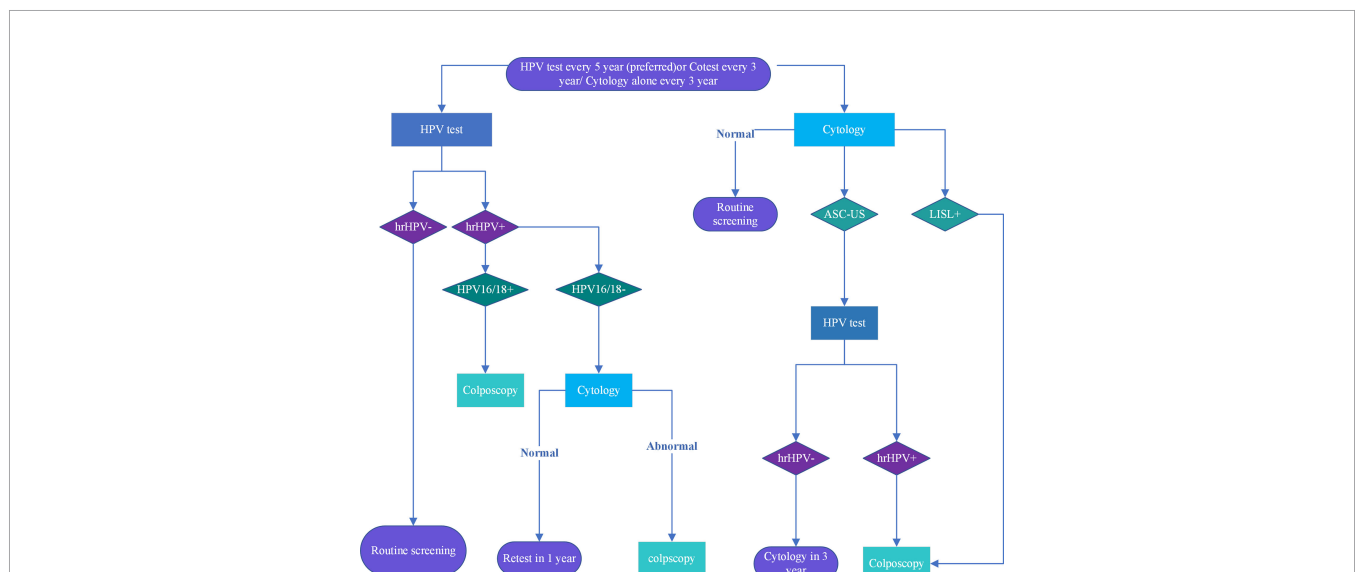
FIGURE 2 | Cervical cancer screening procedures are recommended for women aged 25 to 65. The American Cancer Society recommends screening starting at age 25 Colposcopy is recommended for HPV16/18 +, ASC-US and high risk HPV+ cytology with cytological results above ASC-H. Re-screening is recommended after 1 year for other abnormalities, and after 3 years for normal ones.

TABLE 2 | Application of AI in HPV testing.

Reference	Year	Aim of study	Number of subjects	Methods	Results
Wong et al. (29)	2019	Identifying high-grade lesions and in triaging equivocal smears	605 cervical cytology samples	Decision tree, random forest SVM-linear SVM-nonlinear	Specificity: 94.32% Specificity: 90.91% Specificity: 90.91% Specificity: 90.91%
Pathania D et al. (30)	2019	Point-of-care HPV screening	Training sets: 13000 images Validation: 35 cervical specimens	CNN	Sensitivity: down to a single cell specificity: 100%
Tian R et al. (31)	2019	Predicting cervical lesion grades	10 HPV+ cases 10 CIN1 cases 14 CIN2+cases	Random forest unsupervised clustering	Accuracy 0.814

HPV, human papillomavirus; CIN, cervical intraepithelial neoplasia; SVM, support vector machine; CNN, convolutional neural network.

the most important gene combinations (29). Pathania proposed the HPV AI surveillance, which uses a deep learning (DL) algorithm combined with digital micro-holography, and reported excellent sensitivity and specificity (100% coincidence) in detecting HPV 16 DNA and HPV 18 DNA in cell lines (30).

However, more studies are underway. The high sensitivity of HPV testing results in an increased rate of colposcopy referrals, which may lead to more potentially harmful treatments (33). Tian et al. analyzed HPV integration status, somatic mutation, and copy number variation through capture-based next-generation sequencing and obtained enriched biomarkers of CIN 2. They then used a machine learning algorithm (random forest) to build a risk stratification model for cervical precursor lesions, which successfully predicted CIN2+ with an average accuracy probability score of 0.814 (31). This method effectively stratified the risk of cervical lesions and provided valuable integrated triage strategies.

At present, HPV typing mostly depends on test kits; however, these have some disadvantages, such as false-negative rate and high cost. AI has shown great potential and application in the detection of HPV types and associated molecular markers that can aid in the diagnosis of cervical lesions.

3.2 Screening of Cervical Cytology

Cytology-based cervical cancer prevention programs have reduced the incidence of cervical cancer in many Western countries (34). Cytology screening for high-grade cervical precancerous lesions is highly specific but less sensitive (50–70%) (11) and requires careful microscopy observation by well-trained cytologists. Each process is cumbersome, labor-intensive, and error-prone (35). In addition, cytological reproducibility is low, resulting in low accuracy (36). Furthermore, changing the observer yields inconsistent and subjective results (37). So the researchers hope to develop automatic image analysis methods to relieve these pressures.

The first commercial automatic screening system was PAPNET (38) in 1992. The system was approved as a method of re-screening for slides that were judged negative by cytologists. In 2004, FAD approved the Thinprep imaging system as a commercial screening product. The system can select the 22 most concerned fields of view (FOV) according to the proprietary algorithm, and if abnormal cells are found, cytotechnologists need to manually screen the entire slide (39).

The system improves the sensitivity and efficiency of screening. Later, the Focal point GS imaging system emerged in 2008. It identified 10 FOV of cervical cells most likely to be abnormal and stratified the risk to improve the efficiency (40). However, some reviews indicate that the cost-effectiveness of these automation systems is limited and is not suitable for use in low-and medium-developing countries (41). And its research technology still has weaknesses (42) and still depends on the final manual screening process. Therefore, some researchers continue to optimize the application of artificial intelligence technology in cervical cytology.

3.2.1 Segmentation of Cervical Cells

A typical automatic smear analysis system comprises the following five stages: image acquisition, preprocessing, segmentation, feature extraction, and classification (43). AI technology is applied in the segmentation and classification stages for the automatic analysis of a smear, which is helpful to improve screening efficiency.

The first step in cytological diagnosis is the accurate identification of cells and their respective structural components. As the diagnostic criteria for cervical cytology are mainly based on nuclear and cytoplasm abnormalities, accurate segmentation is a prerequisite for screening solutions (44–46). Studies on the application of AI in cell segmentation have been carried out continuously and have shown good results in the segmentation of hepatoma cells (47), human metaphase II oocytes (43), and pluripotent stem cells (48). It has also been introduced for the automatic segmentation of cervical cells, and good results have been reported (49). For example, Chankong et al. used fuzzy c-means clustering technology to segment single-cell images into the nucleus, cytoplasm, and background to realize whole-cell segmentation (41). Some researchers extracted adaptive shape from cytoplasmic contour fragments and shape statistics to segment the overlapped cytoplasm of cells in cervical smear images using supervised learning. Experimental results show that this method is efficient and always superior to the most advanced methods (50). Segmentation model on images from pap smear slide also was explored which has been achieved through using nucleus localization to classify normal and abnormal cells, combined with single cell classification algorithm. The accuracy and sensitivity are 91.7% respectively and the model consists of two stages as shown in Mask-RCNN architecture part in **Figure 3** (51). Review of relevant literature results are provided in **Table 3**.
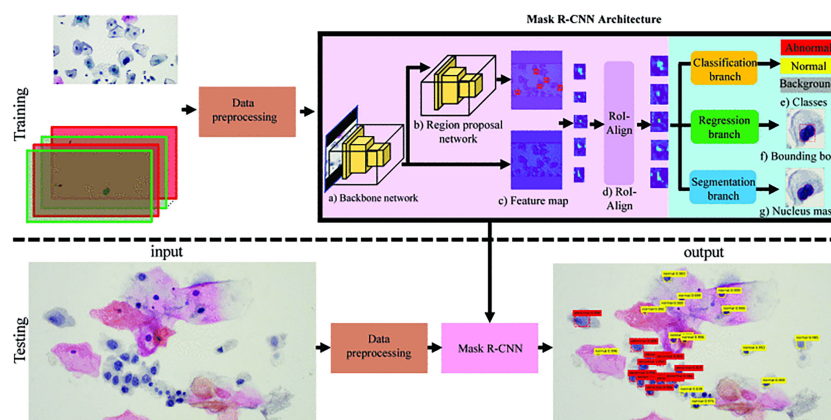
FIGURE 3 | A example segmentation model based on Mask-RCNN architecture. Reproduced with the permission of ref. (51), copyright@IEEE, 2019. In training phase, input was pap smear slide image and nucleus ground truth mask with class label was preprocessed and then trained in Mask R-CNN. In testing phase, pap smear slide image was preprocessed. Mask RCNN was used to specify bounding box, nucleus mask, and class of each cell.

AI makes cervical cell automatic segmentation true, accurate, and unified. Thus, time-intensive manual segmentation process and subjective shortcomings can be overcome to realize accurate abnormal cell classification.

3.2.2 Classification of Cervical Cells

Accurate classification of cervical cells in smears is a crucial step in cervical cancer screening. The low accuracy of manual classification and the high requirement for professional degree of the observer limit the application of cytology (52), particularly in areas where trained cytopathologists are scarce. The use of AI has addressed these limitations (**Table 4**).

In the past few decades, many classification methods have been proposed, most of which are based on segmentation or texture feature extraction. Chankong et al. segmented the cervical single-cell image into the nucleus, cytoplasm, and background, and obtained the morphological features to realize automatic multi-label classification. The results showed an accuracy rate of more than 93% (44). Mariarputham et al. extracted seven groups of texture features of cervical cells for classification. The support vector machine (SVM) classifier had the highest accuracy and the best performance (57). Three classifiers, i.e., least square support vector machine (LSSVM),

multilayer perceptron (MLP) and random forest (RF), were used in the integrated classifier designed by Kden et al. The accuracy of these classifiers was 98.11% at the smear level and 99.01% at the cell level (53). Reducing the time of manual observation eliminates observer bias and improves efficiency.

Classification that does not rely on an accurate segmentation algorithm has also been proposed and accepted by an increasing number of scholars. Zhang et al. applied DL and transfer learning (58) to cervical cell classification for the first time. Automatic extraction of embedded deep-level features in cell images for classification is a superior method compared with previous algorithms in terms of classification accuracy (98.3%), AUC (0.99), and specificity (98.3%) (54). Six different convolutional neural networks (CNNs) were used for the first time for the diagnosis of cervical precancerous lesions. The accuracy, sensitivity, and specificity of the integrated classifier were 0.989, 0.978, and 0.979, respectively (43). Shi et al. proposed a method of cervical cell classification based on a graph convolution network to explore the potential relationship between cervical cell images and improvement of classification performance. Its accuracy (98.37%), sensitivity (99.80%), specificity (99.60%), and F-measure (99.80%) were all better than those of the existing method (55). In addition, hybrid

TABLE 3 | Application of AI in cervical cell segmentation.

Reference	Year	Number of subjects	Methods	Datasets	Results
Wang et al. (44)	2014	362 cervical cell images (3722 cells)	Mean-Shift clustering algorithm	Private	Sensitivity: 94.25% Specificity: 93.45%
Song et al. (50)	2019	8 cervical cell images 22 cervical images	CNN	ISBI2015 Private	DSC: 0.84 DSC: 0.83
Zhao et al. (45)	2016	917 single-cell images	Superpixel-based Markov random field	Herlev The real-word Datasets	Herlev ZSI of nuclei: 0.93 ZSI of cytoplasm: 0.82
Gautam et al. (46)	2018	917 single-cell images	Patch-based CNN	Herlev	DSC: 0.90 Precision: 89%

CNN, convolutional neural network; DSC, dice similarity coefficient; ZSI, zijdenbos similarity index.

TABLE 4 | Application of AI in cervical cell classification.

Reference	Year	Methods	Datasets (Num. of images)	Classes	Results
Chankong et al. (41)	2014	Bayesian classifier KNN ANN	ERUDIT (552)	4-class	Accuracy 96.20%
				2-class	Accuracy 97.83%
			Herlev (917)	7-class	Accuracy 93.78%
				2-class	Accuracy 99.27%
			LCH (300)	4-class	Accuracy 95.00%
				2-class	Accuracy 97.00%
Borakden et al. (53)	2017	Ensemble classifier: LSSVM MLP RF	Cell level (1610)	2-class	Accuracy 99.07%
					Specificity 98.90%
			Smear level (1320)	3-class	Accuracy 98.11%
					Specificity 99.35%
			Hervel (917)	2-class	Accuracy 96.51%
					Specificity 89.67%
Zhang et al. (54)	2017	CNN; Transfer learning	Herlev (917)	7-class	Accuracy 98.30%
					Specificity 98.30%
			HEMLBC (2370)	2-class	Accuracy 98.60%
					Specificity 99.00%
					sensitivity 98.30%
Hussain et al. (52)	2020	CNN; Transfer learning	LBC (own) (1670), Conventional(own) (1320)	4-class	Accuracy 98.90%
					Sensitivity 79.80%
					Specificity 97.90%
Shi J et al. (55)	2020	CGN	SIPAKMeD (4049)	5-class	Accuracy 98.37%
					Sensitivity 99.80%
			MOTIC (25378)	7-class	Accuracy 94.93%
					Sensitivity 92.98%
Rahaman et al. (56)	2021	HDFF	Herlev (917)	2-class	Accuracy 98.32%
				7-class	Accuracy 90.32%
			SIPAKMeD (4049)	2-class	Accuracy 90.32%
				5-class	Accuracy 99.14%

KNN, K- Nearest Neighbor; ANN, Artificial Neural Network; LSSVM, Least Squares Support Vector Machine.
CNN, convolutional neural network; CGN, graph convolution network; HDFF, hybrid deep feature fusion techniques.

deep feature fusion techniques were proposed, with high accuracy in the SIPAKMeD dataset (56).

3.2.3 AI Improves the Screening accuracy of Cervical Intraepithelial Lesions

After the establishment of a good automated cytological detection model based on the AI method, some studies have found that cytological examination assisted by AI can classify cervical cells to guide triage and improved the detection rate of CIN compared with that of standard pathological biopsy results (32, 59) (**Table 5**).

A prospective cohort study of 700,000 women in a population-based cervical cancer screening program using a validated AI-assisted cytological diagnostic system was conducted by Bao et al. They reported a total coincidence rate of 94.7% and a 5.8% increase in sensitivity (3.0–8.6%) compared to manual reading (60). Another observational study was conducted to evaluate the ability of AI-assisted cytology to histologically detect CIN or cancer. Detection rates for CIN 2 and CIN 3+ of 92.6% and 96.1%, respectively, were obtained. These were significantly higher than those of manual reading (61). Furthermore, Wang et al. established a DL-based cervical disease diagnosis system that detects high squamous intraepithelial lesions (HSILs) or higher, and an accuracy of 0.93 was achieved (62). Zhu et al. developed an AI-assisted TBS (AIATBS) (21) diagnostic system, which showed higher sensitivity than the diagnosis by senior cytologists. The

sensitivity of the AIATBS in detecting CIN was 94.74% in a clinical prospective validation (63).

The evidence above overall indicates that AI has been widely used for HPV testing and cytology and has achieved a good detection rate and accuracy. More studies and applications are underway in this regard. For example, Tang et al. developed an AI microscope with an augmented reality (AR) display for cervical cytology screening. They reported that it significantly improved detection sensitivity for low squamous intraepithelial lesion (LSIL) and HSIL and consistency in multiple classifications and atypical squamous cells of uncertain significance recognition. In addition to diagnostic applications, training novice cytopathologists could be another potential application for AI microscopes (64).

4 APPLICATIONS OF AI IN CERVICAL CANCER DIAGNOSIS

Cervical cancer and precancerous lesions are diagnosed by colposcopy-guided biopsy and staged according to the Federation International of Gynecology and Obstetrics (FIGO) staging standard (65). In 2018, the FIGO allowed the use of imaging and pathologic findings (if any) in staging (66). AI technology has been used in colposcopy and magnetic resonance imaging (MRI) to assist in the diagnosis and staging of cervical cancer and has shown satisfactory results. **Figure 4** illustrates the

TABLE 5 | Application of AI in cytology to detect CIN.

Reference	Year	N	Methods	Databases	Results
Yu et al. (32)	2018	1839	Risk score algorithm	Cytological image HPV testing	CIN2+ AUC 0.710 CIN3+ AUC 0.740
Bao et al. (60)	2020	703103	DL	Cytological image	CIN1+ Sensitivity 88.9% Specificity 95.8% CIN2+ Sensitivity 90.10% Specificity 94.80%
					CIN3+Sensitivity 90.90% Specificity 94.40%
Bao et al. (61)	2020	2145	ResNet	Cytological image	CIN2+ AUC 0.762 CIN3+ AUC 0.755
Wang et al. (62)	2020	143	DL	whole slide images (WSIs)	precision 93.00% recall 90.00%, F-measure 88.00%
Holmström O et al. (59)	2021	740	DL	Cytological image	HSIL+ AUC 0.970Sensitivity 85.7% Specificity 98.5%
Zhu et al. (63)	2021	980	AIATBS	Cytological imageBiopsy diagnosis results	Sensitivity 94.74%

DL, deep learning; CNN, convolutional neural network; AIATBS, artificial intelligence-assisted TBS; CIN, cervical intraepithelial neoplasia; AUC, area under the curve; HSIL, high squamous intraepithelial lesion.

workflow of the CNN model and transfer learning used in colposcopy image classification.

4.1 Coloscopy

At present, the consistency between colposcopy and pathology is poor, which may lead to misdiagnosis and missed diagnosis. Colposcopy performed by an unskilled clinician could result in potential harm (including bleeding, infection, vaginal discharge, pain, or discomfort) and therefore, requires adequate training and experience to achieve proficiency and ensure maintenance of operating procedures. However, the long training period of professional colposcopy doctors and the lack of qualified

personnel create challenges for the use of colposcopy in the diagnosis of cervical cancer (67).

4.1.1 AI Boosts Image Classification Performance

Recently, DL has been widely used in medical imaging (15). The application of DL technology in the classification of colposcopy is helpful in solving the bottleneck of traditional colposcopy and improving its diagnostic performance (**Table 6**).

Miyagi et al. developed and trained a CNN AI classifier for the LISIL/HSIL classification of colposcopy images. The accuracy, sensitivity, and specificity of the AI classifier and oncologist in diagnosing HSIL were 0.823 and 0.797, 0.800 and 0.831, and
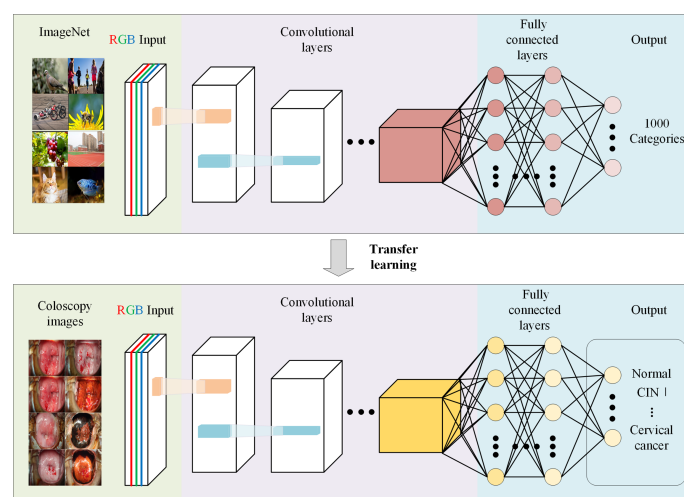
FIGURE 4 | Schematic representation of application of Convolutional Neural Network in colposcopy images. Schematic depicting that a CNN pre-trained on other large-scale image datasets can be adapted to significantly increase the accuracy and shorten the training duration of a network trained on a novel dataset of colposcopy images.

TABLE 6 | Application of AI in colposcopy.

Reference	Year	Aim of the study	Number of subjects	Methods	Images	Results
Kim E et al. (68)	2013	Detection of CIN2+	2000images	SVM	Cervicography	Sensitivity 75.00% Specificity 75.00%
Song et al. (69)	2015	Detection of CIN2+	7669patients	MCNN	Cervicography	Accuracy 80.00% Sensitivity 83.21% Specificity 94.79%
Hu et al. (70)	2019	Detection of CIN2+	9406patients	Faster-CNN	Cervicography	AUC 0.91
Chao et al. (71)	2020	Detection lesions need to biopsy and classification	791 patients	CNN	Optical colposcopy image	Sensitivity 85.20% Specificity 88.20% AUC 0.947
Asiedu et al. (72)	2019	Classification of cervical lesions	134 patients	SVM	Digital colposcopy images	Accuracy 80.00% Sensitivity 81.30% Specificity 78.60%
Yuan et al. (26)	2020	Classification of cervical lesions	22330images	CNN	Digital colposcopy images	Sensitivity 85.38% Specificity 82.62%
Miyagi et al. (73)	2019	Classification of cervical lesions	253patients	CNN	Traditional colposcopy images	Accuracy 83.30% Sensitivity 95.60%
Miyagi et al. (23)	2019	Classification of cervical lesions	310images	CNN	Traditional colposcopy images	Accuracy 82.30% Sensitivity 80.00% Specificity 88.20%
Xue et al. (74)	2020	Classification of cervical lesions	19435patients	CAIADS	Digital colposcopy images	LSIL Sensitivity 90.50% Specificity 51.80% HSIL Sensitivity 71.90% Specificity 93.90%
Yue et al. (75)	2020	Classification of cervical lesions	4753images	CNN,	cervigram images	Accuracy 96.13% Sensitivity 95.09% Specificity 98.22% AUC 0.94
Venkatesan et al. (76)	2021	Classification of cervical lesions	5679images	CNN	colposcopy photographs	Accuracy 83.30% Sensitivity 95.60%
Peng et al. (77)	2021	Classification of cervical lesions	300images	VGG16	colposcopy images	Accuracy 86.30% Sensitivity 84.10% Specificity 89.80%

CAIADS, Colposcopic Artificial Intelligence Auxiliary Diagnostic System.

0.882 and 0.773, respectively (24). Later, a classifier based on DL was developed, which uses HPV types and cervical SIL images to classify HSIL/LSIL. The accuracy of the classifier was 0.941 (73). Xue et al. developed an AI method (CAIADS) to grade the colposcopy impression and guide the biopsy. The consistency of CAIADS-graded colposcopy impression and pathological results (82.2%) was higher than that traditional colposcopy (65.9%) (74). The ResNet model based on DL was established by Yuan et al. Its sensitivity and specificity based on DL were 85.38% and 82.62%, respectively. The model helps in colposcopy diagnosis and guides biopsy (26). The C-RCNN algorithm was proposed by Yue et al. to classify cervical lesions, and the time and spatial features were extracted using long-term and short-term memory network. Models with better specificity (98.22%), sensitivity (95.09%), accuracy (96.13%), and area under the curve (0.94) were obtained (75).

4.1.2 AI Helps Detect High-Grade Cervical Lesions and Guides Biopsy

Clinically, one of the most important goals of cervical cancer screening is to distinguish between normal/CIN 1 and CIN 2/3+. If the lesion is classified as CIN 2/3+, treatment is required. In contrast, mild dysplasia in CIN 1 is usually cleared following approximately a year of immune response and can therefore be observed or treated more conservatively. Kim et al. developed a data-driven computer interpretation algorithm for cervical images based on color and texture. They obtained a sensitivity of 74% and a specificity of 90% in differentiating high-grade cervical lesions (CIN 3+) from low-grade lesions and normal tissues (68). Hu et al. conducted a longitudinal cohort study on 9,406 women for 7 years. The cervical images obtained were used to validate the model based on the fast R-CNN method. The AUC of the model for diagnosing CIN 2+ was 0.91, which exceeded the interpretation of the same image by the colposcope evaluator and was superior to those of traditional Pap smears and alternative types of cytology (70). Cho et al. developed a binary decision model to determine the need to biopsy for a cervical lesion. The Need-To-Biopsy was defined as 'not being normal', referring to CIN+ and LSIL+. The performance of the best RESNET-152 model showed an average AUC of 0.947, a sensitivity of 85.2%, and a specificity of 88.2% (71); thus, the model helps an inexperienced clinician judge whether to perform a cervical biopsy or refer the patient to a specialist.

The powerful image analysis ability of AI has solved the problem of diagnosing cervical cancer using a large number of

colposcopy images. With the assistance of AI technology, the accuracy of detecting lesions and performing biopsy under colposcopy becomes relatively high, thus reducing the misdiagnosis rate of colposcopy (69, 72, 76, 77).

4.2 Pelvic MRI

MRI has proven to be highly accurate in the preoperative staging of cervical cancer (78, 79). Therefore, MRI is the first choice for local staging, evaluation of treatment response, detection of tumor recurrence, and follow-up of patients with cervical cancer (80). The primary objective of MRI is to determine the presence of peritumoral infiltration and lymph node metastasis (LNM) (81) (**Table 7**).

4.2.1 Segmentation of Cervical Cancer Lesions

MRI has a higher soft tissue resolution than CT. It can determine tumor size and adjacent pelvic structures and assess periuterine invasion and uterine and vaginal involvement (68). Lin et al. developed a U-Net CNN to accurately locate and segment cervical carcinoma in diffuse-weighted imaging (DWI). They reported the highest learning efficiency during image training, with a dice coefficient of 0.8, sensitivity of 0.89, and a positive predictive value of 0.92 (82). Liang et al. established a computational model of a DL algorithm based on wireless network, which can be used to segment cervical cancer MRI images with a 98% accuracy, which is evidently better than that of traditional depth-learning algorithms (<90%) (84). AI is more accurate, objective, and faster than manual segmentation. Wang et al. established a non-invasive radiologic model based on T2-weighted imaging (T2WI) and DWI, divided MRI images, and extracted features to predict periuterine invasion. The AUCs of T2WI and T2WI combined with DWI in the validation cohort were 0.780 and 0.921, respectively (83).

4.2.2 Diagnosis of Cervical Cancer LNM

AI also contributes to the early diagnosis of cervical cancer LNM. Although the accuracy of computed tomography and MRI in assessing lymph node involvement only ranged from 83% to 85%, their specificity was very high, ranging from 66% to 93% (74). In 2018, the cervical cancer staging system was revised to include lymph node status as a staging criterion for the first time. Cervical cancer with lymph node involvement on imaging or pathology was classified as stage IIIC (66). Wu et al. developed a DL model using preoperative MRI to predict LNM in patients with cervical cancer. The AUC using both intratumoral and peritumoral DL models in T1WI was 0.844, whereas that of the hybrid model, which combines the tumor image information from DL mining with the lymph node status reported by MRI, was 0.933 (89), thus improving the detection rate of LNM.

Over the past decade, radiology has evolved to bridge the gap between imaging and precision medicine. Radiology uses complex image analysis tools combined with statistical analysis to extract rich information hidden in medical images (90). Wu et al. used MRI radiomic analysis to improve the diagnostic level of LNM in patients with cervical cancer. The combination of T2WI and decision tree of lymph node status had the best diagnostic effect; in the training and validation cohorts, the AUC and sensitivity were 0.895% and 94.3% and 0.847% and 100%, respectively (89). Wang et al. showed that radiographic images based on T2WI and DWI showed a good predictive power for pelvic LNM in early cervical cancer (83). More values are listed in **Table 7** (85–89).

5 LIMITATIONS AND FUTURE DIRECTIONS

AI performs well in both computing and image analyses. These characteristics make it a rising star in the field of medical research, helping clinicians in decision-making, reducing the workload of doctors, and reducing the rate of misdiagnosis. Overall, AI can improve the specificity and accuracy of screening and diagnostic programs, overcome time constraints and limited professional and technical personnel, and avoid bias caused by subjective factors, which will enable cervical cancer screening to be implemented in resource-poor areas, thus markedly reducing the incidence of cervical cancer.

TABLE 7 | Application of AI in MRI to diagnosis cervical cancer.

Reference	Year	Aim of study	Number of cases	Methods	Results
Lin et al. (82)	2020	Cervical Cancer MRI Image segmentation and location	169 patients (training set 144; validation set 25)	DL Radiomics	A dice coefficient: 0.82; Sensitivity: 0.89, PPV:0.92
Wang et al. (83)	2020	Segmentation: Prediction of parametrial invasion	137 patients (training set 91; validation set 46)	Radiomics	Training set AUC T2WI: 0.797 T2WI and DWI0.780 (95% CI) Validation set T2WI 0.946 (95% CI) T2WI and DWI 0.921 (95% CI)
Peng et al. (84)	2019	Enhancing Cervical Cancer MRI Image Segmentation	Not mention	Wireless network; DL	AUC 0.980
Yu et al. (85)	2019	Assisting diagnosis of lymph node metastasis	153 patients (training set 102; validation set 51)	Radiomics	Training set AUC: 0.870Validation set AUC 0.864
Wu et al. (86)	2019	Assisting diagnosis of lymph node metastasis	189 patients (training set 126; validation set 63)	Radiomics	Training set AUC 0.895 Sensitivity 94.3%Validation set AUC 0.847 Sensitivity 100%
Wang et al. (87)	2019	Assisting diagnosis of lymph node metastasis	96 patients (training set 96; validation set 96)	RadiomicsSVM	Training set C-index 0.893($P=4.311*10^{-5}$)Validation set C-index 0.922 ($P=3.412*10^{-2}$)
Xiao et al. (88)	2020	Assisting diagnosis of lymph node metastasis	233 patients (training set 155; validation set 78)	Radiomics	Training set C-index 0.856 (95% CI)Validation set C-index 0.883 (95% CI)
Wu et al. (89)	2020	Assisting diagnosis of lymph node metastasis	479 patients (training set 338; validation set 141)	DL	AUC 0.933 (95% CI)

However, the application of AI involves some challenges. First is data; machine learning (ML) algorithms sometimes lack data in that they typically require millions of observations to achieve acceptable performance levels (86). However, current clinical data may be scarce, lack markers, and have uncertain quality. The management of medical data is another major obstacle for the development of automated clinical solutions (15). The establishment of not only multiple but also standardized and large databases is a future concern. Data security issues and overfitting should also be considered as they can give rise to exaggerated results that can lead to overdiagnosis (90). Second, models established using AI have not been applied and popularized in clinical practice; therefore, a series of prospective clinical studies are urgently needed to verify these results. Third, AI cannot replace clinicians as it is only an auxiliary diagnostic approach. AI may also cause system paralysis, requiring technical maintenance skills. Furthermore, maintenance systems need to be trained and established.

AI is promising in cervical cancer screening, especially its application in cervical cytology is relatively mature. But the segmentation technology is still faced with many challenges which is important for automatic classification. Such as the segmentation of overlapping nuclei, the processing of non-target cells, and fragments and the quality control of slide dyeing differences are still problem that needs to be optimized. We also mentioned that some classification methods do not rely on segmentation techniques in the previous. It will avoid many pre-processing steps and may be a direction for future development. In addition to the application of early screening and diagnosis mentioned in this paper, AI can be applied to the treatment, prognosis prediction, and prevention of cervical cancer. In the future, more research on treatment and prediction is needed for better treatment decision-making. This will facilitate cervical cancer eradication programs worldwide. Furthermore, as the incidence of cervical adenocarcinoma and other rare pathological types increases, AI should be applied for the early diagnosis of such diseases in the future. AI can also be used for noninvasive differentiation of cervical cancer from other diseases. Further development of AI technologies will greatly enhance the prediction of cervical cancer, maximize the improvements in cervical cancer screening and diagnosis, optimize staging systems, and improve patient prognosis.

AUTHOR CONTRIBUTIONS

XH and YL contributed to the collection of relevant literature. GS and YL contributed to literature analysis. XH reorganized the literature and wrote the original draft of the manuscript. LZ and TW provided considerable help in the revision of the manuscript. XM was responsible for the design of the review and revision of the manuscript. All authors contributed to the article and approved the submitted version.

FUNDING

ACKNOWLEDGMENTS

REFERENCES

1. Sung H, Ferlay J, Siegel RL, Laversanne M, Soerjomataram I, Jemal A, et al. Global Cancer Statistics 2020: GLOBOCAN Estimates of Incidence and Mortality Worldwide for 36 Cancers in 185 Countries. *CA: A Cancer J Clin* (2021) 71:209–49. doi: 10.3322/caac.21660

2. Brisson M, Kim JJ, Canfell K, Drolet M, Gingras G, Burger EA, et al. Impact of HPV Vaccination and Cervical Screening on Cervical Cancer Elimination: A Comparative Modelling Analysis in 78 Low-Income and Lower-Middle-Income Countries. *Lancet* (2020) 395(10224):575–90. doi: 10.1016/S0140-6736(20)30068-4

3. Schiffman M, Castle PE, Jeronimo J, Rodriguez AC, Wacholder S. Human Papillomavirus and Cervical Cancer. *Lancet* (2007) 370(9590):890–907. doi: 10.1016/S0140-6736(07)61416-0

4. Simms KT, Steinberg J, Caruana M, Smith MA, Lew JB, Soerjomataram I, et al. Impact of Scaled Up Human Papillomavirus Vaccination and Cervical Screening and the Potential for Global Elimination of Cervical Cancer in 181 Countries, 2020-99: A Modelling Study. *Lancet Oncol* (2019) 20(3):394–407. doi: 10.1016/S1470-2045(18)30836-2

5. Fontham ETH, Wolf AMD, Church TR, Etzioni R, Flowers CR, Herzig A, et al. Cervical Cancer Screening for Individuals at Average Risk: 2020 Guideline Update From the American Cancer Society. *CA Cancer J Clin* (2020) 70(5):321–46. doi: 10.3322/caac.21628

6. Redman CWE, Kesic V, Cruickshank ME, Gultekin M, Carcopino X, Castro Sanchez M, et al. European Federation for Colposcopy and Pathology of the Lower Genital Tract (EFC) and the European Society of Gynecologic Oncology (ESGO). *Eur Consensus Statement Essential Colposcopy Eur J Obstet Gynecol Reprod Biol* (2021) 256:57–62. doi: 10.1016/jejogrb.2020.06.029

7. WHO. *World Health Organization Human Papillomavirus (HPV) and Cervical Cancer, Fact Sheet.* Available at: https://www.who.int/news-room/fact-sheets/detail/human-papillomavirus-(hpv)-and-cervical-cancer (Accessed 17 September 2019).

8. Bray F, Ferlay J, Soerjomataram I, Siegel RL, Torre LA, Jemal A. Global Cancer Statistics 2018: GLOBOCAN Estimates of Incidence and Mortality Worldwide for 36 Cancers in 185 Countries. *CA Cancer J Clin* (2018) 68(6):394–424. doi: 10.3322/caac.21492

9. Pollack AE, Tsu VD. Preventing Cervical Cancer in Low-Resource Settings: Building a Case for the Possible. *Int J Gynaecol Obstet* (2005) 89 Suppl 2:S1–3. doi: 10.1016/j.ijgo.2005.01.014

10. World Health Organization. Cervical Cancer Screening in Developing Countries: Report of a WHO Consultation. Geneva: World Health Organization (2002).

11. Nanda K, McCrory DC, Myers ER, Bastian LA, Hasselblad V, Matchar DB, et al. Accuracy of the Papanicolaou Test in Screening for and Follow-Up of Cervical Cytologic Abnormalities: A Systematic Review. *Ann Intern Med* (2000) 132(10):810–9. doi: 10.7326/0003-4819-132-10-200005160-00009

12. Esteva A, Kuprel B, Novoa RA, Ko J, Swetter SM, Blau HM, et al. Dermatologist-Level Classification of Skin Cancer With Deep Neural Networks. *Nature* (2017) 542(7639):115–8. doi: 10.1038/nature21056

13. Maron RC, Weichenthal M, Utikal JS, Hekler A, Berking C, Hauschild A, et al. Systematic Outperformance of 112 Dermatologists in Multiclass Skin Cancer

Image Classification by Convolutional Neural Networks. *Eur J Cancer* (2019) 119:57–65. doi: 10.1016/j.ejca.2019.06.013

14. Schmidt-Erfurth U, Sadeghipour A, Gerendas BS, Waldstein SM, Bogunović H. Artificial Intelligence in Retina. *Prog Retin Eye Res* (2018) 67:1–29. doi: 10.1016/j.preteyeres.2018.07.004

15. Bi WL, Hosny A, Schabath MB, Giger ML, Birkbak NJ, Mehrtash A, et al. Artificial Intelligence in Cancer Imaging: Clinical Challenges and Applications. *CA Cancer J Clin* (2019) 69(2):127–57. doi: 10.3322/caac.21552

16. Marth C, Landoni F, Mahner S, McCormack M, Gonzalez-Martin A, Colombo N. Cervical Cancer: ESMO Clinical Practice Guidelines for Diagnosis, Treatment and Follow-Up. *Ann Oncol* (2017) 28(suppl_4):iv72–83. doi: 10.1093/annonc/mdx220

17. Screening for Cervical Cancer. *CA Cancer J Clin* (2020) 70(5):347–8. doi: 10.3322/caac.21629

18. Cox S. Guidelines for Papanicolaou Test Screening and Follow-Up. *J Midwifery Wom Heal* (2012) 57:86–9. doi: 10.1111/j.1542-2011.2011.00116.x

19. Phaliwong P, Pariyawateekul P, Khuakoonratt N, Sirichai W, Bhamarapravatana K, Suwannarurk K. Cervical Cancer Detection Between Conventional and Liquid Based Cervical Cytology: A 6-Year Experience in Northern Bangkok Thailand. *Asian Pac J Cancer Prev* (2018) 19(5):1331–6. doi: 10.22034/APJCP.2018.19.5.1331

20. Hoda RS, Loukeris K, Abdul-Karim FW. Gynecologic Cytology on Conventional and Liquid-Based Preparations: A Comprehensive Review of Similarities and Differences. *Diagn Cytopathol* (2013) 41(3):257–78. doi: 10.1002/dc.22842

21. Nayar R, Wilbur DC. The Pap Test and Bethesda 2014. *Cancer Cytopathol* (2015) 123(5):271–81. doi: 10.1002/cncy.21521

22. Hussain E, Mahanta LB, Das CR, Choudhury M, Chowdhury M. A Shape Context Fully Convolutional Neural Network for Segmentation and Classification of Cervical Nuclei in Pap Smear Images. *Artif Intell Med* (2020) 107:101897. doi: 10.1016/j.artmed.2020.101897

23. Khan MJ, Werner CL, Darragh TM, Guido RS, Mathews C, Moscicki AB, et al. ASCCP Colposcopy Standards: Role of Colposcopy, Benefits, Potential Harms, and Terminology for Colposcopic Practice. *J Low Genit Tract Dis* (2017) 21(4):223–9. doi: 10.1097/LGT.0000000000000338

24. Miyagi Y, Takehara K, Miyake T. Application of Deep Learning to the Classification of Uterine Cervical Squamous Epithelial Lesion From Colposcopy Images. *Mol Clin Oncol* (2019) 11(6):583–9. doi: 10.3892/mco.2019.1932

25. Sawaya GF, Smith-McCune K, Kuppermann M. Cervical Cancer Screening: More Choices in 2019. *JAMA* (2019) 321(20):2018–9. doi: 10.1001/jama.2019.4595

26. Yuan C, Yao Y, Cheng B, Cheng Y, Li Y, Li Y, et al. The Application of Deep Learning Based Diagnostic System to Cervical Squamous Intraepithelial Lesions Recognition in Colposcopy Images. *Sci Rep* (2020) 10(1):11639. doi: 10.1038/s41598-020-68252-3

27. Walboomers JM, Jacobs MV, Manos MM, Bosch FX, Kummer JA, Shah KV, et al. Human Papillomavirus Is a Necessary Cause of Invasive Cervical Cancer Worldwide. *J Pathol* (1999) 189(1):12–9. doi: 10.1002/(SICI)1096-9896(199909)189:1<12::AID-PATH431>3.0.CO;2-F

28. Guo M, Gong Y, Wang J, Dawlett M, Patel S, Liu P, et al. The Role of Human Papillomavirus Type 16/18 Genotyping in Predicting High-Grade Cervical/Vaginal Intraepithelial Neoplasm in Women With Mildly Abnormal Papanicolaou Results. *Cancer Cytopathol* (2013) 121(2):79–85. doi: 10.1002/cncy.21240

29. Wong OGW, Ng IFY, Tsun OKL, Pang HH, Ip PPC, Cheung ANY. Machine Learning Interpretation of Extended Human Papillomavirus Genotyping by Onclarity in an Asian Cervical Cancer Screening Population. *J Clin Microbiol* (2019) 57(12):e00997–19. doi: 10.1128/JCM.00997-19

30. Pathania D, Landeros C, Rohrer L, D'Agostino V, Hong S, Degani I, et al. Point-of-Care Cervical Cancer Screening Using Deep Learning-Based Microholography. *Theranostics* (2019) 9(26):8438–47. doi: 10.7150/thno.37187

31. Tian R, Cui Z, He D, Tian X, Gao Q, Ma X, et al. Risk Stratification of Cervical Lesions Using Capture Sequencing and Machine Learning Method Based on HPV and Human Integrated Genomic Profiles. *Carcinogenesis* (2019) 40(10):1220–8. doi: 10.1093/carcin/bgz094

32. Yu K, Hyun N, Fetterman B, Lorey T, Raine-Bennett TR, Zhang H, et al. Automated Cervical Screening and Triage, Based on HPV Testing and Computer-Interpreted Cytology. *J Natl Cancer Inst* (2018) 110(11):1222–8. doi: 10.1093/jnci/djy044

33. Melnikow J, Henderson JT, Burda BU, Senger CA, Durbin S, Weyrich MS. Screening for Cervical Cancer With High-Risk Human Papillomavirus Testing: Updated Evidence Report and Systematic Review for the US Preventive Services Task Force. *JAMA* (2018) 320(7):687–705. doi: 10.1001/jama.2018.10400

34. Dijkstra MG, Snijders PJ, Arbyn M, Rijkaart DC, Berkhof J, Meijer CJ. Cervical Cancer Screening: On the Way to a Shift From Cytology to Full Molecular Screening. *Ann Oncol* (2014) 25(5):927–35. doi: 10.1093/annonc/mdt538

35. Perkins RB, Langrish SM, Stern LJ, Figueroa J, Simon CJ. Comparison of Visual Inspection and Papanicolau (PAP) Smears for Cervical Cancer Screening in Honduras: Should PAP Smears be Abandoned? *Trop Med Int Heal* (2007) 12(9):1018–25. doi: 10.1111/j.1365-3156.2007.01888.x

36. Stoler MH, Schiffman M. Interobserver Reproducibility of Cervical Cytologic and Histologic Interpretations: Realistic Estimates From the ASCUS-LSIL Triage Study. *JAMA* (2001) 285(11):1500–5. doi: 10.1001/jama.285.11.1500

37. William W, Ware A, Basaza-Ejiri AH, Obungoloch J. A Review of Image Analysis and Machine Learning Techniques for Automated Cervical Cancer Screening From Pap-Smear Images. *Comput Methods Programs Biomed* (2018) 164:15–22. doi: 10.1016/j.cmpb.2018.05.034

38. Bengtsson E, Malm P. Screening for Cervical Cancer Using Automated Analysis of PAP-Smears. *Comput Math Methods Med* (2014) 2014:842037. doi: 10.1155/2014/842037

39. Chivukula M, Saad RS, Elishaev E, White S, Mauser N, Dabbs DJ. Introduction of the Thin Prep Imaging System (TIS): Experience in a High Volume Academic Practice. *Cytojournal* (2007) 4:6. doi: 10.1186/1742-6413-4-6

40. Thrall MJ. Automated Screening of Papanicolaou Tests: A Review of the Literature. *Diagn Cytopathol* (2019) 47(1):20–7. doi: 10.1002/dc.23931

41. Chankong T, Theera-Umpon N, Auephanwiriyakul S. Automatic Cervical Cell Segmentation and Classification in Pap Smears. *Comput Methods Programs Biomed* (2014) 113(2):539–56. doi: 10.1016/j.cmpb.2013.12.012

42. Landau MS, Pantanowitz L. Artificial Intelligence in Cytopathology: A Review of the Literature and Overview of Commercial Landscape. *J Am Soc Cytopathol* (2019) 8(4):230–41. doi: 10.1016/j.jasc.2019.03.003

43. Firuzinia S, Afzali SM, Ghasemian F, Mirroshandel SA. A Robust Deep Learning-Based Multiclass Segmentation Method for Analyzing Human Metaphase II Oocyte Images. *Comput Methods Programs Biomed* (2021) 201:105946. doi: 10.1016/j.cmpb.2021.105946

44. Wang P, Wang L, Li Y, Song Q, Lv S, Hu X. Automatic Cell Nuclei Segmentation and Classification of Cervical Pap Smear Images. *Biomed Signal Process Control* (2019) 48:93–103. doi: 10.1016/j.bspc.2018.09.008

45. Zhao L, Li K, Wang M, Yin J, Zhu En, Wu C, et al. Automatic Cytoplasm and Nuclei Segmentation for Color Cervical Smear Image Using an Efficient Gap-Search MRF. *Comput Biol Med* (2016) 71:46–56. doi: 10.1016/j.compbiomed.2016.01.025. ISSN 0010-4825.

46. Gautam S, Bhavsar A, Sao AK, Harinarayan KK. CNN Based Segmentation of Nuclei in PAP-Smear Images With Selective Pre-Processing. *Digital Pathol* (2018) 10581:105810X. doi: 10.1117/12.2293526

47. Lal S, Das D, Alabhya K, Kanfade A, Kumar A, Kini J. NucleiSegNet: Robust Deep Learning Architecture for the Nuclei Segmentation of Liver Cancer Histopathology Images. *Comput Biol Med* (2021) 128:104075. doi: 10.1016/j.compbiomed.2020.104075

48. Piotrowski T, Rippel O, Elanzew A, Nießing B, Stucken S, Jung S, et al. Deep-Learning-Based Multi-Class Segmentation for Automated, Non-Invasive Routine Assessment of Human Pluripotent Stem Cell Culture Status. *Comput Biol Med* (2021) 129:104172. doi: 10.1016/j.compbiomed.2020.104172

49. Conceição T, Braga C, Rosado L, Vasconcelos MJM. A Review of Computational Methods for Cervical Cells Segmentation and Abnormality Classification. *Int J Mol Sci* (2019) 20(20):5114. doi: 10.3390/ijms20205114

50. Song Y, Zhu L, Qin J, Lei B, Sheng B, Choi KS. Segmentation of Overlapping Cytoplasm in Cervical Smear Images *via* Adaptive Shape Priors Extracted

From Contour Fragments. *IEEE Trans Med Imaging* (2019) 38(12):2849–62. doi: 10.1109/TMI.2019.2915633

51. Sompawong N, Mopan J, Pooprasert P, Himakhun W, Suwannarurk K, Ngamvirojcharoen J, et al. Automated Pap Smear Cervical Cancer Screening Using Deep Learning. *Annu Int Conf IEEE Eng Med Biol Soc* (2019) 2019:7044–8. doi: 10.1109/EMBC.2019.8856369

52. Hussain E, Mahanta LB, Das CR, Talukdar RK. A Comprehensive Study on the Multi-Class Cervical Cancer Diagnostic Prediction on Pap Smear Images Using a Fusion-Based Decision From Ensemble Deep Convolutional Neural Network. *Tissue Cell* (2020) 65:101347. doi: 10.1016/j.tice.2020.101347

53. Bora K, Chowdhury M, Mahanta LB, Kundu MK, Das AK. Automated Classification of Pap Smear Images to Detect Cervical Dysplasia. *Comput Methods Programs Biomed* (2017) 138:31–47. doi: 10.1016/j.cmpb.2016.10.001

54. Zhang L, Lu Le, Nogues I, Summers RM, Liu S, Yao J. DeepPap: Deep Convolutional Networks for Cervical Cell Classification. *IEEE J BioMed Health Inform* (2017) 21(6):1633–43. doi: 10.1109/JBHI.2017.2705583

55. Shi J, Wang R, Zheng Y, Jiang Z, Zhang H, Yu L. Cervical Cell Classification With Graph Convolutional Network. *Comput Methods Programs Biomed* (2021) 198:105807. doi: 10.1016/j.cmpb.2020.105807

56. Rahaman MM, Li C, Yao Y, Kulwa F, Wu X, Li X, et al. DeepCervix: A Deep Learning-Based Framework for the Classification of Cervical Cells Using Hybrid Deep Feature Fusion Techniques. *Comput Biol Med* (2021) 136:104649. doi: 10.1016/j.compbiomed.2021.104649

57. Mariarputham EJ, Stephen A. Nominated Texture Based Cervical Cancer Classification. *Comput Math Methods Med* (2015) 2015:1–10. doi: 10.1155/2015/586928

58. Yosinski J, Clune J, Bengio Y, Lipson H. How Transferable Are Features in Deep Neural Networks? *Adv Neural Inf Process Syst* (2014) 27:3320–8.

59. Holmström O, Linder N, Kaingu H, Mbuuko N, Mbete J, Kinyua F, et al. Point-Of-Care Digital Cytology With Artificial Intelligence for Cervical Cancer Screening in a Resource-Limited Setting. *JAMA Netw Open* (2021) 4 (3):e211740. doi: 10.1001/jamanetworkopen.2021.1740

60. Bao H, Sun X, Zhang Y, Pang B, Li H, Zhou L, et al. The Artificial Intelligence-Assisted Cytology Diagnostic System in Large-Scale Cervical Cancer Screening: A Population-Based Cohort Study of 0.7 Million Women. *Cancer Med* (2020) 9(18):6896–906. doi: 10.1002/cam4.3296

61. Bao H, Bi H, Zhang X, Zhao Y, Dong Y, Luo X, et al. Artificial Intelligence-Assisted Cytology for Detection of Cervical Intraepithelial Neoplasia or Invasive Cancer: A Multicenter, Clinical-Based, Observational Study. *Gynecol Oncol* (2020) 159(1):171–8. doi: 10.1016/j.ygyno.2020.07.099

62. Wang CW, Liou YA, Lin YJ, Chang CC, Chu PH, Lee YC, et al. Artificial Intelligence-Assisted Fast Screening Cervical High Grade Squamous Intraepithelial Lesion and Squamous Cell Carcinoma Diagnosis and Treatment Planning. *Sci Rep* (2021) 11(1):16244. doi: 10.1038/s41598-021-95545-y

63. Zhu X, Li X, Ong K, Zhang W, Li W, Li L, et al. Hybrid AI-Assistive Diagnostic Model Permits Rapid TBS Classification of Cervical Liquid-Based Thin-Layer Cell Smears. *Nat Commun* (2021) 12(1):3541. doi: 10.1038/s41467-021-23913-3

64. Tang HP, Cai D, Kong YQ, Ye H, Ma ZX, Lv HS, et al. Cervical Cytology Screening Facilitated by an Artificial Intelligence Microscope: A Preliminary Study. *Cancer Cytopathol* (2021). doi: 10.1002/cncy.22425

65. Janicek MF, Averette HE. Cervical Cancer: Prevention, Diagnosis, and Therapeutics. *CA Cancer J Clin* (2001) 51(2):92–114; quiz 115-8. doi: 10.3322/canjclin.51.2.92

66. Bhatla N, Berek JS, Cuello Fredes M, Denny LA, Grenman S, Karunaratne K, et al. Revised FIGO Staging For Carcinoma of The Cervix Uteri. *Int J Gynaecol Obstet.* (2019) 145(1):129-35. doi: 10.1002/ijgo.12749

67. Xue P, Ng MTA, Qiao Y. The Challenges of Colposcopy for Cervical Cancer Screening in LMICs and Solutions by Artificial Intelligence. *BMC Med* (2020) 18(1):169. doi: 10.1186/s12916-020-01613-x

68. Kim E, Huang X. A Data Driven Approach to Cervigram Image Analysis and Classification. In: ME Celebi, G Schaefer, editors. *Color Medical Image Analysis. Lecture Notes in Computational Vision and Biomechanics 6.* Dordrecht: Springer Netherlands (2013) 1-13. doi: 10.1007/978-94-007-5389-1_1

69. Song D, Kim E, Huang X, Patruno J, Munoz-Avila H, Heflin J, et al. Multimodal Entity Coreference for Cervical Dysplasia Diagnosis. *IEEE Trans Med Imaging* (2015) 34(1):229–45. doi: 10.1109/TMI.2014.2352311

70. Hu L, Bell D, Antani S, Xue Z, Yu K, Horning MP, et al. An Observational Study of Deep Learning and Automated Evaluation of Cervical Images for Cancer Screening. *J Natl Cancer Inst* (2019) 111(9):923–32. doi: 10.1093/jnci/djy225

71. Cho BJ, Choi YJ, Lee MJ, Kim JH, Son GH, Park SH, et al. Classification of Cervical Neoplasms on Colposcopic Photography Using Deep Learning. *Sci Rep* (2020) 10(1):13652. doi: 10.1038/s41598-020-70490-4

72. Asiedu MN, Simhal A, Chaudhary U, Mueller JL, Lam CT, Schmitt JW, et al. Development of Algorithms for Automated Detection of Cervical Pre-Cancers With a Low-Cost, Point-of-Care, Pocket Colposcope. *IEEE Trans BioMed Eng* (2019) 66(8):2306–18. doi: 10.1109/TBME.2018.2887208

73. Miyagi Y, Takehara K, Nagayasu Y, Miyake T. Application of Deep Learning to the Classification of Uterine Cervical Squamous Epithelial Lesion From Colposcopy Images Combined With HPV Types. *Oncol Lett* (2020) 19 (2):1602–10. doi: 10.3892/ol.2019.11214

74. Xue P, Tang C, Li Q, Li Y, Shen Y, Zhao Y, et al. Development and Validation of an Artificial Intelligence System for Grading Colposcopic Impressions and Guiding Biopsies. *BMC Med* (2020) 18(1):406. doi: 10.1186/s12916-020-01860-y

75. Yue Z, Ding S, Zhao W, Wang H, Ma J, Zhang Y, et al. Automatic CIN Grades Prediction of Sequential Cervigram Image Using LSTM With Multistate CNN Features. *IEEE J BioMed Health Inform* (2020) 24(3):844–54. doi: 10.1109/JBHI.2019.2922682

76. Chandran V, Sumithra MG, Karthick A, George T, Deivakani M, Elakkiya B, et al. Diagnosis of Cervical Cancer Based on Ensemble Deep Learning Network Using Colposcopy Images. *BioMed Res Int* (2021) 2021:5584004. doi: 10.1155/2021/5584004

77. Peng G, Dong H, Liang T, Li L, Liu J. Diagnosis of Cervical Precancerous Lesions Based on Multimodal Feature Changes. *Comput Biol Med* (2021) 130:104209. doi: 10.1016/j.compbiomed.2021.104209

78. Choi SH, Kim SH, Choi HJ, Park BK, Lee HJ. Preoperative Magnetic Resonance Imaging Staging of Uterine Cervical Carcinoma: Results of Prospective Study. *J Comput Assist Tomogr* (2004) 28(5):620–7. doi: 10.1097/01.rct.0000138007.77725.0a

79. Hricak H, Gatsonis C, Chi DS, Amendola MA, Brandt K, Schwartz LH, et al. American College of Radiology Imaging Network 6651; Gynecologic Oncology Group 183. Role of Imaging in Pretreatment Evaluation of Early Invasive Cervical Cancer: Results of the Intergroup Study American College of Radiology Imaging Network 6651-Gynecologic Oncology Group 183. *J Clin Oncol* (2005) 23(36):9329–37. doi: 10.1200/JCO.2005.02.0354

80. Merz J, Bossart M, Bamberg F, Eisenblaetter M. Revised FIGO Staging for Cervical Cancer - A New Role for MRI. *Rofo* (2020) 192(10):937–44. doi: 10.1055/a-1198-5729

81. Cohen PA, Jhingran A, Oaknin A, Denny L. Cervical Cancer. *Lancet* (2019) 393(10167):169–82. doi: 10.1016/S0140-6736(18)32470-X

82. Lin YC, Lin CH, Lu HY, Chiang HJ, Wang HK, Huang YT, et al. Deep Learning for Fully Automated Tumor Segmentation and Extraction of Magnetic Resonance Radiomics Features in Cervical Cancer. *Eur Radiol* (2020) 30(3):1297–305. doi: 10.1007/s00330-019-06467-3

83. Wang T, Gao T, Guo H, Wang Y, Zhou X, Tian J, et al. Preoperative Prediction of Parametrial Invasion in Early-Stage Cervical Cancer With MRI-Based Radiomics Nomogram. *Eur Radiol* (2020) 30(6):3585–93. doi: 10.1007/s00330-019-06655-1

84. Liang P, Sun G, Wei S. Application of Deep Learning Algorithm in Cervical Cancer MRI Image Segmentation Based on Wireless Sensor. *J Med Syst* (2019) 43(6):156. doi: 10.1007/s10916-019-1284-7

85. Yu YY, Zhang R, Dong RT, Hu QY, Yu T, Liu F, et al. Feasibility of an ADC-Based Radiomics Model for Predicting Pelvic Lymph Node Metastases in Patients With Stage IB-IIA Cervical Squamous Cell Carcinoma. *Br J Radiol* (2019) 92(1097):20180986. doi: 10.1259/bjr.20180986

86. Obermeyer Z, Emanuel EJ. Predicting the Future - Big Data, Machine Learning, and Clinical Medicine. *N Engl J Med* (2016) 375(13):1216–9. doi: 10.1056/NEJMp1606181

87. Wang T, Gao T, Yang J, Yan X, Wang Y, Zhou X, et al. Preoperative Prediction of Pelvic Lymph Nodes Metastasis in Early-Stage Cervical Cancer Using Radiomics Nomogram Developed Based on T2-Weighted MRI and Diffusion-Weighted Imaging. *Eur J Radiol* (2019) 114:128–35. doi: 10.1016/j.ejrad.2019.01.003

88. Xiao M, Ma F, Li Y, Li Y, Li M, Zhang G, et al. Multiparametric MRI-Based Radiomics Nomogram for Predicting Lymph Node Metastasis in Early-Stage

Cervical Cancer. *J Magn Reson Imaging* (2020) 52(3):885–96. doi: 10.1002/jmri.27101

89. Wu Q, Wang S, Zhang S, Wang M, Ding Y, Fang J, et al. Development of a Deep Learning Model to Identify Lymph Node Metastasis on Magnetic Resonance Imaging in Patients With Cervical Cancer. *JAMA Netw Open* (2020) 3(7):e2011625. doi: 10.1001/jamanetworkopen.2020.11625

90. Guiot J, Vaidyanathan A, Deprez L, Zerka F, Danthine D, Frix AN, et al. A Review in Radiomics: Making Personalized Medicine a Reality via Routine Imaging. *Med Res Rev* (2022) 42(1):426-40. doi: 10.1002/med.21846

Focal Serous Tubal Intra-Epithelial Carcinoma Lesions Are Associated With Global Changes in the Fallopian Tube Epithelia and Stroma

Jingni Wu[1†], Yael Raz[1†], Maria Sol Recouvreux[1], Márcio Augusto Diniz[2], Jenny Lester[1], Beth Y. Karlan[1,3], Ann E. Walts[4], Arkadiusz Gertych[4,5,6] and Sandra Orsulic[1,3,7*]

[1] Department of Obstetrics and Gynecology, David Geffen School of Medicine, University of California, Los Angeles, Los Angeles, CA, United States, [2] Biostatistics Research Center, Cedars-Sinai Medical Center, Los Angeles, CA, United States, [3] Jonsson Comprehensive Cancer Center, University of California, Los Angeles, Los Angeles, CA, United States, [4] Department of Pathology and Laboratory Medicine, Cedars-Sinai Medical Center, Los Angeles, CA, United States, [5] Department of Surgery, Cedars-Sinai Medical Center, Los Angeles, CA, United States, [6] Faculty of Biomedical Engineering, Silesian University of Technology, Zabrze, Poland, [7] Department of Veterans Affairs (VA) Greater Los Angeles Healthcare System, Los Angeles, CA, United States

Objective: Serous tubal intra-epithelial carcinoma (STIC) lesions are thought to be precursors to high-grade serous ovarian cancer (HGSOC), but HGSOC is not always accompanied by STIC. Our study was designed to determine if there are global visual and subvisual microenvironmental differences between fallopian tubes with and without STIC lesions.

Methods: Computational image analyses were used to identify potential morphometric and topologic differences in stromal and epithelial cells in samples from three age-matched groups of fallopian tubes. The Benign group comprised normal fallopian tubes from women with benign conditions while the STIC and NoSTIC groups consisted of fallopian tubes from women with HGSOC, with and without STIC lesions, respectively. For the morphometric feature extraction and analysis of the stromal architecture, the image tiles in the STIC group were further divided into the stroma away from the STIC (AwaySTIC) and the stroma near the STIC (NearSTIC). QuPath software was used to identify and quantitate secretory and ciliated epithelial cells. A secretory cell expansion (SCE) or a ciliated cell expansion (CCE) was defined as a monolayered contiguous run of >10 secretory or ciliated cells uninterrupted by the other cell type.

Results: Image analyses of the tubal stroma revealed gradual architectural differences from the Benign to NoSTIC to AwaySTIC to NearSTIC groups. In the epithelial topology analysis, the relative number of SCE and the average number of cells within SCE were higher in the STIC group than in the Benign and NoSTIC groups. In addition, aging was associated with an increased relative number of SCE and a decreased relative number of CCE. ROC analysis determined that an average of 15 cells within SCE was the optimal cutoff value indicating the presence of a STIC lesion in the tubal epithelium.

Conclusions: Our findings suggest that global stromal alterations and age-associated reorganization of tubal secretory and ciliated cells are associated with STIC lesions. Further studies will need to determine if these alterations precede STIC lesions and provide permissible conditions for the formation of STIC.

Keywords: ovarian cancer, fallopian tube, secretory, ciliated, STIC, computational image analysis, computational pathology

INTRODUCTION

HGSOC accounts for ~70% of epithelial ovarian cancers, frequently presents at an advanced stage, and is associated with poor prognosis (1). Epidemiologic studies showed that the incidence of HGSOC increased with age and that advanced stage disease was more common in elderly women (1). Postmenopausal status and BRCA mutations were additional independent predictive factors for ovarian cancer (1, 2). However, the etiology of HGSOC is still unclear and discrete rate-limiting steps in ovarian cancer initiation that could inform early detection and prevention of ovarian cancer have not yet been identified.

A significant breakthrough in the understanding of HGSOC initiation was made upon close inspection of ovaries and fallopian tubes from risk reducing salpingo-oophorectomies (RRSO) in women at high risk for developing HGSOC due to inherited mutations in the BRCA genes (3–9). Early cancer lesions were detected in 5-10% of these women (3–9). The majority of the early lesions were present in the fallopian tube epithelia, rather than the ovary, indicating that the fallopian tube epithelial cells were the most likely precursors of HGSOC (10, 11).

The fallopian tube epithelium is composed of two major morphologic cell types: secretory and ciliated. In women of reproductive age, secretory and ciliated cells occur in an alternating pattern of 1-5 cells of the same type. Most early morphologic and genetic alterations have been observed in secretory cells but not in ciliated cells; hence, secretory cells are considered a precursor cell type for HGSOC (6–8, 12, 13). The lesion that morphologically most resembles early stage HGSOC is STIC (6–8, 12, 13). Cytohistologic characteristics of STIC lesions include: 1) nuclear changes, such as enlargement, hyperchromasia, atypia, and nucleolar prominence, 2) disorganization and loss of polarity, 3) epithelial tufting, 4) pleomorphism, 5) increased number of mitotic figures, and 6) the absence of ciliated cells (14–17). Additionally, STIC lesions usually exhibit the p53 signature and Ki67 >10% (18). Initially, only STIC lesions were thought to be the true fallopian tube precursor to HGSOC as they have similar morphologic and molecular features (19–21). However, ovarian cancer risk has been associated with other potential early serous precursors (ESPs) that have a benign appearance and a low proliferative index and do not satisfy the criteria of a STIC diagnosis (3, 9, 22–24). These ESPs include: serous tubal intraepithelial lesions (STIL) (17), which are characterized by lower Ki67 positivity and less cytologic atypia than STIC (16, 18), p53 signatures

defined as a single layer of >12 consecutive secretory cells with aberrant p53 expression (7, 25, 26), benign secretory cell outgrowth (SCOUT) defined as a continuous run of >30 secretory cells (3, 5, 9, 22, 23, 27), and secretory cell expansion (SCE) defined as a continuous run of >10 secretory cells with normal p53 expression (3, 22, 23). It is unclear if these secretory cell alterations are precursors to STIC or independent precursors to HGSOC (24, 28).

If STIC is an intermediate step in the transition between ESP and HGSOC, we hypothesized that ESPs and other aberrations in epithelial and stromal cell architecture would be more common in the fallopian tubes of HGSOC patients with STIC compared to the tubes of HGSOC patients without STIC. Because age as well as the presence/absence of HGSOC are expected to influence the tubal epithelial and stromal architecture, our analyses were controlled for these variables.

MATERIALS AND METHODS

Case Collection

After approval by the Cedars-Sinai Medical Center (CSMC) and University of California Los Angeles (UCLA) institutional review boards, H&E slides of fallopian tubes from a total of 89 cases were retrieved from the pathology files at CSMC and UCLA. The fallopian tubes had been surgically removed due to: 1) benign conditions (endometriosis, fibroids, or uterine prolapse), 2) RRSO (i.e. women with heritable BRCA mutations or first-degree family history of ovarian cancer), and 3) diagnosis of HGSOC. The presence or absence of STIC lesions was confirmed by a pathologist (AEW) using standard diagnostic criteria for STIC in H&E-stained sections with the aid of p53- and Ki67-immunoreactivity analyses in ambiguous cases (14–17).

Digital Image Analysis

Glass slides were digitized at 20x magnification using the Aperio AT Turbo slide scanner (Leica Biosystems). The Aperio ImageScope v.12.4.3 digital slide viewer was used to extract stromal tiles (256 x 256 pixels). The tiles were positioned so that at least one side or corner of the tile was as close as possible to epithelial cells without the risk of including epithelial cells in the tile (**Figure 1A**). In the extracted tiles, stromal architecture was characterized using our previously developed panel of algorithms (29) which computes 45 segmentation-based fractal texture analysis features (SFTA) (30), 256 local phase quantization features (LPQ) (31), and 256 binarized statistical image features (BSIF) (32). When applied to H&E channels
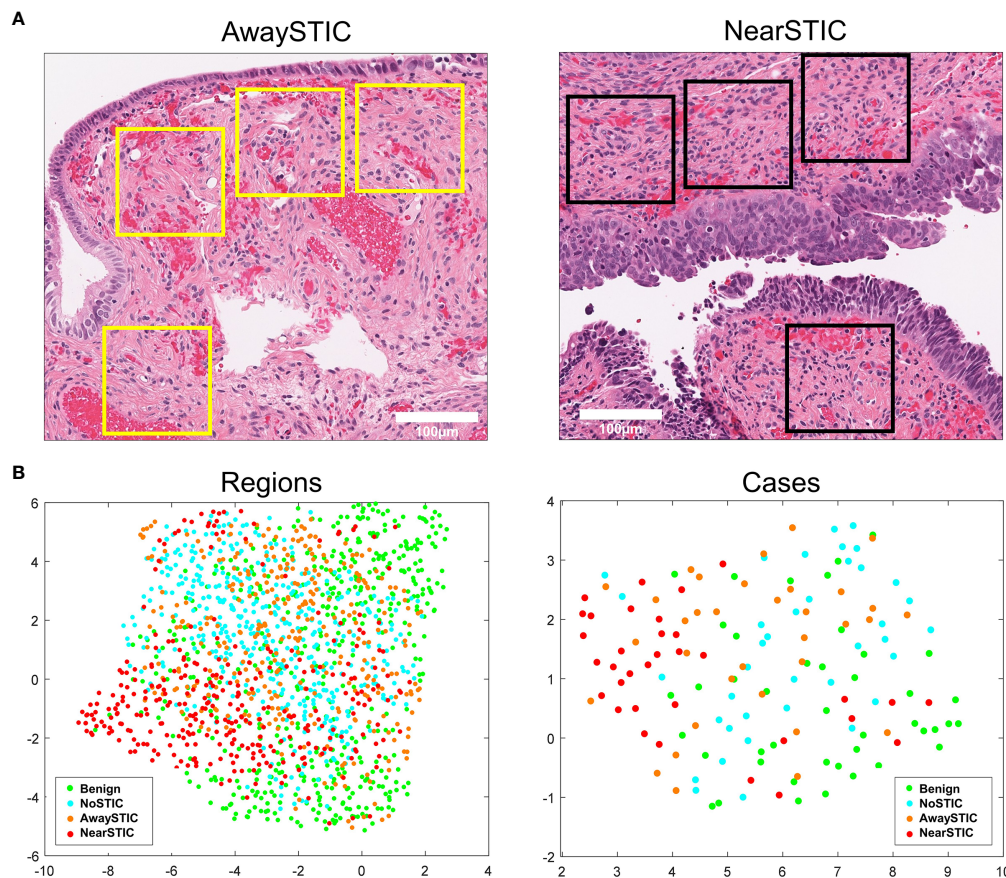
FIGURE 1 | The fallopian tube stromal architecture changes both locally and globally in the presence of STIC lesions. **(A)** Yellow boxes illustrate stromal regions where tiles were extracted away from the STIC lesion (left panel) and black boxes illustrate stromal regions where tiles were extracted near the STIC lesion (right panel). **(B)** Low-dimensional UMAP representation of stromal morphometric features in regions and cases with benign fallopian tubes (Benign), uninvolved fallopian tubes from patients with HGSOC (NoSTIC), and fallopian tubes with STIC lesions and HGSOC. Image regions from fallopian tubes with STIC lesions were stratified based on proximity to the lesion (awaySTIC and nearSTIC). Expression in an individual case represents median expressions from regions in that case. The UMAP plots were generated using the run_umap.m function in MATLAB.

color-deconvoluted from a single H&E tile, the panel yielded 1114 features (557 eosin and 557 hematoxylin). Prior to feature extraction, the H&E tiles were color-normalized to reduce staining variability across cases (33). The tiles were divided into four groups: Benign, NoSTIC, AwaySTIC, and NearSTIC. NearSTIC was defined as a stromal tile subjacent to STIC (at least one side or corner of the image tile was adjacent to the epithelial cells in the STIC lesion) (**Figure 1A**). AwaySTIC was defined as a stromal tile subjacent to epithelial cells in a section of the tube that was >2 mm away from the STIC region demarcated by a pathologist. Within each case, the computed features were aggregated into vectors containing feature medians such that each case provided one vector per group. Feature vectors were z-scored and statistically analyzed using one-way ANOVA followed by the Tukey-Kramer test for multiple comparisons to identify differential morphologic features between the groups. The significance level α in the ANOVA was Bonferroni-corrected (α=0.05/1114). The topology of low dimensional representation of the feature vectors was visualized by the

uniform manifold approximation and projection (UMAP) plot. The MATLAB implementation of UMAP was downloaded from https://www.mathworks.com/matlabcentral/fileexchange/71902-uniform-manifold-approximation-and-projection-umap.

QuPath software (34) was used for H&E digital image analyses of the fallopian tube epithelium. Areas of the slide that contained a monolayer of visually recognizable secretory and epithelial cells were selected with a brush tool as regions of interest (ROIs). STIC lesions were excluded from the analysis. Cell segmentation algorithms, color deconvolution, and supervised classifiers were used as machine-learning methods. QuPath was used for cell identification and cell counting. We chose a random forest supervised classifier to recognize the cell types. The ciliated epithelial cells were identified by the presence of cilia on the apical surface while epithelial cells without cilia were considered to be secretory cells (**Figure 2**). After setting the appropriate cell segmentation and color deconvolution parameters in QuPath, we trained the object classifier to identify and count total epithelial cells, stromal cells, secretory
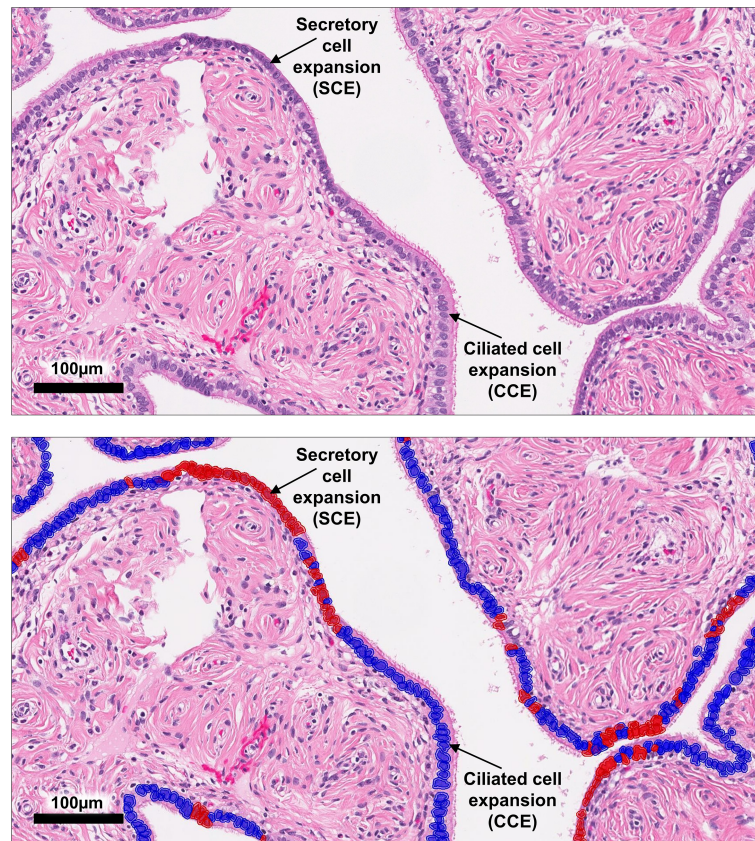
FIGURE 2 | QuPath analysis of epithelial cells in the fallopian tube. A representative image of an ampulla region with SCE and CCE, which are defined as a monolayer of >10 contiguous secretory or ciliated cells uninterrupted by the other cell type. The top panel shows the original H&E image while the bottom panel shows epithelial cell classification after ROI selection, cell segmentation, and classifier application.

cells, and ciliated cells. To account for differences in the number of epithelial cells available for examination on each slide, the relative number of SCE or CCE was defined as the number of monolayered contiguous runs of >10 secretory or ciliated cells divided by the total number of epithelial cells in all ROIs.

Statistical Analysis of Epithelial Cell Topology

Continuous variables with a normal distribution were summarized using means and standard deviations (SD), otherwise they were summarized using medians and interquartile ranges. The categorical variables were summarized with rates using the Kruskal-Wallis test or the Fisher's exact test. Two independent groups were analyzed by the Mann-Whitney test and two paired samples were analyzed by the Wilcoxon signed-rank test. Three or more independent groups were analyzed using the Kruskal-Wallis test. Variables with $P< 0.05$ by univariable analysis were included in the multivariable analysis using the log-transformed values. Multivariable linear regression was used to control for potential confounders, such as age, menopausal status, BRCA

mutation status, and prior chemotherapy. The correlation between age and SCE, CCE, or cell number within the respective expansions was determined using the Spearman correlation method. The Receiver Operating Characteristic (ROC) curve was plotted to define the optimal cutoff values for the parameters of SCE and the cell number within SCE. All analyses were two-sided and the significance level was set at $P< 0.05$. The statistical analyses were conducted using SPSS 23.0 (SPSS Inc., Chicago, IL, USA).

Sample Groups

The number of patients and the number of samples analyzed in each group depended upon the availability of the tube specimen that fulfilled specific criteria for individual analyses. In the majority of patients, only one tube and/or one tube region (fimbria or ampulla) fulfilled the criteria for a specific analysis. The following groups were analyzed:

- Stromal morphometric feature analyses: 1) Benign, 2) NoSTIC, 3) AwaySTIC, and 4) NearSTIC. No distinction was made between the fimbria and ampulla regions. Since the morphometric feature analysis was independent of clinical

variables, each fallopian tube was considered a separate case even if it came from the same patient.

- SCE and CCE analyses: 1) Benign, 2) NoSTIC, and 3) STIC. The fimbria and ampulla regions were analyzed separately.
- Age-related analyses: 1) Benign, 2) NoSTIC, and 3) STIC. Only the fimbria region was analyzed.
- Confounder analyses: 1) Benign, 2) NoSTIC, and 3) STIC. The fimbria and ampulla regions were analyzed separately.
- ROC curve analyses: 1) STIC and 2) Benign+NoSTIC. The fimbria and ampulla regions were analyzed separately.

RESULTS

Compared to Benign Fallopian Tubes, Local and Global Stromal Alterations Are Present in Fallopian Tubes With STIC Lesions and, to a Lesser Extent, Fallopian Tubes Without STIC Lesions From Patients With HGSOC

To study the stromal architecture associated with fallopian tubes, we extracted digital image tiles depicting fallopian tube stroma from women with benign gynecologic conditions (Benign group, n=43; 490 extracted tiles), fallopian tube stroma from women with HGSOC without STIC lesions (NoSTIC group, n=38; 446 extracted tiles), and fallopian tube stroma from women with HGSOC that contain STIC lesions (STIC group, n=34) (**Supplementary Figure 1A**). During extraction, the tiles in the STIC group were divided into two groups based on their proximity to the STIC lesions: AwaySTIC group (n=34; 338 extracted tiles) and NearSTIC group (n=34; 322 extracted tiles) (**Figure 1A** and **Supplementary Figure 1B**). There were no "visible" differences appreciated in the stroma upon review of the H&E stained slides or the stroma tile images from the four groups. However, ANOVA analysis revealed 250/1114 features with different means ($P<4.48e-5$) among the four groups of stromal tiles. Through the multiple comparison tests that followed ANOVA, we found features that distinguished Benign from NoSTIC (5 features), Benign from AwaySTIC (17 features), Benign from NearSTIC (208 features), NoSTIC from AwaySTIC (1 feature), NoSTIC from NearSTIC (188 features), and AwaySTIC from NearSTIC (54 features) ($P<2.0e-4$) (**Supplementary Figure 1C**). The presence of differentially expressed features is displayed through clustering of the region types and cases represented by UMAP feature embeddings (**Figure 1B**). Thus, although stromal changes in the fallopian tubes were not appreciable to the human eye with regular light microscopy, computational morphometric analysis revealed gradual global differences in the fallopian tube stroma from Benign to NoSTIC to AwaySTIC to NearSTIC (**Figure 1B**). These data suggest that STIC lesions are associated with local (NearSTIC) as well as global (AwaySTIC) stromal changes. The data also suggest that uninvolved fallopian tubes from HGSOC patients (NoSTIC) acquire global stromal changes that are in-between those

in normal fallopian tubes from women with benign conditions (Benign) and those in fallopian tubes with STIC lesions (AwaySTIC).

The Relative Number of SCE as Well as the Number of Cells Within SCE Are Higher in Fallopian Tubes With STIC Lesions

The distribution of secretory and ciliated cells in samples with or without STIC lesions was evaluated using the QuPath digital image analysis software (34). Epithelial cell types were classified and quantitated in H&E slides in which monolayers of secretory and ciliated cells were recognizable by light microscopy. **Figure 2** shows a representative example of SCE and CCE (>10 contiguous cells of the same type). Areas of the fallopian tube that contained a STIC lesion were excluded from the analysis. The fimbria and ampulla regions were analyzed separately. For the analysis of the fimbria region, 77 cases (**Supplementary Table 1**) were divided into three groups: Benign (n=39), NoSTIC (n=13), and STIC (n=25). As shown in **Supplementary Table 1**, there was no significant age difference across the three groups. For the analysis of the ampulla region, 42 cases (**Supplementary Table 2**) were divided into three groups: Benign (n=16), NoSTIC (n=13), and STIC (n=13). As shown in **Supplementary Table 2**, there was no significant age difference across the three groups. In both the fimbria and ampulla regions, the relative number of SCE in the STIC group was higher compared to the Benign group and the NoSTIC group (**Figure 3A**) although statistical significance was only reached in the fimbria region. In both the fimbria and ampulla regions, the average number of cells within SCE was significantly higher in the STIC group compared to the Benign and NoSTIC groups (**Figure 3B**). Although the relative number of CCE and the average number of cells within CCE were higher in the STIC group compared to the Benign group (**Supplementary Figure 2**), these differences were not significant in subsequent multivariable analyses.

Age Is Associated With an Increased Relative Number of SCE and a Decreased Relative Number of CCE in the Fallopian Tube Fimbriae

Spearman correlation analyses were performed to determine whether the numbers of SCE and CCE in the fimbriae were associated with age. With increasing age, the relative number of SCE was increased (r = 0.5, $P<0.0001$) while the relative number of CCE was decreased (r = -0.58, $P<0.0001$) (**Figure 4A**). There was a weak positive correlation between age and the number of cells within SCE, while the correlation between age and the number of cells within CCE was not significant (**Figure 4B**).

Potential Confounders

Given the differences in menopausal status, BRCA mutation status, and prior chemotherapy among the Benign, NoSTIC, and STIC groups (**Supplementary Tables 1, 2**), multivariable linear regression models were developed to control for these potential confounders. The results of the analyses showed that fallopian
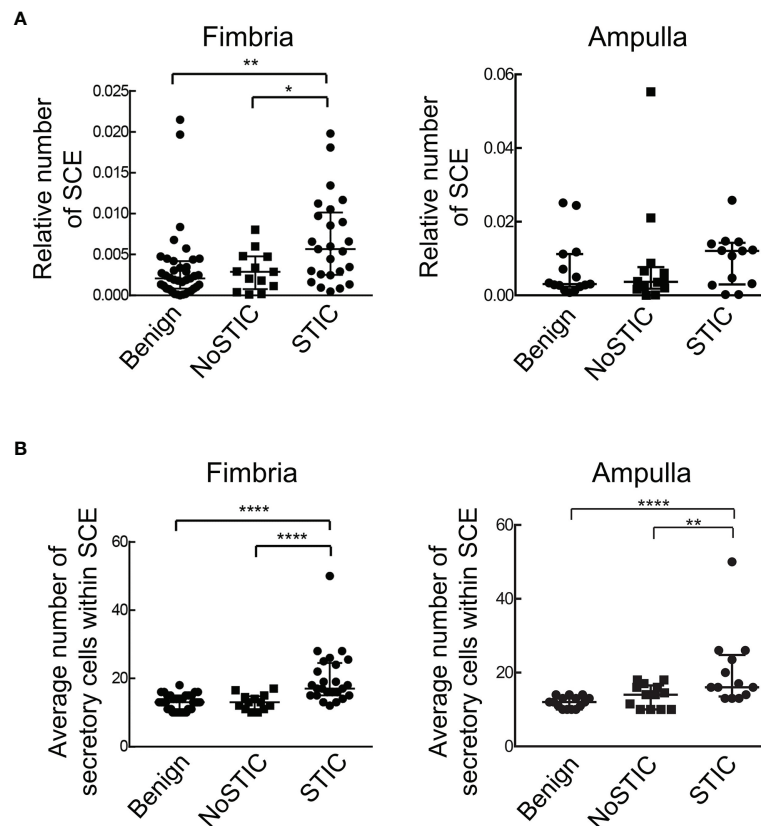
FIGURE 3 | Fallopian tubes with STIC lesions exhibit a higher relative number of SCE as well as a higher number of secretory cells within SCE. **(A)** The relative number of SCE (number of SCE divided by the total number of epithelial cells in all ROIs on the slide). **(B)** The average number of secretory cells within SCE. Statistically significant differences were determined using the Kruskal-Wallis test; *$P < 0.05$; **$P < 0.01$; ****$P < 0.0001$. Benign: fallopian tubes from women with benign gynecologic conditions. NoSTIC: fallopian tubes without STIC lesions from women with HGSOC. STIC: fallopian tubes with STIC lesions from women with HGSOC.

tube fimbria from postmenopausal women had an increased relative number of SCE ($P<0.0001$, **Supplementary Figure 3A**) and a decreased relative number of CCE ($P<0.05$, **Supplementary Figure 3B**). The fallopian tube fimbria from postmenopausal women also had an increased average number of cells within SCE ($P<0.01$, **Supplementary Figure 3C**) but no significant difference in the average number of cells within CCE (**Supplementary Figure 3D**). Similarly, BRCA mutation status and prior chemotherapy treatment had an effect on the distribution of the tubal epithelial cells (**Supplementary Figure 3**). Even after controlling for these potential confounders, the relative number of SCE and the number of secretory cells within the SCEs were higher in the fallopian tube fimbriae with STIC lesions compared to the Benign and NoSTIC groups (**Supplementary Table 3**). Also, after considering confounders, we found differences in the secretory cell number within SCEs in the fallopian tube ampullae with STIC lesions (**Supplementary Table 4**). Other potential confounders, such as parity, duration of breast feeding, history of oral contraceptive use, and history of hormone therapy, were not evaluated in this study due to limited data availability. Of note, these factors were

not significantly associated with STIC lesions in prior studies of large cohorts of patients (9, 35).

Increased Number of Cells Within SCE Is a Potential Biomarker of STIC Lesions

Despite the development and validation of algorithms for STIC (14–17), the identification of STIC lesions remains challenging due to subjectivity and technical limitations. It has been shown that a review of slides by multiple pathologists increased the diagnosis of STICs by 50% while additional tissue sampling more than doubled the number of identified STICs (9). We conducted ROC curve analyses to evaluate whether the relative number of SCE or the number of cells within SCE could be used as biomarkers for easier identification of STIC lesions (STIC group compared to Benign +NoSTIC groups). The analyses showed that the number of cells within SCE can identify fallopian tube fimbriae with STIC lesions with an area under the ROC curve (AUC) of 0.885 (cutoff value=15, sensitivity=84%, specificity=75%; $P< 0.0001$; 95% CI: 0.806-0.965) in the fimbria region (**Figure 5A**) and 0.817 (cutoff value=15, sensitivity=69%, specificity=78%; $P< 0.001$; 95% CI: 0.619-0.861) in the ampulla region (**Figure 5B**). Additionally, we
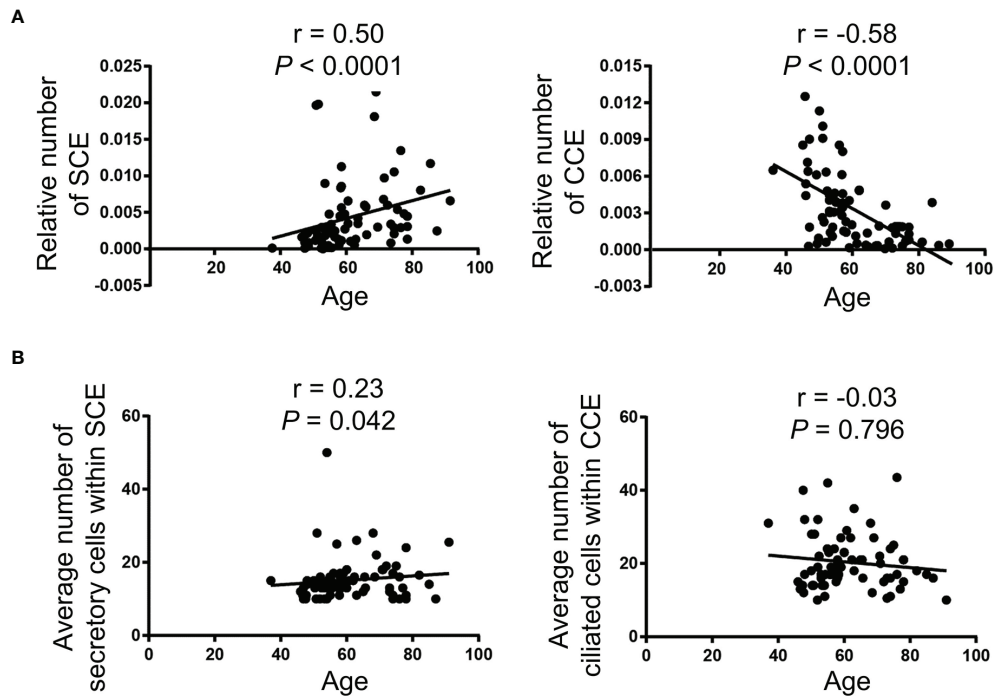
FIGURE 4 | Age is correlated with an increased relative number of SCE and a decreased relative number of CCE in the fallopian tube fimbriae. **(A)** The relative number of SCE (left panel) and CCE (right panel) divided by the total number of epithelial cells in all ROIs on an individual slide. **(B)** The average number of secretory cells within SCE (left panel) and ciliated cells within CCE (right panel). The Spearman correlation (r) was used for the correlation analysis.

showed that in the fimbria region, the relative number of SCE can discriminate between the fallopian tubes with and without STIC lesions with an AUC of 0.740 (cutoff value=0.005, sensitivity=56%, specificity=86.5%; $P < 0.001$; 95% CI: 0.686-0.947) (**Figure 5A**).

DISCUSSION

HGSOC is the most lethal gynecologic cancer, largely due to delayed symptom presentation and the lack of effective early
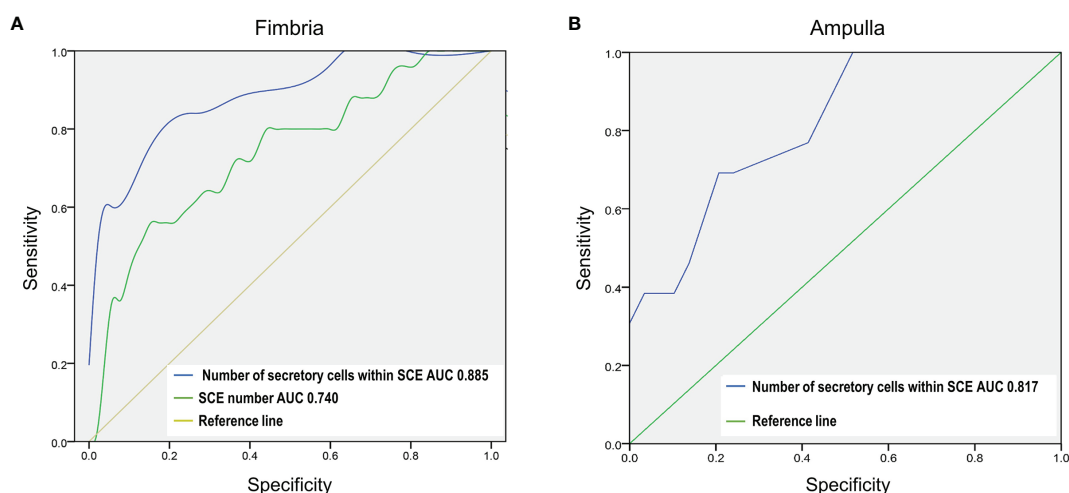
FIGURE 5 | The number of secretory cells within a SCE is a potential biomarker of STIC lesions in the fallopian tube fimbria and ampulla. The ROC test was used to assess the diagnostic potential of global fallopian tube histopathology in identifying fallopian tubes with STIC lesions (STIC vs Benign+NoSTIC). **(A)** ROC curve analysis of the relative number of SCE and the number of secretory cells within SCE in the fimbria region. **(B)** ROC curve analysis of the number of secretory cells within SCE in the ampulla region.

detection strategies. A poor understanding of the initiating events in ovarian cancer has significantly hampered efforts toward early detection and prevention. In the past two decades, detection of various morphologic and molecular changes in fallopian tube secretory cells, classified as STICs, STILs, p53 signatures, SCOUTs, SCEs and other ESPs, led to the hypothesis that HGSOC originates in the fallopian tube (3–11). Until recently, only STIC lesions were considered to be bona fide early precursors to HGSOC because of the existence of matching STIC and HGSOC site-specific TP53 mutations which strongly suggested the same lineage identity (20). However, the recent discovery of matching site-specific TP53 mutations between other ESPs and HGSOC as well as associations between ESPs and the increased risk of HGSOC (3, 22, 23) led to the "precursor escape" theory in which ESPs undergo malignant transformation after shedding into the peritoneal cavity, thus bypassing the formation of STIC lesions in the fallopian tube as a required intermediate step to HGSOC (24). Genomic profiling did not reveal significant differences between HGSOC with and without STIC lesions (10).

We addressed a different question: Is the presence of a STIC lesion associated with global changes in the tubal stroma and epithelium? Our computational morphometric feature analyses of the fallopian tube stroma from HGSOC patients revealed distinguishing morphometric features between fallopian tubes with and without STIC lesions. We also found that fallopian tubes with STIC lesions had an increased relative number of SCE as well as an increased number of cells within SCE. Together, these data suggest that STIC lesions are associated with global changes in the fallopian tube. Although it is unclear if these changes precede, occur concomitantly with, or are a consequence of STIC lesions, it is more likely that global alterations in the fallopian tube provide a favorable microenvironment for STIC formation than focal STIC lesions inducing global changes in the tube. Future studies are needed to determine whether these STIC-associated global topologic alterations also exhibit molecular changes that initiate STIC formation and could serve as targets for prevention. Of note, although the morphology of fallopian tube epithelia from HGSOC patients without STIC lesions resembled that of benign fallopian tubes, our data suggest that subtle architectural changes in the stroma precede HGSOC in the peritoneal cavity or that HGSOC can exert a long-distance field effect on the otherwise uninvolved fallopian tube stroma.

After examining the distribution of secretory and ciliated cells in fallopian tubes with or without STIC lesions, we further explored the relationship between the presence of expansions of secretory and ciliated cells and age. Epidemiologic studies have shown that the risk of HGSOC increases with age and that HGSOC is predominantly a disease of postmenopausal women (31, 32). Consistent with previously published studies (3, 36), we found that the number of cells within SCE increases with age while the number of cells within CCE decreases with age. The increase in the prevalence of p53 signatures with age in fallopian tubes with STIC lesions has been previously demonstrated (37, 38). However, to our knowledge, there are no publications that have determined the distribution of SCE and CCE alterations

associated with age in the presence or absence of a STIC lesion. Most of the specimens in our study were obtained from postmenopausal women in order to minimize the influence of the follicular phase, which has been shown to markedly influence the proliferation and morphology of fallopian tube epithelial cells (39). Importantly, we showed that after controlling for age and menopausal status, the relative number of SCE as well as the number of cells within SCE were higher in the fallopian tube fimbria with STIC lesions.

Computational image analysis has advantages as well as disadvantages. Two major advantages are the ability to identify features not appreciable by conventional light microscopy and the ability to conduct rapid quantitative analyses. A disadvantage, however, is that machine learning-assisted cell segmentation and phenotype determination may not be as precise as pathologic examination and depends on careful manual selection of ROIs comprising monolayer runs of epithelial cells devoid of out-of-focus areas and artefacts. Nevertheless, we obtained concordant results in cases where we manually counted the numbers of secretory and ciliated cells within SCE and CCE, respectively.

While most prior histopathologic characterizations of fallopian tubes from patients with HGSOC focused on precursor lesions and essentially ignored other portions of the fallopian tube epithelia, we explored global histopathologic changes in the epithelial and stromal compartments in fallopian tubes with and without STIC lesions. This holistic view of fallopian tubes could and assist in identifying STIC lesions and assessing cancer risk. Currently, precursor lesions in fallopian tubes removed from women with a genetic predisposition to ovarian cancer are identified by trained pathologists. Since visual morphologic changes in precursor lesions are subtle, interpretations by pathologists are unavoidably subjective (9, 40). Yet, it is important to establish the correct diagnosis because women with isolated premalignant lesions in the fallopian tube are at increased risk of developing carcinomatosis, presumably because cancer cells have spread from the precursor lesion to other organs in the peritoneal cavity prior to preventive surgery. We anticipate that the global alterations in the tubal epithelia and stroma that we report here will assist pathologists in correctly classifying ambiguous cases. Additionally, a careful consideration of the global changes in the fallopian tube with STIC lesions could simplify the current protocol for pathologic examination of fallopian tubes. Since early cancer lesions are typically microscopic, entire fallopian tubes are cut into thin sections using the SEE-FIM (sectioning and extensive examination of the fimbria) dissection protocol with the distal fimbriae cut sagittally at 1 mm intervals (21). This can yield a large number of slides that need to be reviewed by a pathologist to potentially identify one section with an early cancer lesion. Even this meticulous method of sectioning might miss early cancer lesions if they occur within the 1 mm region between sections (9). Since our results show that fallopian tubes containing a STIC lesion exhibit a greater number of cells within SCE even after controlling for potential confounders, such as menopausal status, chemotherapy, and age, we suggest that SCEs containing more than 15 secretory cells should prompt a review

of available sections and further microscopic examination of deeper levels of the fallopian tube paraffin blocks for features of a microscopic STIC lesion. Future validation and clinical standardization of cutoff parameters could improve risk stratification and personalization of preventive strategies for women with a predisposition to HGSOC.

To our knowledge, this is the first study of morphometric changes in the fallopian tube stroma associated with a STIC lesion. To date, only two studies have addressed the stromal changes associated with precursor lesions in the fallopian tube. One study measured changes in sulfated chondroitin sulfate expression in the extracellular matrix (41) while the other study measured the degree of collagen alterations by second harmonic generation microscopy (42). Both techniques revealed computationally discernable gradual differences in the fallopian tube stroma proceeding from normal tissue to STIC lesions to HGSOC.

Our study does not suggest that STIC is a requisite intermediate step to HGSOC, as about half of HGSOC and primary peritoneal cancers develop without any evidence of STIC lesions in the fallopian tubes. Rather, we have shown that in patients with HGSOC, the presence of a STIC is associated with other global alterations in the fallopian tube. It is possible that such alterations provide a permissible microenvironment for the development of STIC lesions, however, the underlying molecular mechanism remains unknown. A higher proliferation rate in the fallopian tube mucosa could explain the increased numbers of SCE and cells within SCE in the presence of a STIC lesion. Another factor that could contribute to an increased chance of STIC formation is a defect in an apoptotic mechanism to purge transformed cells. Future investigations and the elucidation of cellular and molecular processes that promote and inhibit the formation of premalignant lesions in the fallopian tube will facilitate the development of markers for early detection as well as the identification of rate-limiting events in the early stages of cancer development.

DATA AVAILABILITY STATEMENT

The original contributions presented in the study are included in the article/**Supplementary Material**. Further inquiries can be directed to the corresponding author.

ETHICS STATEMENT

The studies involving human participants were reviewed and approved by Cedars-Sinai Medical Center Institutional Review Board and The UCLA Office of the Human Research Protection Program. Written informed consent for participation was not required for this study in accordance with national legislation and institutional requirements.

AUTHOR CONTRIBUTIONS

JW designed the project, conducted computational image analyses of the fallopian tube epithelial cells, performed statistical analyses of the data, and wrote the manuscript. YR and MR contributed to the image data analysis. MD conducted statistical analyses of the image data of the fallopian tube stroma. JL and BK contributed samples and annotated clinical data. AW reviewed the histologic slides, confirmed clinical diagnoses, and outlined STIC lesions on the slides. AG conducted computational image analyses of the fallopian tube stroma. SO conceived the project and contributed to the writing of the manuscript. All authors contributed to manuscript revisions. All authors contributed to the article and approved the submitted version.

FUNDING

ACKNOWLEDGMENTS

SUPPLEMENTARY MATERIAL

The Supplementary Material for this article can be found online at: https://www.frontiersin.org/articles/10.3389/fonc.2022.853755/full#supplementary-material

REFERENCES

1. Cabasag CJ, Butler J, Arnold M, Rutherford M, Bardot A, Ferlay J, et al. Exploring Variations in Ovarian Cancer Survival by Age and Stage (ICBP SurvMark-2): A Population-Based Study. *Gynecol Oncol* (2020) 157:234. doi: 10.1016/j.ygyno.2019.12.047

2. Spriggs DR, Longo DL. Progress in BRCA-Mutated Ovarian Cancer. *N Engl J Med* (2018) 379:2567. doi: 10.1056/NEJMe1812644

3. Li J, Ning Y, Abushahin N, Yuan Z, Wang Y, Wang Y, et al. Secretory Cell Expansion With Aging: Risk for Pelvic Serous Carcinogenesis. *Gynecol Oncol* (2013) 131:555. doi: 10.1016/j.ygyno.2013.09.018

4. Gaddum-Rosse P, Rumery RE, Blandau RJ, Thiersch JB. Studies on the Mucosa of Postmenopausal Oviducts: Surface Appearance, Ciliary Activity, and the Effect of Estrogen Treatment. *Fertil Steril* (1975) 26:951. doi: 10.1016/S0015-0282(16)41408-1

5. Chen EY, Mehra K, Mehrad M, Ning G, Miron A, Mutter GL, et al. Secretory Cell Outgrowth, PAX2 and Serous Carcinogenesis in the Fallopian Tube. *J Pathol* (2010) 222:110. doi: 10.1002/path.2739

6. Zeppernick F, Meinhold-Heerlein I, Shih Ie M. Precursors of Ovarian Cancer in the Fallopian Tube: Serous Tubal Intraepithelial Carcinoma–an Update. *J Obstet Gynaecol Res* (2015) 41:6. doi: 10.1111/jog.12550

7. Mehra K, Mehrad M, Ning G, Drapkin R, McKeon FD, Xian W, et al. STICS, SCOUTs and P53 Signatures; a New Language for Pelvic Serous Carcinogenesis. *Front Biosci (Elite Ed)* (2011) 3:625. doi: 10.2741/e275

8. Kuhn E, Kurman RJ, Sehdev AS, Shih Ie M. Ki-67 Labeling Index as an Adjunct in the Diagnosis of Serous Tubal Intraepithelial Carcinoma. *Int J Gynecol Pathol* (2012) 31:416. doi: 10.1097/PGP.0b013e31824cbeb4

9. Visvanathan K, Shaw P, May BJ, Bahadirli-Talbott A, Kaushiva A, Risch H, et al. Fallopian Tube Lesions in Women at High Risk for Ovarian Cancer: A Multicenter Study. *Cancer Prev Res (Phila)* (2018) 11:697. doi: 10.1158/1940-6207.CAPR-18-0009

10. Ducie J, Dao F, Considine M, Olvera N, Shaw PA, Kurman RJ, et al. Molecular Analysis of High-Grade Serous Ovarian Carcinoma With and Without Associated Serous Tubal Intra-Epithelial Carcinoma. *Nat Commun* (2017) 8:990. doi: 10.1038/s41467-017-01217-9

11. Labidi-Galy SI, Papp E, Hallberg D, Niknafs N, Adleff V, Noe M, et al. High Grade Serous Ovarian Carcinomas Originate in the Fallopian Tube. *Nat Commun* (2017) 8:1093. doi: 10.1038/s41467-017-00962-1

12. Perets R, Wyant GA, Muto KW, Bijron JG, Poole BB, Chin KT, et al. Transformation of the Fallopian Tube Secretory Epithelium Leads to High-Grade Serous Ovarian Cancer in Brca;Tp53;Pten Models. *Cancer Cell* (2013) 24:751. doi: 10.1016/j.ccr.2013.10.013

13. Medeiros F, Muto MG, Lee Y, Elvin JA, Callahan MJ, Feltmate C, et al. The Tubal Fimbria is a Preferred Site for Early Adenocarcinoma in Women With Familial Ovarian Cancer Syndrome. *Am J Surg Pathol* (2006) 30:230. doi: 10.1097/01.pas.0000180854.28831.77

14. Nik NN, Vang R, Shih Ie M, Kurman RJ. Origin and Pathogenesis of Pelvic (Ovarian, Tubal, and Primary Peritoneal) Serous Carcinoma. *Annu Rev Pathol* (2014) 9:27. doi: 10.1146/annurev-pathol-020712-163949

15. Visvanathan K, Vang R, Shaw P, Gross A, Soslow R, Parkash V, et al. Diagnosis of Serous Tubal Intraepithelial Carcinoma Based on Morphologic and Immunohistochemical Features: A Reproducibility Study. *Am J Surg Pathol* (2011) 35:1766. doi: 10.1097/PAS.0b013e31822f58bc

16. Gross AL, Kurman RJ, Vang R, Shih Ie M, Visvanathan K. Precursor Lesions of High-Grade Serous Ovarian Carcinoma: Morphological and Molecular Characteristics. *J Oncol* (2010) 2010:126295. doi: 10.1155/2010/126295

17. Vang R, Visvanathan K, Gross A, Maambo E, Gupta M, Kuhn E, et al. Validation of an Algorithm for the Diagnosis of Serous Tubal Intraepithelial Carcinoma. *Int J Gynecol Pathol* (2012) 31:243. doi: 10.1097/PGP.0b013e31823b8831

18. Li HX, Lu ZH, Shen K, Cheng WJ, Malpica A, Zhang J, et al. Advances in Serous Tubal Intraepithelial Carcinoma: Correlation With High Grade Serous Carcinoma and Ovarian Carcinogenesis. *Int J Clin Exp Pathol* (2014) 7:848.

19. Kindelberger DW, Lee Y, Miron A, Hirsch MS, Feltmate C, Medeiros F, et al. Intraepithelial Carcinoma of the Fimbria and Pelvic Serous Carcinoma: Evidence for a Causal Relationship. *Am J Surg Pathol* (2007) 31:161. doi: 10.1097/01.pas.0000213335.40358.47

20. Kuhn E, Kurman RJ, Vang R, Sehdev AS, Han G, Soslow R, et al. TP53 Mutations in Serous Tubal Intraepithelial Carcinoma and Concurrent Pelvic High-Grade Serous Carcinoma–Evidence Supporting the Clonal Relationship of the Two Lesions. *J Pathol* (2012) 226:421. doi: 10.1002/path.3023

21. Samimi G, Trabert B, Geczik AM, Duggan MA, Sherman ME. Population Frequency of Serous Tubal Intraepithelial Carcinoma (STIC) in Clinical Practice Using SEE-Fim Protocol. *JNCI Cancer Spectr* (2018) 2:pky061. doi: 10.1093/jncics/pky061

22. Asaturova AV, Ezhova LS, Faizullina NM, Adamyan LV, Khabas GN, Sannikova MV. Expansion of Secretory Cells in the Fallopian Tubal Epithelium in the Early Stages of the Pathogenesis of Ovarian Serous Carcinomas. *Arkh Patol* (2017) 79:10. doi: 10.17116/patol201779310-18

23. Wang Y, Li L, Wang Y, Tang SN, Zheng W. Fallopian Tube Secretory Cell Expansion: A Sensitive Biomarker for Ovarian Serous Carcinogenesis. *Am J Transl Res* (2015) 7:2082.

24. Soong TR, Howitt BE, Horowitz N, Nucci MR, Crum CP. The Fallopian Tube, "Precursor Escape" and Narrowing the Knowledge Gap to the Origins of High-Grade Serous Carcinoma. *Gynecol Oncol* (2019) 152:426. doi: 10.1016/j.ygyno.2018.11.033

25. Lee Y, Miron A, Drapkin R, Nucci MR, Medeiros F, Saleemuddin A, et al. A Candidate Precursor to Serous Carcinoma That Originates in the Distal Fallopian Tube. *J Pathol* (2007) 211:26. doi: 10.1002/path.2091

26. Yamamoto Y, Ning G, Howitt BE, Mehra K, Wu L, Wang X, et al. In Vitro and In Vivo Correlates of Physiological and Neoplastic Human Fallopian Tube Stem Cells. *J Pathol* (2016) 238:519. doi: 10.1002/path.4649

27. Quick CM, Ning G, Bijron J, Laury A, Wei TS, Chen EY, et al. PAX2-Null Secretory Cell Outgrowths in the Oviduct and Their Relationship to Pelvic Serous Cancer. *Mod Pathol* (2012) 25:449. doi: 10.1038/modpathol.2011.175

28. Cassetta L, Fragkogianni S, Sims AH, Swierczak A, Forrester LM, Zhang H, et al. Human Tumor-Associated Macrophage and Monocyte Transcriptional Landscapes Reveal Cancer-Specific Reprogramming, Biomarkers, and Therapeutic Targets. *Cancer Cell* (2019) 35:588. doi: 10.1016/j.ccell.2019.02.009

29. Miller E, Salemi H, Klimov S, Lewis M, Garraway IP, Knudsen BS, et al. PD71-09 Quantitative Digital Image Analysis and Machine Learning Accurately Classifies Primary Prostate Tumors of Bone Metastatic Disease Based on Histomorphometric Features in Diagnostic Prostate Needle Biopsies. *J Urol* (2017) 197:e1358. doi: 10.1016/j.juro.2017.02.3176

30. Costa AF, Humpire-Mamani G, Traina AJM. An Efficient Algorithm for Fractal Analysis of Textures. In: *2012 25th SIBGRAPI Conference on Graphics, Patterns and Images*. Brazil: IEEE (2012). p. 39.

31. Ojansivu V, Heikkilä J. *Blur Insensitive Texture Classification Using Local Phase Quantization*. Berlin, Heidelberg: Springer Berlin Heidelberg (2008). p. 236.

32. Kannala J, Rahtu E. BSIF: Binarized Statistical Image Features. In: *Proceedings of the 21st International Conference on Pattern Recognition (Icpr2012)*. Japan: IEEE (2012). p. 1363.

33. Reinhard E, Adhikhmin M, Gooch B, Shirley P. Color Transfer Between Images. *IEEE Comput Graphics Appl* (2001) 21:34. doi: 10.1109/38.946629

34. Bankhead P, Loughrey MB, Fernandez JA, Dombrowski Y, McArt DG, Dunne PD, et al. QuPath: Open Source Software for Digital Pathology Image Analysis. *Sci Rep* (2017) 7:16878. doi: 10.1038/s41598-017-17204-5

35. Wentzensen N, Poole EM, Trabert B, White E, Arslan AA, Patel AV, et al. Ovarian Cancer Risk Factors by Histologic Subtype: An Analysis From the Ovarian Cancer Cohort Consortium. *J Clin Oncol* (2016) 34:2888. doi: 10.1200/JCO.2016.66.8178

36. Tao T, Lin W, Wang Y, Zhang J, Chambers SK, Li B, et al. Loss of Tubal Ciliated Cells as a Risk for "Ovarian" or Pelvic Serous Carcinoma. *Am J Cancer Res* (2020) 10:3815.

37. Shaw PA, Rouzbahman M, Pizer ES, Pintilie M, Begley H. Candidate Serous Cancer Precursors in Fallopian Tube Epithelium of BRCA1/2 Mutation Carriers. *Mod Pathol* (2009) 22:1133. doi: 10.1038/modpathol.2009.89

38. Vicus D, Shaw PA, Finch A, Rosen B, Murphy J, Armel S, et al. Risk Factors for non-Invasive Lesions of the Fallopian Tube in BRCA Mutation Carriers. *Gynecol Oncol* (2010) 118:295. doi: 10.1016/j.ygyno.2010.05.012

39. George SH, Milea A, Shaw PA. Proliferation in the Normal FTE is a Hallmark of the Follicular Phase, Not BRCA Mutation Status. *Clin Cancer Res* (2012) 18:6199. doi: 10.1158/1078-0432.CCR-12-2155

40. Bogaerts JMA, Steenbeek MP, van Bommel MHD, Bulten J, van der Laak J, de Hullu JA, et al. Recommendations for Diagnosing STIC: A Systematic Review and Meta-Analysis. *Virchows Arch* (2021). doi: 10.1007/s00428-021-03244-w

41. van der Steen S, Bulten J, Van de Vijver KK, van Kuppevelt TH, Massuger L. Changes in the Extracellular Matrix Are Associated With the Development of Serous Tubal Intraepithelial Carcinoma Into High-Grade Serous Carcinoma. *Int J Gynecol Cancer* (2017) 27:1072. doi: 10.1097/IGC.0000000000000933

42. Gant KL, Jambor AN, Li Z, Rentchler EC, Weisman P, Li L, et al. Evaluation of Collagen Alterations in Early Precursor Lesions of High Grade Serous Ovarian Cancer by Second Harmonic Generation Microscopy and Mass Spectrometry. *Cancers (Basel)* (2021) 13:2794. doi: 10.3390/cancers13112794

Comprehensive Molecular Analyses of a TNF Family-Based Gene Signature as a Potentially Novel Prognostic Biomarker for Cervical Cancer

Yan Ma, Xiaoyan Zhang, Jiancheng Yang, Yanping Jin, Ying Xu and Jianping Qiu *

Department of Gynecology and Obstetrics, The Affiliated Suzhou Hospital of Nanjing Medical University, Suzhou Municipal Hospital, Suzhou, China

Background: Increasing evidence suggests that tumour necrosis factor (TNF) family genes play important roles in cervical cancer (CC). However, whether TNF family genes can be used as prognostic biomarkers of CC and the molecular mechanisms of TNF family genes remain unclear.

Methods: A total of 306 CC and 13 normal samples were obtained from The Cancer Genome Atlas (TCGA) and Genotype-Tissue Expression (GTEx) databases. We identified differentially expressed TNF family genes between CC and normal samples and subjected them to univariate Cox regression analysis for selecting prognostic TNF family genes. Least absolute shrinkage and selection operator (LASSO) regression and multivariate Cox regression analyses were performed to screen genes to establish a TNF family gene signature. Gene set enrichment analysis (GSEA) was performed to investigate the biological functions of the TNF family gene signature. Finally, methylation and copy number variation data of CC were used to analyse the potential molecular mechanisms of TNF family genes.

Results: A total of 26 differentially expressed TNF family genes were identified between the CC and normal samples. Next, a TNF family gene signature, including CD27, EDA, TNF, TNFRSF12A, TNFRSF13C, and TNFRSF9 was constructed based on univariate Cox, LASSO, and multivariate Cox regression analyses. The TNF family gene signature was related to age, pathological stages M and N, and could predict patient survival independently of clinical factors. Moreover, KEGG enrichment analysis suggested that the TNF family gene signature was mainly involved in the TGF-β signaling pathway, and the TNF family gene signature could affect the immunotherapy response. Finally, we confirmed that the mRNA expressions of CD27, TNF, TNFRSF12A, TNFRSF13C, and TNFRSF9 were upregulated in CC, while that of EDA was downregulated. The mRNA expressions of CD27, EDA, TNF, TNFRSF12A, TNFRSF13C, and TNFRSF9 might be influenced by gene methylation and copy number variation.

Conclusion: Our study is the first to demonstrate that CD27, EDA, TNF, TNFRSF12A, TNFRSF13C, and TNFRSF9 might be used as prognostic biomarkers of CC and are associated with the immunotherapy response of CC.

Keywords: cervical cancer, TNF family genes, prognosis, immunotherapy response, TCGA

BACKGROUND

Cervical cancer (CC) is a common gynaecological malignancy. Approximately 570,000 new cases of CC and 311,365 deaths were reported worldwide in 2018, making CC the third most common cancer among women (1). Although improved screening and health literacy have decreased the incidence rates of CC in recent years, CC remains the leading cause of cancer-related deaths among women in developing countries (2). Many risk factors can affect the development of CC, such as high-risk HPV infection, smoking, health status, and economic status (3, 4). CC rates dropped by 1.3% in 2015 compared to that in 2012, given the production of HPV vaccines, improvements in living conditions, and early screening (5). However, although 80% of early CC cases can be treated with surgery, radiotherapy, or chemotherapy, the number of patients in advanced CC stages is high and where the prognosis remains poor (6). Additionally, some patients relapse easily despite undergoing appropriate surgery and chemotherapy (7). Therefore, it is important to screen new biomarkers suitable for CC prognosis to improve the effectiveness of treatment and also develop precise treatment strategies.

The tumour necrosis factor (TNF) and TNF receptor (TNFR) superfamilies (TNFSF/TNFRSF) include 19 ligands and 29 receptors (8). A previous study has shown that communication pathways mediated by TNFSF/TNFRSF members can regulate inflammation and control cell death, proliferation, and differentiation (8). TNFSF/TNFRSF members exert proinflammatory effects by activating the nuclear factor NF-κB pathway, which is majorly involved in protection against pathogens and cancer (9). Inflammation can also be conducive to tumour proliferation, metastasis, and angiogenesis in many types of cancer (10). In addition, TNF-induced apoptosis has high potential in anticancer therapy. For example, the TNF-related apoptosis-inducing ligand (TRAIL), a member of the TNF family (11), can selectively induce cancer cell apoptosis by binding or trimerising their functional receptors (12). In CC, all TRAIL receptors are expressed in both normal cervical epithelial cells and tumour cells. Moreover, the TRAIL receptors TRAIL-R1 and -R2 are highly expressed in tumour cells than in normal

epithelial cells, and their expression is associated with CC cell apoptosis (13). Another study showed that melatonin enhances TNF-α-induced mitochondrial apoptosis in HeLa cells by inactivating the CaMKII/Parkin/mitophagy axis. TNF-α-induced lncRNA LOC105374902 may act as a ceRNA of miR-1285-3p to promote the expression of RPL14 as well as the migration, invasion, and epithelial-mesenchymal transition (EMT) of CC cells (14). TNF family genes have a significant impact on the occurrence and development of tumours (15); these can be used as prognostic markers of tumours and can affect the immunotherapy response of tumours (16). However, the role of TNF family genes in CC remains unclear, and their potential functional role in the prognosis of cancer should be studied further.

In this study, we downloaded transcriptomic data of CC and matched normal samples from The Cancer Genome Atlas (TCGA, https://portal.gdc.cancer.gov/). The transcriptomic data of normal cervical samples were downloaded from Genotype-Tissue Expression (GTEx) database (https://commonfund.nih.gov/gtex). First, we sought to identify differentially expressed TNF family genes in cervical tumours versus normal cervical tissues. The TNF family gene signal was established based on univariate and multivariate Cox and LASSO regression analyses assess CC prognosis. In addition, we further analysed the molecular mechanism by which TNF family gene signaling affects immunotherapy and gene alterations in patients. Finally, we analysed the mRNA expression levels of risk model genes using qRT-PCR. This study can help facilitate the prognosis of CC and the development of phasic immunotherapy strategies.

METHODS

Data Selection

RNA-seq data [fragments per kilobase of exon model per million mapped fragments (FPKM)] of 306 CC and three matched normal cervical samples, copy number variation data of 297 CC samples, DNA methylation data of 312 CC samples, and clinical information (including overall survival information) data of 306 patients with CC in TCGA database were acquired from the Cancer Genomics Browser of the University of California Santa Cruz (UCSC) Xena database (https://xenabrowser.net). After excluding samples without survival information, 293 samples with survival information were used for survival analysis, and their detailed clinical information was shown in **Table 1**. Moreover, the RNA-seq of 10 normal cervical samples were acquired from the GTEx database (17). Furthermore, the GSE44001 dataset, including 300 CC patients with survival

---

Abbreviations: AUC, area under the curve; BRCA, breast cancer; CC, cervical cancer; cDNA, complementary DNA; DEGs, differentially expressed genes; HPV, human papilloma virus; EMT, epithelial-mesenchymal transition; GSEA, gene set enrichment analysis; GTEx, Genotype-tissue expression; KEGG, Kyoto encyclopedia of genes and genomes; KM, Kaplan-Meier; LASSO, least absolute shrinkage and selection operator; OV, ovarian cancer; PCA, principal component analysis; ROC, receiver operating characteristic; SNVs, single-nucleotide variants; TCGA, The Cancer Genome Atlas; TIDE, tumour immune dysfunction and exclusion; TNF, tumour necrosis factor; TRAIL, TNF-related apoptosis-inducing ligand; UCEC, uterine corpus endometrial carcinoma; UCS, uterine carcinosarcoma; UCSC, University of California Santa Cruz.

Characteristics	No.
Total Cases	293
Age (<50)	176
Age (>=50)	111
clinical_stage (Stage I)	159
clinical_stage (Stage II)	64
clinical_stage (Stage III)	81
clinical_stage (Stage IV)	22
neoplasm_histologic_grade (G1)	19
neoplasm_histologic_grade (G2)	129
neoplasm_histologic_grade (G3)	118
neoplasm_histologic_grade (G4)	1
neoplasm_histologic_grade (GX)	24
new_tumor_event_after_initial_treatment (NO)	15
new_tumor_event_after_initial_treatment (YES)	12
pathologic_M (M0)	107
pathologic_M (M1)	11
pathologic_M (MX)	127
pathologic_N (N0)	129
pathologic_N (N1)	56
pathologic_N (N0)	65
pathologic_T (T1)	137
pathologic_T (T2)	68
pathologic_T (T3)	16
pathologic_T (T4)	11
pathologic_T (TX)	18

information, was downloaded from the Gene Expression Omnibus (GEO) database (https://www.ncbi.nlm.nih.gov/geo/) and acted as a testing set. The 47 TNF family genes were obtained from Zhang et al. (16). Finally, the RNA-seq data of 1,082 breast cancer (BRCA), 378 ovarian cancer (OV), 544 uterine corpus endometrial carcinoma (UCEC), and 54 uterine carcinosarcoma (UCS) samples with overall survival information were analysed to further investigate the role of TNF family genes in gynaecologic tumours as well as in BRCA.

Identification of Differentially Expressed TNF Family Genes

The limma package in R was used to eliminate batch benefits between CC and three matched normal cervical samples from TCGA and 10 normal cervical samples from the GTEx database and to identify the differentially expressed genes (DEGs) between CC and normal samples (18). Differentially expressed TNF family genes were identified by overlapping DEGs and TNF family genes. Box plots and heatmaps were plotted to present the expression levels of differentially expressed TNF family genes using the ggplot2 and pheatmap packages in R, respectively.

Construction and Validation of TNF Family Gene Signature

After excluding patients with CC for whom overall survival information was not available, 293 patients with CC were selected to construct a TNF family gene signature to predict the overall survival of patients with CC. To ensure the validity of the TNF family gene signature, the entire set of 293 patients with CC was randomly divided into a training set (205 patients with CC) and a validation set (88 patients with CC) according to a 7:3 ratio.

First, univariate Cox regression analysis was used to identify genes related to the overall survival of patients with CC from differentially expressed TNF family genes in the training set (P < 0.05). Next, least absolute shrinkage and selection operator (LASSO) regression analysis based on the glmnet package in R were conducted to determine the best combination of genes for constructing a TNF family gene signature in the training set (19). Then, the "step" function in R was used to perform a multivariate Cox regression analysis to construct the optimal TNF family gene signature. In addition, the TNF family gene signature was established using gene expression values and the corresponding Cox coefficient. The algorithm of the risk score value for one patient with CC was as follows: (gene 1 expression × gene 1 coefficient) + (gene 2 expression × gene 2 coefficient) + … + (gene n expression × gene n coefficient) (20). The risk scores of patients with CC in the training set, validation set, and entire set were calculated using the aforementioned algorithm. patients with CC in the training, validation, and entire sets were divided into high- and low-risk groups based on the optimal threshold of risk scores. Finally, the Kaplan-Meier (KM) and time-dependent receiver operating characteristic (ROC) curves were used to assess the validity of the TNF family gene signature.

Association Between TNF Family Gene Signature and Clinical Characteristics

The association between the TNF family gene signature and clinical characteristics of patients with CC in the entire set, including radiation therapy, race, pathological grade, pathological M, N, and T stages, age, and histologic grade, were investigated using either one-way ANOVA or the Wilcoxon test.

Construction and Evaluation of a TNF Family Gene Signature-Related Nomogram

The TNF family gene signature and clinical characteristics, including radiation therapy, race, pathological grade, pathological M, N, and T stages, age, and histologic grade, were used to screen independent prognostic factors by performing univariate and multivariate Cox regression analyses in the entire set. Next, a nomogram based on independent prognostic factors identified using multivariate Cox regression analysis was established using the rms package in R (21). Calibration curves were used to observe the predictive power of the nomogram.

Functional Analysis of TNF Family Gene Signature

Gene set enrichment analysis (GSEA) was used to investigate the dysregulated Kyoto encyclopedia of genes and genomes (KEGG) signaling pathways between the high- and low-risk groups based on all of their gene expression matrices using the clusterProfiler package in R (22). The gene sets c2.cp.kegg.v7.4.symbols.gmt and c5.go.v7.4.symbols.gmt were selected as reference gene sets, and NOM P < 0.05 was considered significant.

Correlation Between TNF Family Gene Signature and Immunotherapy Response

To explore whether the TNF family gene signature could predict immunotherapy response, Cell-type Identification By Estimating Relative Subsets Of RNA Transcripts (CIBERSORT) algorithm was firstly used to characterize 22 immune cell composition of the patients with CC in the high- and low-risk groups (23). Next, the expression levels of immune checkpoint molecules were compared between the high- and low-risk groups using the Wilcoxon test. Tumour immune dysfunction and exclusion (TIDE) scores of the high- and low-risk groups were calculated and compared to explore whether the gene signature predicts the immunotherapy response (24). Subclass mapping was used to determine the immunotherapy response (25).

Potential Regulatory Mechanisms of Genes in TNF Family Gene Signature

To explore the potential regulatory mechanisms of genes in the TNF family gene signature, the methylation levels of genes in the TNF family gene signature were first investigated using the ChAMP package in R. The copy number variations of genes in the TNF family gene signature were analysed, and the potential miRNAs of genes in this signature were predicted using the miRDB and miRwalk databases.

Prognostic Significance of the TNF Family Gene Signature in Gynaecologic Tumours and BRCA

To investigate whether genes in the TNF family gene signature could affect the prognosis of other gynaecologic tumours and BRCA, univariate Cox regression analysis based on the overall survival information and expression of genes in the TNF family gene signature was performed.

Quantitative Real-Time PCR

To investigate the mRNA expression of genes in the TNF family gene signature, seven patients with CC were underwent treatment at Suzhou Municipal Hospital were included in this study, and carcinoma and paracancerous tissue samples were collected from each patient to perform quantitative real-time PCR. Informed consent was obtained from all participating individuals, and all steps involving human subjects were approved by the ethics committee of Suzhou Municipal Hospital.

Total RNA of 14 matched tissues from the seven patients with CC was extracted using the traditional TRIzol-based method. The extracted RNA was reverse-transcribed into complementary DNA (cDNA) using a SureScript First-Strand cDNA Synthesis Kit (Xavier Corporation, Guangzhou, China), according to the manufacturer's instructions. Quantitative real-time PCR was performed using a 2720 Thermal Cycler General PCR instrument (Applied Biosystems, Inc., Carlsbad, CA, USA) and a CFX96 real-time quantitative fluorescence thermal cycler (Bio-Rad, Hercules, CA, USA). The $2^{-11\Delta\Delta Ct}$ method was used to calculate the relative expression of genes with internal reference *GAPDH*. The primer sequences are listed in **Table S1**.

Statistical Analysis

Data analyses were performed based on the R version 4.1.1. The log-rank test was used to test the difference in overall survival between the high- and low-risk groups. Unless otherwise stated, statistical significance was set at P < 0.05.

RESULTS

Identification of Differentially Expressed TNF Family Genes

Considering the heterogeneity of TCGA and GTEx samples, we first performed a batch effect treatment. The 306 CC and 13 normal samples that were processed met the criteria for further analysis (**Figures 1A, B**). With a cut-off value of P < 0.05 and |log2FC| > 0.5, 8,050 DEGs were screened between CC and normal samples, including 4,416 upregulated and 3,634 downregulated ones (**Figure 1C**). After overlapping with 47 TNF family genes, 26 differentially expressed TNF family genes were identified (**Figure 1D**); their expression levels are shown in **Figure 1E**.

Construction and Validation of a TNF Family Gene Signature

Based on univariate Cox regression analysis of the training set, the 10 differentially expressed TNF family genes *CD27*, *EDA*, *FASLG*, *TNF*, *TNFRSF10B*, *TNFRSF12A*, *TNFRSF13C*, *TNFRSF14*, *TNFRSF9*, and *TNFSF13B* were found to be associated with CC prognosis (P < 0.05, **Table 2**). Subsequently, *CD27*, *EDA*, *TNF*, *TNFRSF10B*, *TNFRSF12A*, *TNFRSF13C*, *TNFRSF9*, and *TNFSF13B* were preserved by LASSO regression analysis and used for multivariate Cox regression analysis (**Figure 2A**). In addition, the expression levels and regression coefficients of *CD27*,
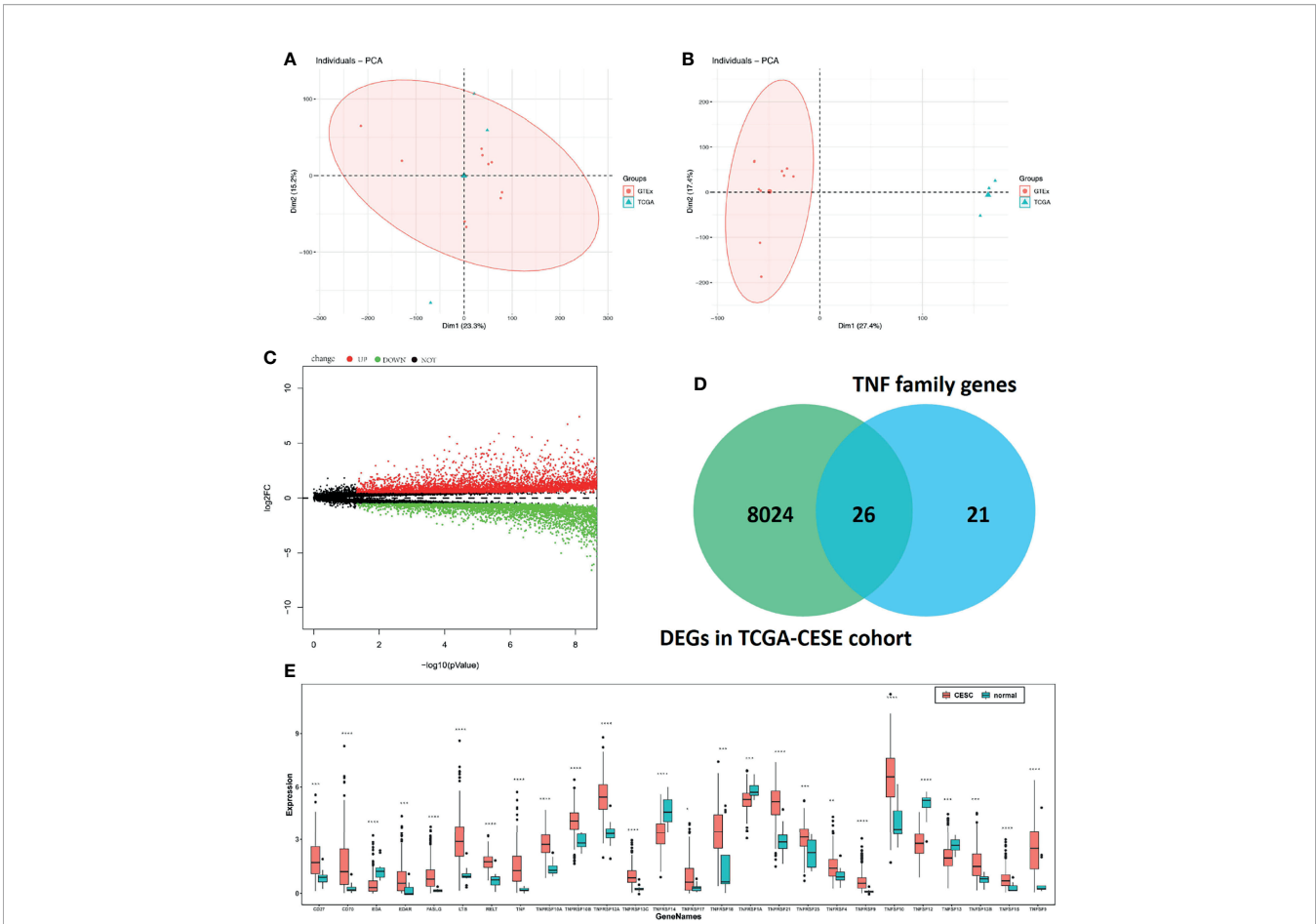
FIGURE 1 | Molecular characteristics and expression profile of tumour necrosis factor (TNF) family members in cervical cancer. Principal component analysis (PCA) before **(A)** and after **(B)** batch effect treatment of TCGA and GTEx samples. **(C)** Volcano plots showing the number of differentially expressed genes. Red dots represent upregulated genes, and green dots represent downregulated genes. **(D)** Venn diagram showing the intersections of genes between TCGA data and TNF family genes. **(E)** Boxplots show differences in the expression levels of TNF family members. *means $p < 0.05$; **means $p < 0.01$; ***means $p < 0.001$; ****means $p < 0.0001$.

EDA, *TNF*, *TNFRSF12A*, *TNFRSF13C*, and *TNFRSF9* were used to construct a TNF family gene signature through multivariate Cox regression analysis (**Table 3**). *CD27*, *TNFRSF13C*, and *TNFRSF9* were found protective factors (hazard ratio [HR] < 1), while *EDA*, *TNF*, and *TNFRSF12A* as risk factors (HR > 1) (**Table 3**).

The risk score of each patient was calculated as follows: risk score = $(-0.370) \times$ *CD27* expression + $0.579 \times$ *EDA* expression + $0.400 \times$ *TNF* expression $+(0.403) \times$ *TNFRSF12A* expression + $(-0.582) \times$ *TNFRSF13C* expression + $(-0.682) \times$ *TNFRSF9* expression (**Table 3**).

TABLE 2 | Identification of 10 TNF family genes by univariate Cox regression analysis.

Gene	HR	Lower 95% CI	Upper 95% CI	p value
CD27	0.58	0.421	0.798	0.000838
EDA	2.016	1.222	3.327	0.00606
FASLG	0.638	0.423	0.96	0.031296
TNF	1.489	1.118	1.982	0.00646
TNFRSF10B	1.63	1.064	2.498	0.024742
TNFRSF12A	1.541	1.159	2.05	0.002971
TNFRSF13C	0.317	0.153	0.656	0.001956
TNFRSF14	0.675	0.479	0.95	0.024258
TNFRSF9	0.449	0.233	0.863	0.016397
TNFSF13B	0.619	0.438	0.874	0.00642

HR, hazard ratio; CI, Confidence interval.
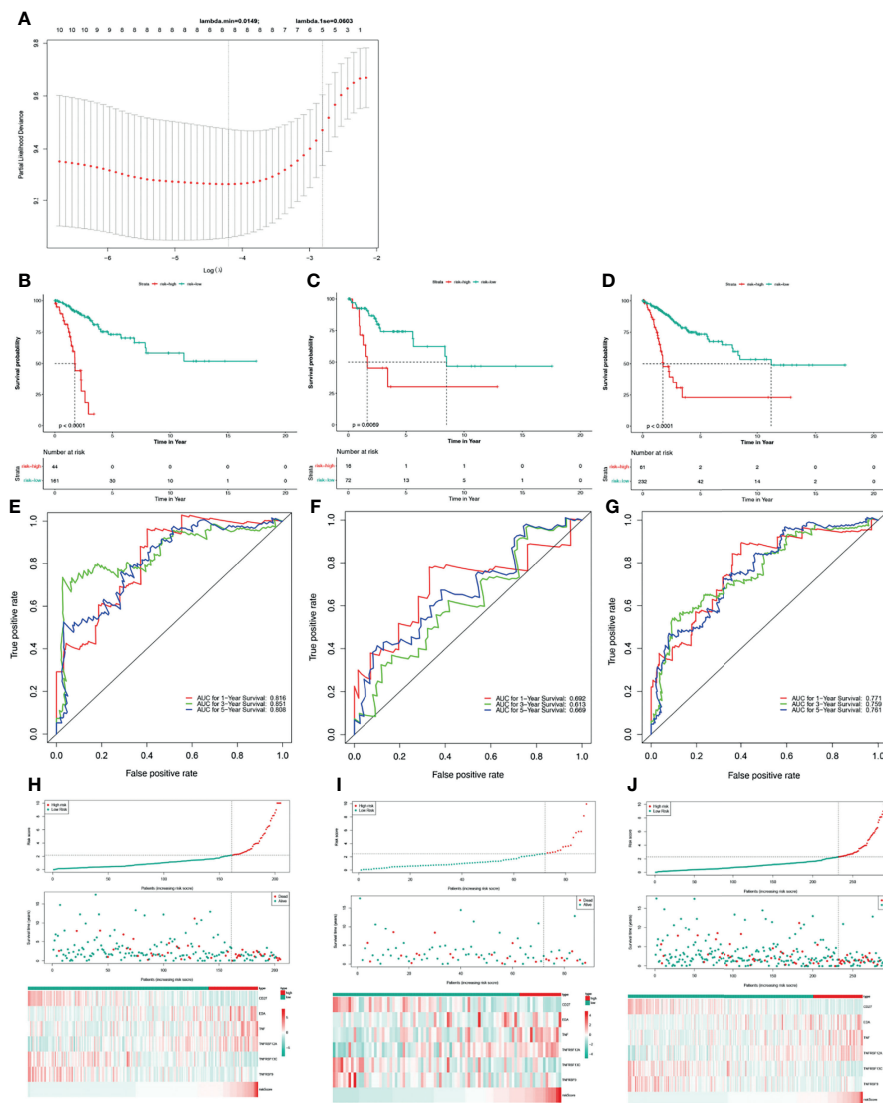
FIGURE 2 | Construction and validation of a TNF family gene signature. **(A)** The most proper log (lambda) value in the LASSO model. **(B)** The Kaplan-Meier curve of the OS for patients with CC based on the risk score for the training set. **(C)** The Kaplan-Meier curve of the OS for patients with CC based on the risk score for the testing set. **(D)** The Kaplan-Meier curve of the OS for patients with CC based on the risk score for the entire set. **(E)** Time-dependent ROC curves of the risk score for the 1-, 3-, and 5-year OS rate prediction for the training set. **(F)** Time-dependent ROC curves of the risk score for the 1-, 3-, and 5-year OS rate prediction for the testing set. **(G)** Time-dependent ROC curves of the risk score for the 1-, 3-, and 5-year OS rate prediction for the entire set. **(H)** Distribution of the risk score, survival status, and gene expression panel for the training set. **(I)** Distribution of the risk score, survival status, and gene expression panel for the testing set. **(J)** Distribution of the risk score, survival status, and gene expression panel for the entire set.

Thus, we stratified patients with CC in the training set into low- and high-risk groups based on the optimum threshold of the risk score. Interestingly, we found that the overall survival of patients in the low-risk group was clearly better than that of patients in the high-risk group (**Figure 2B**), and patients in the low-risk group had longer survival times than those in the high-risk group (**Figure 2H**). ROC analysis revealed that the areas under curves (AUCs) used to predict the 1-, 3-, and 5-year survival rates of patients with CC were 0.816, 0.851, and 0.808, respectively (**Figure 2E**). *CD27, TNFRSF13C,* and *TNFRSF9* showed higher expression in the low-risk group than in the

high-risk group. However, the other three genes exhibited lower expression in the low-risk group than in the high-risk group (**Figure 2H**), which was consistent with the results of multivariate Cox regression analysis (**Table 3**). Finally, we assessed the predictive capabilities of the TNF family gene signature in the validation, testing, and entire sets. The KM analyses in the validation and entire sets yielded results consistent with those of the training set; namely, the low-risk patients were associated with better prognosis (**Figures 2C, D**). The ROC curves of both the validation and entire sets also suggested that the TNF family gene signature is a good

TABLE 3 | TNF family gene signature constructed with six TNF family genes using multivariate Cox regression analysis.

Gene	HR	HR.95L	HR.95H	P value	Cox Coefficient
CD27	0.690594	0.448524	1.06331	0.092726	-0.370
EDA	1.784758	1.058791	3.008489	0.029675	0.579
TNF	1.491831	1.13535	1.960239	0.00409	0.400
TNFRSF12A	1.496109	1.112881	2.011306	0.007623	0.403
TNFRSF13C	0.558982	0.283221	1.103241	0.093596	-0.582
TNFRSF9	0.505494	0.211322	1.20917	0.125244	-0.682

prognostic factor of CC (**Figures 2F, G**). Similarly, *CD27*, *TNFRSF13C*, and *TNFRSF9* also showed higher expression in the low-risk group than in the high-risk group. However, the other three genes exhibited lower expression in the low-risk group than in the high-risk group (**Figures 2I, J**). Notably, the KM curve of the testing set revealed that the high-risk patients were related to poor prognosis, the ROC curve of the testing set showed that the TNF family gene signature did not have good predictive power (**Figure S1**).

Relationship Between TNF Family Gene Signature and Clinical Characteristics

To investigate the relationship between the TNF family gene signature and clinical characteristics, we compared the risk scores between different clinical characteristics across the entire set. As illustrated in **Figure 3A**, patients younger than 50 years had higher risk scores. Moreover, M1 patients showed higher risk scores than M0 patients (**Figure 3D**), and T3/T4 patients exhibited higher risk scores than T1/T2 patients (**Figure 3E**). However, the TNF family gene signature was not related to any other clinical characteristic (**Figure 3**).

Construction of a TNF Family Gene Signature-Related Nomogram

To better use the TNF family gene signature, we aimed to construct a nomogram by integrating all TNF family gene signatures and clinical characteristics in the entire set. Based on univariate Cox regression analysis, pathological M and T stages and risk score were found to be associated with CC prognosis (**Figure 4A**), which were the only independent factors for patients with CC (**Figure 4B**). A nomogram integrating pathological T stage and risk score was constructed to predict the 1-, 3-, and 5-year overall survival of patients with CC (**Figure 4C**). The calibration curves suggested that the nomogram could predict CC onset owing to good agreement between the predictions and observations (**Figure 4D**).

Functional Enrichment of the TNF Family Gene Signature

To further explore the potential functions of the TNF family gene signature, GSEA was performed to observe the potential KEGG signaling pathway related to the TNF family gene signature in the entire set. As is shown in **Table 4**, genes in the high-risk group were mainly involved in the galactose metabolism, N glycan biosynthesis, O glycan biosynthesis, purine metabolism, and TGF-β signaling pathways. Moreover, we found that genes in the low-risk group were mainly involved in the immune-related pathways, such as B cell receptor signaling pathway, primary immunodeficiency pathway, intestinal immune network for IgA production, T cell receptor signaling pathway, and chemokine signaling pathway (**Table 5**). Thus, the TNF family gene signature
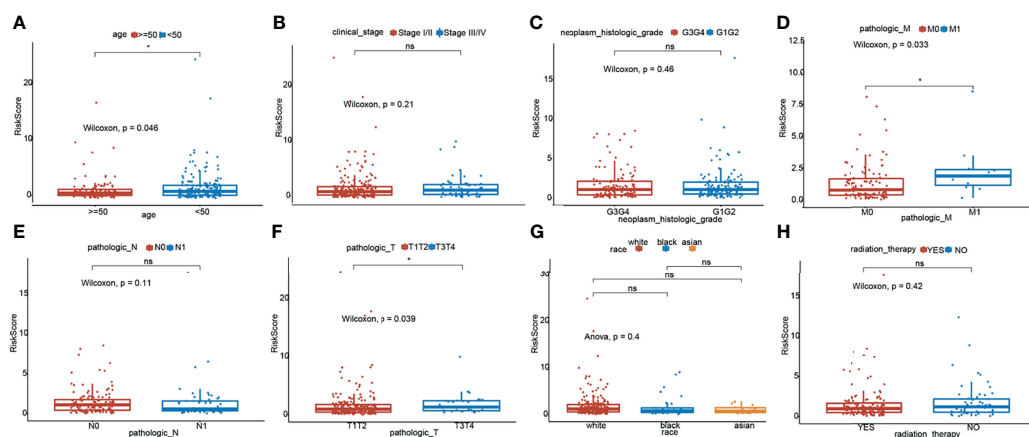
FIGURE 3 | Relationship of risk score and clinicopathological characteristics of CC patients. Distribution of the risk scores in different cohorts stratified by the subtype of age **(A)**, clinical stage **(B)**, neoplasm histologic grade **(C)**, pathological M stage **(D)**, pathological N stage **(E)**, pathological T stage **(F)**, race **(G)** and radition therapy **(H)**. *means p < 0.05; ns represents no significance.
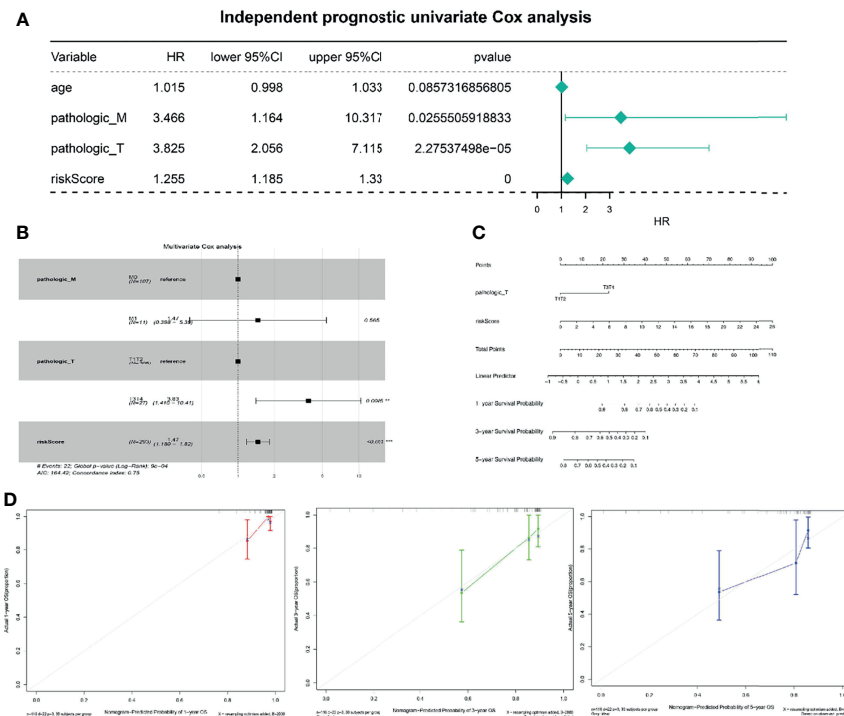
FIGURE 4 | Independent prognostic analysis of risk scores. **(A)** Four factors were included in the univariate Cox analysis, and three of them were significant. HR is the risk ratio, and the lower/upper 95% CI is the 95% confidence interval of the risk value. **(B)** Multivariate analysis results show that T staging and risk score are significant. **(C)** The nomogram shows that T staging and risk score have significant influence on the prognostic survival time of CC patients. **(D)** Calibration curve suggesting that the nomogram holds implications in the prognosis of CC.

might affect prognosis of CC mainly through regulating of immune, metabolic and tumor-related pathways.

Correlation Between the TNF Family Gene Signature and Immunotherapy Response

To further explore whether the TNF family gene signature affected the immunotherapy response of patients with CC, we first calculated and compared the 22 human immune cell subpopulations between the high- and low-risk groups. Notably, we found dendritic cells resting, macrophage M1, mast cells resting, plasma cells, T cells CD8, T cells follicular

helper, and T cells regulatory were obviously up-regulated in the low-risk group compared with the high-risk group, while macrophage M0, mast cells activated, NK cells resting were significantly down-regulated in the low-risk group (**Figure 5A**), which were consistent with the results of functional enrichment analysis. Moreover, we also compared the expression levels of immune checkpoint molecules, including CD274 (PD-L1), CTLA4, LAG3, and PDCD1 (PD-1), between the high- and low-risk groups (**Figure 5B**). Interestingly, we found that these genes were upregulated in the low-risk group. Moreover, the low-risk group had a lower TIDE score than the

TABLE 4 | The significantly enriched KEGG pathways based on GSEA results (P < 0.01, FDR < 0.25).

NAME	SIZE	ES	NES	NOM p-val
KEGG_GALACTOSE_METABOLISM	25	0.570	1.751	0.011
KEGG_N_GLYCAN_BIOSYNTHESIS	46	0.535	1.786	0.016
KEGG_GLYCOSAMINOGLYCAN_BIOSYNTHESIS_CHONDROITIN_SULFATE	22	0.655	1.716	0.020
KEGG_O_GLYCAN_BIOSYNTHESIS	30	0.580	1.644	0.021
KEGG_HYPERTROPHIC_CARDIOMYOPATHY_HCM	83	0.459	1.567	0.030
KEGG_PURINE_METABOLISM	159	0.315	1.441	0.031
KEGG_FOCAL_ADHESION	199	0.496	1.662	0.034
KEGG_TGF_BETA_SIGNALING_PATHWAY	86	0.456	1.565	0.040
KEGG_AXON_GUIDANCE	129	0.393	1.476	0.042

TABLE 5 | The top10 KEGG pathway significantly enriched in the low-risk group.

NAME	SIZE	ES	NES	NOM p-val
KEGG_B_CELL_RECEPTOR_SIGNALING_PATHWAY	75.00	-0.64	-2.09	0.00
KEGG_PRIMARY_IMMUNODEFICIENCY	35.00	-0.88	-2.00	0.00
KEGG_INTESTINAL_IMMUNE_NETWORK_FOR_IGA_PRODUCTION	46.00	-0.80	-1.91	0.00
KEGG_T_CELL_RECEPTOR_SIGNALING_PATHWAY	108.00	-0.60	-1.94	0.00
KEGG_ARACHIDONIC_ACID_METABOLISM	58.00	-0.55	-1.77	0.00
KEGG_CHEMOKINE_SIGNALING_PATHWAY	188.00	-0.55	-1.89	0.00
KEGG_ALDOSTERONE_REGULATED_SODIUM_REABSORPTION	42.00	-0.54	-1.71	0.01
KEGG_FC_GAMMA_R_MEDIATED_PHAGOCYTOSIS	96.00	-0.48	-1.78	0.01
KEGG_FC_EPSILON_RI_SIGNALING_PATHWAY	79.00	-0.46	-1.69	0.01
KEGG_AUTOIMMUNE_THYROID_DISEASE	50.00	-0.72	-1.82	0.01

high-risk group and was potentially more sensitive to anti-PD1 therapy (**Figures 5C, D**).

Potential Regulatory Mechanisms of Genes in the TNF Family Gene Signature

To further understand the reasons for the altered expression of these genes in the TNF family gene signature, we further observed the methylation levels and copy number variation of *CD27, EDA, TNF, TNFRSF12A, TNFRSF13C,* and *TNFRSF9*. For methylation analysis, we only found data for *CD27, TNF, TNFRSF12A, TNFRSF13C,* and *TNFRSF9*. Most methylation sites were differentially expressed in normal and patients with CC, and most differential methylation levels were negatively correlated with expression levels (**Figures 6A, B**). Copy number variants occurred in *CD27, EDA, TNF, TNFRSF12A, TNFRSF13C,* and *TNFRSF9* in patients with CC, where the copy number variation possibly affected their expression levels (**Figures 6C, D**). Finally, we predicted 291 target miRNAs of *CD27, EDA, TNF, TNFRSF12A, TNFRSF13C,* and *TNFRSF9* and

constructed a miRNA-mRNA network (**Figure 6E**). We speculated that CD27 might be regulated by hsa-miR-214-3p and hsa-miR-8052 and that TNFRSF13C might be regulated by hsa-miR-4710, hsa-miR-3135b, and hsa-miR6848-5p (**Figure 6F**).

Prognostic Significance of Genes in the TNF Family Gene Signature in Gynaecologic Tumours As Well As BRCA

To investigate whether *CD27, EDA, TNF, TNFRSF12A, TNFRSF13C,* and *TNFRSF9* expression affects the prognosis of other gynaecologic tumours and BRCA, we performed univariate Cox regression analysis based on the overall survival information and expression of the aforementioned genes. *CD27* expression was associated with the overall survival of patients with BRCA, OV, UCEC, and UCS, while *EDA* was associated with UCEC prognosis and *TNFRSF13C* with BRCA prognosis (**Figure 7**).
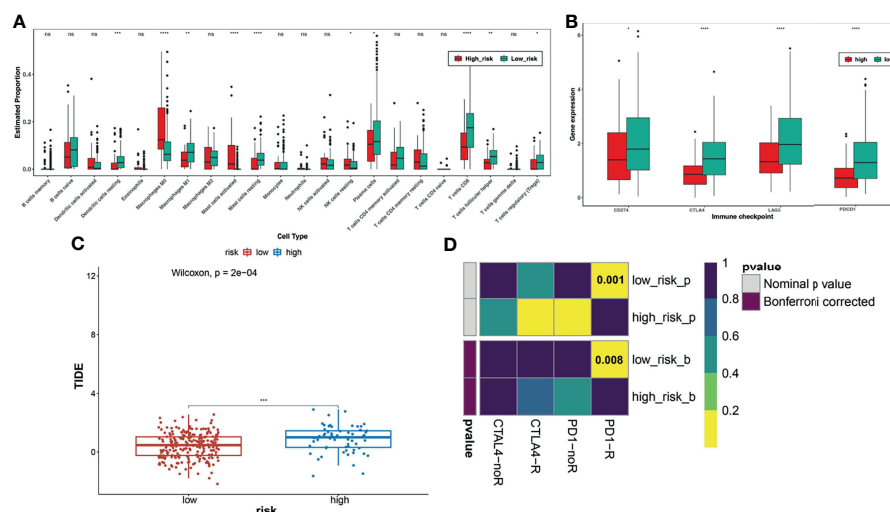
FIGURE 5 | Analysis of immune checkpoint differences in high- and low-risk groups. **(A)** The differences in immune cell infiltration between high and low risk groups. **(B)** Expression levels of immune checkpoint molecules between the high-risk and low-risk groups. **(C)** TIDE scores significantly differ between the high- and low-risk groups, suggesting a higher probability of immune escape in the high-risk group. **(D)** The low-risk group is more likely to be more sensitive to anti-PD1 therapy. *FDR < 0.05; **means p < 0.01; ***means p < 0.001; ****means p < 0.0001. ns represents no significance.
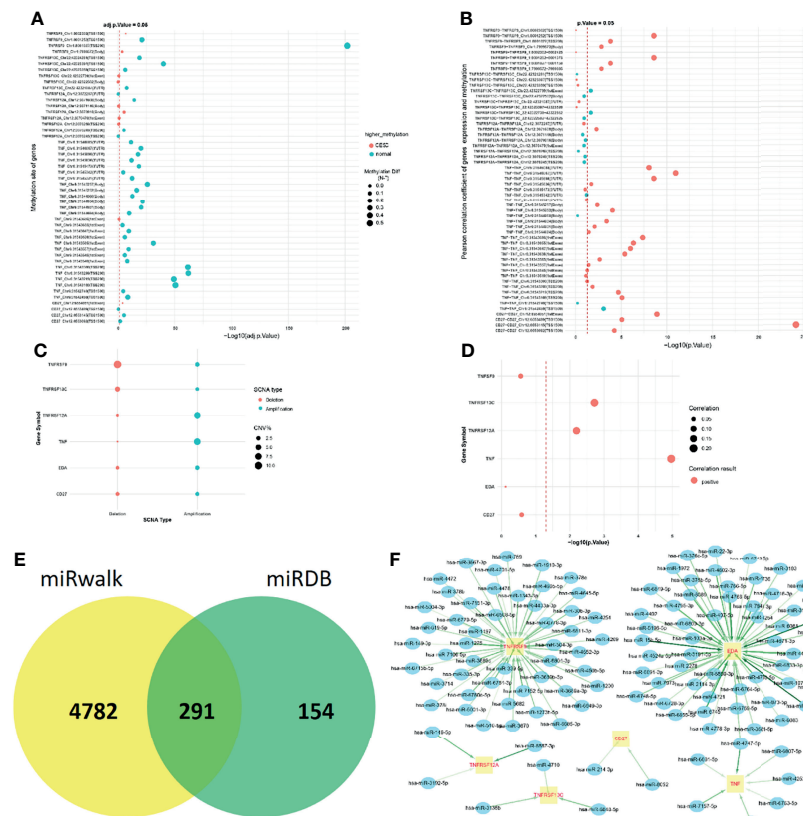
FIGURE 6 | Potential regulatory mechanisms of genes in the TNF family gene signature. **(A)** Different biomarker methylation sites in normal and tumour tissues. The figure shows a total of five biomarkers and 49 different methylation sites. **(B)** Fifty-six genes are correlated with the mRNA expression levels of corresponding methylation sites, of which 29 pairs were significant. **(C)** Copy number variation of the six biomarkers. **(D)** Correlation between copy number variation and gene expression. **(E)** Venn diagrams for the EmiRwalk and miRDB databases. **(F)** Construction of miRNA-mRNA regulatory networks: the green arrow indicates the interaction, and the darker the colour, the stronger the interaction. Blue ellipses represent miRNAs and yellow rectangles represent target genes.
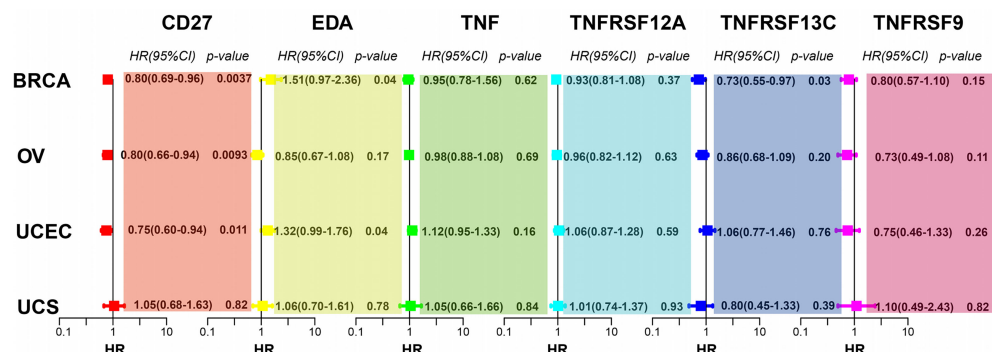
FIGURE 7 | *CD27, EDA*, and *TNFRSF13C* are significantly correlated with BRCA. CD27 is significantly correlated with OV. *CD27* and *EDA* are significantly correlated with UCEC.

Validation of mRNA Expression of the TNF Family Gene Signature

To validate the mRNA expression of *CD27*, *EDA*, *TNF*, *TNFRSF12A*, *TNFRSF13C*, and *TNFRSF9*, we performed quantitative real-time PCR using clinical samples. The expression levels of *CD27*, *TNF*, *TNFRSF12A*, *TNFRSF13C*, and *TNFRSF9* were upregulated in the tissues from CC compared with those in paraneoplastic tissues; however, *EDA* expression was downregulated (**Figure 8**), which was consistent with the results of TCGA (**Figure 1C**).

DISCUSSION

Despite increasing human papilloma virus (HPV) vaccination and CC screening, the latter remains the fourth most common cancer worldwide (26). Although early-stage CC has an excellent prognosis, the 5-year overall survival rate for patients diagnosed as having stage III CC remains <40% (27). Currently, the first-line treatment for patients with early CC is radical hysterectomy and lymph node dissection, whereas radiotherapy and cisplatin-based chemotherapy are the optimal treatments for patients with advanced CC (28). Unfortunately, many patients with CC develop resistance to these drugs owing to the occurrence of adaptive chemotherapy resistance. The median overall survival of patients with advanced CC is 16.8 months, while the 5-year survival rate for all cases is only 68%, indicating that treatment is still not ideal (29). Therefore, elucidating the mechanisms leading to CC progression and identifying new prognostic markers are urgently needed.

In this study, using transcriptomic data of 306 patients with CC and 13 normal control samples, we screened 26 differentially expressed TNF family genes. A TNF family gene signature comprising *CD27*, *EDA*, *TNF*, *TNFRSF12A*, *TNFRSF13C*, and

TNFRSF9 was constructed based on univariate Cox, LASSO, and multivariate Cox regression analyses. Moreover, the KM and ROC curve analyses showed that the TNF family gene signature is a good prognostic marker for CC. Interestingly, we found that our gene signature was superior to other signatures. For example, the AUC of ROC curves for autophagy-related gene risk model predicting 1-, 3-, and 5-year overall survival was 0.678, 0.648, and 0.674, separately (30). The AUC of ROC curves for m6A RNA methylation regulator-related signature predicting 3- and 5-year overall survival was 0.67 and 0.72, separately (31). The AUC of ROC curves for hypoxia-related gene signature predicting 1-, 3-, and 5-year overall survival was 0.685, 0.683, and 0.683, separately (32). More importantly, univariate and multivariate Cox analyses showed that the TNF family gene signature was a useful prognostic factor independent of any other clinical factors in patients with CC. CD27, expressed by CD4, CD8 T lymphocytes, and NK cells, plays an important role in cancer immunotherapy (33). CD27 affects the prognosis of CC, and the higher its expression level, the better the prognosis (34). Likewise, CD27 is also particularly important for prognosis in multiple myeloma and clear cell renal cell carcinoma (35). EDA, a type II transmembrane protein whose receptor acts as a component of the Wnt/β-catenin signaling pathway, can affect the occurrence of colorectal cancer (36). Knockdown of the EDA receptor-associated adaptor protein has a tumour-suppressive effect on tongue squamous cell carcinoma (37). EDA receptors act as dependent receptors to control the progression of melanoma (38). However, the role of EDA in CC has not yet been reported. TNF is a proinflammatory and pro-apoptotic cytokine. TNF single-nucleotide variants (SNVs) have been found to be risk factors for the development of CC (39). The encoding protein tumour necrosis factor-α (TNF-α) of TNF can inhibit the survival of cancer cells and ultimately improve the prognosis of CC (40). TNFRSF12A, a member of the TNF receptor superfamily 12A, also known as FN14, CD266, and
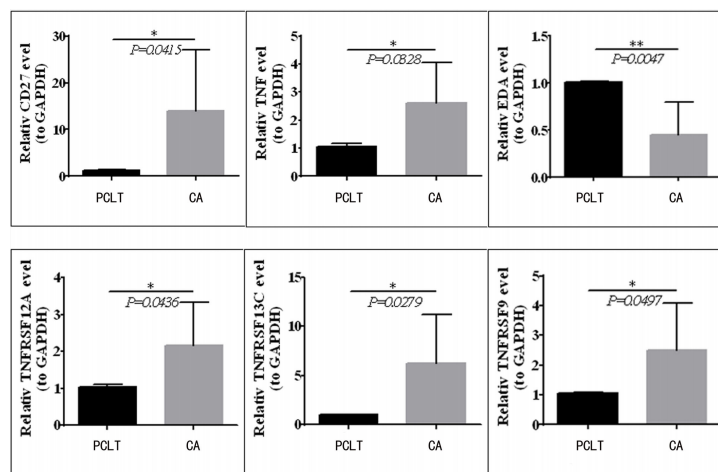
FIGURE 8 | CD27, TNF, TNFRSF12A, TNFRSF13C, and TNFRSF9 expression is upregulated in CC tissues compared to paraneoplastic tissues, but EDA was downregulated in clinical samples.*means p < 0.05; **means p < 0.01.

TWEAK, is the smallest member of the TNF superfamily receptor and contains a short cytoplasmic extinction domain (41). TNFRSF12A can be used as a prognostic marker for thyroid cancer (42) as it is associated with the progression of CC (43). TNFRSF13C (BAFFR or CD268), the receptor of BAFF, is an important regulator of B cell proliferation, development, and maturation (44). TNFRSF13C is associated with drug-resistant B cell malignancies and affects the prognosis and immunotherapy response of lung adenocarcinoma (45). TNFRSF9, also known as CD137, is found on activated T cells and plays an important role in tumour immunotherapy (46). CD137 is an important recognition factor for poor prognosis in patients with non-small cell lung cancer (47). In this study, we found that CD27 was associated with the overall survival of BRCA, OV, UCEC, and UCS patients, EDA was associated with the prognosis of UCEC, and TNFRSF13C was associated with BRCA prognosis. Therefore, we speculate that *CD27*, *EDA*, *TNF*, *TNFRSF12A*, *TNFRSF13C*, and *TNFRSF9* expression may play important roles in CC and may be good prognostic markers of CC.

To further study the mechanism by which the TNF family gene signature affects the prognosis of CC, we investigated the possible involvement of the TNF family gene signature in KEGG signaling pathways through GSEA. Notably, we found that the TGF-β signaling pathway was activated in the high-risk group. Therefore, we hypothesised that CD27, EDA, TNF, TNFRSF12A, TNFRSF13C, and TNFRSF9 may affect tumour prognosis mainly by regulating the TGF-β signaling pathway. The TGF-β signaling pathway is critical for the progression of CC (48, 49). For example, NSD2 can affect the metastasis of CC by regulating the TGF-β/TGF-βRI/SMAD signaling pathway (48). RHCG inhibits the development of CC by suppressing migration and inducing TGF-β 1-mediated apoptosis. On the other hand, genes in the high-risk group were mainly associated with immune-related pathways, and immune cells infiltrated more in the low-risk group compared with the high-risk group. It has been suggested that CD27 plays a key role in T-cell activation by providing a costimulatory signal (50). Moreover, CD27 improves expansion and differentiation of activated B cells into plasma cells in T cell-dependent B cell responses (51). Moreover, increasing evidence has revealed that TNF can promote tumor growth by recruiting neutrophils and macrophages, which benefit from inflammatory cytokines and chemokines (52). Furthermore, accumulation of preclinical data has suggested that TNF receptor family genes may neutralize tumor immunity by directly activating tumor-specific T cells or inhibiting dominant inhibitory mechanisms (53). TNFR family genes play a role in the intervention of CD28 to increase activation, survival and differentiation of effector and memory cells (54). Therefore, we speculated that better prognosis in the low-risk group might be related to immune activation. In addition, we analyzed the immunotherapy response differences between the high- and low-risk groups. The low-risk group exhibited significantly higher immune checkpoint molecular expression and lower TIDE score than the high-risk group. Additionally, subclass mapping analysis showed that the low-risk group was indeed more suitable for immunotherapy, which

was consistent with the results of Wang et al. (55). Therefore, the TNF family gene signature not only affects the prognosis of CC but also affects the effect of immunotherapy on patients with CC. In other words, CD27, EDA, TNF, TNFRSF12A, TNFRSF13C, and TNFRSF9 expression may also affect the immunotherapy effect on tumours by regulating the expression of immune checkpoint molecules in the tumour microenvironment.

Finally, we found that the alterations in the mRNA expression of *CD27*, *EDA*, *TNF*, *TNFRSF12A*, *TNFRSF13C*, and *TNFRSF9* are caused by changes in gene methylation or copy number. Therefore, we not only propose a prognostic marker for CC but also provide a new reference for the molecular basis of CC occurrence and development. Notably, TCGA and GTEx differential analyses results are consistent. The qRT-PCR results of the clinical samples also showed that the mRNA expression of *CD27*, *TNF*, *TNFRSF12A*, *TNFRSF13C*, and *TNFRSF9* is upregulated in cancer tissues, except *EDA* whose mRNA expression is downregulated in cancer tissues. The qRT-PCR results further emphasise the significance of *CD27*, *EDA*, *TNF*, *TNFRSF12A*, *TNFRSF13C*, and *TNFRSF9* expression in CC. However, a higher expression of *CD27*, *TNFRSF13C*, and *TNFRSF9* and a lower expression of *EDA* in tumours indicated better prognosis. This may be due to the dual role of genes in tumour progression and prognosis. For example, Wu et al. found that *INPP4B* is an oncogene as well as a tumour suppressor gene in different tissue grades and clinical stages (56). Cao et al. also found that *CXCL11* is highly expressed in colon cancer tissues, and the higher the expression level in cancer tissues, the better the prognosis (57). Generally speaking, our study firstly found that the TNF family gene signature could predict the prognosis of patients with CC, and had stronger predictive power than other gene signatures. Meanwhile, we found that the TNF family gene signature might affect the immunotherapy of patients with CC, thus providing a basis for guiding the immunotherapy of CC. However, this study had some limitations. Even though bioinformatics tools are helpful to identify the interactions of hub genes, wet-lab experiments using actual tissue samples are warranted to validate the molecular mechanisms underlying CC progression. Therefore, in future, we will further investigate the involvement as well as the mechanism underlying the actions of these genes in CC.

CONCLUSIONS

We established a TNF family gene signature for patients with CC based on *CD27, EDA, TNF, TNFRSF12A, TNFRSF13C,* and *TNFRSF9*, which could predict the prognosis and immunotherapy of patients with CC. Collectively, in this study, we present a potential and novel prognostic biomarker for CC.

DATA AVAILABILITY STATEMENT

The original contributions presented in the study are included in the article/**Supplementary Material**. Further inquiries can be directed to the corresponding author.

ETHICS STATEMENT

The studies involving human participants were reviewed and approved by Ethics Review Committee of Suzhou Municipal Hospital (Suzhou, China). The patients/participants provided their written informed consent to participate in this study.

AUTHOR CONTRIBUTIONS

MYYM and JQ designed this study. YM, XZ and YX were responsible for data collection and preparation. YM, JY and YJ contributed to data analysis. YM wrote the manuscript. JQ reviewed the data and manuscript. All authors read and approved final version of the manuscript.

SUPPLEMENTARY MATERIAL

The Supplementary Material for this article can be found online at: https://www.frontiersin.org/articles/10.3389/fonc.2022.854615/full#supplementary-material

Supplementary Figure 1 | Evaluating the efficiency of the TNF family gene signature in the testing set. **(A)** Time-dependent ROC curve evaluated the efficiency of the TNF family gene signature for predicting 1-, 3- and 5-year OS. **(B)** KM survival curve showed the prognostic value of the TNF family gene signature.

REFERENCES

1. Bray F, Ferlay J, Soerjomataram I, Siegel RL, Torre LA, Jemal A. Global Cancer Statistics 2018: GLOBOCAN Estimates of Incidence and Mortality Worldwide for 36 Cancers in 185 Countries. *CA Cancer J Clin* (2018) 68:394–424. doi: 10.3322/caac.21492

2. Arbyn M, Weiderpass E, Bruni L, de Sanjosé S, Saraiya M, Ferlay J, et al. Estimates of Incidence and Mortality of Cervical Cancer in 2018: A Worldwide Analysis. *Lancet Glob Health* (2020) 8:e191–203. doi: 10.1016/s2214-109x(19)30482-6

3. Olusola P, Banerjee HN, Philley JV, Dasgupta S. Human Papilloma Virus-Associated Cervical Cancer and Health Disparities. *Cells* (2019) 8. doi: 10.3390/cells8060622

4. Gaffney DK, Hashibe M, Kepka D, Maurer KA, Werner TL. Too many women are dying from cervix cancer: Problems and solutions. *Gynecol Oncol* (2018) 151:547–54. doi: 10.1016/j.ygyno.2018.10.004

5. Ferlay J, Soerjomataram I, Dikshit R, Eser S, Mathers C, Rebelo M, et al. Cancer Incidence and Mortality Worldwide: Sources, Methods and Major Patterns in GLOBOCAN 2012. *Int J Cancer* (2015) 136:E359–86. doi: 10.1016/j.ejca.2013.04.024

6. Dizon DS, Mackay HJ, Thomas GM, Werner TL, Kohn EC, Hess D, et al. State of the Science in Cervical Cancer: Where We Are Today and Where We Need to Go. *Cancer* (2014) 120:2282–8. doi: 10.1002/cncr.28722

7. GuYu Z YZ, ChongDong L, GuangMing C, Ran C,ZZ. Current Status and Future of Targeted Therapy for Patients With Local Advanced Cervical Cancer. *Chin J Pract Gynecol Obstet* (2018) 34:1216–20. doi: 10.19538/j.fk2018110108

8. Dostert C, Grusdat M, Letellier E, Brenner D. The TNF Family of Ligands and Receptors: Communication Modules in the Immune System and Beyond. *Physiol Rev* (2019) 99:115–60. doi: 10.1152/physrev.00045.2017

9. Yi F, Frazzette N, Cruz AC, Klebanoff CA, Siegel RM. Beyond Cell Death: New Functions for TNF Family Cytokines in Autoimmunity and Tumor Immunotherapy. *Trends Mol Med* (2018) 24:642–53. doi: 10.1016/j.molmed.2018.05.004

10. Wang J, Cheng FHC, Tedrow J, Chang W, Zhang C, Mitra AK. Modulation of Immune Infiltration of Ovarian Cancer Tumor Microenvironment by Specific Subpopulations of Fibroblasts. *Cancers (Basel)* (2020) 12:3184. doi: 10.3390/cancers12113184

11. Kretz AL, von Karstedt S, Hillenbrand A, Henne-Bruns D, Knippschild U, Trauzold A, et al. Should We Keep Walking Along the Trail for Pancreatic Cancer Treatment? Revisiting TNF-Related Apoptosis-Inducing Ligand for Anticancer Therapy. *Cancers (Basel)* (2018) 10:77. doi: 10.3390/cancers10030077

12. Ren Y, Wang X, Huang S, Xu Y, Weng G, Yu R. Alternol Sensitizes Renal Carcinoma Cells to TRAIL-Induced Apoptosis. *Front Pharmacol* (2021) 12:560903. doi: 10.3389/fphar.2021.560903

13. Ryu HS, Chang KH, Chang SJ, Kim MS, Joo HJ, Oh KS. Expression of TRAIL (TNF-Related Apoptosis-Inducing Ligand) Receptors in Cervical Cancer. *Int J Gynecol Cancer* (2000) 10:417–24. doi: 10.1046/j.1525-1438.2000.010005417.x

14. Feng Y, Ma J, Fan H, Liu M, Zhu Y, Li Y, et al. TNF-α-Induced lncRNA LOC105374902 Promotes the Malignant Behavior of Cervical Cancer Cells by Acting as a Sponge of miR-1285-3p. *Biochem Biophys Res Commun* (2019) 513:56–63. doi: 10.1016/j.bbrc.2019.03.079

15. Xiao Z, Nie K, Han T, Cheng L, Zhang Z, Peng W, et al. Development and Validation of a TNF Family-Based Signature for Predicting Prognosis, Tumor Immune Characteristics, and Immunotherapy Response in Colorectal Cancer Patients. *J Immunol Res* (2021) 2021:6439975. doi: 10.1155/2021/2676996

16. Zhang C, Zhang G, Sun N, Zhang Z, Zhang Z, Luo Y, et al. Comprehensive Molecular Analyses of a TNF Family-Based Signature With Regard to Prognosis, Immune Features, and Biomarkers for Immunotherapy in Lung Adenocarcinoma. *EBioMedicine* (2020) 59:102959. doi: 10.1016/j.ebiom.2020.102959

17. Carithers LJ, Ardlie K, Barcus M, Branton PA, Britton A, Buia SA, et al. A Novel Approach to High-Quality Postmortem Tissue Procurement: The GTEx Project. *Biopreserv Biobank* (2015) 13:311–9. doi: 10.1089/bio.2015.0032

18. Ritchie ME, Phipson B, Wu D, Hu Y, Law CW, Shi W, et al. Limma Powers Differential Expression Analyses for RNA-Sequencing and Microarray Studies. *Nucleic Acids Res* (2015) 43:e47. doi: 10.1093/nar/gkv007

19. Friedman J, Hastie T, Tibshirani R. Regularization Paths for Generalized Linear Models *via* Coordinate Descent. *J Stat Software* (2010) 33:1–22. doi: 10.18637/jss.v033.i01

20. Wang Y, Liu X, Guan G, Zhao W, Zhuang M. A Risk Classification System With Five-Gene for Survival Prediction of Glioblastoma Patients. *Front Neurol* (2019) 10:745. doi: 10.3389/fneur.2019.00745

21. Iasonos A, Schrag D, Raj GV, Panageas KS. How to Build and Interpret a Nomogram for Cancer Prognosis. *J Clin Oncol* (2008) 26:1364–70. doi: 10.1200/jco.2007.12.9791

22. Yu G, Wang LG, Han Y, He QY. clusterProfiler: An R Package for Comparing Biological Themes Among Gene Clusters. *Omics* (2012) 16:284–7. doi: 10.1089/omi.2011.0118

23. Newman AM, Liu CL, Green MR, Gentles AJ, Feng W, Xu Y, et al. Robust Enumeration of Cell Subsets From Tissue Expression Profiles. *Nat Methods* (2015) 12:453–7. doi: 10.1038/nmeth.3337

24. Jiang P, Gu S, Pan D, Fu J, Sahu A, Hu X, et al. Signatures of T Cell Dysfunction and Exclusion Predict Cancer Immunotherapy Response. *Nat Med* (2018) 24:1550–58. doi: 10.1038/s41591-018-0136-1

25. Lu X, Jiang L, Zhang L, Zhu Y, Hu W, Wang J, et al. Immune Signature-Based Subtypes of Cervical Squamous Cell Carcinoma Tightly Associated With Human Papillomavirus Type 16 Expression, Molecular Features, and Clinical Outcome. *Neoplasia* (2019) 21:591–601. doi: 10.1016/j.neo.2019.04.003

26. Torre LA, Bray F, Siegel RL, Ferlay J, Lortet-Tieulent J, Jemal A. Global Cancer Statistics, 2012. *CA Cancer J Clin* (2015) 65:87–108. doi: 10.3322/caac.21262

27. *Fiveyear Relative Survival by Stage, Women (Aged 15-99 Years)*. Available at: http://www.cancerresearchuk.org/healthprofessional/cancer-statistics/statistics-by-cancer-type/cervical-cancer/survival#heading-Three.

28. Cohen PA, Jhingran A, Oaknin A, Denny L. Cervical Cancer. *Lancet* (2019) 393:169–82. doi: 10.1016/s0140-6736(18)32470-x

29. Kagabu M, Nagasawa T, Fukagawa D, Tomabechi H, Sato S, Shoji T, et al. Immunotherapy for Uterine Cervical Cancer. *Healthcare (Basel)* (2019) 7:108. doi: 10.3390/healthcare7030108

30. Shi H, Zhong F, Yi X, Shi Z, Ou F, Xu Z, et al. Application of an Autophagy-Related Gene Prognostic Risk Model Based on TCGA Database in Cervical Cancer. *Front Genet* (2020) 11:616998. doi: 10.3389/fgene.2020.616998

31. Pan J, Xu L, Pan H. Development and Validation of an m6A RNA Methylation Regulator-Based Signature for Prognostic Prediction in Cervical Squamous Cell Carcinoma. *Front Oncol* (2020) 10:1444. doi: 10.3389/fonc.2020.01444

32. Yang Y, Li Y, Qi R, Zhang L. Constructe a Novel 5 Hypoxia Genes Signature for Cervical Cancer. *Cancer Cell Int* (2021) 21:345. doi: 10.1186/s12935-021-02050-3

33. Han BK, Olsen NJ, Bottaro A. The CD27-CD70 Pathway and Pathogenesis of Autoimmune Disease. *Semin Arthritis Rheumatol* (2016) 45:496–501. doi: 10.1016/j.coi.2017.02.001

34. Chen Q, Qiu B, Zeng X, Hu L, Huang D, Chen K, et al. Identification of a Tumor Microenvironment-Related Gene Signature to Improve the Prediction of Cervical Cancer Prognosis. *Cancer Cell Int* (2021) 21:182. doi: 10.1186/s12935-021-01867-2

35. Wang Y, Wang Y, Liu F. A 44-Gene Set Constructed for Predicting the Prognosis of Clear Cell Renal Cell Carcinoma. *Int J Mol Med* (2018) 42:3105–14. doi: 10.18632/oncotarget.22131

36. Wang B, Liang Y, Chai X, Chen S, Ye Z, Li R, et al. Ectodysplasin A Receptor (EDAR) Promotes Colorectal Cancer Cell Proliferation *via* Regulation of the Wnt/β-Catenin Signaling Pathway. *Exp Cell Res* (2020) 395:112170. doi: 10.1016/j.yexcr.2020.112170

37. Li M, Bai YT, Han K, Li XD, Meng J. Knockdown of Ectodysplasin-A Receptor-Associated Adaptor Protein Exerts a Tumor-Suppressive Effect in Tongue Squamous Cell Carcinoma Cells. *Exp Ther Med* (2020) 19:3337–47. doi: 10.3892/etm.2020.8578

38. Vial J, Royet A, Cassier P, Tortereau A, Dinvaut S, Maillet D, et al. The Ectodysplasin Receptor EDAR Acts as a Tumor Suppressor in Melanoma by Conditionally Inducing Cell Death. *Cell Death Differ* (2019) 26:443–54. doi: 10.1038/s41418-018-0128-1

39. Babapour N, Mehramiz M, Rastgar Moghadam A, Behboodi N, Yousefi Z, Maftouh M, et al. Association of TNF-308 G>A Polymorphism Located in Tumor Necrosis Factor a With the Risk of Developing Cervical Cancer and Results of Pap Smear. *J Cell Biochem* (2019) 120:5444–48. doi: 10.1002/jcb.27823

40. Zhao Q, Wang W, Cui J. Melatonin Enhances TNF-α-Mediated Cervical Cancer HeLa Cells Death *via* Suppressing CaMKII/Parkin/Mitophagy Axis. *Cancer Cell Int* (2019) 19:58. doi: 10.1186/s12935-019-0777-2

41. Wiley SR, Cassiano L, Lofton T, Davis-Smith T, Winkles JA, Lindner V, et al. A Novel TNF Receptor Family Member Binds TWEAK and Is Implicated in Angiogenesis. *Immunity* (2001) 15:837–46. doi: 10.1016/s1074-7613(01)00232-1

42. Wu ZH, Niu X, Wu GH, Cheng Q. Decreased Expression of TNFRSF12A in Thyroid Gland Cancer Predicts Poor Prognosis: A Study Based on TCGA Data. *Med (Baltimore)* (2020) 99:e21882. doi: 10.1097/md.0000000000021882

43. Zou H, Wang D, Gan X, Jiang L, Chen C, Hu L, et al. Low TWEAK Expression is Correlated to the Progression of Squamous Cervical Carcinoma. *Gynecol Oncol* (2011) 123:123–8. doi: 10.1016/j.ygyno.2011.07.003

44. Gross JA, Dillon SR, Mudri S, Johnston J, Littau A, Roque R, et al. TACI-Ig Neutralizes Molecules Critical for B Cell Development and Autoimmune Disease. Impaired B Cell Maturation in Mice Lacking BLyS. *Immunity* (2001) 15:289–302. doi: 10.1016/s1074-7613(01)00183-2

45. Qin H, Wei G, Sakamaki I, Dong Z, Cheng WA, Smith DL, et al. Novel BAFF-Receptor Antibody to Natively Folded Recombinant Protein Eliminates Drug-Resistant Human B-Cell Malignancies *In Vivo*. *Clin Cancer Res* (2018) 24:1114–23. doi: 10.1080/2162402x.2020.1824641

46. Kwon BS, Weissman SM. cDNA Sequences of Two Inducible T-Cell Genes. *Proc Natl Acad Sci USA* (1989) 86:1963–7. doi: 10.1136/esmoopen-2020-000733

47. Guo X, Zhang Y, Zheng L, Zheng C, Song J, Zhang Q, et al. Global Characterization of T Cells in Non-Small-Cell Lung Cancer by Single-Cell Sequencing. *Nat Med* (2018) 24:978–85. doi: 10.1038/s41591-018-0045-3

48. Zhu L, Yu CL, Zheng Y. NSD2 Inhibition Suppresses Metastasis in Cervical Cancer by Promoting TGF-β/TGF-βri/SMADs Signaling. *Biochem Biophys Res Commun* (2019) 519:489–96. doi: 10.1016/j.bbrc.2019.08.020

49. Wang DG, Li TM, Liu X. RHCG Suppresses Cervical Cancer Progression Through Inhibiting Migration and Inducing Apoptosis Regulated by TGF-β1. *Biochem Biophys Res Commun* (2018) 503:86–93. doi: 10.1016/j.bbrc.2018.05.183

50. Starzer AM, Berghoff AS. New Emerging Targets in Cancer Immunotherapy: CD27 (Tnfrsf7). *ESMO Open* (2020) 4:e000629. doi: 10.1136/esmoopen-2019-000629

51. Denoeud J, Moser M. Role of CD27/CD70 Pathway of Activation in Immunity and Tolerance. *J Leukoc Biol* (2011) 89:195–203. doi: 10.1189/jlb.0610351

52. Popivanova BK, Kitamura K, Wu Y, Kondo T, Kagaya T, Kaneko S, et al. Blocking TNF-Alpha in Mice Reduces Colorectal Carcinogenesis Associated With Chronic Colitis. *J Clin Invest* (2008) 118:560–70. doi: 10.1073/pnas.0812347106

53. Pardee AD, Wesa AK, Storkus WJ. Integrating Costimulatory Agonists to Optimize Immune-Based Cancer Therapies. *Immunotherapy* (2009) 1:249–64. doi: 10.2217/1750743x.1.2.249

54. Watts TH. TNF/TNFR Family Members in Costimulation of T Cell Responses. *Annu Rev Immunol* (2005) 23:23–68. doi: 10.1146/annurev.immunol.23.021704.115839

55. Wang Q, Li M, Yang M, Yang Y, Song F, Zhang W, et al. Analysis of Immune-Related Signatures of Lung Adenocarcinoma Identified Two Distinct Subtypes: Implications for Immune Checkpoint Blockade Therapy. *Aging (Albany NY)* (2020) 12:3312–39. doi: 10.18632/aging.102814

56. Wu Y, Wang X, Lu Y, Wang H, Wang M, You Y, et al. INPP4B Exerts a Dual Role in Gastric Cancer Progression and Prognosis. *J Cancer* (2021) 12:7201–13. doi: 10.7150/jca.58397

57. Cao Y, Jiao N, Sun T, Ma Y, Zhang X, Chen H, et al. CXCL11 Correlates With Antitumor Immunity and an Improved Prognosis in Colon Cancer. *Front Cell Dev Biol* (2021) 9:646252. doi: 10.3389/fcell.2021.646252

Immune-and Metabolism-Associated Molecular Classification of Ovarian Cancer

Zhenyue Chen[1], Weiyi Jiang[2], Zhen Li[3], Yun Zong[1] and Gaopi Deng[4*]

[1] The First Clinical Medical College, Guangzhou University of Chinese Medicine, Guangzhou, China, [2] College of First Clinical Medicine, Shandong University of Traditional Chinese Medicine, Jinan, China, [3] The Second Clinical Medical College, Guangzhou University of Chinese Medicine, Guangzhou, China, [4] Department Obstetrics and Gynecology, First Affiliated Hospital of Guangzhou University of Chinese Medicine, Guangzhou, China

Ovarian cancer (OV) is a complex gynecological disease, and its molecular characteristics are not clear. In this study, the molecular characteristics of OV subtypes based on metabolic genes were explored through the comprehensive analysis of genomic data. A set of transcriptome data of 2752 known metabolic genes was used as a seed for performing non negative matrix factorization (NMF) clustering. Three subtypes of OV (C1, C2 and C3) were found in analysis. The proportion of various immune cells in C1 was higher than that in C2 and C3 subtypes. The expression level of immune checkpoint genes TNFRSF9 in C1 was higher than that of other subtypes. The activation scores of cell cycle, RTK-RAS, Wnt and angiogenesis pathway and ESTIMATE immune scores in C1 group were higher than those in C2 and C3 groups. In the validation set, grade was significantly correlated with OV subtype C1. Functional analysis showed that the extracellular matrix related items in C1 subtype were significantly different from other subtypes. Drug sensitivity analysis showed that C2 subtype was more sensitive to immunotherapy. Survival analysis of differential genes showed that the expression of PXDN and CXCL11 was significantly correlated with survival. The results of tissue microarray immunohistochemistry showed that the expression of PXDN was significantly correlated with tumor size and pathological grade. Based on the genomics of metabolic genes, a new OV typing method was developed, which improved our understanding of the molecular characteristics of human OV.

Keywords: ovarian cancer, metabolic genes, subtypes, molecular characteristics, tumor

1 INTRODUCTION

Ovarian cancer (OV) is a heterogenous gynecological disease with high mortality rate in the women (1–3). The treatment of OV is based on surgical debulking or chemotherapy with carboplatin and paclitaxel (4, 5). The unelucidated genetic heterogeneity of OV complicates its diagnosis and the development of appropriate therapeutics approaches. Thus, it is vital to stratify OV patients based on molecular characteristics.

In recent years, the accumulation of genomic data has incited researchers to classify diseases according to the distinct profiles of their molecular characteristics and their correlation with clinical features (6–10). In the past, different classification systems were proposed for OV. The basic classification is the classification based on morphological characteristics, but this classification approach does not provide substantial information for the prognosis and treatment of OV patients. For this reason, researchers have endeavored to identify the different molecular subtypes of OV (11). Studies based on RNA-seq data have allowed the classification of patients with serous OV into nine molecular subtypes differing in immunologic activity, MAPK signaling pathway, mesenchymal development, and hormonal metabolism (12). Other investigators have classified high-grade serous OV into 4 subtypes including C1 (mesenchymal), C2 (immunoreactive), C4 (differentiated) and C5 (proliferative) (13–15). Other classifications of high-grade OV based on hormone receptor expression have provided a clinically applicable molecular subtype classification (16). OV classification based on gene expression profiles, gene methylation, and metabolic profile have also been developed (17–19). Nevertheless, all these efforts have not yet been able to definitively overcome the challenge imposed by the pathological severity of OV.

Metabolic genes have been reported as key players in human cancers. Especially, studies have shown that metabolic genes play a major role in the tumorigenesis and progression of cancers as it was reviewed previously (20). Different studies have indicated that the classification of diseases based on metabolic genes can help understand the genetic diversity of human diseases such as hepatocellular carcinoma (21) and colorectal cancer (22) and their clinical implications. However, only one study has proposed the classification of OV patients based on 594 energy-metabolism related genes (23). A classification based on a large set of metabolic genes and an integrative characterization of the identified subtypes is needed, which may be advantageous for diagnosis and therapeutic purposes.

For this reason, our present study attempted to establish a classification based on the expression of a large set of metabolic genes. Our results showed that these genes have a considerable influence on the status of patients with OV. We were able to classify and highlight the immunological, mutational and transcriptomic profiles of patients with a favorable prognosis and those with a severe prognosis. In addition, the sensitivity of each of the identified subtypes to anticancer therapy was established. Therefore, we believe that the results of our study may lead to new approaches in the effective management of OV patients.

2 MATERIALS AND METHODS

2.1 Data Acquisition
We downloaded the processed mRNA expression data of ovarian serous cystadenocarcinoma (OV) cohort from the TCGA database (https://portal.gdc.cancer.gov/). A total of 377 specimens with complete survival information were collected. The mutation data was obtained by downloading the SNP data of

OV cohort while the GISTIC2 copy number data of this cohort was acquired from GDAC FireBrowse (http://firebrowse.org/). Predicted neoantigens for the OV cohort were retrieved from a previous analysis of the TCGA dataset (24). The GSE63885 (n=75 samples) and GSE17260 (n=110 samples) datasets were downloaded from the GEO database for gene expression profile and survival analyses of the corresponding patients in external validation. The combat function in the R SVA library was used for batch effect correction of merged datasets.

2.2 Classification of OV Subtypes
The flowchart of the study design is as indicated in **Additional Figure S1**. The previously published metabolism-related genes (25) were retrieved and used for subsequent NMF clustering. Then, the R library "survival" was used for performing Cox regression analysis to evaluate the correlation between all candidate genes and overall survival (OS) of OV patients. Subsequently, the NMF package was used to perform an unsupervised NMF clustering method. The same candidate genes were used to apply the NMF clustering method to the two GEO external validation datasets. The k value at which the correlation coefficient begins to decrease was selected as the optimal number of clusters. SubMap analysis (Gene Pattern) is a method for evaluating the similarity of classification between patient cohorts based on expression profiles; this method was used to determine whether the subcategories identified in the above datasets were relevant. Then, based on the t-SNE method, the mRNA expression data of the above-mentioned metabolic genes were used to verify the subtype assignment.

2.3 Immune Cell Infiltration
The MCP algorithm was used to evaluate eight immune (immune cell populations: T cells, CD8+T cells, natural killer cells, cytotoxic lymphocytes, B cell lines, monocyte cell lines, and marrow cells, dendritic cells and neutrophils) and two non-immune stromal cell populations (endothelial cells and fibroblasts). In addition, the ssGSEA analysis, which calculates an enrichment score indicating the degree to which genes in a specific gene set are coordinated in a single sample, was also used to estimate immune infiltration. The GSVA-R software package was used to estimate six other immune cell populations, including regulatory T cells (Treg), helper T cells 1 (Th1), helper T cells 2 (Th2), and helper T cells 17 (Th17), central memory T cells and effective memory T cells (Tem), helper T cell (TFH), gamma delta T cells (Tgd). In addition, the ESTIMATE algorithm was used to calculate the immune score and matrix score, which can reflect the richness of the genetic characteristics of the matrix and immune cells.

2.4 Generation and Performance Verification of Ovarian Cancer Classifier
The LIMMA library in R was used to analyze differentially expressed genes (DEGs) among OV subtypes; the selection was based on the condition of corrected $P < 0.05$ and $\log_2 FC$ greater or equal to 2. Only genes whose expression were significantly

different in all three possible comparisons were considered subtype-specific genes. The top 30 genes with the largest log$_2$FC value in each subcategory were further selected to build a prediction model, and a 90-gene classifier was generated. Then, NTP algorithm was used to predict the sample subtypes based on the expression of the 90 genes in validation GEO datasets, followed by comparison of the classification results based on the NMF algorithm.

2.5 Prediction of Immunotherapy and Targeted Therapy Responses of Subtypes

By measuring the similarity of gene expression profiles between the subtypes obtained in the present study and previously published SubMap analysis (gene pattern) of gene profiles in patients with melanoma immunotherapy, we indirectly predicted the efficacy of immunotherapy on the predicted subtypes. In addition, based on the largest pharmacogenomics database (GDSC Cancer Drug Sensitivity Genomics Database, https://www.cancerrxgene.org/), we used the R library "pRRophetic" to predict the chemotherapy sensitivity of each tumor sample. The regression method was used to obtain the IC50 estimated value of each specific chemotherapy drug treatment, and the GDSC training set was used to perform 10 cross-validation tests to test the regression and prediction accuracy.

2.6 Tissue Microarray and Immunohistochemistry

Tissue chips were purchased from Shanghai Outdo Biotech Co., Ltd. The chip number is HOvaC070PT01 include 69 cases. Immunohistochemical assay used the CXCL11(Affinity, Cat#DF9917) and PXDN (Cloud-Clone Corp, Cat#PAM070 Hu01).The dilution of CXCL11 antibody is 1:200 and that of PXDN antibody is 1:100. The total score is the product of "staining intensity score" and "staining positive rate score" which represents CXCL11 and PXDN expression. According to the total score > 5 or < 5, they were divided into high expression group or low expression group. Use of all human samples was approved by the committee for ethical review of research involving human subjects at Shantou University and Jinan University.

2.7 Analytical Method of Immunohistochemistry

Use the tissue slice digital scanner or imaging system to collect the scanned documents or images on the immunohistochemical section, automatically read the tissue measurement area by using the Seville image analysis system, and analyze and calculate the number of weak, medium and strong positive cells in the measurement area (negative without coloring, 0 point; weak positive light yellow, 1 point; medium positive brownish yellow, 2 points; strong positive brownish brown, 3 points), the total number of cells and the positive cumulative optical density IOD value, Positive pixel area, tissue area mm². The following results were calculated to reflect the degree of positivity. The following indexes can be selected according to the section to evaluate the intensity of positive cells.

2.7.1 Positive Rate

Number of positive cells/total number of cells. Reflect the number of positive cells.

2.7.2 Positive Cell Density

Number of positive cells/area of tissue to be tested. It reflects the number of positive cells per unit area and is mostly used to evaluate the distribution and quantity of certain types of cells, such as the distribution and quantity of lymphocytes (CD3, CD4, CD8, etc.) in tumor tissue.

2.7.3 Average Optical Density

Positive cumulative optical density IOD value/positive area. Reflect the average depth of positive signals.

2.7.4 H-Score

The abbreviation of histochemistry score. It is a histological scoring method to deal with immunohistochemistry. It converts the positive number and staining intensity in each section into corresponding values to achieve the purpose of semi quantitative staining of tissues. H-Score(H-SCORE=Σ(pi × i)=(percentage of weak intensity cells × 1)+(percentage of moderate intensity cells × 2)+(percentage of strong intensity cells × 3) In the formula, I represents the grade of positive cells: negative without coloring, 0 point; Weak positive light yellow, 1 point; Medium positive brownish yellow, 2 points; 3 points for strong positive tan. PI is the percentage of positive cells). H-score is a value between 0 and 300. The larger the value, the stronger the comprehensive positive intensity.

2.7.5 Positive Score

The average positive intensity of the measurement area is 0,1,2,3 points: negative without coloring, 0 point; Weak positive light yellow, 1 point; Medium positive brownish yellow, 2 points; 3 points for strong positive tan. Score the positive rate of cells: 0-5% is 0, 6% ~ 25% is 1, 26% ~ 50% is 2, 51% ~ 75% is 3, and > 75% is 4. The positive comprehensive score is the staining intensity value × Positive cell ratio score. The larger the data, the stronger the comprehensive positive intensity.

2.8 Statistical Analysis

All statistical analyses were performed using the R language software (version 4.0). Survival analysis was performed by Kaplan-Meier method, and the log-rank test was used for comparison. Univariate Cox proportional hazards regression model was used to estimate the hazard ratio of univariate analysis. All statistical tests were two-sided, and $p<0.05$ was retained as statistical significance treshold.

3 RESULTS

3.1 Identification of Novel OV Subtypes Based on Metablism-Related Genes

A list of 2752 previously published metabolism-related genes (these genes encode all known human metabolic enzymes and

transport proteins) were used as input in the NMF analysis. After merging of TCGA and 2752 metabolism-related genes and correction of the batch effects using the Combat PCA algorithm (**Figure 1A**), Cox regression analysis was applied and a total of 177 prognostic-related candidate genes were identified (**Additional File S1**). Next, the NMF consensus clustering method was used for OV classification based on the expression profiles of the above 177 candidate genes. The clustering was performed on the TCGA dataset, and after a comprehensive consideration, k=3 was selected as the optimal number of clusters based on the cophenitic coefficient (**Figure 1B**). For k=3, we performed dimensionality reduction analysis by t-SNE and found that the distribution of the subtypes was largely consistent with the two-dimensional t-SNE distribution pattern (**Figure 1C**). We observed significant prognostic differences among the three subtypes in the TCGA data set (**Figure 1D**). Compared with C2 and C3, C1 had a shorter median survival time (**Figure 1D**). Subsequently, the OV samples from the GEO datasets were used in independent verification, using the aforementioned k=3 classification, which also revealed three different molecular subtypes. Obvious differences between the three subtypes were observed in the GSE63885 (**Figure 1E**) and GSE17260 (**Figure 1F**) datasets, and the overall survival (OS) of the C1 subtype was significantly shorter than that of C2 and C3 subtypes.

Metabolic and Immune Characteristics Among OV Subtypes

Considering that the subtyping of OV samples was based on metabolism-related genes, we used the ssGSEA algorithm to quantitatively analyze the metabolic process. We uncovered multiple metabolic pathways that were significantly different among the three subtypes. Such as, the pathways predominant in the C1 subtype were the inositol phosphate metabolism (some specific metabolic genes: ALDH6A1, CDIPT, IMPA1, IMPA2), reactome inositol phosphate metabolism (some specific metabolic genes: CALM1, IMPA1, IMPA2, INPP1), wp melatonin metabolism and their effects (some specific metabolic genes: AANAT, ACHE, ADRB1, APOE) were significantly higher than the other two subtypes. Also, there were some pathways, certain differences between the C2 and C3 subtypes, such as kegg glyoxylate and dicarboxylate metabolism (some specific metabolic genes: ACO1, ACO2, AFMID, CS), kegg pyrimidine metabolism (some specific metabolic genes: AK3, CAD, CANT1, CDA) and wp pyrimidine metabolism (some specific metabolic genes: CAD, CDA, CMPK1, CMPK2) (**Figure 2A**). We further explored the immune characteristics between different subtypes. First, the immune process was quantified using the ssGSEA algorithm and differential analysis was performed to discover subtype-specific immune characteristics. The results showed that the immune
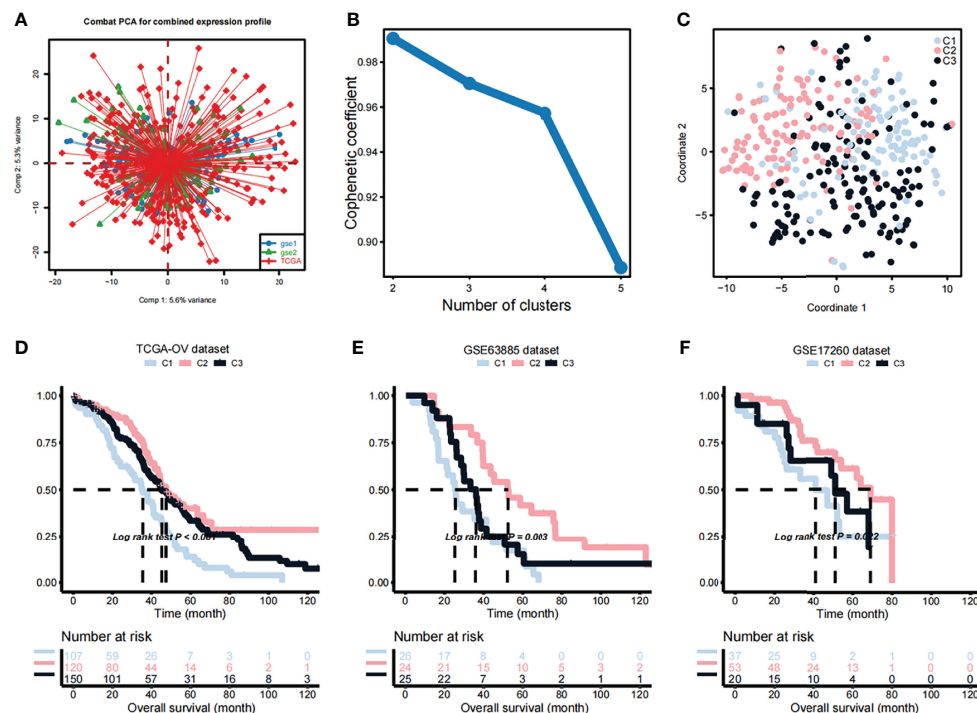
FIGURE 1 | Identification of OV subtypes based on metabolic genes. **(A)** Combat principal component analysis (PCA) was performed to identify the distribution of the expression profiles of genes in the dataset merged TCGA and 2752 metabolism-related genes. **(B)** Cophenetic plot indicating the cophenetic coefficient in function of the number of cluster components. **(C)** Two-dimensional t-SNE distribution pattern distribution in the identified subtypes. **(D)** Differences in the survival probabilities of patients in the identified subtypes based on the TCGA dataset. **(E)** Differences in the survival probabilities of patients in the identified subtypes based on the GSE63885 dataset. **(F)** Differences in the survival probabilities of patients in the identified subtypes based on the GSE17260 dataset.
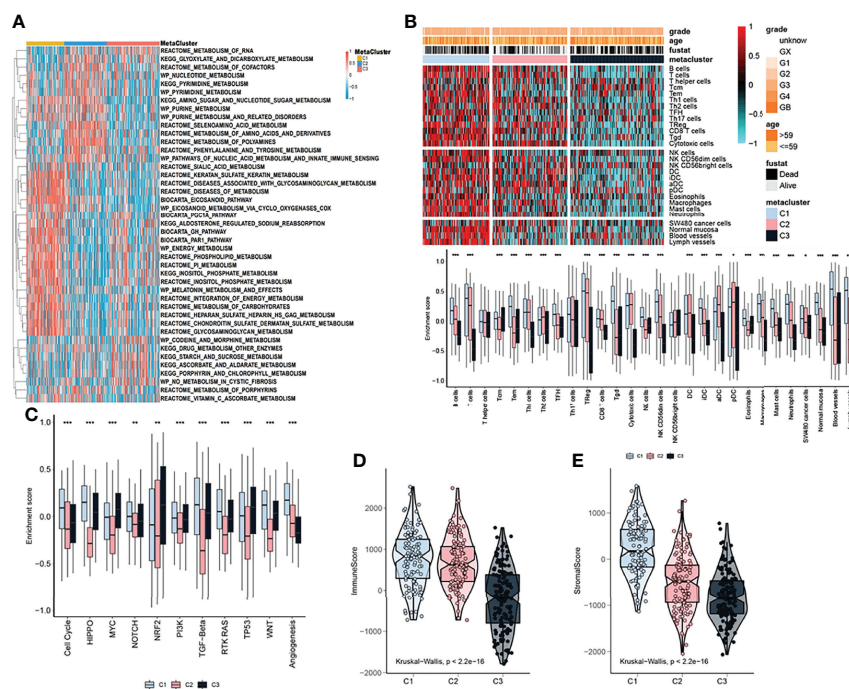
FIGURE 2 | Metabolic and immune characteristics of OV subtypes. **(A)** Heatmap showing that the ssGSEA algorithm quantitatively identified differential metabolic pathways among the identified subtypes. **(B)** Heatmap (upper pane) and boxplot (lower pane) indicating the differences in immune characteristics of the identified subtypes. **(C)** Boxplot showing the differences in pathway enrichment scores among the three identified subtypes. **(D)** Immune score differences among the identified subtypes. **(E)** Stromal score differences among the identified subtypes. The statistical difference was compared through the Kruskal–Wallis test, and the P values are labeled above each boxplot with asterisks (*P < 0.05, **P < 0.01, ***P < 0.001).

characteristics of the three subtypes were clearly classifiable, and differences in the enrichment scores of B cells, Th1 cells, Th2 cells, TFH, Tgd, NK CD56dim cells, macrophages, mast cells, normal mucosa, blood vessels, lymph vessels were significant between C1 and other subtypes (**Figure 2B**). In addition, C1 had higher cell cycle, RTK RAS, WNT, and angiogenesis pathway activation scores than C2 and C3 (**Figure 2C**). Moreover, the ESTIMATE algorithm was used to calculate the immune scores and significant differences in the immune scores were observed between the three groups with the immune score of C3 being significantly lower than that of C1 and C2 (**Figure 2D**). The immune score of C1 was the highest (**Figure 2D**). Meanwhile, the stromal scores showed a tendency similar to that of the immune score (**Figure 2E**).

3.3 Immune Checkpoints in OV Subtypes
Due to the significant differences in the immune scores between the subtypes, the MCP and ssGSEA algorithms were further used to conduct in-depth research on immune infiltration. The abundance of 16 immune-related cell types was calculated using MCP counter and ssGSEA algorithm and displayed in the heatmap (**Figure 3A**). The results showed that there were significant differences in the level of immune infiltration between the three subtypes (**Figure 3A**), suggesting that the immune characteristics of the three subtypes are reproducible. In addition, the enrichment score of T cells, B lineage, monocytic

lineage, myeloid dendritic cells, neutrophils, endothelial cells, fibroblasts, Tcm, Tem and TReg in C1 were higher than in C2 and C3 subtypes.(**Figure 3B**). We further studied the association between the subtypes and the expression of 12 potentially targetable immune checkpoint genes, which were selected based on current inhibitor drugs in clinical trials or drugs approved for specific cancer types, and the results indicated remarkable differences in the expression of these genes between the three subtypes, except for FGL1, CTAG1B and MAGEA4 (**Figure 3C**). The immune checkpoint genes TNFRSF9 showed higher expression in C1 compared to the other two subtypes (**Figure 3C**).

3.4 Correlation Between Clinical Symptoms and Signaling Pathways With OV Subtypes
We further explored the relationship between different subtypes and clinical symptoms in order to reveal their clinicopathological characteristics. Based on the TCGA dataset, the results of the chi-square test showed that the correlation between clinicopathological characteristics and OV subtypes in the TCGA cohort was not obvious (**Figure 4A**). However, in validation set 1 (**Figure 4B**), the proportion of chemotherapy and residuals in the three groups was consistent with the results of KM analysis in **Figures 1E–G** whereas in validation set 2, the grade was higher in C1 (**Figure 4C**). In addition, we used GSEA to analyze the
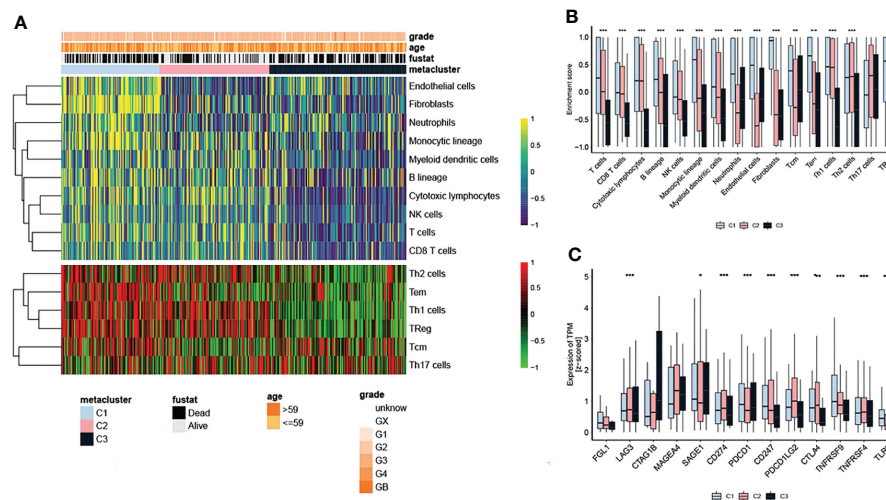
FIGURE 3 | Immune checkpoints in OV subtypes. **(A)** Heatmap showing the level of immune infiltration in the different subtypes. **(B)** Differences in the enrichment score of infiltrated immune cells among the three subtypes. **(C)** Expression of immune checkpoint genes among the three subtypes. The statistical difference was compared through the Kruskal–Wallis test, and the P values are labeled above each boxplot with asterisks (*P < 0.05, **P < 0.01, ***P < 0.001).

differences in signaling pathways between the subtypes. GO analysis results showed that the C1 subtype was mainly enriched in the extracellular matrix structural constituent and collagen binding signaling pathways while the C2 subtype was mainly enriched in the structural constituent of ribosome and ribosomal subunit signaling pathways (**Figure 4D**). The C3 subtype was mainly enriched in microtubule bundle formation, plasma membrane and cell projection cytoplasm signaling pathway (**Figure 4D**). KEGG analysis results showed that the C1 subtype was mainly enriched in the ECM-receptor interaction and focal adhesion signaling pathways (**Figure 4E**). The C2 subtype was mainly enriched in the ribosome and oxidative phosphorylation signaling pathways while the C3 subtype was mainly enriched in basal cell carcinoma and hedgehog signaling pathway signal pathway (**Figure 4E**).

3.5 Mutation Landscape of OV Subtypes

The instability of the genome promotes the accumulation of mutations in cancer cells and leads to the rapid evolution of the cancer genome in response to the tumor microenvironment and treatment-induced related stresses during evolution (26). Detecting and characterizing these tumor somatic mutations has become an important means to analyze the occurrence and development of tumors. In order to study the differences in the frequency of somatic mutations among OV subtypes, and to observe different mutation patterns among OV subtypes, the somatic mutation data from the TCGA database was analyzed. The mutation characteristics among the three subtypes were shown in **Figure 5A**. Most of the mutations in the three subtypes were nonsense mutation, but C2 has fewer mutated genes than C1 and C3 (**Figure 5A**). On the other hand, in a multi-group comparison, the results showed that the C2 subtype had a higher

number of neoantigens than the C1 and C3 subtypes but not significant (**Figure 5B**, P>0.05). Moreover, the tumor mutation burden in the C2 subtype was slightly higher than that of the C1 and C3 subtypes but not significant (**Figure 5C**, P>0.05).

3.6 Performance Verification of Immune Classifiers

After comprehensively considering accuracy and clinical application potential, the top 30 genes with the largest $\log_2 FC$ values in each subtype were selected for the development of subtype classification. Therefore, a 90-gene classifier was generated and visualized (**Figure 6A**). Subsequently, the 90-gene classifier was used to repeat the subtype prediction in the GEO dataset. The results showed a consitency between the NMF and the NTP predicted clusters, confirming that the subtypes were predictable based on the 90-gene classifier (**Figure 6B**). In addition, based on the pRRophetic oftware package, we predicted the sensitivity of each OV subtypes to anticancer drugs. The results showed that the C2 subtype had a lower IC50 for BMS.708163 than C1 and C3, while the C1 subtype had a lower IC50 for AZD6482 than other two subtypes (**Figure 6C**). Moreover, we further based on the data set of melanoma immunotherapy to predict the sensitivity of the three subtypes to anti-tumor immunotherapy. The results showed that the C2 subtype was more sensitive to immunotherapy (**Figure 6D**).

3.7 Significant Difference Gene Analysis

Through the previous subtype analysis, we divided the samples into three subgroups: C1, C2 and C3. We performed difference analysis among subgroups (C1_vs_C2(**Figure 7A**), C3_vs_C1 (**Figure 7B**) and C3_vs_C2(**Figure 7C**) respectively) (|$\log_2 FC$| > 0.585 and. p value < 0.01). According to the Wayne analysis
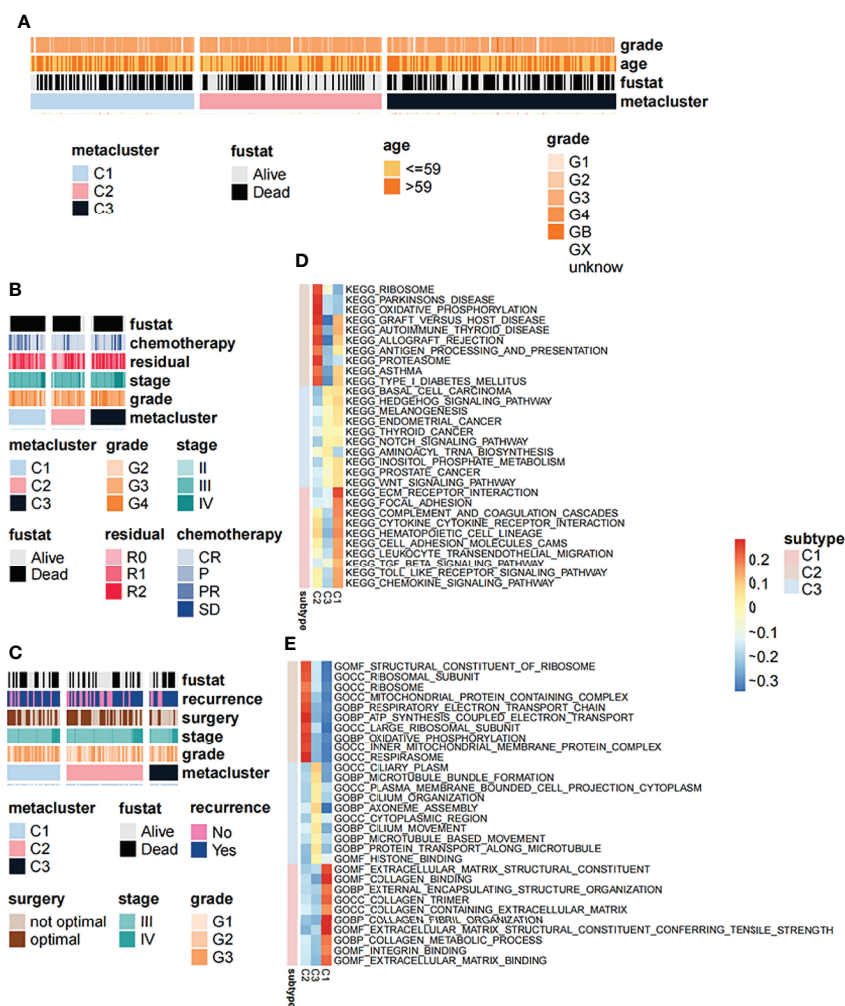
FIGURE 4 | Correlation between clinical symptoms and signaling pathways with OV subtypes. **(A)** Correlation of OV subtypes with age, pathological stage, grade and survival of OV patients in TCGA dataset. **(B)** Correlation of OV subtypes with age, pathological stage, grade and survival of OV patients in GSE63885 dataset. **(C)** Correlation of OV subtypes with age, pathological stage, grade, tumor recurrence and survival of OV patient in GSE17260 dataset. **(D)** Differences in gene ontology enrichment functional terms among the three subtypes. **(E)** Differences in KEGG enrichment functional pathways among the three subtypes.

(**Figure 7D**), 1111 genes were differentially expressed between C2 and C1 groups; 1064 genes were differentially expressed between C3 and C1 groups; 1127 genes were differentially expressed between C3 and C2 groups. In the three differential analysis, 67 genes were differentially expressed at the same time. Finally, we analyzed the survival of these 67 genes and found that the expression of two genes was very significant in the survival analysis (p value < 0.01). The sequence is CXCL11(**Figure 7E**) and PXDN (**Figure 7F**).

3.8 Association Between the Expression of CXCL11 and PXDN and the Progression of OV

We used immunohistochemistry to stain the tissue chip, and then scored according to the staining intensity and staining area. **Figure 8A** shows the staining corresponding to different scores.

After comparing the score with the patient information, we found that the expression of PXDN was inversely proportional to the tumor size (**Figure 8B**) and H-score increases with the increase of pathological grade positively correlated with the pathological grade (**Figure 8D**). The expression of CXCL11 was inversely proportional to the tumor size (**Figure 8C**), while the H-score was no correlation with the pathological grade (**Figure 8E**). Furthermore, it was found that there was an inverse correlation between tumor size and pathological grade (**Figure 8F**).

4 DISCUSSION

The present study was devoted to the discovery of novel OV subtypes and their clinical value based on metabolic features. A
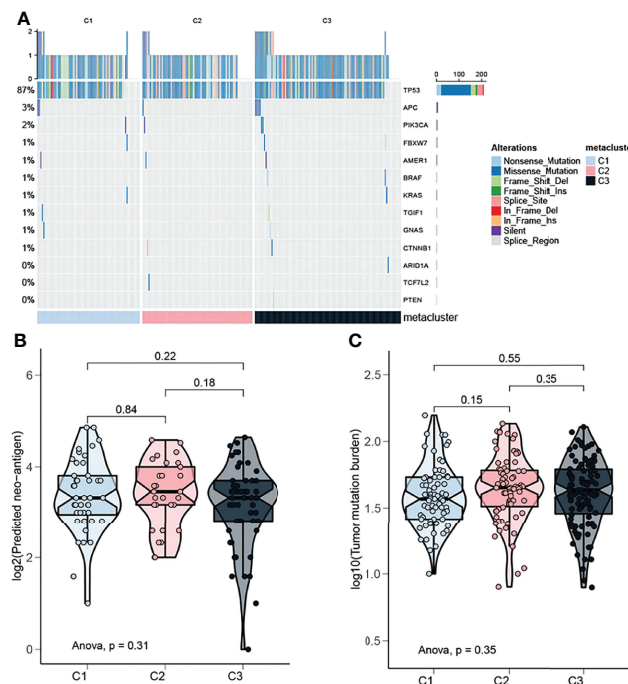
FIGURE 5 | Mutation landscape of OV subtypes. **(A)** Oncoplot showing the distribution of mutated genes in the identified OV subtypes. **(B)** Proportion of neoantigens in the different subtypes. **(C)** Proportion of tumor mutation burden in the different subtypes.

list of 2752 metabolism-related genes, previously reported in the literature, were used as a seed for NMF clustering. We identified three OV subtypes based on our clustering approach and on the expression of 177 prognostic-related metabolic genes identified by cox regression analysis. C1 had a shorter median survival time, higher cell cycle, RTK, RAS, WNT, and angiogenesis pathway activation scores and the pathway predominantly affected in this subtype was the inositol phosphate metabolism pathway, and the inositol phosphate metabolism pathway involved in cell proliferation, migration and phosphatidylinositol-3-kinase (PI3K)/Akt signaling, play a crucial in cancer and are frequently dysregulated in cancer (27). According to KEGG pathway map analysis, we found that the inositol phosphate metabolism pathway which C1 enriched in, aldehyde dehydrogenase 6 family member A1 (ALDH6A1) overexpressed the Acetyl coenzyme A (CoA). Researcher found that in highly proliferating cancer cells, the intermediate of the TCA cycle is rapidly consumed (28). In the inositol phosphate metabolism pathway, the CoA participates in the next pathway TCA cycle which increases the synthesis of the intermediate of the TCA cycle and accelerates cell proliferation. While the Glyoxylate and dicarboxylate metabolism pathway which C2 enriched in, acyl-CoA synthetase short chain family member 2(ACSS2) was involved in the activation of Acetyl coenzyme A and the fatty acid degradation pathway can indirectly promote the process and researchers have found that ACSS2 activates the CoA under metabolic stress to encourage the tumor cells to use acetic acid

as an additional nutrient source that allows the tumor cells to adapt to the harsh metabolic environment and keep the tumor cells alive (29). These processes maybe work together to promote OV occurrence. Significant differences in the enrichment scores of B cells, Th1 cells, Th2 cells, TFH, Tgd, NK CD56dim cells, macrophages, mast cells, normal mucosa, blood vessels and lymph vessels were observed between C1 and the other subtypes which was reflected by higher immune and stromal scores associated with C1. Differences in the expression of immune checkpoint genes were recorded between the three subtypes, with TNFRSF9 being significantly and highly expressed in C1 compared to the other subtypes. The pathways mostly in play were ECM-receptor interaction and focal adhesion signaling pathways in the C1 subtype, ribosome and oxidative phosphorylation signaling pathways in the C2 subtype and basal cell carcinoma and hedgehog signaling pathway signal pathway in C3 subtype. Differences in gene mutations were observed among the three subtypes. Moreover, the C1 subtype was more sensitive to drugs AZD6482, and C2 subtype was more sensitive to drugs BMS.708163, this evidence may provide a hint for future treatment.

Immune score has been reported as an important prognostic and indicator of chemosensitivity for OV (30, 31). Here, the three subtypes identified showed significant differences in immune score, and the highest immune score was recorded in C1. We anticipated that C1 was the highest risk score subtype, which was in corroboration with previous findings indicating that higher
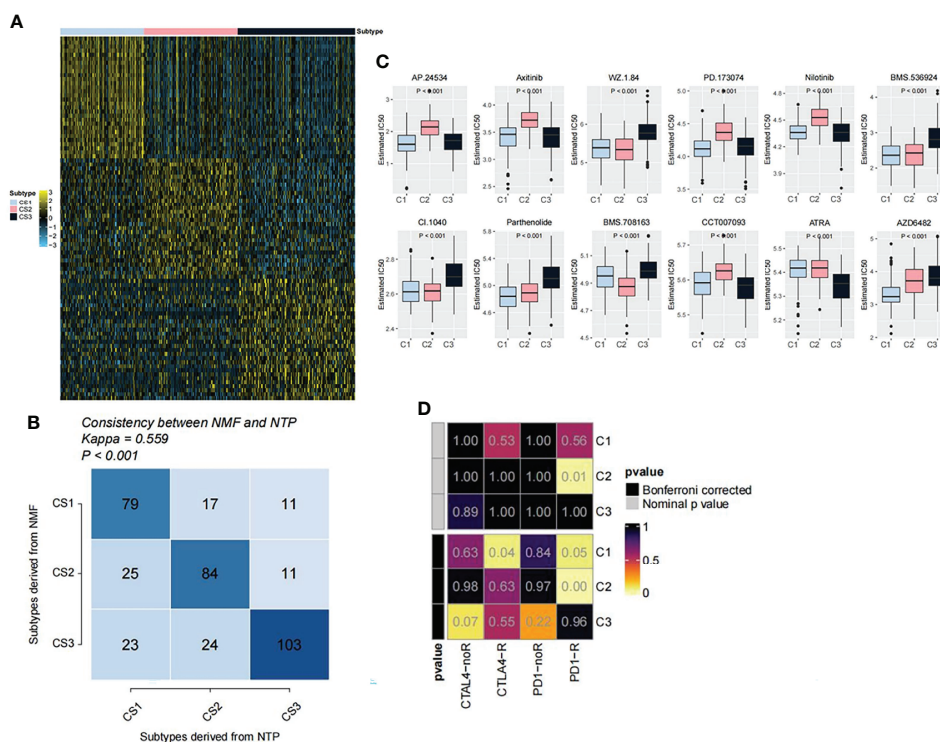
FIGURE 6 | Performance verification of immune classifiers. **(A)** Heatmap showing the classification of the 90-gene classifier for OV subtypes. **(B)** Correlation between NTP classification and NMF classification. **(C)** Drug sensitivity analysis of OV subtypes. **(D)** Prediction of the sensitivity of the three subtypes to anti-tumor immunotherapy.

risk score subtypes are correlated with higher immune score (32–34). This observation was further supported by the increase of immune cells in C1 subtype compared to C2 and C3. Indeed, the increased proportions of B cells, CD8+ T cells, NK cells, cytotoxic lymphocytes, Neutrophils, monocytic lineage, Th2 cells, Tem and Treg cells in the C1 subtype indicated increased recruitment of immune cells to counteract the pathological status in OV patients. Moreover, obviously higher levels of fibroblasts and endothelial cells were observed in the C1 subtype of OV. Studies have conveyed that the stromal compartment is also associated with the prognostic outcome (35–37), which supports the increased stromal score observed in the present study. As important elements of the stromal compartment, the cancer-associated fibroblasts (CAFs) constitute a determinant repertoire in the regulation of the cancer cell proliferation, invasion and metastasis and are associated with poor prognostication of tumors, especially after treatment (37–42). In addition, endothelial cells are known for their involvement in cancer angiogenesis. The increased levels of endothelial cells in the C1 subtype further confirmed the high-risk score status of this subtype. The other C2 and C3 groups could be classified in the medium and low risk score subtypes, but the heterogeneity of cell enrichment scores in these subtypes renders this conclusion somehow difficult.

TNFRSF9 is an important check point in cancer immunotherapy. However, as stated in previous studies, the

significance of TNFRSF9 in cancer is not clear, but it was suggested to be immunosuppressive (43–46). Increased expression of TNFRSF9 was observed in platinum resistant ovarian tumors (27, 47, 48), which implies that this gene may promote tumor progression. In this study, we found that the expression level of TNFRSF9 was the highest in the C1 subtype, which make us suspected the high expression of TNFRSF9 may have something to do with the low survival of C1 subtype.

The mechanism OV in C1 subtype patients chiefly involved inositol phosphate metabolism pathway, indicating poor prognosis when contrasted with C2 and C3. Indeed, genes participating in the inositol phosphate metabolism pathway have been incriminated in cancer risk and known to be regulators of cell cycle, metastasis and PI3K/Akt signaling (49).

The enrichment in metabolic signatures showed significant enrichment of a large number of pathways in C1 patients, indicating that this subtype may be more sensitive to metabolic therapies, which have been proven efficient in cancer chemotherapy (50). However, due to the huge number of enriched pathways, additional experimental works are needed to confirm the most important pathways. Up to now, several metabolism-targeting drugs for OV have been developed and evaluated in clinical trials. These drugs include those targeting the hexokinases in glycolysis pathway (2-deoxy glucose, 3-bromopyruvate, lonidamine, methyl jasmonate), PDK1 in
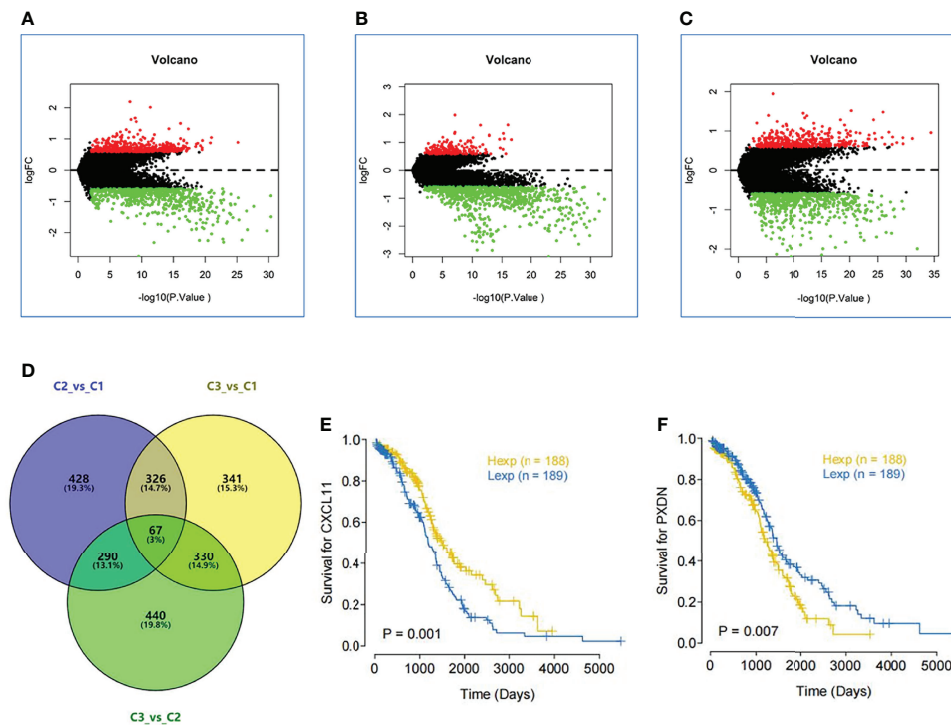
FIGURE 7 | Significant difference gene analysis. **(A)** Different expression analysis among subgroups C1 vs C2. **(B)** Different expression analysis among subgroups C3 vs C1. **(C)** Different expression analysis among subgroups C3 vs C2.($|\log_2FC|$ > 0.585 and. p value < 0.01). **(D)** Wayne analysis shows mount of different expression gene in three subgroups. **(E)** The survival curve of the different expression of CXCL11. **(F)** The survival curve of the different expression of PXDN.

Krebs cycle (dichloroacetate), LDH and Bcl-xL in the Bcl-xL pathway (Gossypol) and mitochondria complex I in the mitochondrial respiration pathway (metformin) (51). However, the efficacy of these drugs is questionable due to their side effects or broad range of targets. Here, the classification of OV in different subtypes may potentiate metabolic therapies due to the accurate knowledge of metabolic profiles of OV patients. Especially, we found that drugs targeting genes in pathways such as energy metabolism, inositol phosphate metabolism, metabolism of carbohydrates, melatonin metabolism, glycosaminoglycan metabolism, keratan sulfate/keratin metabolism, eicosanoid metabolism *via* cyclo-oxygenases cox, PGC1a pathway, aldosterone regulated sodium reabsorption, phospholipid metabolism and PAR1 pathway may be efficient for the treatment of patients classified in the C1 OV subtype identified in this study. For the C2 OV subtype, drugs targeting the selenoamino acid metabolism, metabolism of amino acids and derivatives, metabolism of polyamines, phenylalanine and tyrosine metabolism, pathways of nucleic acid metabolism and innate immune sensing and metabolism of cofactors may be potential metabolic drugs. In tissue microarray staining, we found that the relationship between PXDN and tumor size and pathological grade showed an opposite trend, but the literature described that PXDN was positively correlated with tumor proliferation (52). This contradictory phenomenon may be due

to the limited sample size of this study and need for more in-depth research on the influence of PXDN on tumor size and pathological grade in the future. CXCL11 shows no difference in the chip, possibly because the sample size is too small and needs to be increased to continue the analysis.

In pathway enrichment analysis, we found that ECM-receptor interaction pathway was mainly enriched in patients classified in the C1 subtype. This pathway is an integral part of malignant microenvironments and regulates homeostasis. Studies have implicated the dysregulation of ECM components in OV tumorigenesis and progression and suggested that the elucidation of ECM function in OV is important for developing effective biomarkers and novel drugs (53–57). Studies have also shown that the potential biomarkers of OV metastasis are enriched in ECM-receptor interaction pathway (57) among other pathways including PI3K/Akt signaling pathway which was also found implicated in the inositol phosphate metabolism as described above. ECM-receptor interaction pathway was also incriminated in the survival and prognosis of high-grade serous OV patients (58–60). ECM-Receptor pathway was similarly reported to be enriched in C1 in a previous classification of OV patients based on energy-metabolism related genes (51).

In conclusion, this proposed a metabolism-related molecular classification of OV patients and identified three subtypes
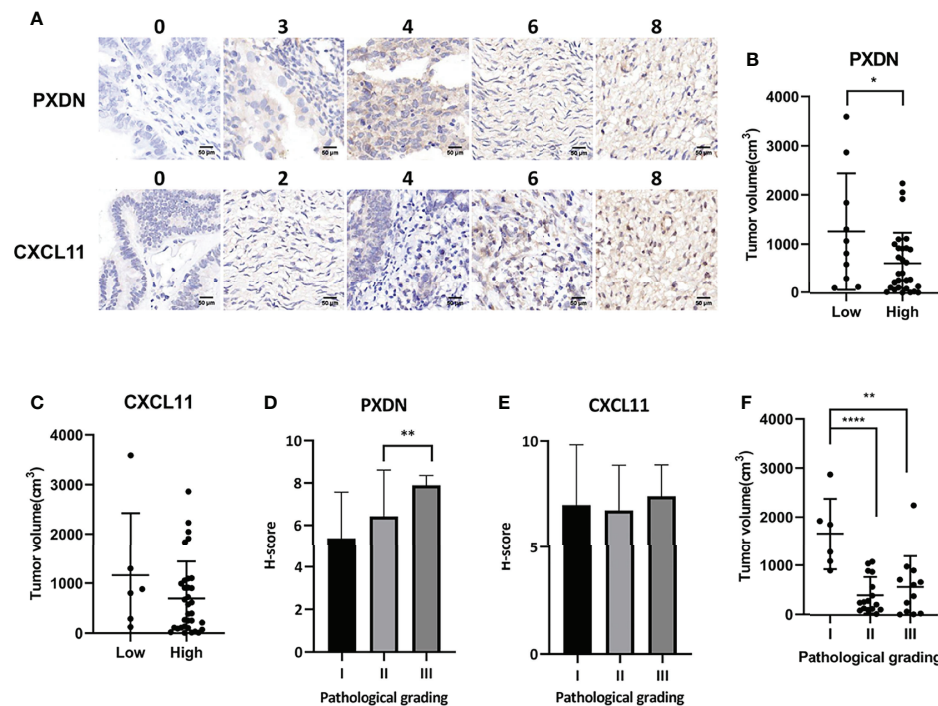
FIGURE 8 | Association between the expression of CXCL11 and PXDN and the progression of OV. **(A)** We divided two subgroups in each gene: PXDN high group (n=51); PXDN low group(n=14); CXCL11 high group(n=54); CXCL11 low group(n=11). Results shows the staining corresponding to different scores. **(B)** The relationship between tumor size and the expression of PXDN. **(C)** The relationship between tumor size and the expression of CXCL11. **(D)** The correlation between H-score and Pathological grade of PXDN. **(E)** The correlation between H-score and Pathological grade of CXCL11. **(F)** There was an inverse correlation between tumor size and pathological grade. Error bars, SD. *$P < 0.05$, **$P < 0.01$, ****$P < 0.0001$.

characterized by active, medium, or low metabolic activities, respectively. C1 showed low survival probability while C2 showed high sensitivity to immune blockade and chemotherapy. C3 had high heterogeneity and may be further investigated. Our classification system may display predictive value for the prognosis of OV patients and discovery of novel therapies.

DATA AVAILABILITY STATEMENT

The original contributions presented in the study are included in the article/**Supplementary Material**. Further inquiries can be directed to the corresponding author.

ETHICS STATEMENT

The studies involving human participants were reviewed and approved by Shanghai outdo biotech company. The patients/participants provided their written informed consent to participate in this study. Written informed consent was obtained from the individual(s) for the publication of any potentially identifiable images or data included in this article.

AUTHOR CONTRIBUTIONS

ZC and GD conceived and designed the experiments. WJ, ZL, and YZ analyzed the data and prepared the figures. ZC wrote the main manuscript text. All authors contributed to the article and approved the submitted version.

ACKNOWLEDGMENTS

We sincerely thank all staff of Lingnan Medical Resarch Center, Guangzhou University of Chinese Medicine for participating in and supporting this study.

SUPPLEMENTARY MATERIAL

The Supplementary Material for this article can be found online at: https://www.frontiersin.org/articles/10.3389/fonc.2022.877369/full#supplementary-material

Supplementary Figure 1 | The flowchart of the study design.

Additional File S1 | List of potential prognostic genes.

REFERENCES

1. Stewart C, Ralyea C, Lockwood S. Ovarian Cancer: An Integrated Review. *Semin Oncol Nurs* (2019) 35(2):151–6. doi: 10.1016/j.soncn.2019.02.001

2. Banerjee S, Rustin G, Paul J, Williams C, Pledge S, Gabra H, et al. A Multicenter, Randomized Trial of Flat Dosing Versus Intrapatient Dose Escalation of Single-Agent Carboplatin as First-Line Chemotherapy for Advanced Ovarian Cancer: An Sgctg (Scotroc 4) and Anzgog Study on Behalf of Gcig. *Ann Oncol* (2013) 24(3):679–87. doi: 10.1093/annonc/mds494

3. Coleman RL, Oza AM, Lorusso D, Aghajanian C, Oaknin A, Dean A, et al. Rucaparib Maintenance Treatment for Recurrent Ovarian Carcinoma After Response to Platinum Therapy (Ariel3): A Randomised, Double-Blind, Placebo-Controlled, Phase 3 Trial. *Lancet* (2017) 390(10106):1949–61. doi: 10.1016/S0140-6736(17)32440-6

4. Jayson GC, Kohn EC, Kitchener HC, Ledermann JA. Ovarian Cancer. *Lancet* (2014) 384(9951):1376–88. doi: 10.1016/S0140-6736(13)62146-7

5. Clamp AR, James EC, McNeish IA, Dean A, Kim JW, O'Donnell DM, et al. Weekly Dose-Dense Chemotherapy in First-Line Epithelial Ovarian, Fallopian Tube, or Primary Peritoneal Carcinoma Treatment (Icon8): Primary Progression Free Survival Analysis Results From a Gcig Phase 3 Randomised Controlled Trial. *Lancet* (2019) 394(10214):2084–95. doi: 10.1016/S0140-6736(19)32259-7

6. Mi X, Zou B, Zou F, Hu J. Permutation-Based Identification of Important Biomarkers for Complex Diseases *Via* Machine Learning Models. *Nat Commun* (2021) 12(1):3008. doi: 10.1038/s41467-021-22756-2

7. Garmpis N, Damaskos C, Garmpi A, Nikolettos K, Dimitroulis D, Diamantis E, et al. Molecular Classification and Future Therapeutic Challenges of Triple-Negative Breast Cancer. *In Vivo* (2020) 34(4):1715–27. doi: 10.21873/invivo.11965

8. Akoury E, Ma G, Demolin S, Bronner C, Zocco M, Cirilo A, et al. Disordered Region of H3k9 Methyltransferase Clr4 Binds the Nucleosome and Contributes to Its Activity. *Nucleic Acids Res* (2019) 47(13):6726–36. doi: 10.1093/nar/gkz480

9. Gainor JF, Shaw AT. Emerging Paradigms in the Development of Resistance to Tyrosine Kinase Inhibitors in Lung Cancer. *J Clin Oncol* (2013) 31 (31):3987–96. doi: 10.1200/JCO.2012.45.2029

10. Sheils O. Molecular Classification and Biomarker Discovery in Papillary Thyroid Carcinoma. *Expert Rev Mol Diagn* (2005) 5(6):927–46. doi: 10.1586/14737159.5.6.927

11. Disis ML, Taylor MH, Kelly K, Beck JT, Gordon M, Moore KM, et al. Efficacy and Safety of Avelumab for Patients With Recurrent or Refractory Ovarian Cancer: Phase 1b Results From the Javelin Solid Tumor Trial. *JAMA Oncol* (2019) 5(3):393–401. doi: 10.1001/jamaoncol.2018.6258

12. Zhang Z, Huang K, Gu C, Zhao L, Wang N, Wang X, et al. Molecular Subtyping of Serous Ovarian Cancer Based on Multi-Omics Data. *Sci Rep* (2016) 6:26001. doi: 10.1038/srep26001

13. Lo Gullo R, Daimiel I, Morris EA, Pinker K. Combining Molecular and Imaging Metrics in Cancer: Radiogenomics. *Insights Imaging* (2020) 11(1):1. doi: 10.1186/s13244-019-0795-6

14. Cho SY, Kim K, Park MS, Jang MY, Choi YH, Han S, et al. Expression of Yes-Associated Protein 1 and Its Clinical Significance in Ovarian Serous Cystadenocarcinoma. *Oncol Rep* (2017) 37(5):2620–32. doi: 10.3892/or.2017.5517

15. Leong HS, Galletta L, Etemadmoghadam D, George JAustralian Ovarian Cancer S, , Kobel M, et al. Efficient Molecular Subtype Classification of High-Grade Serous Ovarian Cancer. *J Pathol* (2015) 236(3):272–7. doi: 10.1002/path.4536

16. Feng Z, Wen H, Bi R, Ju X, Chen X, Yang W, et al. A Clinically Applicable Molecular Classification for High-Grade Serous Ovarian Cancer Based on Hormone Receptor Expression. *Sci Rep* (2016) 6:25408. doi: 10.1038/srep25408

17. Cybulska P, Paula ADC, Tseng J, Leitao MM Jr, Bashashati A, Huntsman DG, et al. Molecular Profiling and Molecular Classification of Endometrioid Ovarian Carcinomas. *Gynecol Oncol* (2019) 154(3):516–23. doi: 10.1016/j.ygyno.2019.07.012

18. Bodelon C, Killian JK, Sampson JN, Anderson WF, Matsuno R, Brinton LA, et al. Molecular Classification of Epithelial Ovarian Cancer Based on Methylation Profiling: Evidence for Survival Heterogeneity. *Clin Cancer Res* (2019) 25(19):5937–46. doi: 10.1158/1078-0432.CCR-18-3720

19. Klein O, Kanter F, Kulbe H, Jank P, Denkert C, Nebrich G, et al. Maldi-Imaging for Classification of Epithelial Ovarian Cancer Histotypes From a Tissue Microarray Using Machine Learning Methods. *Proteomics Clin Appl* (2019) 13(1):e1700181. doi: 10.1002/prca.201700181

20. Furuta E, Okuda H, Kobayashi A, Watabe K. Metabolic Genes in Cancer: Their Roles in Tumor Progression and Clinical Implications. *Biochim Biophys Acta* (2010) 1805(2):141–52. doi: 10.1016/j.bbcan.2010.01.005

21. Yang C, Huang X, Liu Z, Qin W, Wang C. Metabolism-Associated Molecular Classification of Hepatocellular Carcinoma. *Mol Oncol* (2020) 14(4):896–913. doi: 10.1002/1878-0261.12639

22. Zhang M, Wang HZ, Peng RY, Xu F, Wang F, Zhao Q. Metabolism-Associated Molecular Classification of Colorectal Cancer. *Front Oncol* (2020) 10:602498. doi: 10.3389/fonc.2020.602498

23. Wang L, Li X. Identification of an Energy Metabolism-Related Gene Signature in Ovarian Cancer Prognosis. *Oncol Rep* (2020) 43(6):1755–70. doi: 10.3892/or.2020.7548

24. Rooney MS, Shukla SA, Wu CJ, Getz G, Hacohen N. Molecular and Genetic Properties of Tumors Associated With Local Immune Cytolytic Activity. *Cell* (2015) 160(1-2):48–61. doi: 10.1016/j.cell.2014.12.033

25. Possemato R, Marks KM, Shaul YD, Pacold ME, Kim D, Birsoy K, et al. Functional Genomics Reveal That the Serine Synthesis Pathway Is Essential in Breast Cancer. *Nature* (2011) 476(7360):346–50. doi: 10.1038/nature10350

26. Smith J, Tho LM, Xu N, Gillespie DA. The Atm-Chk2 and Atr-Chk1 Pathways in DNA Damage Signaling and Cancer. *Adv Cancer Res* (2010) 108:73–112. doi: 10.1016/B978-0-12-380888-2.00003-0

27. Tan J, Yu CY, Wang ZH, Chen HY, Guan J, Chen YX, et al. Genetic Variants in the Inositol Phosphate Metabolism Pathway and Risk of Different Types of Cancer. *Sci Rep* (2015) 5:8473. doi: 10.1038/srep08473

28. Leone RD, Powell JD. Metabolism of Immune Cells in Cancer. *Nat Rev Cancer* (2020) 20(9):516–31. doi: 10.1038/s41568-020-0273-y

29. Schug ZT, Peck B, Jones DT, Zhang Q, Grosskurth S, Alam IS, et al. Acetyl-Coa Synthetase 2 Promotes Acetate Utilization and Maintains Cancer Cell Growth Under Metabolic Stress. *Cancer Cell* (2015) 27(1):57–71. doi: 10.1016/j.ccell.2014.12.002

30. Hao D, Liu J, Chen M, Li J, Wang L, Li X, et al. Immunogenomic Analyses of Advanced Serous Ovarian Cancer Reveal Immune Score Is a Strong Prognostic Factor and an Indicator of Chemosensitivity. *Clin Cancer Res* (2018) 24(15):3560–71. doi: 10.1158/1078-0432.CCR-17-3862

31. Liu W, Ye H, Liu YF, Xu CQ, Zhong YX, Tian T, et al. Transcriptome-Derived Stromal and Immune Scores Infer Clinical Outcomes of Patients With Cancer. *Oncol Lett* (2018) 15(4):4351–7. doi: 10.3892/ol.2018.7855

32. Cao T, Shen H. Development of a Multi-Gene-Based Immune Prognostic Signature in Ovarian Cancer. *J Ovarian Res* (2021) 14(1):20. doi: 10.1186/s13048-021-00766-4

33. Calura E, Ciciani M, Sambugaro A, Paracchini L, Benvenuto G, Milite S, et al. Transcriptional Characterization of Stage I Epithelial Ovarian Cancer: A Multicentric Study. *Cells* (2019) 8(12). doi: 10.3390/cells8121554

34. Thakar MS, Broglie L, Logan B, Artz A, Bunin N, Burroughs LM, et al. The Hematopoietic Cell Transplant Comorbidity Index Predicts Survival After Allogeneic Transplant for Nonmalignant Diseases. *Blood* (2019) 133(7):754–62. doi: 10.1182/blood-2018-09-876284

35. Sun X, Shan Y, Li Q, Chollet-Hinton L, Kirk EL, Gierach GL, et al. Intra-Individual Gene Expression Variability of Histologically Normal Breast Tissue. *Sci Rep* (2018) 8(1):9137. doi: 10.1038/s41598-018-27505-y

36. Uso M, Jantus-Lewintre E, Bremnes RM, Calabuig S, Blasco A, Pastor E, et al. Analysis of the Immune Microenvironment in Resected Non-Small Cell Lung Cancer: The Prognostic Value of Different T Lymphocyte Markers. *Oncotarget* (2016) 7(33):52849–61. doi: 10.18632/oncotarget.10811

37. Paulsson J, Micke P. Prognostic Relevance of Cancer-Associated Fibroblasts in Human Cancer. *Semin Cancer Biol* (2014) 25:61–8. doi: 10.1016/j.semcancer.2014.02.006

38. Gu J, Li X, Zhao L, Yang Y, Xue C, Gao Y, et al. The Role of Pkm2 Nuclear Translocation in the Constant Activation of the Nf-Kappab Signaling Pathway in Cancer-Associated Fibroblasts. *Cell Death Dis* (2021) 12(4):291. doi: 10.1038/s41419-021-03579-x

39. Fang Z, Xu J, Zhang B, Wang W, Liu J, Liang C, et al. The Promising Role of Noncoding Rnas in Cancer-Associated Fibroblasts: An Overview of Current Status and Future Perspectives. *J Hematol Oncol* (2020) 13(1):154. doi: 10.1186/s13045-020-00988-x

40. Barnhoorn MC, Hakuno SK, Bruckner RS, Rogler G, Hawinkels L, Scharl M. Stromal Cells in the Pathogenesis of Inflammatory Bowel Disease. *J Crohns Colitis* (2020) 14(7):995–1009. doi: 10.1093/ecco-jcc/jjaa009

41. Xu Z, Zheng X, Zheng J. Tumor-Derived Exosomes Educate Fibroblasts to Promote Salivary Adenoid Cystic Carcinoma Metastasis *Via* Ngf-Ntrk1 Pathway. *Oncol Lett* (2019) 18(4):4082–91. doi: 10.3892/ol.2019.10740

42. Saigusa S, Toiyama Y, Tanaka K, Yokoe T, Okugawa Y, Fujikawa H, et al. Cancer-Associated Fibroblasts Correlate With Poor Prognosis in Rectal Cancer After Chemoradiotherapy. *Int J Oncol* (2011) 38(3):655–63. doi: 10.3892/ijo.2011.906

43. Meng Q, Li CX, Long D. Cars as a Prognosis Factor in Clear Cell Renal Cell Carcinoma and Its Association With Tumor Immunity. *Int J Gen Med* (2021) 14:3197–211. doi: 10.2147/IJGM.S318278

44. Huo Y, Sheng Z, Lu DR, Ellwanger DC, Li CM, Homann O, et al. Blinatumomab-Induced T Cell Activation at Single Cell Transcriptome Resolution. *BMC Genomics* (2021) 22(1):145. doi: 10.1186/s12864-021-07435-2

45. Xie M, Wei J, Xu J. Inducers, Attractors and Modulators of Cd4(+) Treg Cells in Non-Small-Cell Lung Cancer. *Front Immunol* (2020) 11:676. doi: 10.3389/fimmu.2020.00676

46. Glorieux C, Huang P. Cd137 Expression in Cancer Cells: Regulation and Significance. *Cancer Commun (Lond)* (2019) 39(1):70. doi: 10.1186/s40880-019-0419-z

47. Mairinger F, Bankfalvi A, Schmid KW, Mairinger E, Mach P, Walter RF, et al. Digital Immune-Related Gene Expression Signatures in High-Grade Serous Ovarian Carcinoma: Developing Prediction Models for Platinum Response. *Cancer Manag Res* (2019) 11:9571–83. doi: 10.2147/CMAR.S219872

48. Riera Leal A, Ortiz-Lazareno PC, Jave-Suarez LF, Ramirez De Arellano A, Aguilar-Lemarroy A, Ortiz-Garcia YM, et al. 17betaestradiolinduced Mitochondrial Dysfunction and Warburg Effect in Cervical Cancer Cells Allow Cell Survival Under Metabolic Stress. *Int J Oncol* (2020) 56(1):33–46. doi: 10.3892/ijo.2019.4912

49. Cai S, Ma J, Wang Y, Cai Y, Xie L, Chen X, et al. Biomarker Value of Mir-221 and Mir-222 as Potential Substrates in the Differential Diagnosis of Papillary Thyroid Cancer Based on Data Synthesis and Bioinformatics Approach. *Front Endocrinol (Lausanne)* (2021) 12:794490. doi: 10.3389/fendo.2021.794490

50. Luengo A, Gui DY, Vander Heiden MG. Targeting Metabolism for Cancer Therapy. *Cell Chem Biol* (2017) 24(9):1161–80. doi: 10.1016/j.chembiol.2017.08.028

51. Han CY, Patten DA, Richardson RB, Harper ME, Tsang BK. Tumor Metabolism Regulating Chemosensitivity in Ovarian Cancer. *Genes Cancer* (2018) 9(5-6):155–75. doi: 10.18632/genesandcancer.176

52. Kurihara-Shimomura M, Sasahira T, Shimomura H, Kirita T. Peroxidan Plays a Tumor-Promoting Role in Oral Squamous Cell Carcinoma. *Int J Mol Sci* (2020) 21(15). doi: 10.3390/ijms21155416

53. Zhang S, Xie Y, Tian T, Yang Q, Zhou Y, Qiu J, et al. High Expression Levels of Centromere Protein a Plus Upregulation of the Phosphatidylinositol 3-Kinase/Akt/Mammalian Target of Rapamycin Signaling Pathway Affect Chemotherapy Response and Prognosis in Patients With Breast Cancer. *Oncol Lett* (2021) 21(5):410. doi: 10.3892/ol.2021.12671

54. Alkmin S, Brodziski R, Simon H, Hinton D, Goldsmith RH, Patankar M, et al. Role of Collagen Fiber Morphology on Ovarian Cancer Cell Migration Using Image-Based Models of the Extracellular Matrix. *Cancers (Basel)* (2020) 12(6). doi: 10.3390/cancers12061390

55. Yue H, Wang J, Chen R, Hou X, Li J, Lu X. Gene Signature Characteristic of Elevated Stromal Infiltration and Activation Is Associated With Increased Risk of Hematogenous and Lymphatic Metastasis in Serous Ovarian Cancer. *BMC Cancer* (2019) 19(1):1266. doi: 10.1186/s12885-019-6470-y

56. Cho A, Howell VM, Colvin EK. The Extracellular Matrix in Epithelial Ovarian Cancer - A Piece of a Puzzle. *Front Oncol* (2015) 5:245. doi: 10.3389/fonc.2015.00245

57. Kim MS, Ha SE, Wu M, Zogg H, Ronkon CF, Lee MY, et al. Extracellular Matrix Biomarkers in Colorectal Cancer. *Int J Mol Sci* (2021) 22(17). doi: 10.3390/ijms22179185

58. Abdul Pari AA, Singhal M, Augustin HG. Emerging Paradigms in Metastasis Research. *J Exp Med* (2021) 218(1). doi: 10.1084/jem.20190218

59. Tassi RA, Gambino A, Ardighieri L, Bignotti E, Todeschini P, Romani C, et al. Fxyd5 (Dysadherin) Upregulation Predicts Shorter Survival and Reveals Platinum Resistance in High-Grade Serous Ovarian Cancer Patients. *Br J Cancer* (2019) 121(7):584–92. doi: 10.1038/s41416-019-0553-z

60. Li S, Li H, Xu Y, Lv X. Identification of Candidate Biomarkers for Epithelial Ovarian Cancer Metastasis Using Microarray Data. *Oncol Lett* (2017) 14(4):3967–74. doi: 10.3892/ol.2017.6707

Single-Cell Proteomics Analysis of Recurrent Low-Grade Serous Ovarian Carcinoma and Associated Brain Metastases

Tanja Pejovic[1]*, Pierre-Valérien Abate[2,3], Hongli Ma[1], Jaclyn Thiessen[4], Christopher L. Corless[1], Abigail Peterson[1], Hugues Allard-Chamard[5] and Marilyne Labrie[2,3]*

[1] Knight Cancer Institute, Oregon Health & Science University, Portland, OR, United States, [2] Department of Immunology and Cell Biology, Université de Sherbrooke, Sherbrooke, QC, Canada, [3] Department of Obstetrics and Gynecology, Université de Sherbrooke, Sherbrooke, QC, Canada, [4] Department of Diagnostic Radiology, Oregon Health & Science University, Portland, OR, United States, [5] Service of Rheumatology, Department of Medicine, Université de Sherbrooke, Sherbrooke, QC, Canada

Between 2% and 6% of epithelial ovarian cancer (EOC) patients develop brain metastases (brain mets), which are incurable and invariably result in death. This poor outcome is associated with a lack of established guidelines for the detection and treatment of brain mets in EOC patients. In this study, we characterize an unusual case of low-grade serous ovarian carcinoma (LGSOC) that metastasized to the brain. Using a spatially oriented single-cell proteomics platform, we compared sequential biopsies of a primary tumor with a peritoneal recurrence and brain mets. We identified several targetable oncogenic pathways and immunosuppressive mechanisms that are amplified in the brain mets and could be involved in the progression of LGSOC to the brain. Furthermore, we were able to identify cell populations that are shared between the primary tumor and the brain mets, suggesting that cells that have a propensity for metastasis to the brain could be identified early during the course of disease. Taken together, our findings further a path for personalized therapeutic decisions in LGSOC.

Keywords: low-grade serous ovarian cancer, single-cell proteomics, cyclic immunofluorescence, spatial analysis, brain metastases

INTRODUCTION

The incidence of brain metastases (brain mets) in epithelial ovarian cancer (EOC) patients is about 2%–6% and invariably results in death (1). This represents a clinical challenge, since there are currently no established guidelines for the detection and treatment of this severe and irreversible condition (2–7). Previous studies in EOC have shown that brain mets display a unique phenotype and do not respond to systemic therapy in the same way as extracranial tumors (1, 8, 9). This can be explained in part by the inability of some drugs to reach therapeutically relevant concentrations in the brain due to the blood–brain barrier (BBB) and by the brain microenvironment that selectively exerts an evolutionary pressure on the invading cancer cells, thus modifying their phenotype (10–12). The brain tumor microenvironment (TME) is profoundly different from the TME of other

organs due to its distinct cell type repertoire, immune cell colonization, a specialized anatomic BBB, and its highly specialized metabolic milieu. Consequently, the brain TME imposes distinct selective pressure on EOC cells and shapes their response to treatment (10–12). Most importantly, studies have clearly shown that brain mets represent a condition for which a specific therapeutic armamentarium is essential.

Low-grade serous ovarian carcinoma (LGSOC) accounts for approximately 3.6% of all ovarian tumor and is characterized by a unique molecular profile and clinical course (13). Abnormalities in Mitogen-activated protein kinase (MAPK) pathway genes are commonly found in LGSOC and include activating mutations in *KRAS* and *BRAF* that act *via* constitutive activation of the MAPK/Extracellular signal-regulated kinase (ERK) pathway (14). The AACR GENIE Cohort of clinical-grade genomic sequencing data generated in eight Clinical Laboratory Improvement Amendments / International Organization for Standardization (CLIA-/ISO)-certified laboratories in the USA revealed the frequency of *KRAS* mutations in LGSOC to be similar to the combined frequencies in cohorts of LGSOC published over the last two decades and represent 27% of the cases (14). The majority of these mutations are in codon 12 of exon 2, and the most frequent variants are KRAS G12V and KRAS G12D. Other mutations with increased frequency are in *BRAF* and *NRAS* genes (14).

Although LGSOC contained to the ovary is associated with a favorable progression-free and overall survival, most LGSOCs are diagnosed at an advanced stage due to lack of specific symptoms and are relatively chemoresistant, leading to a poor outcome (13, 15). Extraperitoneal metastases are very rare, and brain mets are uniquely uncommon. Advanced disease is treated with aggressive surgery that is a cornerstone of treatment, and adjuvant treatment that until recent years included chemotherapy, or anti-estrogen hormonal therapy (13, 15). Most recently, trametinib, an Mitogen-activated protein kinase kinase (MEK) inhibitor, has shown efficacy over chemotherapy and endocrine therapy and has been suggested as the first-line adjuvant treatment for advanced disease (16). To increase response rates, ongoing strategies include combining hormonal treatment with cyclin-dependent kinase 4 and 6 (CDK4/6) inhibitors and exploring the role of Vascular endothelial growth factor (VEGF) inhibitors and immune therapy.

Here, we studied the evolution of an unusual case of LGSOC that metastasized to the brain by performing a detailed spatially oriented single-cell proteomics analysis of brain mets and comparing them with peritoneal disease from the same patient. Importantly, our analyses highlight important pathways that could be involved in the brain metastasis process and reveal several clinically relevant therapeutic vulnerabilities that could inform personalized medicine for LGSOC patients with concomitant brain mets.

METHODS

All tumor samples were obtained in accordance with IRB 3485 protocol at Oregon Health & Science University. All specimens

have been evaluated by a board-certified pathologist. A somatic KRAS p.G12D mutation was identified using clinical next-generation sequencing test (GeneTrails® Solid Tumor Panel).

Histology and Immunofluorescence

LGSOC tissues were fixed in neutral buffered formalin and processed for paraffin embedding. Tissue sections of 5 μm were used for this study. H&E staining was performed by the Histopathology Shared Resource at the Knight Cancer Institute, and whole-slide images were acquired with an Axioscan Z1 (Zeiss) slide scanner.

Cyclic immunofluorescence (Cyc-IF) was performed as previously described by our group (17). Briefly, Cyc-IF allows the detection and spatial single-cell analysis of more than 40 proteins on a single Formalin-Fixed Paraffin-Embedded (FFPE) slide. Multiple sequential rounds of immunofluorescence staining, imaging, and quenching were performed on each sample. The samples were processed as follows: 5-μm FFPE slides were deparaffinized, and antigen retrieval was performed in a Cuisinart pressure cooker (model CPC-600), using pH 6 citrate buffer for 20 min, followed by a quick rinse in distilled water and incubation into pH 9 Tris/Ethylenediamine tetraacetic acid (EDTA) buffer for 15 min. Slides were then blocked in a solution of Phosphate-buffered saline (PBS) with 10% normal goat serum and 1% Bovine Serum Albumin (BSA). The autofluorescence level of each tissue was acquired using an Axioscan fluorescence slide scanner (Zeiss). We then proceeded to sequential staining, imaging, and quenching of each antibody set (a list of primary antibodies used in this study is presented in **Supplementary Table S1**. Briefly, in each cycle, 4 primary antibodies conjugated with Alexa-Fluor 488, 555, 647, or 750 were incubated on the tissue sections for 2 h at room temperature. After washing, each slide was scanned and then quenched in a solution of 3% peroxide and 20 mM NaOH in PBS. After confirming the quenching of the immunofluorescence signal, a new set of antibodies was applied to the slides until all antibodies were sequentially probed.

Cyclic Immunofluorescence Image Processing and Data Analysis

After all of the images were acquired, registration was performed based on the 4′,6-diamidino-2-phenylindole (DAPI) signal using MATLAB (18). The visualization of the multiplex image, cell segmentation, and feature extraction were performed using QI Tissue Image analysis software. The mean intensities of each marker were extracted from each cell in the appropriate cell compartments. Cells with abnormal features were first filtered based on the nucleus size, and the autofluorescence level acquired in the Alexa-Fluor 555 channel. For each marker, the autofluorescence level acquired at the same wavelength was subtracted on a single-cell basis, and the protein expression values were normalized by a z-score calculation. All heatmaps and clustering analysis were performed using python (github: https://github.com/biodev/cycIF-workflow/tree/v1.0). The spatial analysis of immune cells was performed as follows. Each tumor sample was reconstructed digitally based on the x

and y coordinates of the cells. A grid analysis was performed by superposing 150 × 150 pixel squares over the tissue image. In each square, the percentage of each cell type (endothelial, stromal, epithelial, and immune) was calculated. The percentage of each immune cell type was also calculated. To remove areas with no tissue or low cell densities, squares containing 5 cells or less were removed from the analysis. Squares that contained a minimum of 50% epithelial cells were considered as tumor regions. The rest was classified as stroma regions. Furthermore, squares with a minimum of 30% immune cells were considered as immune hot spots.

RESULTS

Patient Characteristics

A 26-year-old woman was diagnosed with a borderline serous tumor of the ovary with micropapillary features after she underwent right salpingo-oophorectomy (RSO). A year later, she underwent additional surgery that included partial removal of the left ovary, and the diagnosis was confirmed. Five years after diagnosis, the patient underwent removal of a 13-cm recurrent pelvic tumor, and pathology confirmed borderline serous tumor with micropapillary features and no invasive implants. A somatic $KRAS^{G12D}$ mutation was identified by next-generation sequencing of tumor from the pelvis. $KRAS$ gene mutations are commonly found in LGSOC but not in high-grade serous ovarian carcinoma (HGSOC). A year later, she was diagnosed with multiple brain masses (**Figure 1A**), for which the largest in the left cerebellum was resected. Pathologic analysis revealed an invasive LGSOC. The specimens analyzed in this study included the left ovary (primary) 1 year post diagnosis, recurrent pelvic tumor (recurrence) 5 years post diagnosis, and brain mets 6 years post diagnosis (**Figure 1**). No adjuvant treatment was given prior to emergence of brain mets, per patient's choice.

Tumoral Architecture and Composition

The histology of LGSOC, characterized by glandular cells with a low mitotic index [less than 12 mitoses per 10 high-power fields (HPF)] and positive Immunohistochemistry (IHC) staining for WT1 and PAX8, was confirmed by a board-certified pathologist. As LGSOC can present with various architectural patterns,
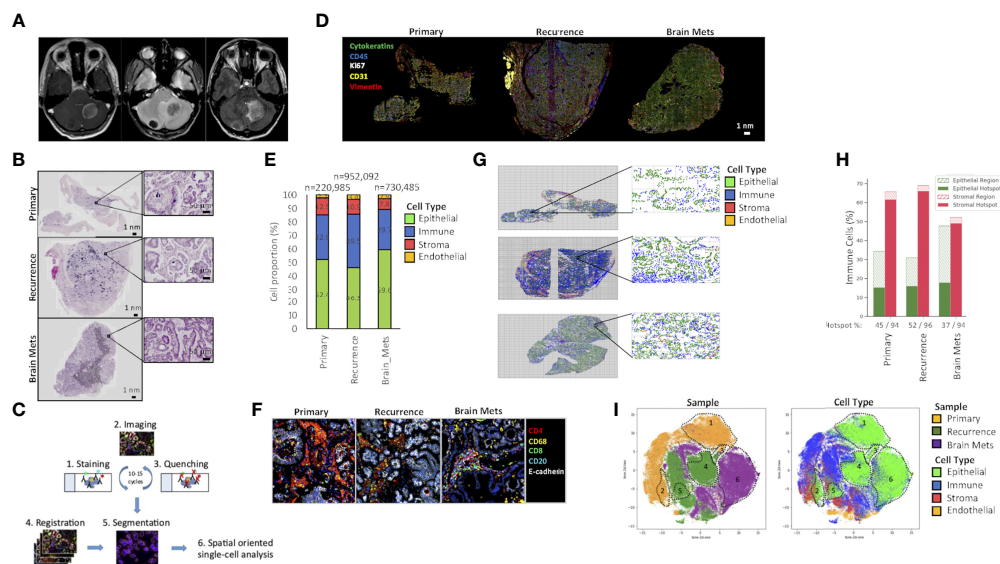
FIGURE 1 | Tumor architecture and composition. **(A)** Brain mets magnetic resonance imaging (MRI). Axial T1 post contrast (left panel) showing two peripherally enhancing masses in the cerebellum. Axial T2* (center panel) demonstrates hypointensity within these masses, indicative of mineralization, and confirmed by hyperdensity on MRI. Axial FLAIR (right panel) with mild hyperintense edema surrounding these masses, particularly the large left cerebellar mass, with mild mass effect on the fourth ventricle. **(B)** H&E staining of the primary ovarian tumor, a pelvic recurrence, and brain mets. **(C)** Cyc-IF framework. For each sample, sequential cycles of staining, imaging, and quenching are performed on a single tissue slide. The images are then aligned through registration, and the segmentation is performed. After extracting the mean intensities of each marker in each cell, a spatially oriented single-cell analysis is performed. **(D)** Immunostaining of epithelial (E-cadherin, cytokeratins), endothelial (CD31), stromal (vimentin), and proliferative (Ki67) markers of the primary ovarian tumor, a pelvic recurrence, and brain mets. **(E)** Tumor composition. The Cyc-IF analysis allows the classification of all cells within epithelial, immune, stromal, and endothelial compartments. The histogram represents the percentage of epithelial, immune, stromal, and endothelial cells in each tumor sample. **(F)** Example of a region enriched in immune cells with the presence of immune "hot spots". **(G)** Grid analysis. Each tissue analyzed by Cyc-IF was reconstructed using the x and y coordinates of the nucleus. A grid was used to analyze the proportion of each cell type in discrete regions of the tumors. **(H)** For each tumor, the immune cell distribution within the epithelial and stromal compartments was calculated based on the grid analysis. Cells found in aggregates were considered as part of an immune "hot spot". **(I)** UMAP analysis performed on a subset of 200,000 cells randomly selected across each tumor. Colors represent the samples and the cell type. The full name of each protein can be found in **Supplementary Table S1**.

including compact cell nests, cribriform, and micropapillary and glandular structures (13), we assessed changes in the tumor's architecture patterns during progression. An H&E coloration of the samples (**Figure 1B**) revealed the pelvic recurrence, and brain mets harbored a more invasive phenotype compared to the primary tumor. The primary tumor presented as a serous borderline tumor of low malignant potential with micropapillary architecture but no invasion of surrounding tissue. The pelvic recurrence was a serous borderline tumor of low malignant potential with transformation into LGSOC. Immune microinvasion was characterized by the presence of eosinophilic cell clusters with a fibrous core on large papillae (foci of <5 mm). Additional complex proliferation of variably sized papillae with mild nuclear atypia and occasional mitoses was also observed. Characteristics of invasive low-grade ovarian carcinoma were observed, including inverted micropapillae, micropapillae with no stroma, and compact cell nests that consisted of small clusters of well-differentiated cells in fibrous stroma that was surrounded by clear spaces. Stromal and capsular invasion was also present. The brain mets showed similar histopathological features to the recurrent tumor. These tumor cells retained low-grade nuclear features with frequently ciliated apical borders, and the number of mitoses remained low at 4/10 HPF. At the interface with cerebellar tissue, small clusters of cells showed invasion into the brain tissue.

To characterize the evolution in the tumor composition during progression from a localized tumor to brain metastasis, single-cell proteomics analysis was performed using multiplex Cyc-IF, as previously described (17). By performing sequential cycles of staining, imaging, and quenching, Cyc-IF allowed the visualization and spatially oriented analysis of 42 proteins at the single-cell level in a single tissue slide of each sample (19) (**Figure 1C**). First, markers that are specific to epithelial, immune, endothelial, and stromal cells were used to determine the cell composition of each tumor sample (**Figure 1D; Supplementary Table S1**). As shown in **Figure 1E**, immune and stromal cell populations were slightly decreased in the brain mets (immune: 29.7%, stromal: 7.8%) compared to the primary tumor (immune: 32.9%, stromal: 12.5%) and the recurrence (immune: 39.5%, stromal: 10.9%). In all samples, immune cells were located mostly in the stroma rather than in contact with tumor cells. Some of them were also found clustered together, forming immune hot spots in the tumor stroma (**Figure 1F**). These immune hot spots were composed of CD4+ lymphocytes and CD68+ macrophages. In the brain mets however, these clusters also included CD8+ T cells and CD20+ B cells, consistent with changes in the tumor immune landscape. In order to investigate the spatial organization of the immune cells and the presence of immune hot spots, a grid analysis was performed (**Figure 1G**). Counting the number of cells in tumor and stromal regions of the grid indicated that in the tumor masses analyzed, ~95% of the immune cells found in the stroma were aggregated together in hot spots. While the primary and recurrent tumor had similar proportions of immune cells infiltrating the tumor cell areas (30%–35%), a larger proportion of the brain metastasis immune cells were found in association

with the tumor cells (48%). Furthermore, immune cells in the brain mets tended to be more dispersed throughout the specimen, rather than forming immune cell aggregates. Although the role of immune hot spots in the antitumor response in ovarian cancer has yet to be explored, non-uniform distribution of immune cells in the tumor has previously been associated with a differential selective pressure in tumor regions, which can lead to increased tumor heterogeneity (20).

To assess tumoral heterogeneity, a Uniform Manifold Approximation and Projection (UMAP) clustering analysis was performed. As shown in **Figure 1H**, most of the cells clustered by sample, indicating distinct features that are tumor lesion dependent. The brain metastasis tumor cells were concentrated into one main cluster (region #6), while the primary and pelvic recurrence tumor cells clustered in two main populations each (Primary: #1–#2; Recurrence: #4–#5) and one smaller shared region (region #3). Immune endothelial and stromal cells clustered in many populations, which could be attributed to the different cell types targeted by our antibody panel and cell localization (stroma, stroma–epithelial transition, and epithelial compartments). Of note, brain mets and the recurrent tumor cell populations clustered closer together than with the primary tumor, suggesting similarities in the composition of the metastatic TME.

Tumor Cell Heterogeneity Is Decreased in Brain Metastases

To characterize the difference between cell populations across samples (cancer cells, immune, and stromal), we compared protein expression profiles using Cyc-IF. For cancer cells (**Figures 2A, B**), we found that the primary disease expressed higher levels of the transcriptional repressor H3K27me3 and antiapoptotic protein BCL-xL, which could be attributed to a stress response (21). Cancer cells in the recurrence displayed a phenotype of epithelial–mesenchymal transition (EMT), as evidenced by increased expression of mesenchymal proteins CD44 and vimentin (22, 23). GATA3, which has been associated with tumor progression in ovarian cancer, was also increased (24). In the brain mets, we observed an increased expression of Sting, a potent inducer of interferon, and its downstream effector Human Leukocyte Antigen – DR isotype (HLA-DR). Importantly, both are known to be involved in the antitumor immune response (25, 26). The brain mets also harbor increased B7-H4 expression, a mediator of T-cell suppression that is thought to behave as an immune checkpoint inducer. This member of the B7 superfamily has been previously associated with tumor immune escape (27) and T-cell suppression (28). Finally, the brain mets had higher expression of Estrogen receptor alpha (ERα and phosphorylation of the MAPK signaling intermediate ERK1/2. Interestingly, GATA3 that is a target of Estrogen receptor alpha (ERα) remained low, indicating that ERα might target genes through a non-canonical pathway (29). Importantly, non-canonical estrogen signaling has been previously associated with resistance to endocrine therapy, which is an important management option for LGSOC (30). Taken together, the overall protein expression pattern in epithelial cells suggested an
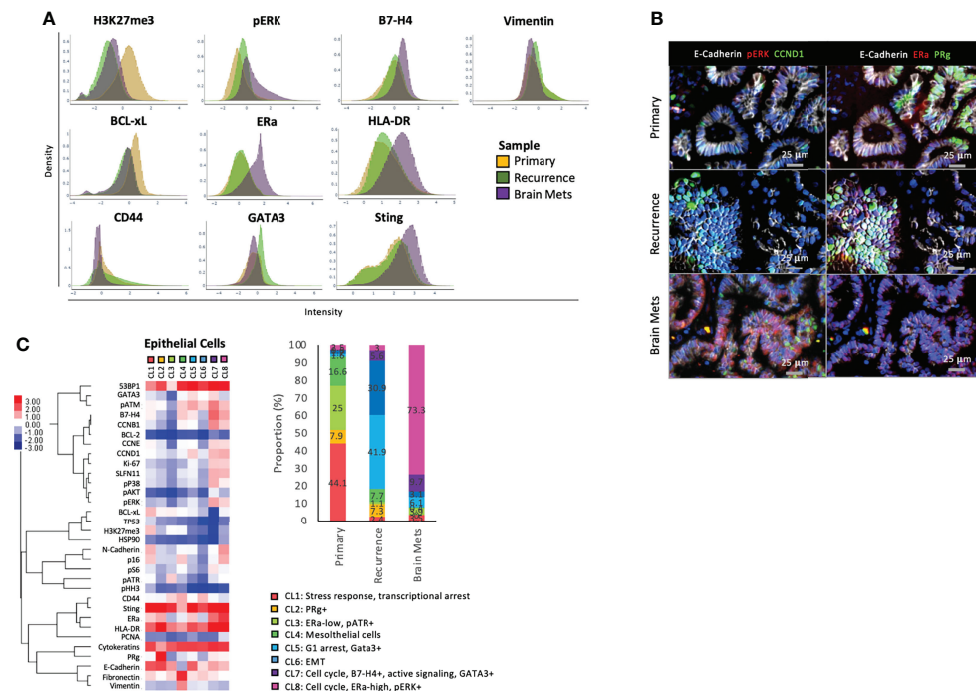
FIGURE 2 | Epithelial cell phenotype. (A) Density plot showing the distribution of expression of specific markers across epithelial cells from each sample. (B) Representative immunostaining of markers that are differentially expressed across samples. (C) A K-Mean clustering was performed on epithelial cells. The heat maps represent the median expression of each marker within each cluster (CL), and the phenotype of each cluster is annotated. The histogram represents the frequency of each cluster within the samples, and the cluster phenotypes are described below the histogram. The full name of each protein can be found in **Supplementary Table S1**.

increased invasive phenotype of the recurrent tumor and increased oncogenic signaling and altered immunogenic phenotype of the brain mets compared to the primary tumor.

To delineate tumor epithelial cell heterogeneity, we performed a K-mean clustering using the single-cell data from the epithelial compartment of each tumor (**Figure 2C**). A total of 8 clusters representing different cell phenotypes were characterized and quantified across the tumor samples. CL1, CL3, and CL4 were almost exclusively found in the primary tumor and represented populations with active stress responses and transcriptional arrest (CL1: high H3K27me3, BCL-xL, p16, pATM, low Ki67), low ERα expression, and elevated phosphorylation of the DNA damage response protein ATR (31) (CL3), as well as a population of mesothelial cells [CL4: Cytokeratins (CKs) and vimentin-high, E-cadherin-low]. CL2, which was absent from the brain mets, was only detected in the primary (7.9% of total epithelial cells) and recurrence (7.3% of total epithelial cells) and was characterized by increased expression of the progesterone receptor (PRg). CL5 and CL6 were found mostly in the recurrence and represented the population of cells with G1 arrest and high GATA3 expression (CL5) and cells with an EMT phenotype (CL6: low CKs and E-cadherin and high vimentin and fibronectin). CL7, which represented cells with an active cell cycle (CCND1, CCNB1, CCNE, and/or Ki67 expression), oncogenic signaling pathways (increased pERK, pS6, and pAKT), and high GATA3 and B4-H7 were found in each sample, but with a predominance in the brain

mets (primary 0.6%, recurrence 5.6%, and brain mets 9.7% of total epithelial cells). Finally, CL8 was mostly found in the brain mets and was its main cell population (73.3% compared to 2.5% in the primary and 7.33% in the recurrence). This cluster was enriched in cells that expressed cell cycle proteins (CCND1, CCNB1, Ki67, CCNE) and a high level of ERα and phosphorylation of ERK1/2. The expression of GATA3 remained low, confirming our previous observation of a low canonical signaling pathway activity downstream of ERα. Taken together, this clustering analysis demonstrated that although most cell populations were shared across all samples, the frequency of these populations was markedly altered in brain mets. These mets displayed a more homogeneous pattern, with the predominance of cluster CL8, that could be a result of selective pressure from the brain microenvironment.

Increased Heterogeneity and Oncogenic Signaling Pathway Activity in the Stromal Compartment of Brain Metastases

The protein expression analysis demonstrated that stromal cells displayed different protein expression profiles across tumors. In the brain mets, a decreased expression of fibronectin and vimentin was observed in the stromal compartment compared to the peritoneal tumors, indicating a different composition of the TME (**Figures 3A, B**). Furthermore, this sample expressed a higher
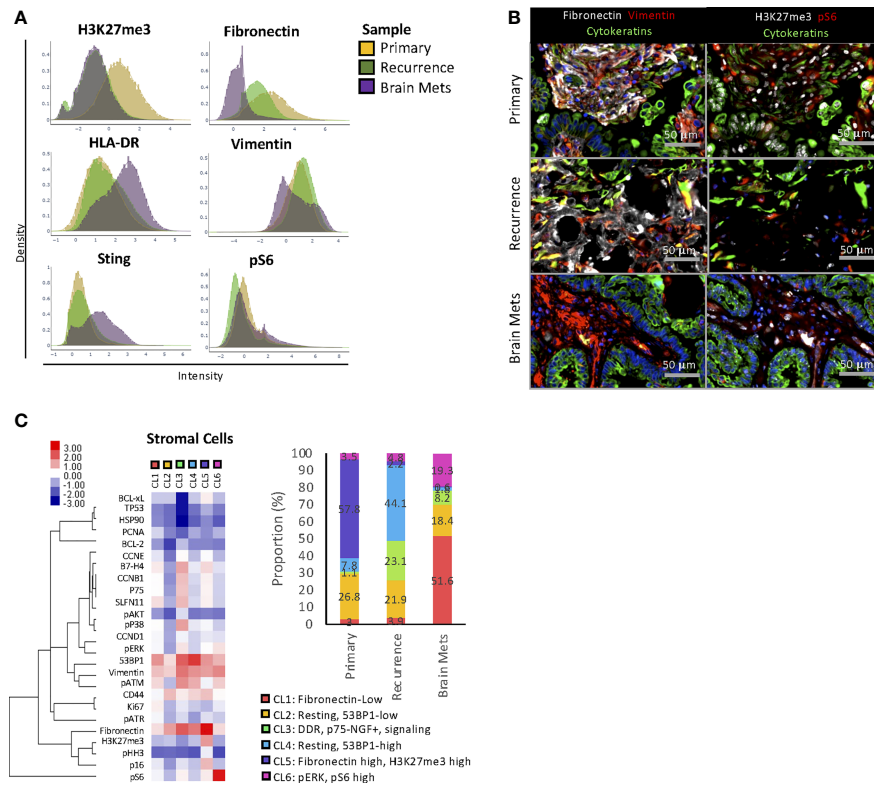
FIGURE 3 | Stromal cell phenotype. **(A)** Density plot showing the distribution of expression of specific markers across stromal cells from each sample. **(B)** Representative immunostaining of markers that are differentially expressed across samples. **(C)** A K-Mean clustering was performed on stromal cells. The heat maps represent the median expression of each marker within each cluster (CL), and the phenotype of each cluster is annotated. The histogram represents the frequency of each cluster within the samples, and the cluster phenotypes are described below the histogram. The full name of each protein can be found in **Supplementary Table S1**.
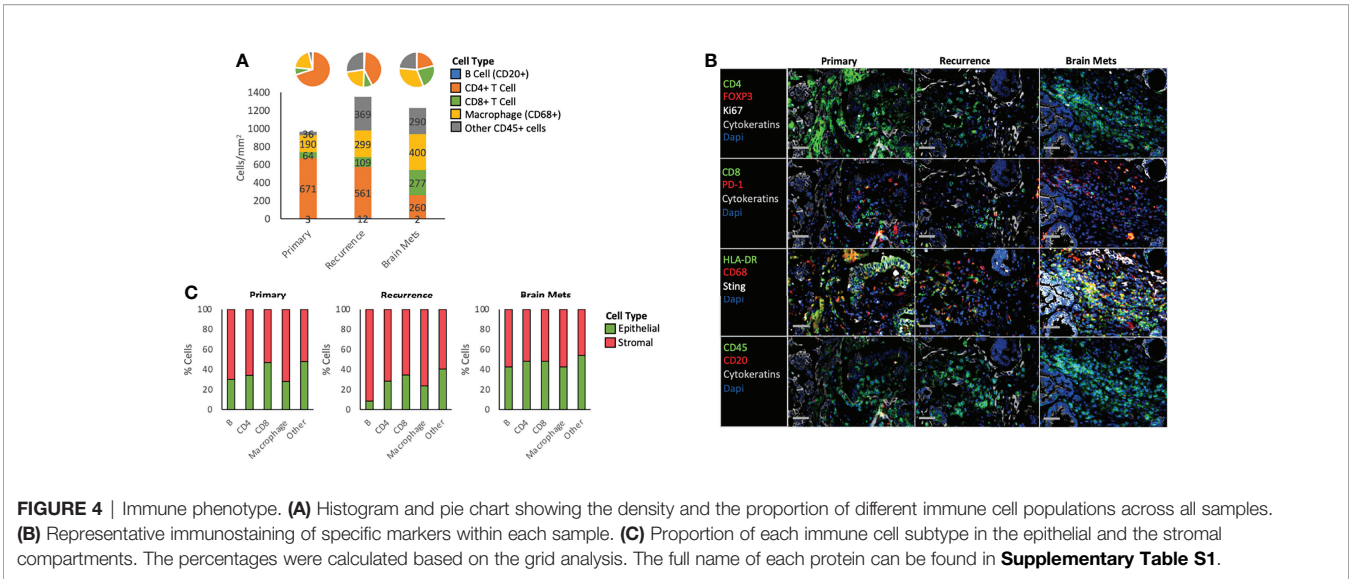
level of immunostimulatory proteins HLA-DR and Sting, as well as an increased phosphorylation of ribosomal protein S6, suggesting enhanced Mammalian target of rapamycin complex (mTORC) activity (32). Conversely, stromal cells from the primary tumor displayed a higher level of the transcriptional repressor H3K27me3. In fibroblasts, H3K27me3 has been reported as a negative regulator of fibroblastic activation and transformation into cancer-associated fibroblasts (CAFs) (33, 34).

To identify changes in stromal cell heterogeneity, K-mean clustering analysis (**Figure 3C**) was performed. Among the 6 clusters identified, CL2 and CL5 were the main clusters found in the primary tumor. CL2 represented resting and 53BP1-low cells, while CL5 was enriched in H3K27me3 and fibronectin-high cells. The recurrence was mostly composed of CL2, CL3, and CL4. CL3 was enriched in cells with active DNA damage response (DDR) and signaling pathways (p-ERK1/2, p-AKT moderate, p-S6) and high expression of B7-H4 and p75-nerve growth factor receptor (p75-NGFR). Of note, p75-NGFR has been previously associated with local recurrence and tumor metastasis (35). CL4 was enriched in resting 53BP1-high cells. The brain mets had a markedly different stromal composition compared to the peritoneal disease, with an enrichment in cells from CL1 (fibronectin-low), CL2, CL3, and CL6 (pERK and pS6-high).

Aside from CL2 that was shared with similar proportions in each tumor and CL3 that was present in both the recurrent pelvic tumor and the brain mets, the clustering analysis demonstrated that the stromal composition was tumor location dependent. Furthermore, as expected, the brain metastasis stromal composition was vastly different from that of peritoneal disease, indicating a unique TME.

Altered Immune Landscape in Brain Metastases

To determine the immune composition of each sample, the immune cells were classified and quantified using Cyc-IF and classic lineage-defining markers (**Figures 4A, B**). We first determined the density of each immune cell population by measuring the number of cells per mm^2 of tissue. Notably, while B cells were underrepresented, the immune cell density increased in the recurrence and the brain mets, with a decrease in the density of CD4+ T cells and increase in CD68+ macrophages. Additionally, the CD8+ T cell population increased slightly in the recurrence (109 cells/mm^2) and more drastically in the brain mets, reaching a density of 277 cells/mm^2, which is considered a "hot" tumor (36). Furthermore, a large proportion of other CD45+ cells were found in the recurrence (369 cells/mm^2) and the brain

FIGURE 4 | Immune phenotype. **(A)** Histogram and pie chart showing the density and the proportion of different immune cell populations across all samples. **(B)** Representative immunostaining of specific markers within each sample. **(C)** Proportion of each immune cell subtype in the epithelial and the stromal compartments. The percentages were calculated based on the grid analysis. The full name of each protein can be found in **Supplementary Table S1**.

mets (290 cells/mm^2). In terms of immune spatial organization, grid analysis (**Figure 4C**) showed little difference between the stromal and epithelial distribution of immune cells in the primary and recurrence tumor, except for B cells that tended to be more stroma-localized in the recurrence compared to the primary tumor. In the brain mets, an increased proportion of B cells, CD4 T cells, and macrophages were observed in the epithelial compartment when compared to the primary tumor. The CD8 T cells, which are the main effector of the antitumor immune response, remained unchanged, indicating the possible activation of immunosuppressive mechanisms in the TME. By further

characterizing these immune cell populations (**Table 1**), we found that Programmed cell death protein 1 (PD-1) immune checkpoint protein expression was increased in the recurrence and the brain mets on both B cells (primary: 0%, recurrence: 1.9%, brain mets: 4.9%), indicating an immunosuppressive phenotype (37), and CD8+ T cells (primary: 0.8%, recurrence: 1.9%, brain mets: 3.6%), in line with an exhausted T-cell phenotype (38). Regulatory T cells (Tregs) (CD4+ FOXP3+) were also more abundant in the recurrence and the brain mets (primary: 0.2%, recurrence: 0.4%, brain mets: 0.5%), which could also contribute to immune evasion. CD44, which is a marker of T-cell activation and

TABLE 1 | Immune cell phenotypes.

Phenotype	Cell Type	Primary (%)	Recurrence (%)	Brain Mets (%)
PD-1+	B cell	0.0	1.9	4.9
	CD4 T cells	0.3	0.6	0.3
	CD8 T cells	0.8	1.9	3.6
	Macrophages	0.1	0.2	0.3
	Other CD45+ cells	0.7	0.2	0.2
Tregs (FOXP3+)	CD4 T cells	0.2	0.4	0.5
Ki67+	B cell	3.5	2.0	6.7
	CD4 T cells	2.3	2.9	2.3
	CD8 T cells	2.1	3.1	6.2
	Macrophages	1.6	2.5	2.2
	Other CD45+ cells	3.1	4.2	2.0
CD44-High	CD4 T cells	84.3	40.7	32.5
	CD8 T cells	63.4	44.7	27.5
HLA-DR-High	B cell	6.0	21.0	36.8
	CD4 T cells	9.7	26.4	38.5
	CD8 T cells	6.6	8.1	23.8
	Macrophages	23.8	54.6	58.4
	Other CD45+ cells	4.2	9.8	23.9
Sting-High	B cell	31.0	34.3	38.0
	CD4 T cells	11.5	14.6	54.3
	CD8 T cells	17.8	28.9	52.0
	Macrophages	7.6	17.3	26.5
	Other CD45+ cells	22.9	30.5	61.4

*The full name of each protein can be found in **Supplementary Table S1**.*

memory T cells, was massively decreased in the pelvic recurrence and the brain mets compared to the primary tumor in both CD4+ (primary: 84.3%, recurrence: 40.7%, brain mets: 32.5%) and CD8+ (primary: 63.4%, recurrence: 44.7%, brain mets: 27.5%) T cells. On the other hand, Ki67 staining indicated a higher proliferation rate of B cells (primary: 3.5%, recurrence: 2%, brain mets: 6.7%) and CD8+ T cells in the brain mets (primary: 2.1%, recurrence: 3.1%, brain mets: 6.2%). The interferon pathways encompassing Sting and HLA-DR immunostimulatory molecules were also increased in brain mets. Taken together, this analysis demonstrates that the immune landscape has been profoundly altered during tumor progression. Although a higher immune infiltration has been observed in the brain mets, several immunosuppressive molecules were increased concomitantly, which could contribute to tumor immune escape.

DISCUSSION

The main objective of this study was to characterize the histopathologic progression of an unusual case of LGSOC from local disease to pelvic recurrence and subsequent metastasis to the brain, with the goal of uncovering therapeutic vulnerabilities that could be exploited in the treatment of patients with EOC and brain mets. This represents the first spatially oriented single-cell proteomics analysis of the progression of an LGSOC tumor using sequential biopsies acquired from the same patient. Our spatially oriented single-cell proteomics analysis showed a major remodeling of the epithelial, stromal, and immune compartments in the brain mets compared to the peritoneal tumors. This remodeling is accompanied by activation of oncogenic prosurvival signaling pathways and increased estrogen receptor expression. Additionally, we observed a profound alteration of the immune landscape and dysregulation of the balance between protumoral and antitumoral immune pathways.

The brain microenvironment can exert selective pressure on cancer cells and shape their response to therapy (10–12), but there is a gap in knowledge about the functional programs used by ovarian cancer cells to thrive in that environment. Furthermore, there is little understanding about the EOC brain metastatic niche itself and how it supports metastasis survival and growth. Since proteins are the functional unit of the cell, single-cell proteomics analysis represents a unique (both high-grade and low-grade serous) opportunity to characterize tumor composition and architecture and define the activity of targetable oncogenic pathways. Because of the high resolution that can be achieved with Cyc-IF, we were able to demonstrate a major remodeling of the epithelial, stromal, and immune compartments. Interestingly, the phenotype of the brain mets was less heterogeneous than in the recurrent peritoneal disease. It could be a result of the selective pressure from the brain microenvironment on the invading cells and highlighting the phenotypic features required for the survival of ovarian cancer cells in that environment. We saw a complete absence of cells that express PR, but concomitantly, all cells expressed a high level of ERα in the brain mets. It is unclear if this change in hormonal receptor profile is due to a change in tumor cell phenotypes or if it is

an indication that only certain clones from the peritoneal disease were able to disseminate to the brain. In all cases, cancer cells from the brain mets adopted a prosurvival phenotype, showed by increased MAPK and Phosphoinositide 3-kinase (PI3K) pathway activity. While the frequency of each cancer cell population varied from one tumor to another, some cell phenotypes were shared across the three tumors, suggesting that cells with a propensity for brain invasion and colonization are already detectable in the primary tumor at the time of diagnosis. This supports the hypothesis that brain mets can be established early during the course of disease but may take a long period of time to adapt to the brain microenvironment and progress to cause symptoms. This hypothesis is also supported by the clinical impression that brain mets have become slightly more frequent with the improvement in the systemic treatment of EOC (2–7) and the increase in overall survival. Thus, confirming this hypothesis in a larger cohort of patients with EOC brain mets will be critical to identify and implement effective prevention and therapeutic strategies against EOC brain mets.

In regard to the microenvironment in brain mets, we observed reduced stromal content with major changes in immune cell populations. In contrast with the cancer cells, the stromal cell populations remained as heterogeneous in the brain mets as in the peritoneal tumors but harbored a more "active" phenotype, with increased MAPK and mTORC signaling pathway activity. This was accompanied by reduced expression of vimentin and fibronectin, which are both known to affect cell motility and metastasis in many cancer models (39, 40). As the peritoneal tumors displayed high levels of fibronectin and vimentin in the stromal space, it is possible that the stroma composition facilitated the dissemination of cancer cells to the brain, but once established, high levels of vimentin and fibronectin were not essential for survival of the brain mets. Importantly, the immune landscape was also greatly altered in the brain mets compared to the peritoneal tumors. Indeed, we observed many signs of an antitumor immune contexture such as increased Sting pathway activity and increased CD8+ T cells. However, immunosuppressive cells populations also increased concurrently. Indeed, macrophage density doubled compared to the primary tumor, a larger proportion of B cells and C8+ T cells expressed the immune checkpoint protein PD-1, and the Treg population increased. This change in balance in protumor and antitumor immune response is consistent with ongoing immune activation within the brain mets triggering immunomodulation that can eventually lead to exhaustion/dysfunction of the T cells. Importantly, several studies have tested the efficacy of immune checkpoint blockade (ICB) for the treatment of patients with brain mets. In melanoma and non-small cell lung cancer, for example, ICB is associated with clinical benefit against brain mets (41). Thus, this could also be true for EOC patients with brain mets and could represent a therapeutic opportunity.

In conclusion, our results suggest that brain mets of LGSOC have a unique phenotype compared to that of the peritoneal tumors, which support the premise that standard of care might not be appropriate for the treatment of brain mets. The unique milieu in which brain mets grow can exert selective pressure on the cancer

cells, leading to the induction of prosurvival oncogenic pathways and immunosuppressive mechanisms. Thus, it will be important in future studies to obtain a better understanding of the targetable pathways that the cancer cells use for their invasion and survival in the brain microenvironment. Furthermore, as the BBB restricts the ability of certain drugs to reach therapeutically significant concentrations in the brain, it is crucial that we develop novel personalized therapeutic approaches for the treatment of patients with ovarian cancer while considering the ability of the drugs to reach therapeutic concentrations in the brain microenvironment. Although in this case ovarian cancer displayed molecular and clinical features of LGSOC, the wealth of information obtained from single-cell spatial proteomics analyses of primary tumor and brain mets proves that the analyses are likely to be of importance when applied to high-grade serous EOC and is likely to contribute to discerning the mechanisms of brain mets in all EOCs.

DATA AVAILABILITY STATEMENT

The raw data supporting the conclusions of this article will be made available by the authors without undue reservation.

ETHICS STATEMENT

The studies involving human participants were reviewed and approved by IRB 3485 protocol at Oregon Health & Science University. The patients/participants provided their written informed consent to participate in this study.

AUTHOR CONTRIBUTIONS

FUNDING

ACKNOWLEDGMENTS

SUPPLEMENTARY MATERIAL

The Supplementary Material for this article can be found online at: https://www.frontiersin.org/articles/10.3389/fonc.2022.903806/full#supplementary-material

REFERENCES

1. Borella F, Bertero L, Morrone A, Gambella A, Bovetti M, Cosma S, et al. Brain Metastases From Ovarian Cancer: Current Evidence in Diagnosis, Treatment, and Prognosis. *Cancers (Basel)* (2020) 1:22–12. doi: 10.3390/cancers12082156

2. Cohen ZR, Suki D, Weinberg JS, Marmor E, Lang FF, Gershenson DM, et al. Brain Metastases in Patients With Ovarian Carcinoma: Prognostic Factors and Outcome. *J Neurooncol* (2004) 66:313–25. doi: 10.1023/b:neon.0000014516.04943.38

3. Cormio G, Loizzi V, Falagario M, Calace A, Colamaria A, De Tommasi A, et al. Central Nervous System Metastases From Epithelial Ovarian Cancer: Prognostic Factors and Outcomes. *Int J Gynecol Cancer* (2011) 21:816–21. doi: 10.1097/IGC.0b013e318216cad0

4. D'Andrea G, Roperto R, Dinia L, Caroli E, Salvati M, Ferrante L. Solitary Cerebral Metastases From Ovarian Epithelial Carcinoma: 11 Cases. *Neurosurg Rev* (2005) 28:120–3. doi: 10.1007/s10143-004-0363-4

5. Ratner E, Bala M, Louie-Gao M, Aydin E, Hazard S, Brastianos PK. Increased Risk of Brain Metastases in Ovarian Cancer Patients With BRCA Mutations. *Gynecol Oncol* (2019) 153:568–73. doi: 10.1016/j.ygyno.2019.03.004

6. Stasenko M, Cybulska P, Feit N, Makker V, Konner J, O'Cearbhaill RE. Brain Metastasis in Epithelial Ovarian Cancer by BRCA1/2 Mutation Status. *Gynecol Oncol* (2019) 154:144–9. doi: 10.1016/j.ygyno.2019.05.004

7. Xi S, Li Z, Guo Q, Lin W, Liang X, Ma L. Prognostic Factors Among Brain Metastases in Newly Diagnosed Ovary Cancer: A Large Real-World Study. *J Cancer* (2020) 11:4625–40. doi: 10.7150/jca.44494

8. Pakneshan S, Safarpour D, Tavassoli F, Jabbari B. Brain Metastasis From Ovarian Cancer: A Systematic Review. *J Neurooncol* (2014) 119:1–6. doi: 10.1007/s11060-014-1447-9

9. McMeekin DS, Kamelle SA, Vasilev SA, Tillmanns TD, Gould NS, Scribner DR, et al. Ovarian Cancer Metastatic to the Brain: What is the Optimal Management? *J Surg Oncol* (2001) 78:194–200. doi: 10.1002/jso.1149

10. Fortin D. The Blood-Brain Barrier: Its Influence in the Treatment of Brain Tumors Metastases. *Curr Cancer Drug Targets* (2012) 12:247–59. doi: 10.2174/156800912799277511

11. Suh JH, Kotecha R, Chao ST, Ahluwalia MS, Sahgal A, Chang EL. Current Approaches to the Management of Brain Metastases. *Nat Rev Clin Oncol* (2020) 17:279–99. doi: 10.1038/s41571-019-0320-3

12. Fares J, Cordero A, Kanojia D, Lesniak MS. The Network of Cytokines in Brain Metastases. *Cancers (Basel)* (2021) 13(1):17–13. doi: 10.3390/cancers13010142

13. Gadducci A, Cosio S. Therapeutic Approach to Low-Grade Serous Ovarian Carcinoma: State of Art and Perspectives of Clinical Research. *Cancers (Basel)* (2020) 12(1):13–12. doi: 10.3390/cancers12051336

14. Moujaber T, Balleine RL, Gao B, Madsen I, Harnett PR, DeFazio A. New Therapeutic Opportunities for Women With Low-Grade Serous Ovarian Cancer. *Endocr Relat Cancer* (2021) 29:R1–R16. doi: 10.1530/ERC-21-0191

15. Angarita AM, Cholakian D, Fader AN. Low-Grade Serous Carcinoma: Molecular Features and Contemporary Treatment Strategies. *Expert Rev Anticancer Ther* (2015) 15:893–9. doi: 10.1586/14737140.2015.1052411

16. Gershenson DM, Okamoto A, Ray-Coquard I. Management of Rare Ovarian Cancer Histologies. *J Clin Oncol* (2019) 37:2406–15. doi: 10.1200/JCO.18.02419

17. Labrie M, Li A, Creason A, Betts C, Keck J, Johnson B, et al. Multiomics Analysis of Serial PARP Inhibitor Treated Metastatic TNBC Inform on Rational Combination Therapies. *NPJ Precis Oncol* (2021) 5:92. doi: 10.1038/s41698-021-00232-w

18. Eng J, Thibault G, Luoh SW, Gray JW, Chang YH, Chin K. Cyclic Multiplexed-Immunofluorescence (cmIF), a Highly Multiplexed Method for Single-Cell Analysis. *Methods Mol Biol* (2020) 2055:521–62. doi: 10.1007/978-1-4939-9773-2_24

19. Lin JR, Fallahi-Sichani M, Sorger PK. Highly Multiplexed Imaging of Single Cells Using a High-Throughput Cyclic Immunofluorescence Method. *Nat Commun* (2015) 6:8390. doi: 10.1038/ncomms9390

20. Gonzalez H, Hagerling C, Werb Z. Roles of the Immune System in Cancer: From Tumor Initiation to Metastatic Progression. *Genes Dev* (2018) 32:1267–84. doi: 10.1101/gad.314617.118

21. Braun F, de Carne Trecesson S, Bertin-Ciftci J, Juin P. Protect and Serve: Bcl-2 Proteins as Guardians and Rulers of Cancer Cell Survival. *Cell Cycle* (2013) 12:2937–47. doi: 10.4161/cc.25972

22. Xu H, Tian Y, Yuan X, Wu H, Liu Q, Pestell RG, et al. The Role of CD44 in Epithelial-Mesenchymal Transition and Cancer Development. *Onco Targets Ther* (2015) 8:3783–92. doi: 10.2147/OTT.S95470

23. Liu CY, Lin HH, Tang MJ, Wang YK. Vimentin Contributes to Epithelial-Mesenchymal Transition Cancer Cell Mechanics by Mediating Cytoskeletal Organization and Focal Adhesion Maturation. *Oncotarget* (2015) 6:15966–83. doi: 10.18632/oncotarget.3862

24. El-Arabey AA, Denizli M, Kanlikilicer P, Bayraktar R, Ivan C, Rashed M, et al. GATA3 as a Master Regulator for Interactions of Tumor-Associated Macrophages With High-Grade Serous Ovarian Carcinoma. *Cell Signal* (2020) 68:109539. doi: 10.1016/j.cellsig.2020.109539

25. Axelrod ML, Cook RS, Johnson DB, Balko JM. Biological Consequences of MHC-II Expression by Tumor Cells in Cancer. *Clin Cancer Res* (2019) 25:2392–402. doi: 10.1158/1078-0432.CCR-18-3200

26. Jiang M, Chen P, Wang L, Li W, Chen B, Liu Y, et al. cGAS-STING, an Important Pathway in Cancer Immunotherapy. *J Hematol Oncol* (2020) 13:81. doi: 10.1186/s13045-020-00916-z

27. He C, Qiao H, Jiang H, Sun X. The Inhibitory Role of B7-H4 in Antitumor Immunity: Association With Cancer Progression and Survival. *Clin Dev Immunol* (2011) 2011:695834. doi: 10.1155/2011/695834

28. Sica GL, Choi IH, Zhu G, Tamada K, Wang SD, Tamura H, et al. B7-H4, A Molecule of the B7 Family, Negatively Regulates T Cell Immunity. *Immunity* (2003) 18:849–61. doi: 10.1016/s1074-7613(03)00152-3

29. Hao D, Li J, Wang J, Meng Y, Zhao Z, Zhang C, et al. Non-Classical Estrogen Signaling in Ovarian Cancer Improves Chemo-Sensitivity and Patients Outcome. *Theranostics* (2019) 9:3952–65. doi: 10.7150/thno.30814

30. Ranganathan P, Nadig N, Nambiar S. Non-Canonical Estrogen Signaling in Endocrine Resistance. *Front Endocrinol (Lausanne)* (2019) 10:708. doi: 10.3389/fendo.2019.00708

31. Flynn RL, Zou L. ATR: A Master Conductor of Cellular Responses to DNA Replication Stress. *Trends Biochem Sci* (2011) 36:133–40. doi: 10.1016/j.tibs.2010.09.005

32. Meyuhas O. Ribosomal Protein S6 Phosphorylation: Four Decades of Research. *Int Rev Cell Mol Biol* (2015) 320:41–73. doi: 10.1016/bs.ircmb.2015.07.006

33. Kramer M, Dees C, Huang J, Schlottmann I, Palumbo-Zerr K, Zerr P, et al. Inhibition of H3K27 Histone Trimethylation Activates Fibroblasts and Induces Fibrosis. *Ann Rheum Dis* (2013) 72:614–20. doi: 10.1136/annrheumdis-2012-201615

34. Kuzet SE, Gaggioli C. Fibroblast Activation in Cancer: When Seed Fertilizes Soil. *Cell Tissue Res* (2016) 365:607–19. doi: 10.1007/s00441-016-2467-x

35. Chan MM, Tahan SR. Low-Affinity Nerve Growth Factor Receptor (P75 NGFR) as a Marker of Perineural Invasion in Malignant Melanomas. *J Cutan Pathol* (2010) 37:336–43. doi: 10.1111/j.1600-0560.2009.01349.x

36. Keren L, Bosse M, Marquez D, Angoshtari R, Jain S, Varma S, et al. A Structured Tumor-Immune Microenvironment in Triple Negative Breast Cancer Revealed by Multiplexed Ion Beam Imaging. *Cell* (2018) 174:1373–87.e1319. doi: 10.1016/j.cell.2018.08.039

37. Thibult ML, Mamessier E, Gertner-Dardenne J, Pastor S, Just-Landi S, Xerri L, et al. PD-1 Is a Novel Regulator of Human B-Cell Activation. *Int Immunol* (2013) 25:129–37. doi: 10.1093/intimm/dxs098

38. Ahn E, Araki K, Hashimoto M, Li W, Riley JL, Cheung J, et al. Role of PD-1 During Effector CD8 T Cell Differentiation. *Proc Natl Acad Sci USA* (2018) 115:4749–54. doi: 10.1073/pnas.1718217115

39. Serres E, Debarbieux F, Stanchi F, Maggiorella L, Grall D, Turchi L, et al. Fibronectin Expression in Glioblastomas Promotes Cell Cohesion, Collective Invasion of Basement Membrane *In Vitro* and Orthotopic Tumor Growth in Mice. *Oncogene* (2014) 33:3451–62. doi: 10.1038/onc.2013.305

40. Jeevan DS, Cooper JB, Braun A, Murali R, Jhanwar-Uniyal M. Molecular Pathways Mediating Metastases to the Brain *via* Epithelial-To-Mesenchymal Transition: Genes, Proteins, and Functional Analysis. *Anticancer Res* (2016) 36:523–32.

41. Fares J, Ulasov I, Timashev P, Lesniak MS. Emerging Principles of Brain Immunology and Immune Checkpoint Blockade in Brain Metastases. *Brain* (2021) 144:1046–66. doi: 10.1093/brain/awab012

Conflict of Interest: The authors declare that the research was conducted in the absence of any commercial or financial relationships that could be construed as a potential conflict of interest.

Publisher's Note: All claims expressed in this article are solely those of the authors and do not necessarily represent those of their affiliated organizations, or those of the publisher, the editors and the reviewers. Any product that may be evaluated in this article, or claim that may be made by its manufacturer, is not guaranteed or endorsed by the publisher.

Mesonephric-Like Adenocarcinoma of Uterine Corpus: A Clinicopathological and Targeted Genomic Profiling Study in a Single Institution

Tianshi Ma[1†], Mengyu Chai[1,2†], Huafeng Shou[3], Guoqing Ru[1] and Ming Zhao[1*]

[1] Cancer Center, Department of Pathology, Zhejiang Provincial People's Hospital, Affiliated People's Hospital of Hangzhou Medical College, Hangzhou, China, [2] Department of Pathology, Zhejiang Hospital, Hangzhou, China, [3] Cancer Center, Department of Gynecology, Zhejiang Provincial People's Hospital, Affiliated People's Hospital of Hangzhou Medical College, Hangzhou, China

Background: Mesonephric-like adenocarcinoma (MLA) is a recently characterized, rare, and aggressive neoplasm that mostly arises in the uterine corpus and ovary. MLA shows characteristic pathological features similar to mesonephric adenocarcinoma of the cervix. The origin of MLA is still controversial and recognition of it remains challenging for pathologists. The aim of this study was to enrich the clinicopathological features of MLA in the uterine corpus and explore its molecular alterations by targeted next-generation sequencing (NGS).

Methods: Four cases of MLA were identified among a total of 398 endometrial carcinomas diagnosed in our institution between January 2014 and December 2021. Immunohistochemistry and targeted NGS spanning 437 cancer-relevant genes were performed.

Results: The most common symptom was abnormal vaginal bleeding, and the average age was 68 years. Histologically, the tumors showed a mixture of varied growth patterns including papillary, glandular, tubular, cribriform, solid, and slit-like architectures, which were lined by columnar to cuboidal cells with overlapping vesicular nuclei and sometimes nuclear grooves. Intraluminal eosinophilic colloid-like secretions were focally evident in three of the four cases. Immunohistochemically, the MLAs were positive for GATA3 (4/4), TTF-1 (3/3), luminal CD10 (3/3), calretinin (2/3), and patchy P16 (3/3) and were negative for ER (0/4) and PR (0/4). The expression of P53 was "wild type" (4/4). By targeted NGS, 3/4 (75%), 2/4 (50%), and 1/4 (25%) cases harbored *PIK3CA*, *KRAS*, and *PTEN* mutations, respectively. None of the tumors had mutations in DNA mismatch repair genes, *ARID1A/B*, *POLE*, *CTNNB1*, *SMARCA4*, or *TP53*. At the time of diagnosis, three were presented with FIGO IB stage and one with IIIC stage. Two patients received postoperative chemotherapy and radiotherapy and they were alive without evidence of disease at 8 and 56 months follow-up, respectively. One patient developed pulmonary

metastasis 13 months after surgery and chemotherapy, and one was dead of the disease 24 months after the operation without adjuvant therapy.

Conclusions: MLA is a rare and aggressive malignancy, representing approximately 1% of all endometrial carcinomas. It exhibits mixed architectures associated with distinctive immunophenotype and recurrent *KRAS* and *PIK3CA* mutations, supporting classified as of Müllerian origin with mesonephric differentiation.

Keywords: mesonephric-like adenocarcinoma, uterine corpus, *KRAS*, *PIK3CA*, *PTEN*

INTRODUCTION

Mesonephric adenocarcinoma (MA), originating from normal or hyperplastic mesonephric remnants, is an unusual and aggressive tumor most commonly occurring in the lateral walls of the cervix (1–3). Mesonephric-like adenocarcinoma (MLA) is a recently characterized, rare subtype of gynecologic carcinoma that has been included in the 5th edition *World Health Organization (WHO) Classification of Female Genital Tumours* (4–6). MLA frequently arises in the uterine corpus and ovary and shares overlapping features with MA in morphology, immunophenotype, and molecular changes without the presence of mesonephric remnants (7–11). It is important to recognize MLA in the uterine corpus due to its well-established aggressive behavior (12–15). Patients frequently present at an advanced International Federation of Gynecology and Obstetrics (FIGO) stage (II to IV) with a tendency toward early recurrence and distant metastasis (12–15).

Histologically, akin to MA, MLA is characterized by a variety of growth patterns including tubular, glandular, papillary, retiform, glomeruloid, sex-cord like, and solid. Tubular and glandular patterns often predominate, and a frequent finding is the presence of small tubules containing luminal eosinophilic colloid-like materials (4, 9, 10, 13, 16). Squamous and mucinous differentiation are generally absent (9, 13, 16). The immunophenotype of MLA is also similar to MA with the expression of PAX8, GATA3, TTF1, calretinin, luminal CD10, patchy P16, and "wild type" P53, and negative staining for estrogen and progesterone receptors (4, 8, 13, 15, 16). Molecular genetic findings show both MLA and MA are characterized by recurrent *KRAS* mutations, gain of chromosome 1q, microsatellite stability, as well as alterations in chromatin remodeling genes (*ARID1A/B* and *SMARCA4*) (7, 9, 10). However, accumulated evidence disclose MLAs do not infrequently harbor *PIK3CA* and *PTEN* alterations which are commonly seen in endometrial endometrioid carcinomas (EECs) but are very rare in MAs (11, 13, 16). Furthermore, extra-uterine MLAs are often associated with Müllerian lesions such as endometriosis and serous tumors (17–20). This evidence has led some pathologists to suggest that MLA may represent mesonephric-like transdifferentiation of a Müllerian tumor rather than a true mesonephric tumor (9, 11, 13, 16). Nevertheless, the definite relationship between MLA and MA has not been firmly established.

The purpose of this study was to add cases of uterine corpus MLA diagnosed at our institution with morphologic and immunohistochemical as well as detailed molecular analyses to the existing literature and to provide further evidence to support its Müllerian origination.

MATERIALS AND METHODS

Case Selection

Among a total of 398 endometrial carcinomas (ECs) of the uterine corpus diagnosed in Zhejiang Provincial People's Hospital between January 2014 and December 2021, four cases of MLA were identified, which accounts for approximately 1% of all ECs. The clinical details and follow-up data were obtained from a review of the electronic medical records. For all four cases, the hematoxylin-eosin (HE) stained and immunohistochemical slides were reviewed by two of the authors (TM and MZ) and the diagnosis of MLA was further confirmed according to the diagnostic criteria proposed by the recently published 5th edition *WHO Classification of Female Genital Tumours* (6). This study was approved by the institutional ethics committee of Zhejiang Provincial People's Hospital.

Immunohistochemistry

All specimens were formalin-fixed and paraffin-embedded. Tissues were sliced into 3-μm sections. Immunohistochemistry (IHC) was performed on a Ventana Benchmark autostainer (Ventana Medical Systems, Tucson, AZ, USA). All the used primary antibodies were purchased from Beijing Zhong Shan Gold Bridge Biological Technology Co., Ltd (Beijing, China), including PAX8 (Clone EP298), GATA3 (Clone EP368), TTF1 (Clone 8G7G3/1), P53 (Clone DO-7), estrogen receptor (ER, Clone OTI1B1), progesterone receptor (PR, Clone OTI2E2), P16 (Clone 1C1), calretinin (polyclonal), and CD10 (Clone SP67). The staining process was performed in accordance with the instructions and established positive and negative controls. Stains were considered positive if there was nuclear staining for PAX8, GATA3, TTF1, P53, ER, and PR, nuclear & cytoplasmic staining for calretinin and P16, and luminal staining for CD10. Positive staining in less than 50% of tumor cells or glands was considered focally positive, and positive staining in ≥50% of tumor cells or glands was considered diffusely positive.

Targeted Next-Generation Sequencing

Targeted NGS was performed by Nanjing Geneseeq Technology Inc. (Nanjing, China) on Illumina HiSeq4000 platform. All procedures were conducted according to the manufacturer's protocols. This detection covers a total of about 1.53Mb nucleotide sites of exons, fusion-related introns, alternative splicing regions, and specific microsatellite sites of 437 cancer-specific genes. The sequencing results include point mutations, small indel mutations, gene fusions, copy number variations, microsatellite analysis results, and tumor mutational burden.

RESULTS

Clinical Details

The clinical details of the four patients are summarized in **Table 1**. The age at diagnosis ranged from 56 to 80 years, with an average of 68 years. Three patients were admitted to the hospital for postmenopausal bleeding with a duration from 2 months to 3 years and one presented with abdominal pain for 1 year. Radical hysterectomy and bilateral salpingo-oophorectomy were performed on all four patients and additional pelvic or para-aortic lymph node dissection was performed for three patients (cases 2-4). Grossly, all the tumors involved the uterine corpus and presented as intrauterine mass with invasion to more than one half of the myometrium. The neoplasms ranged in maximum dimension from 2 to 6 cm, with an average of 3.7 cm. Specimen sections revealed solid and soft masses that were white to gray in color (**Figure 1**). The original diagnoses included EEC (case 1), mixed carcinoma (case 2), and MLA (cases 3 and 4). At the time of presentation, three of four (75%) patients were FIGO stage IB with tumor invasion into the outer half of the myometrium and one (25%) was stage IIIC with multiple pelvic nodal metastases. After the surgery, patients 2 and 4 received both chemotherapy and radiotherapy and they were alive without evidence of disease at 56 and 8 months follow-up, respectively. Patient 3 was treated with chemotherapy and she developed pulmonary metastasis 13 months postoperatively; she subsequently underwent resection of the metastatic lesion and was disease-free after 5 months of follow-up. Patient 1 was dead of the disease (due to extensive pelvic spread) 24 months after the operation without adjuvant therapy.

Morphological Characteristics

The morphological features are illustrated in **Table 2**. Histologically, at lower magnification, the tumors showed combinations of various growth patterns, including papillary,
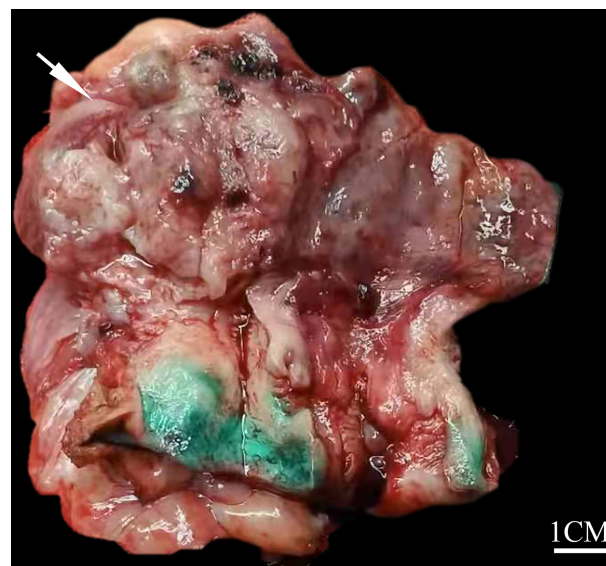
FIGURE 1 | Gross findings of uterine corpus MLA. The tumor presents as a solid and soft mass with white to gray coloring (white arrow), protruding into the endometrial cavity (case 4).

glandular, tubular, cribriform, solid, and slit-like architectures, in a fibrous and hyalinized matrix. In the present case series, papillary (**Figure 2A**) and glandular (**Figure 2B**) patterns represented the two most seen patterns, and both were presented in all four tumors. Two cases (cases 3 and 4) exhibited small tubular (**Figure 2C**), back-to-back cribriform (**Figure 2D**), and solid (**Figure 2E**) patterns. Case 2 showed foci of polycystic pattern with dilated tubules and intracystic micropapillae, similar to those seen in low-grade serous carcinoma (SC) of the ovary (**Figure 2F**). Case 4 displayed focal slit-like architectures (**Figure 2G**). Dense, eosinophilic colloid-like materials (**Figure 2H**) were focally evident in the tubules in three cases. No cases had intracytoplasmic mucin or unequivocal squamous differentiation although intracystic extracellular mucinous depositions (**Figure 2A**) were noted in one case (case 1). Lung metastasis of case 3 exhibited a 0.8-cm, well-defined nodular lesion composed of tubules and glands (**Figures 3A, B**) closely mimicking a primary invasive lung adenocarcinoma except for lacking of an *in situ* component.

Cytologically, the tumor cells were mainly columnar to cuboidal, and occasionally hobnail (**Figures 4A–C**), had scant palely eosinophilic cytoplasm, and exhibited in general moderate

TABLE 1 | Clinical features of uterine corpus mesonephric-like adenocarcinomas.

Patient No.	Age	Symptoms	Size (cm)	FIGO stage	Treatments	Follow-up (mo)
1	80ys	Postmenopausal bleeding for 3 ys	6	IB	HYS+BSO	Dead of disease (24)
2	63ys	Postmenopausal bleeding for 1ys	3.3	IIIC	HYS+BSO+PL+RT+CT(carboplatin+doxorubicin)	NED (56)
3	56ys	Abdominal pain for 1ys	2	IB	HYS+BSO+PL+CT(carboplatin+taxol)	Lung metastasis (13), NED (18)
4	73ys	Postmenopausal bleeding for 2 mo	3.5	IB	HYS+BSO+PL+CT(carboplatin+doxorubicin)	NED (8)

BSO, bilateral salpingo-oophorectomy; CT, chemotherapy; HYS, hysterectomy; NED; no evidence of disease; PL, pelvic lymphadenectomy; RT, radiotherapy.

TABLE 2 | Histomorphological characteristics of uterine corpus mesonephric-like adenocarcinomas.

Case No.	Architectural patterns						Cytologic features			Intraluminal eosinophilic secretions	Intraluminal comedo-like necrosis	LVI
	Papillary	Glandular	Tubular	Cribriform	Solid	Slit-like	Columnar to cuboidal cells with nuclear grooves	Hobnail	Spindle			
1	80%	20%					YES	NO	NO	NO. Extracellular mucus	YES	NO
2	90%	10%					YES	YES	NO	YES	NO	YES
3	10%	10%	40%	30%	5%	5%	YES	NO	YES	YES	YES	YES
4	15%	30%	30%	20%	5%		YES	NO	YES	YES	YES	YES

LVI, lymphovascular invasion.

nuclear atypia. The nuclei were vesicular, overlapping, and sometimes angulated with nuclear grooves, resembling those seen in papillary thyroid carcinoma (**Figures 4D, E**). Spindle cells were noted in the solid areas in two cases (**Figure 2E**). Mitotic activity was conspicuous, and intraluminal comedo-like necrosis was identified in three cases (**Figure 4F**). Lymphovascular invasion was noted in three out of the four cases. For all four cases, the tumor arose in the endometrium and invaded the outer half of the myometrium with a destructively infiltrating pattern. No evidence of endometrial hyperplasia or mesonephric remnants was found, and the cervix was not involved. Twenty-three of 59 pelvic lymph nodes were positive for metastatic lesions in case 2, and no nodal metastatic lesions were identified for cases 3 or 4.

Immunohistochemical Features

The immunohistochemical results are shown in **Table 3**. Not every case was stained for all markers. In all cases tested, the tumor cells were positive for PAX8 (2/2, diffusely in both) (**Figure 5A**), GATA3 (4/4, diffusely in two and focally in two) (**Figures 5B, C**), and TTF1 (3/3, focally in two and diffusely in one) (**Figures 5D, E**), and the one (case 3) which was diffusely positive for TTF1 also diffusely expressed GATA3. Three of three tumors showed focal luminal expression of CD10 (**Figure 5F**), and two out of three exhibited focal calretinin positivity (**Figure 5G**). Patchy P16 expression was noted in three cases analyzed. All cases exhibited a wild-type pattern of P53 expression, and all tumors were negative for both ER (**Figure 5H**) and PR (**Figure 5I**). For the metastatic MLA in the lung in case 3, the tumor cells were positive for PAX8, GATA3, and TTF1 (**Figures 6A–C**), in accordance with the immunoprofile of the primary tumor of the uterine corpus.

Molecular Genetic Findings

The molecular genetic findings are listed in **Table 4**. Genetic testing using targeted NGS spanning 437 cancer-relevant genes was performed on all four cases. The tumor mutational burdens were overall low and varied from 2.1 to 7.4 mutations per megabase. A total of 14 genes with 18 mutations were identified across all cases and contained 14 missense, one nonsense, one frameshift, one nonframeshift deletion mutation, and one splice site mutation. Five genes (*KRAS*, *PIK3CA*, *PTEN*, *ATM*, *MYCN*) of the mutations have been previously reported in MLA. *KRAS* activating mutations were found in two of four (50%) cases harboring G12A (case 1) and G12V (case 2) (**Figures 7A, B**), and *PIK3CA* mutations (all missense mutations) were identified in three of four cases (75%) harboring alterations including R93W (case 2), Q546R (case 3), and G1049R (case 4) (**Figures 7C–E**). Case 2 had concurrent mutations of *KRAS* and *PIK3CA*. *PTEN* missense mutation (L325R) (**Figure 7F**) was identified in case 1 which was accompanied by *KRAS* mutation. Both the two *KRAS*-nonmutated tumors harbored *PIK3CA* mutations (cases 3 and 4). Copy number variation was only identified in case 3, which exhibited a gain of *NKX2-1* (TTF1, copy number, CN: 4.2). None of the tumors had mutations in DNA mismatch repair genes, *ARID1A/B*, *POLE*, *CTNNB1*, *SMARCA4*, or *TP53*.

DISCUSSION

In this study, we used previously characterized knowledge of the morphologic and immunohistochemical features of MLAs to retrospectively identify these tumors in the archives of our institution. Among a total of 398 ECs diagnosed in our institution between January 2014 and December 2021, four cases of MLA were retrieved, accounting for approximately 1% of all ECs, in accordance with the recently reported prevalence of 0.7% (4/570) by Kolin et al. in 2019 (16), and 0.7% (2/300) by Mills et al. in 2022 (21). Despite being very rare, uterine corpus MLA may be under-recognized due to its diverse morphology and close resemblance to other commonly encountered endometrial cancers such as EEC, clear cell carcinoma (CCC), SC, and carcinosarcoma. In fact, for the four cases presented here, only two had been correctly diagnosed as MLA originally, with the other two diagnosed as EEC and mixed carcinoma, respectively. Similarly, in the retrospective case series study by Euscher et al. (13), of the 23 cases of uterine corpus MLA analyzed (most were referral cases), 18 were initially classified as carcinomas other than MLA, including EEC in 13 cases, adenocarcinoma not otherwise specified in four cases, and SC in one case.

The four cases of uterine corpus MLA presented here showed morphologic, immunohistochemical, and molecular features consistent with those in previously described cases (**Table 5**). In general, the most useful morphological clues for diagnosing MLA include: a variety of growth patterns seen in combination and within the same tumor; the presence of distinctive nuclear
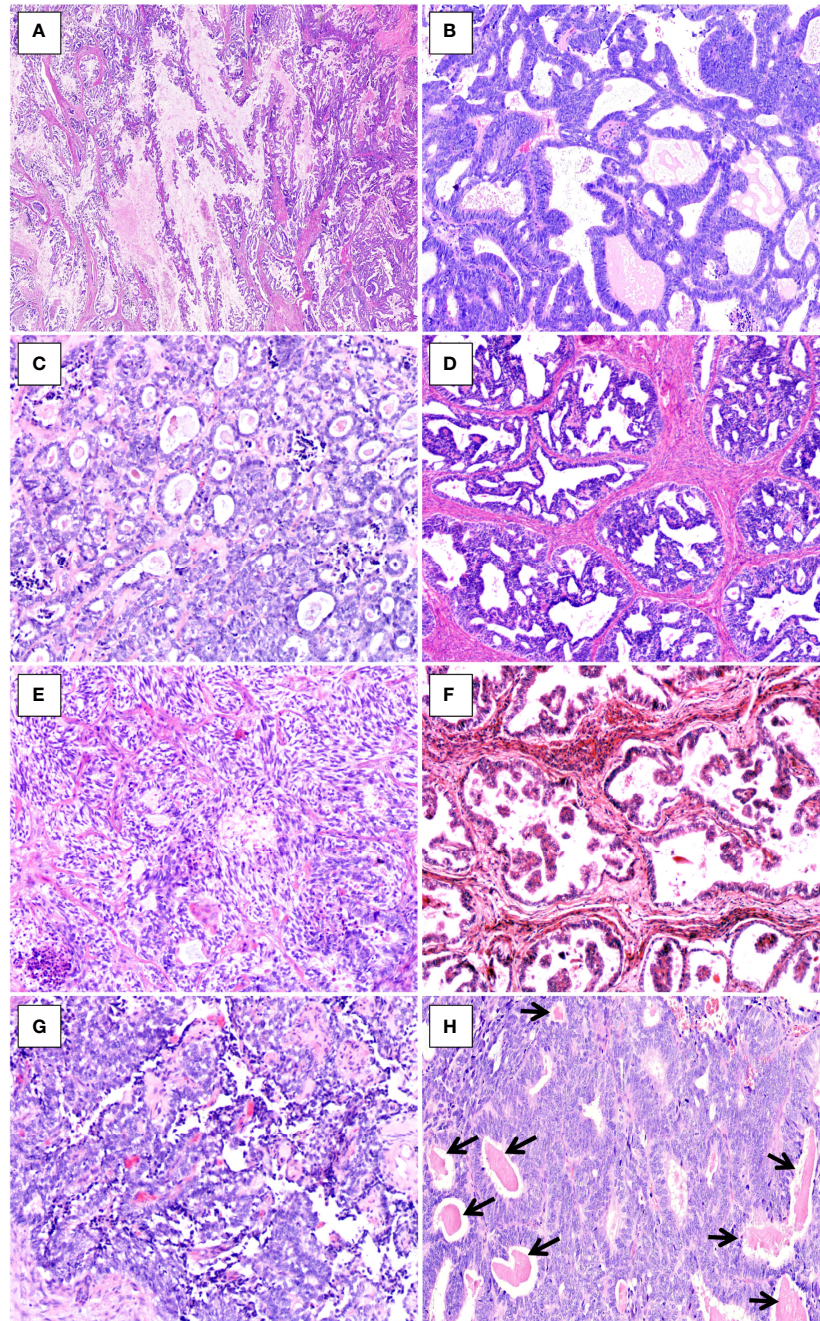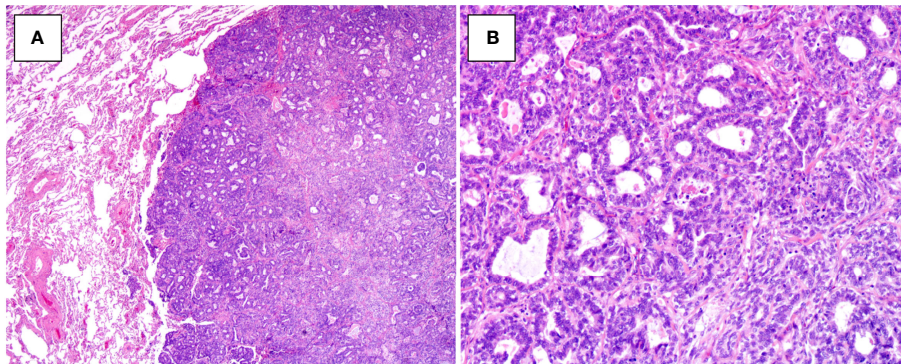
FIGURE 2 | Histopathologic findings of uterine corpus MLA. **(A)** Papillary pattern with extracellular mucinous depositions (case1, HE×20). **(B)** Glandular pattern (case 4, HE×100). **(C)** Tubular pattern(case 3, HE×100). **(D)** Cribriform pattern (case 4, HE×100). **(E)** Solid pattern with spindle-shaped cells (case 3, HE×100). **(F)** Intracystic micropapillary pattern (case 2, HE×100). **(G)** Slit-like architecture (case 3, HE×100). **(H)** Dense, eosinophilic colloid-like materials (arrows, case 4, HE×100).

features that resemble those seen in papillary thyroid carcinoma, such as nuclear grooves, nuclear overlap, and open chromatin; the presence, at least focally, of densely eosinophilic intraluminal secretions in the tubules; and the lack of marked nuclear atypia and pleomorphism, and unequivocal squamous differentiation (4, 9, 10, 13, 16). Foci of solid architecture composed of spindle cells can be noted in MLAs, which should not be regarded as a sign of sarcomatoid differentiation, given the lack of heterologous differentiation in these areas and the consistent absence of *TP53* mutations in these tumors (16). MLAs typically have no intracytoplasmic mucin frequently seen in EECs but they can contain mucin-like material within the luminal spaces 13). Rare features that have been documented in MLAs include sex cord-like/trabecular pattern reminiscent of the corded and
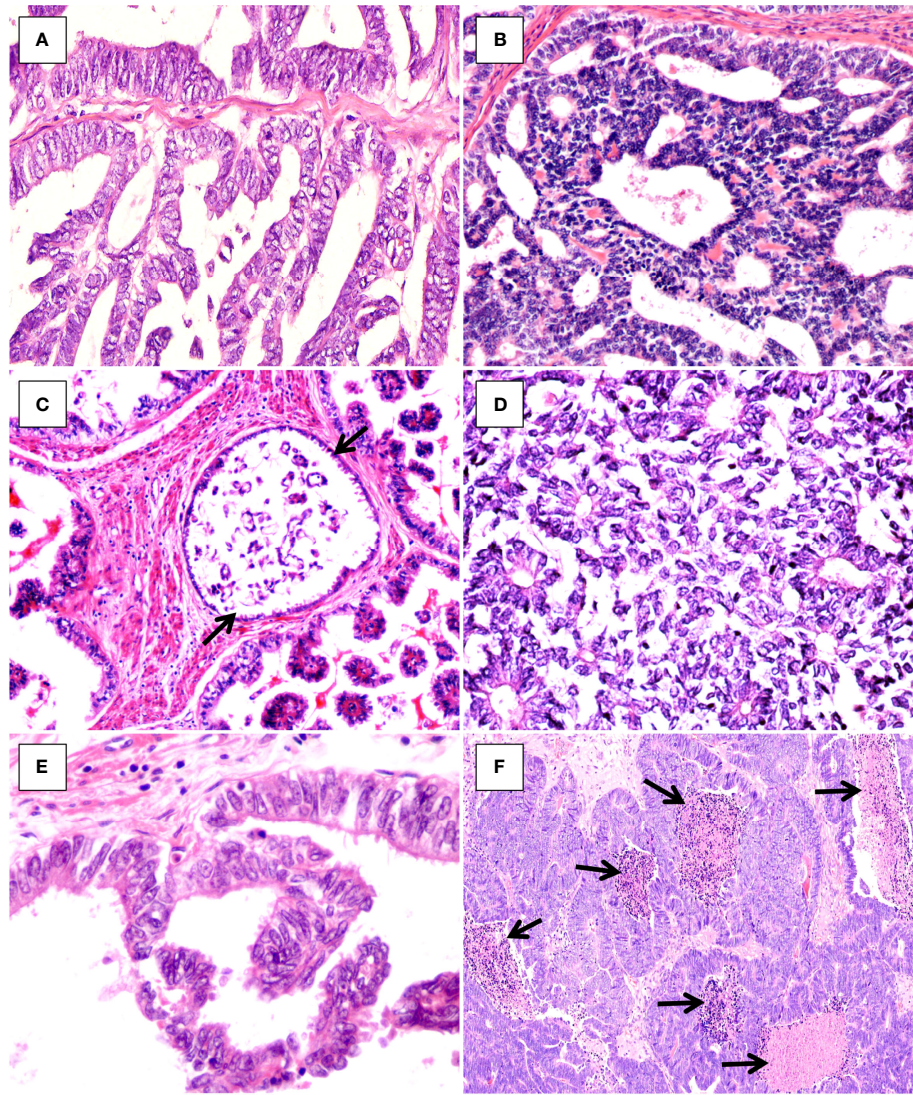
FIGURE 3 | Histopathologic findings of metastatic MLA to the lung in case 3. **(A)** Well-demarcated nodular lesion (HE×20). **(B)** The lesion consists of dense tubules and glands, mimicking a primary invasive lung adenocarcinoma (HE×100).

hyalinized variant of EEC (22), papillary pattern covered by hobnail-type cells or cytoplasmic clearing cells mimicking CCC (13), and dedifferentiation to sheets of anaplastic discohesive cells (23). In addition, EC with architectural and cytologic features suggesting low-grade SC of the ovary (such as polycystic pattern with dilated tubules and intracystic micropapillae, as two of our cases have illustrated), should also prompt consideration of MLA. In three out of the four MLAs, intraluminal comedo-like necrosis resembling that seen in intraductal carcinoma of the breast was noted; this morphology has previously been documented in a subset of MLAs (13). While careful attention to histology can help flag tumors for potential mesonephric-like classification, ultimately ancillary studies are often required for confident classification as MLA. In this study, for all cases tested, the tumor cells are positive for PAX8, GATA3, TTF1, and luminal CD10, and are negative for ER and PR, consistent with the immunohistochemical results previously reported. Pors et al. (8) compared the sensitivity and specificity of GATA3, TTF1, CD10, and calretinin in the diagnosis of MLAs and reported GATA3 to be the best overall marker, but staining can be weak to moderate in intensity and positive in only a minority of cells (<10%). In their study, TTF1 had high sensitivity and specificity comparable to GATA3 for MLAs, however, it was expressed in only 12.5% of MAs, suggesting MLA and MA may be biologically different entities. TTF1 and GATA3 can show an inverse staining pattern in a minority of MLAs (8). It is worth noting that both GATA3 and TTF1 can be seen in 6% and 1% of non-MLA ECs, respectively (8). Previous studies have found that both TTF1 and GATA3 expression are poor prognostic factors for ECs, and some of these TTF1 or GATA3-positive cases may in fact represent MLAs (24, 25). Euscher and colleagues (13) investigated the immunophenotypic features in 23 cases of MLA of the endometrium and found similar results. In their study, 15/16 (94%) and 11/16 (69%) of cases expressed GATA3 and TTF1, respectively, and the intensity and number of cell staining of GATA3 were greater than that of TTF-1 in most cases. These authors suggested that a panel of immunohistochemical stains should be employed to facilitate a

diagnosis of MLA and included first-line markers GATA3, TTF1, ER, and PR, with CD10 and calretinin serving as supplemental immunohistochemical stains. Most recently, Kim et al. (15) found that in 25 cases of endometrial MLA, 68% showed at least moderate nuclear GATA3 immunoreactivity in more than 25% of tumor cells, and 81% of examined cases expressed TTF1 often in a heterogeneous pattern. In that study, all cases expressed at least one of the two markers, with an inverse staining pattern of GATA3 and TTF1 noted in 30% of cases (15). Loss of ER is typically observed in MLAs, however, this is not a universal finding among reported cases. In the study by Euscher et al. (13), focal positivity of ER (usually in less than 10% of tumor cells) can be seen in up to 30% of MLAs. Hence some positivity of ER does not necessarily preclude the diagnosis of MLA. PR was negative in almost all reported cases; thus, it can be concluded that PR is a more reliable negative marker for MLA (5).

Increasing use of mutational analysis techniques in an effort to improve understanding of tumor biology and identify potential therapeutic targets has led to the identification of recurrent *KRAS* mutations in MLAs. Although results from smaller series suggest that *KRAS* mutation is a consistent finding among MLAs, several previously reported larger series reported *KRAS* mutation in 76 to 89% of cases (10, 11, 13). All the cases lacking *KRAS* mutation had histologic and immunohistochemical features diagnostic of MLA. In this study, *KRAS* activating mutations were only found in two of four (50%) cases harboring G12A (case 1) and G12V (case 2), respectively. In our study, the lower proportion of *KRAS* mutation may be related to the small number of samples included. Our two cases without a *KRAS* mutation both had histologic features of MLA as well as diagnostic immunohistochemical support including expression of GATA3 and TTF1. In most of the reported cases in the literature, MLAs have only had mutations in *KRAS*, typically affecting the hotspot codon 12 including G12D, G12V, G12C, and G12A (9–13, 15). A small number of cases have been noted in the literature with concurrent genetic alterations, including mutations in *PIK3CA*, *PTEN*, and *CTNNB1* (9, 10, 13, 16), which are characteristic

FIGURE 4 | Histopathologic findings of uterine corpus MLA. **(A)** Columnar tumor cells (case1, HE×400). **(B)** Cuboidal tumor cells (case 4, HE×400). **(C)** Hobnail tumor cells (arrows, case 2, HE×300). **(D, E)** Vesicular, overlapping nuclei with nuclear grooves **(D)**, case 3, HE×300; **(E)**, case 2, HE×400). **(F)** Intraluminal comedo-like necrosis (arrows, case 4, HE×100).

molecular alternations of EECs (26). Among the small number of endometrial MLAs without a *KRAS* mutation reported, one harbored a mutation involving *BRAF*, another gene in the RAS/MAPK pathway (11), and one had mutations in *PIK3CA*, *PTEN*, and *CTNNB1* (13). Our findings reflect the literature experience. Of the two cases with a *KRAS* mutation, both had additional mutations, including *PIK3CA* and *PTEN* in each case. For the two cases lacking *KRAS* mutation, both had mutations in *PIK3CA*, and one of which had a gain of *NKX2-1* (TTF1, copy number, CN: 4.2), which had previously been reported in MLAs

TABLE 3 | Immunohistochemical characteristics of uterine corpus mesonephric-like adenocarcinomas.

Case No.	ER/PR	PAX8	GATA3	TTF-1	CD10 (luminal)	P53	P16	Calretinin
1	-/-	ND	focally +	ND	ND	WT	ND	ND
2	-/-	ND	focally +	focally +	focally +	WT	patchy+	focally +
3	-/-	diffusely +	diffusely +	diffusely+	focally +	WT	patchy+	focally +
4	-/-	diffusely +	diffusely +	focally +	focally +	WT	patchy+	focally +

*WT, wild type; ND, not done; +, positive; -, negative.*
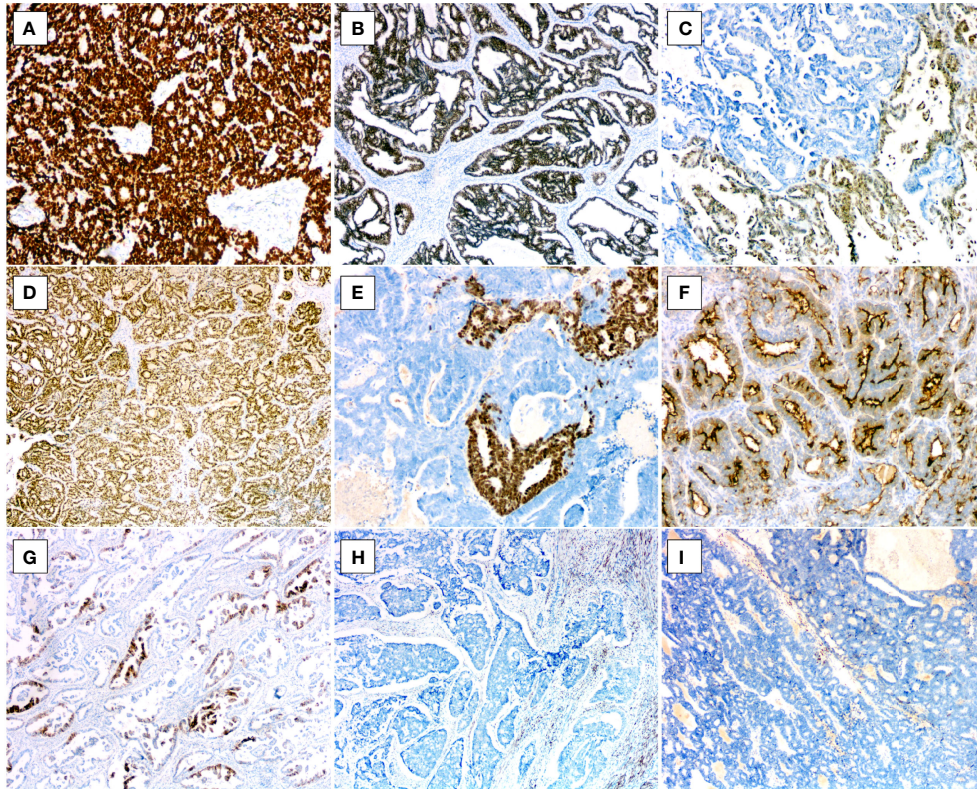
FIGURE 5 | Immunohistochemical features of uterine corpus MLA. **(A)** Diffuse PAX8 positivity (case 3, ×100). **(B)** Diffuse GATA3 positivity (case 4, ×40). **(C)** Focal GATA3 positivity (case 1, ×100). **(D)** Diffuse TTF1 positivity (case 3, ×40). **(E)** Focal TTF1 positivity (case 4, ×100). **(F)** Luminal CD10 positivity (case 3, ×100). **(G)** Focal calretinin positivity (case 2, ×40). **(H)** ER negativity (case 3, ×40). **(I)** PR negativity (case 4, ×40).

(9). The presence of concomitant *PIK3CA* and/or *PTEN* mutations in some cases of endometrial MLA has led to the hypothesis that these tumors are Müllerian or endometrioid derived but differentiating along mesonephric lines, representing a distinctive variant of EC (9, 11, 13, 16). The findings of our study lend further support to this assertion.

Although *KRAS* mutations had been identified in the vast majority of reported MLAs, a *KRAS* mutation is usually not required for the diagnosis of MLA. Furthermore, *KRAS* mutation is not unique to MLA in endometrial cancer. In their evaluation

of 570 ECs which had undergone molecular profiling, Kolin et al. (16) have identified *KRAS* mutation in up to 17% (98/570) of ECs, in which most were endometrioid histotype, followed by carcinosarcoma (nine cases), and SC and MLA (both were four cases). Thus, the diagnosis of the MLA variant of EC remains based primarily on histologic and immunohistochemical grounds. The main differential diagnosis of MLA is EEC, and many of the previously reported endometrial MLA were initially mistaken for EEC (13, 14). This is not surprising given that the various architectural patterns characteristic of MLAs may also
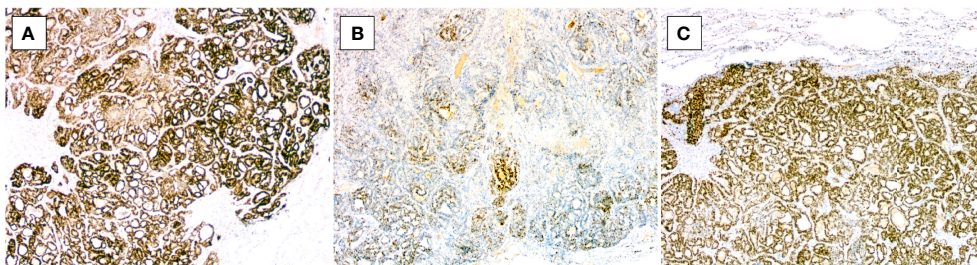
FIGURE 6 | Immunohistochemical findings of metastatic MLA to the lung in case 3. The tumor cells are positive for **(A)** PAX8 (×40), **(B)** GATA3 (×40), and **(C)** TTF1 (×40).

TABLE 4 | Molecular genetic findings of uterine corpus mesonephric-like adenocarcinomas.

Case No.	Case 1	Case 2	Case 3	Case 4
Mutations	PTEN: exon 8 c.974T>G(p.L325R). VAF:78.85% Uncertain significance KRAS: exon2 c.35G>C(p.G12A). VAF:72.29% Likely pathogenic ATM:exon50 c.7466C>T(p.S2489F). VAF:35.14% Uncertain significance ATM:exon10 c.1372_1382dup (p.E461Dfs*16). VAF:21.69% Uncertain significance KMT2C:intron7 c.1012+1G>A. VAF:8.67% Uncertain significance TMPRSS2:exon3 c.230A>C(p.H77P). VAF:8.11% Uncertain significance	DUSP2:*exon2 c.504C>G(p.Y168*). VAF:77.55%* Uncertain significance KRAS: exon2 c.35G>T(p.G12V). VAF:69.45% Likely pathogenic SMAD4:exon8 c.913C>A(p.H305N).VAF:31.61% Uncertain significance PIK3CA:exon1 c.277C>T(p.R93W). VAF:29.91% Uncertain significance DPYD:exon21 c.2737A>G(p.I913V). VAF:23.62% Likely benign PTCH1:exon23 c.4282G>A (p.E1428K).VAF:22.68% Uncertain significance TACC3:exon9 c.1787G>A(p.R596Q). VAF:20.33% Uncertain significance	PIK3CA:exon9 c.1637A>G(p.Q546R). VAF:52.6% Likely pathogenic SMARCB1:exon8 c.1091_1093del (p.K364del).VAF:14.87% Uncertain significance MYCN:exon2 c.131C>T(p.P44L). VAF:11.52% Uncertain significance	PIK3CA:exon20 c.3145G>C(p.G1049R). VAF:45.9% Likely pathogenic CHD4:exon25 c.3740T>C(p.I1247T). VAF:2.03% Uncertain significance
CNV			**NKX2-1** (CN:4.2)	
TMB (per megabase)	7.4 mutations	7.4 mutations	3.2 mutations	2.1 mutations
Microsatellite analysis		No mutations in DNA mismatch repair genes were detected		

CN, copy number; CNV, copy number variation; TMB, tumor mutational burden; VAF, variant allele frequency.

occur in EECs. Features in favor of MLA include a lack of endometrioid intraepithelial neoplasia in the background, absence of unequivocal squamous differentiation and intracytoplasmic mucin, and identification of cytological features of nuclei with vesicular chromatin and nuclear grooves. Positive immunoreactivity for GATA3 and TTF1 and negativity for ER and PR support the diagnosis of MLA. When a micropapillary architectural pattern in association with high-grade nuclear atypia is observed, SC should be considered in the differential diagnosis. SC is characterized by mutation-type p53 immunostaining pattern and p16 block-staining, features that are never seen in MLA. ER and PR are not helpful in differentiating because both MLA and SC share negative hormone receptor expression. The occurrence of admixtures of architectural patterns and, rarely, a papillary pattern covered by hobnail-type cells or cytoplasmic clearing cells sometimes renders it difficult to differentiate MLA from endometrial CCC. Although expression of HNF1β in carcinomas of mesonephric origin suggests this marker could be of limited use in distinguishing MLA from CCC, the combination of napsin A and Alpha methyacyl CoA racemase can be helpful for their distinction, as both markers are usually diffusely expressed in CCCs and only focally expressed in a minority of MLAs (27). Lastly, as mentioned above, the lack of heterologous

differentiation and the consistent absence of *TP53* mutations can distinguish MLAs containing solid areas with spindle cells from Müllerian carcinosarcomas. For metastatic MLA to the lung, the positive TTF1 staining and negative hormone receptors staining can be confused with a primary lung adenocarcinoma. In patients with a history of gynecological malignancy, one should always keep in mind to perform PAX8 staining. The presence of small tubules with eosinophilic secretions and lack of an *in situ* component provide morphological clues to metastatic MLA. Additional staining for GATA3, luminal CD10, and calretinin can further help support the diagnosis. Furthermore, metastatic MLA in the lung may closely resemble a metastatic thyroid carcinoma (28), given their shared histologic and immunophenotypic features (e.g., nuclear grooves, eosinophilic secretions within tubules, positive staining of PAX8 and TTF1, and negative staining of hormone receptors). In this setting, adding IHC for GATA3 and thyroglobulin may help distinguish the two lesions, however, comprehensive clinicopathologic correlation is critical for the distinction.

Although MLAs are difficult to diagnose, their accurate identification is important due to their relatively poor prognosis. According to the previous reports, MLA displays an aggressive biological behavior with more than half of the published cases presenting with advanced stage (FIGO≥II stage) at diagnosis (12).
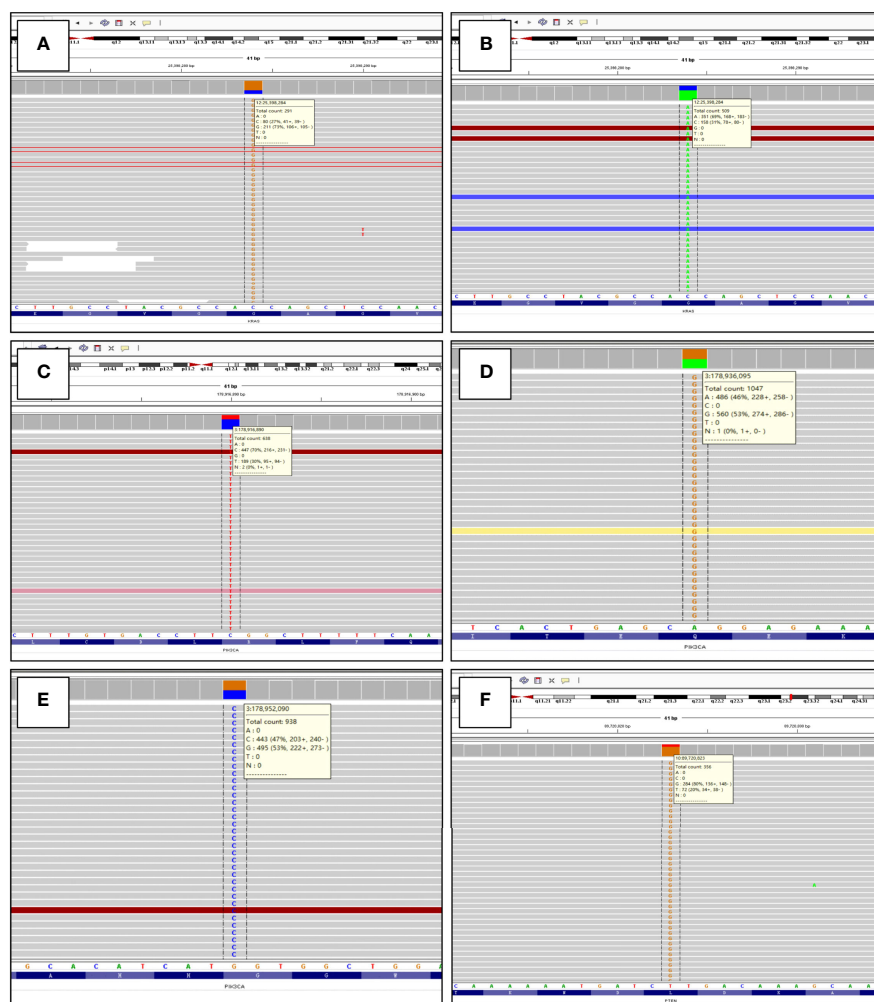
FIGURE 7 | Molecular genetic findings of uterine corpus MLA detected by targeted next-generation sequencing, as shown by the Integrative Genomics Viewer screenshot. **(A)** *KRAS* exon2: c.35G>C (p.G12A) (case 1). **(B)** *KRAS* exon2: c.35G>T (p.G12V) (case 2). **(C)** *PIK3CA* exon1: c.277C>T (p.R93W) (case 2). **(D)** *PIK3CA* exon9: c.1637A>G (p.Q546R) (case 3). **(E)** *PIK3CA* exon20: c.3145G>C (p.G1049R) (case 4). **(F)** *PTEN* exon8: c.974T>G (p.L325R) (case 1).

It is associated with a considerable risk of recurrent disease with a tendency to metastasize beyond the pelvis; especially to the lungs. Euscher et al. (13) have disclosed several frequent adverse prognostic indicators in uterine corpus MLAs, including large tumor size, deep myometrial invasion, cervical stromal invasion, and lymphovascular invasion, as compared with other histologic variants of EC, such as EEC and SC. In that study, the authors also documented that MLA was an independent risk factor for adverse patient outcomes and showed shorter progression-free survival and overall survival compared to low-grade EEC as well as SC

TABLE 5 | The most useful histopathologic and molecular genetic features for the diagnosis of uterine corpus mesonephric-like adenocarcinomas.

Morphological features	(1) In combination of a variety of growth patterns including tubular, glandular, papillary, retiform, glomeruloid, sex-cord like, spindle cells, and solid;
	(2) Columnar to cuboidal cells with distinctive nuclear features resembling those seen in papillary thyroid carcinoma, such as nuclear grooves, nuclear overlap, and open chromatin;
	(3) The presence, at least focally, of densely eosinophilic intraluminal secretions in the tubules;
	(4) The lack of marked nuclear atypia and pleomorphism, and unequivocal squamous differentiation.
Immunohistochemical features	(1) Mostly positive for GATA3 and TTF1, and less commonly for calretinin and luminal CD10;
	(2) Patchy P16 and "wild type" P53 expression;
	(3) Negative for estrogen receptor (can be focally positive) and progesterone receptor.
Molecular genetic features	Somatic *KRAS* mutations (in up to 90% cases), with or without mutations in *PIK3CA*, *PTEN*, and *CTNNB1*.

(13). The aggressive biology of MLA has further been confirmed by two recently published large series of studies. In the first study that included 44 MLAs of the uterine corpus and 25 MLAs of the ovary, 59% of the former and 42% of the latter developed recurrences, most commonly distant. The 5-year disease-specific survival (DFS) for MLA of the uterine corpus and ovary was 72% and 71%, respectively (14). In the second study including 25 MLAs of the uterine corpus, among the 23 cases with follow-up periods of more than 3 months, 72% showed local or metastatic recurrences, with a mean DFS of 22.6 months (15). In our study, three of the four patients presented with advanced-stage disease, developed tumor metastasis, or died of the disease. On the basis of integrated genomic characterization, endometrial cancers are classified into four molecular groups indicating stratified prognosis (26). Since MLAs have an absence of *POLE* mutation, *TP53* mutation, and mismatch repair-deficient, they belong to the group with no specific molecular profile and are probably responsible for the proportion of poor prognosis in this group.

Given their marked propensity for aggressive behaviors, and given that patients who receive surgery for early-stage disease have a tendency to suffer a recurrence and metastasis, previous studies have recommended that uterine MLAs should not be graded by the FIGO grading system but should all be automatically regarded as high-grade and therefore treated by algorithms utilized for high-grade ECs (13, 14). Because of its rarity, there are not yet clear clinical guidelines for the management of MLA, and the efficacy of adjuvant radiation and/or chemotherapy remains largely unknown (12). However, a recently published report showed sustained response to a combination of lenvatinib and pembrolizumab in two patients with recurrent *KRAS*-mutated MLAs (29), providing evidence that uterine corpus MLAs may merit a specialized therapeutic approach. There may be a role for targeted inhibitors of the RAS/MAPK pathway in MLAs, given their underlying *KRAS* mutations and a clinical study had shown that thyroid carcinomas with *KRAS* mutations were very sensitive to lenvatinib (30). Furthermore, because the current standard of surveillance strategies for EC patients usually does not include chest imaging, some authors have proposed chest imaging could be prospectively incorporated into the surveillance strategies for patients with MLAs, given the reported high risk for pulmonary metastases, whether at diagnosis or during disease progression (21).

CONCLUSIONS

In summary, our study confirms that MLA is a rare and aggressive malignancy, representing approximately 1% of all ECs. It exhibits mixed architectures associated with distinctive immunophenotype and recurrent *KRAS* and *PIK3CA* mutations. Our findings provide further evidence to support the concept that uterine corpus MLA is derived from a Müllerian substrate with differentiation along mesonephric lines. Increasing prospective and retrospective recognition of this unusual variant of EC is critical to better understanding the clinical and therapeutic implications of this diagnosis.

DATA AVAILABILITY STATEMENT

The original contributions presented in the study are included in the article/supplementary material, further inquiries can be directed to the corresponding author/s.

ETHICS STATEMENT

The studies involving human participants were reviewed and approved by the Institutional Review Board Committee of Zhejiang Provincial People's Hospital, Affiliated People's Hospital of Hangzhou Medical College. Written informed consent for participation was not required for this study in accordance with the institutional requirements.

AUTHOR CONTRIBUTIONS

TM, MC, and MZ conceptualized the study concept and design. HS provided the follow-up information and analyzed the clinical data. TM and MZ were in charge of the histologic diagnosis and interpretation of immunohistochemistry and analysis of the results of the targeted next-generation sequencing. TM and MC drafted the manuscript, and MZ and GR revised the manuscript. All authors contributed to the article and approved the submitted version..

REFERENCES

1. Clement PB, Young RH, Keh P, Ostör AG, Scully RE. Malignant Mesonephric Neoplasms of the Uterine Cervix. A Report of Eight Cases, Including Four With a Malignant Spindle Cell Component. *Am J Surg Pathol* (1995) 19 (10):1158–71. doi: 10.1097/00000478-199510000-00006

2. Silver SA, Devouassoux-Shisheboran M, Mezzetti TP, Tavassoli FA. Mesonephric Adenocarcinomas of the Uterine Cervix: A Study of 11 Cases With Immunohistochemical Findings. *Am J Surg Pathol* (2001) 25(3):379–87. doi: 10.1097/00000478-200103000-00013

3. Howitt BE, Nucci MR. Mesonephric Proliferations of the Female Genital Tract. *Pathology* (2018) 50(2):141–50. doi: 10.1016/j.pathol.2017.11.084

4. McFarland M, Quick CM, McCluggage WG. Hormone Receptor-Negative, Thyroid Transcription Factor 1-Positive Uterine and Ovarian Adenocarcinomas: Report of a Series of Mesonephric-Like Adenocarcinomas. *Histopathology* (2016) 68(7):1013–20. doi: 10.1111/his.12895

5. Deolet E, Van Dorpe J, Van de Vijver K. Mesonephric-Like Adenocarcinoma of the Endometrium: Diagnostic Advances to Spot This Wolf in Sheep's Clothing. A Review of the Literature. *J Clin Med* (2021) 10(4):698. doi: 10.3390/jcm10040698

6. Singh N, Euscher ED, Hoang LN, Ip PPC, Park KJ. *WHO Classification of Tumours Editorial Board. Other Endometrial Carcinomas. WHO Classification of Female Genital Tumours. 5th ed.* Lyon, France: IARC Press (2020) p. 264–5.

7. Mirkovic J, Sholl LM, Garcia E, Lindeman N, MacConaill L, Hirsch M, et al. Targeted Genomic Profiling Reveals Recurrent KRAS Mutations and Gain of Chromosome 1q in Mesonephric Carcinomas of the Female Genital Tract. *Mod Pathol* (2015) 28(11):1504–14. doi: 10.1038/modpathol.2015.103

8. Pors J, Cheng A, Leo JM, Kinloch MA, Gilks B, Hoang L. A Comparison of GATA3, TTF1, CD10, and Calretinin in Identifying Mesonephric and Mesonephric-Like Carcinomas of the Gynecologic Tract. *Am J Surg Pathol* (2018) 42(12):1596–606. doi: 10.1097/PAS.0000000000001142

9. Mirkovic J, McFarland M, Garcia E, Sholl LM, Lindeman N, MacConaill L, et al. Targeted Genomic Profiling Reveals Recurrent KRAS Mutations in Mesonephric-Like Adenocarcinomas of the Female Genital Tract. *Am J Surg Pathol* (2018) 42(2):227–33. doi: 10.1097/PAS.0000000000000958

10. Na K, Kim HS. Clinicopathologic and Molecular Characteristics of Mesonephric Adenocarcinoma Arising From the Uterine Body. *Am J Surg Pathol* (2019) 43(1):12–25. doi: 10.1097/PAS.0000000000000991

11. da Silva EM, Fix DJ, Sebastiao APM, Selenica P, Ferrando L, Kim SH, et al. Mesonephric and Mesonephric-Like Carcinomas of the Female Genital Tract: Molecular Characterization Including Cases With Mixed Histology and Matched Metastases. *Mod Pathol* (2021) 34(8):1570–87. doi: 10.1038/s41379-021-00799-6

12. Horn LC, Höhn AK, Krücken I, Stiller M, Obeck U, Brambs CE. Mesonephric-Like Adenocarcinomas of the Uterine Corpus: Report of a Case Series and Review of the Literature Indicating Poor Prognosis for This Subtype of Endometrial Adenocarcinoma. *J Cancer Res Clin Oncol* (2020) 146(4):971–83. doi: 10.1007/s00432-019-03123-7

13. Euscher ED, Bassett R, Duose DY, Lan C, Wistuba I, Ramondetta L, et al. Mesonephric-Like Carcinoma of the Endometrium: A Subset of Endometrial Carcinoma With an Aggressive Behavior. *Am J Surg Pathol* (2020) 44(4):429–43. doi: 10.1097/PAS.0000000000001401

14. Pors J, Segura S, Chiu DS, Almadani N, Ren H, Fix DJ, et al. Clinicopathologic Characteristics of Mesonephric Adenocarcinomas and Mesonephric-Like Adenocarcinomas in the Gynecologic Tract: A Multi-Institutional Study. *Am J Surg Pathol* (2021) 45(4):498–506. doi: 10.1097/PAS.0000000000001612

15. Kim H, Na K, Bae GE, Kim HS. Mesonephric-Like Adenocarcinoma of the Uterine Corpus: Comprehensive Immunohistochemical Analyses Using Markers for Mesonephric, Endometrioid and Serous Tumors. *Diagnostics (Basel)* (2021) 11(11):2042. doi: 10.3390/diagnostics11112042

16. Kolin DL, Costigan DC, Dong F, Nucci MR, Howitt BE. A Combined Morphologic and Molecular Approach to Retrospectively Identify KRAS-Mutated Mesonephric-Like Adenocarcinomas of the Endometrium. *Am J Surg Pathol* (2019) 43(3):389–98. doi: 10.1097/PAS.0000000000001193

17. McCluggage WG, Vosmikova H, Laco J. Ovarian Combined Low-Grade Serous and Mesonephric-Like Adenocarcinoma: Further Evidence for a Mullerian Origin of Mesonephric-Like Adenocarcinoma. *Int J Gynecol Pathol* (2020) 39(1):84–92. doi: 10.1097/PGP.0000000000000573

18. Koh HH, Park E, Kim HS. Mesonephric-Like Adenocarcinoma of the Ovary: Clinicopathological and Molecular Characteristics. *Diagnostics (Basel)* (2022) 12(2):326. doi: 10.3390/diagnostics12020326

19. Nilforoushan N, Liu L, Finkelman BS, Andersen J, Liu Y, James J, et al. Ovarian Combined Serous Borderline Tumor/Low-Grade Serous Carcinoma and Mesonephric-Like Lesion: Report of 2 Cases With New Observations. *Int J Gynecol Pathol* (2022). doi: 10.1097/PGP.0000000000000868

20. Deolet E, Arora I, Van Dorpe J, van der Meulen J, Desai S, Van Roy N, et al. Extrauterine Mesonephric-Like Neoplasms: Expanding the Morphologic Spectrum. *Am J Surg Pathol* (2022) 46(1):124–33. doi: 10.1097/PAS.0000000000001766

21. Mills AM, Jenkins TM, Howitt BE, Fan J, Ring KL, Cook I. Mesonephric-Like Endometrial Carcinoma: Results From Immunohistochemical Screening of 300 Endometrial Carcinomas and Carcinosarcomas for This Often Overlooked and Potentially Aggressive Entity. *Am J Surg Pathol* (2022). doi: 10.1097/PAS.0000000000001873

22. Patel V, Kipp B, Schoolmeester JK. Corded and Hyalinized Mesonephric-Like Adenocarcinoma of the Uterine Corpus: Report of a Case Mimicking Endometrioid Carcinoma. *Hum Pathol* (2019) 86:243–8. doi: 10.1016/j.humpath.2018.08.018

23. Choi S, Na K, Kim SW, Kim HS. Dedifferentiated Mesonephric-Like Adenocarcinoma of the Uterine Corpus. *Anticancer Res* (2021) 41(5):2719–26. doi: 10.21873/anticanres.15053

24. Ervine A, Leung S, Gilks CB, McCluggage WG. Thyroid Transcription Factor-1 (TTF-1) Immunoreactivity is an Adverse Prognostic Factor in Endometrioid Adenocarcinoma of the Uterine Corpus. *Histopathology* (2014) 64(6):840–6. doi: 10.1111/his.12332

25. Engelsen IB, Stefansson IM, Akslen LA, Salvesen HB. GATA3 Expression in Estrogen Receptor Alpha-Negative Endometrial Carcinomas Identifies Aggressive Tumors With High Proliferation and Poor Patient Survival. *Am J Obstet Gynecol* (2008) 199(5):543.e1–7. doi: 10.1016/j.ajog.2008.04.043

26. Cancer Genome Atlas Research Network, Kandoth C, Schultz N, Cherniack AD, Akbani R, Liu Y, et al. Integrated Genomic Characterization of Endometrial Carcinoma. *Nature* (2013) 497(7447):67–73. doi: 10.1038/nature12113

27. Pors J, Segura S, Cheng A, Ji JX, Tessier-Cloutier B, Cochrane D, et al. Napsin-A and AMACR are Superior to HNF-1β in Distinguishing Between Mesonephric Carcinomas and Clear Cell Carcinomas of the Gynecologic Tract. *Appl Immunohistochem Mol Morphol* (2020) 28(8):593–601. doi: 10.1097/PAI.0000000000000801

28. Yamamoto S, Sakai Y. Pulmonary Metastasis of Mesonephric-Like Adenocarcinoma Arising From the Uterine Body: A Striking Mimic of Follicular Thyroid Carcinoma. *Histopathology* (2019) 74(4):651–3. doi: 10.1111/his.13798

29. Shen S, Rubinstein MM, Park KJ, Konner JA, Makker V. Sustained Response to Lenvatinib and Pembrolizumab in Two Patients With KRAS-Mutated Endometrial Mesonephric-Like Adenocarcinoma. *Gynecol Oncol Rep* (2021) 37:100844. doi: 10.1016/j.gore.2021.100844

30. Cabanillas ME, Schlumberger M, Jarzab B, Martins RG, Pacini F, Robinson B, et al. A Phase 2 Trial of Lenvatinib (E7080) in Advanced, Progressive, Radioiodine-Refractory, Differentiated Thyroid Cancer: A Clinical Outcomes and Biomarker Assessment. *Cancer* (2015) 121(16):2749–56. doi: 10.1002/cncr.29395

frontiers | Frontiers in Oncology

Role of the Glyoxalase System in Breast Cancer and Gynecological Cancer-Implications for Therapeutic Intervention: a Review

Jingyuan Wang, Xiao Yang, Zhiqi Wang and Jianliu Wang[*]

Peking University People's Hospital, Beijing, China

Methyglyoxal (MGO), an essential endogenous dicarbonyl metabolite, can lead to multiple physiological problems including hyperglycemia, kidney diseases, malignant tumors, beyond its normal concentration range. The glyoxalase system, making MGO maintained at a low level, links glycation to carcinogenesis, growth, metastasis, and cancer chemotherapy. The glyoxalase system comprises glyoxalase 1 (Glo1) and glyoxalase 2 (Glo2), which is often overexpressed in various tumor tissues. However, very little is known about the glyoxalase system in breast cancer and gynecological cancer. In this review, we introduce the role of the glyoxalase system in breast cancer, endometrial cancer, ovarian cancer and cervical cancer, and highlight the potential of the glyoxalase system to be both as a marker for diagnosis and a novel target for antitumor therapy. However, the intrinsic molecular biology and mechanisms of the glyoxalase system in breast cancer and gynecological cancer need further exploration.

Keywords: glyoxalase system, endometrial cancer, methyglyoxal, ovarian cancer, cervical cancer, breast cancer

1. INTRODUCTION

Tumor cells are characterized by uncontrolled growth and proliferation, with an oncometabolic hallmark of favored use of glycolysis for lactate production even under oxygen-rich conditions, referred to as "the Warburg effect" (1–3). This effect is seen as part of metabolic reprogramming in tumors to provide conditions for their proliferation, migration, survival, and drug resistance (3). In fact, the imbalance of energy metabolism is an important driving factor of oncogenesis, with a significant metabolic result being intracellular accumulation of methyglyoxal (MGO). This tends toward causing toxic effects on cells, inhibiting growth and promotion of apoptosis. Increased glyoxalase expression and activity compensate for the accumulation of cytotoxic metabolites in tumor cells. Glyoxalase system, mainly consisting of Glyoxalase 1 (Glo1) and Glyoxalase 2 (Glo2), is a defensive pathway against dicarbonyl stress produced by MGO (4). The formation of MGO increases under conditions of high glycolytic flux, encountered by all cancer cells. When this happens, this detoxification system works and endows tumor cells with adaptive advantage.

Thus, the glyoxalase system is particularly abundant in cancerous cells and this fact has been confirmed by some studies. However, very little is known about the glyoxalase system in gynecological cancer and most work has been done on breast cancer considering female cancers.

Thus, the purpose of this review is to introduce the role of the glyoxalase system in breast cancer and gynecological cancer systematically including endometrial cancer, ovarian cancer and cervical cancer, and highlight the potential to be both as a marker for diagnosis and a novel target for antitumor therapy.

2. METHYGLYOXAL (MGO)

MGO which contains two carbonyl groups and is active in nature, together with glyoxal (GO) and 3-deoxyglucosone (3-DG), are referred to as highly reactive dicarbonyl metabolites (5). Among them, MGO is an important endogenous dicarbonyl metabolite that exists in various tissues and organs in the human body, and will cause multiple physiological problems, including hyperglycemia, kidney diseases and malignant tumors, when it exceeds its normal concentration range (6–9). Dicarbonyl stress, which is abnormal increase in the amount of dicarbonyl metabolites, leads to the increase of protein and DNA modification (10). Dicarbonyl stress can be caused by two mechanisms, including out-of-balance of dicarbonyl metabolites and increased exposure of exogenous dicarbonyls (11).

MGO is produced largely by the degradation of glyceraldehyde-3-phosphate (G3P) and dihydroxyacetone phosphate (DHAP) during glycolysis non-enzymatically (4, 12). It can also be produced during hydrolysis and dephosphorylation of DHAP and G3P (13), lipid peroxidation (14, 15), catabolism of threonine (16), oxidation of acetone catalyzed by cytochrome P4502E1 (17), and autoxidation of glucose and degradation of glycated proteins (18, 19). The likelihood of G3P degrading into MGO is eight times than that of DHAP. However, in cells in situ, the concentration of DHAP is about nine times that of G3P (20). Therefore, both forms of triosephosphates are necessary for the formation of MGO (4). MGO is attained not only during cell metabolism, but also through exogenous dietary intake; its primary sources are coffee and other types of beverages (21, 22). However, ingested MGO is metabolized and exerts dicarbonyl stress pre-systemically before absorption (23).

MGO is mostly eliminated by the glyoxalase system, with minority being metabolized by aldoketo reductases (AKRs) and aldehyde dehydrogenases (ADHs), which convert it into hydroxyacetone and pyruvate, respectively; thus, forming an enzymatic defense to prevent MGO glycation (24–28). In various human tissues, the capacity of the Glo system to metabolize MGO is 30 times that of AKRs; one exception is the renal medulla, where the expression of AKRs is particularly high (29, 30). In general, MGO is produced during glycolysis and metabolized through the glyoxalase system, at low level *in vivo*. However, when glycolysis is abnormal or food containing high MGO is consumed for a long time, the load of the scavenging system in the body becomes too heavy. This results in the over-accumulation of MGO in the body. The serious cytotoxicity and tissue damage in MGO-related metabolic disorders are likely caused by the modification of nucleic acids, free amino groups in proteins and lipids induced by a large family of MGO-derived adducts, called advanced glycation end-products (AGEs) (31). MGO interacts with deoxyguanosine, leading mainly to form the imidazopurinone adduct, MGdG (26, 32). MGdG, comprising the majority of MGO nucleotide adducts physiologically, are mutagenic and possibly related to malignant transformation (25). A small amount of 2-(1, R/S-carboxyethyl)-deoxyguanosine (CEdG) is also formed (33). The irreversible interaction of MGO with arginine results in the formation of MG-derived hydroimidazolones (MG-H1, MG-H2, and MG-H3) (34–36), argpyrimidine (37) and tetrahydropyrimidine (THP) (38). MGO can also modify lysine residues to form Nє-(1-carboxyethyl) lysine (CEL) and 1,3-di(Nє-lysino)-4-methyl-imidazolium (MOLD), although to a much lesser extent than arginine (39). MGO can also react with one lysine and one arginine, leading to the formation of an adduct called MODIC (40). MGO also induces stable lipid modifications (**Figure 1**).

Additionally, AGEs can bind to the receptor for AGEs (RAGE), mediating signal transduction and stimulating intracellular reactive oxygen species (ROS) generation. Activation of RAGE signaling is related to various cellular changes, including inflammation and oxidative stress, which play a role in carcinogenesis, and increased cell death by apoptosis and anoikis (26, 41–44). Decreased expression of RAGE is associated with the inhibition of tumor development and metastasis (45).

3. GYOXAL (GO)

In addition to MGO, GO is also an endogenous highly reactive dicarbonyl metabolites. The formation of GO seems to be inevitable in organism, since they are closely connected with several physiological processes, such as lipid peroxidation and degradation of monosaccharides, saccharide derivatives and glycated proteins (46, 47). Since GO is a potent glycating agent, modification of proteins and nucleotides has been found. GO can react with proteins to form AGE residues directly, with arginine residues being the most reactive protein (48). DNA is also susceptible to glycation by GO, with deoxyguanosine (dG) being the most common modified nucleotide AGEs. GO was responsible for increased mutations and decreased DNA replication. Nearly half of mutations were single-base substitutions with more than 80% occurring at C:G sites. Furthermore, GO was in relation to non-random or hotspot mutation sites (49). Similar to MGO, elevation in GO also leads to dicarbonyl stress, which is associated with various health problems and the modification by GO is regarded as damage to physiological systems. However, this can be suppressed by detoxification of GO, catalysed mainly by the glyoxalase system (47, 50). In most cases, GSH was utilized to convert GO to S-2-hydroxyethylglutathione, mediated by GSH-dependent Glyoxalases, Glo1 and Glo2. In some cases, GO can also be the substrate of Glyoxalase 3 (Glo3), but without any cofactors (51, 52).
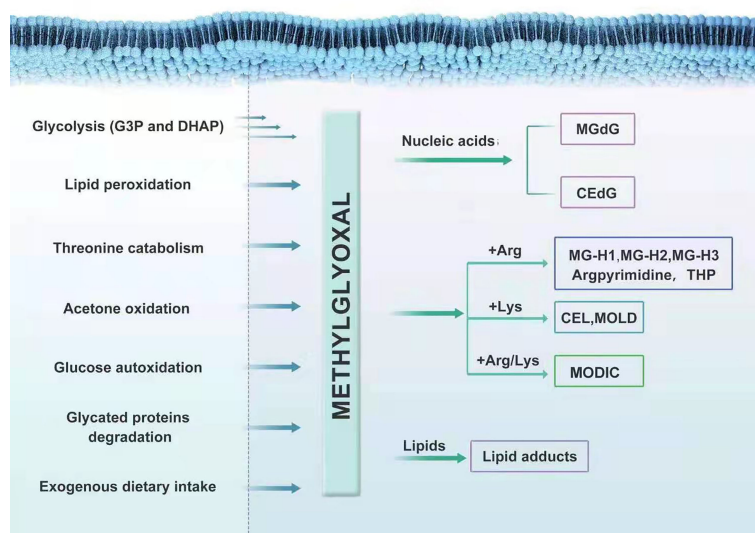
**FIGURE 1** | The formation and metabolism of MGO.

4. GLYOXALASE SYSTEM

The glyoxalase system is one of the well-defined associations between glycation and carcinogenesis and progression. It was first introduced by Dakin, Dudley in 1913 (32). This system, existing in the cytoplasm of all human cells, mainly consists of two cooperating enzymes, namely, Glo1 and Glo2. The main duty of the system is to metabolize MGO and other reactive acyclic a-oxoaldehyde metabolites, to maintain them at a low level, thus preventing cell and tissue dysfunction. MGO and glutathione (GSH) produce hemithioacetal through a non-enzymatic reaction. Then hemithioacetal is converted into S-D-lactoylglutathione, under the catalysis of Glo1. Glo2 catalyzes the hydrolysis of S-D-lactoylglutathione to D-lactate, thereby reforming GSH, to achieve detoxification of MGO (53). In this series of reactions, Glo1, as a rate-limiting enzyme, is of vital importance in the detoxification of MGO (**Figure 2**). There also exists the GSH-independent system involving Glo3 to protect cells from MGO toxicity, besides the GSH-dependent system consisting of Glo1 and Glo2. Glo3 was first identified in the Hsp31 protein from Escherichia coli, which can directly convert MGO into D-lactate in the absence of GSH (54). In recent literature, the DJ-1 proteins from Arabidopsis thaliana and metazoans have also been confirmed to have Glo3 activity like the Hsp31 protein, but they belong to two different subfamilies of the DJ-1 superfamily proteins. In animals, DJ-1 proteins appear to show Glo3 activity and the dysfunction of DJ-1 proteins can make cells sensitive to oxidative stress and cause mitochondrial disorders (54, 55). To date, however, Glo3 remains unidentified in human system. Furthermore, the regulatory mechanisms of Glo3 merit continued study. It is noteworthy that DJ-1 proteins are now considered a deglycase, rather than an alternative glyoxalase (56).

4.1 Glo1

Glo1 is a zinc-dependent metalloenzyme encircled by two identical subunits. It has a molecular mass of 43-48 kDa and is comprised of noncovalent bonds (57, 58). It exists in almost all prokaryotic and eukaryotic organisms, including animals, plants, yeast, bacteria, and protozoa. Furthermore, its widespread distribution reflects its important physiological functions in biological life. Moreover, it has been found that Glo1 has high homology among different species through comparison of amino acid sequences. This implies an evolutionarily conserved function for Glo1. Human Glo1 is located on chromosome 6 at locus 6p21.2, with five introns and six exons. It is often overexpressed in tumor tissues (59–61).

The mechanism by which Glo1 expression is regulated is complex. It is controlled by various regulatory elements and that can be altered by the changes in gene expression and post-translational enzymatic modifications (62, 63). Transcriptional regulators of Glo1 include activator protein-2α (AP-2α), early gene 2 factor isoform 4 (E2F4), nuclear transcription factor-κB (NF-κB), activator protein-1 (AP-1), antioxidant response (ARE), metal response (MRE), and insulin response (IRE) elements. Post-translational modifications are achieved through phosphorylation, nitrosylation, and glutathionylation. Among these, Glo1 expression is positively regulated by AP-2α, E2F4, NF-κB and nuclear factor erythroid 2-related factor 2 (Nrf2) by enhancing the Glo1 promoter. For instance, expression is controlled by Nrf2 during stress by binding with AREs (64, 65). In tumor cells, the enhanced expression of Nrf2 leads to increased activity of the enzyme, thereby preventing dicarbonyl stress. Therefore, Nrf2 is often over-activated in hepatocellular carcinoma and thus contributes to increased mortality (66). It has been demonstrated that Nrf2 activators, including sulforaphane and resveratrol, act as Glo1 inducers (67).
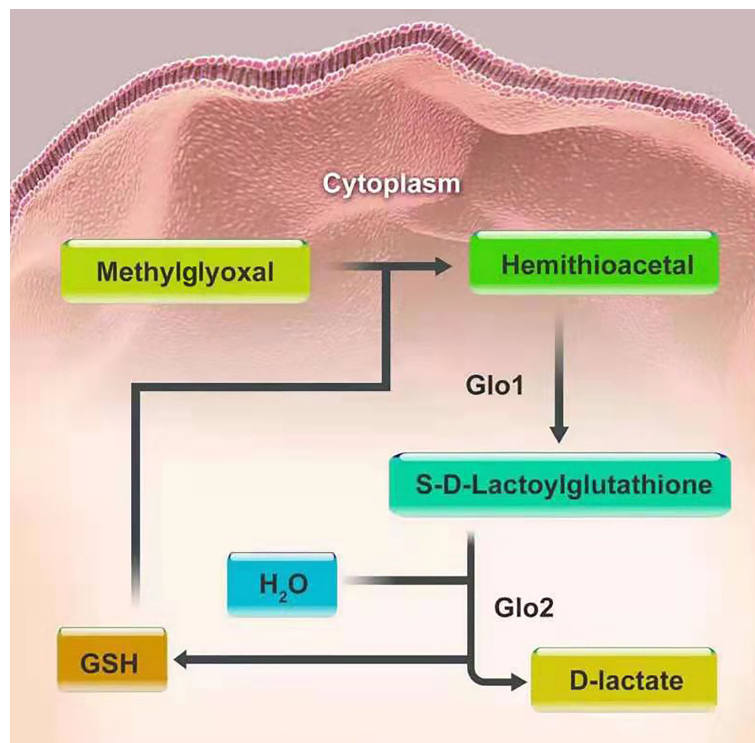
FIGURE 2 | The detoxification of MGO.

Nuclear translocation of Nrf2, which is of vital importance in the activation of Glo1, can be disrupted by the combination of MGOs to Kelch-like ECH-associated protein 1 (Keap1). Based on this principle, MGO inhibitors can help detoxification in cells *via* the Nrf2/Keap1 pathway by elevating GSH levels and accelerating MGO metabolism (68). In contrast, the expression of Glo1 is also negatively mediated by hypoxia-inducible factor-1α(HIF1α), the receptor for advanced glycation end products (RAGE). Its levels are also impacted by conflict between the NF-κB system activated in inflammation and Nrf2 (69, 70).

Copy number variation (CNV) of the Glo1 gene in the human genome will also allow for increased expression of Glo1 with low-level duplication in the healthy population (71). The Glo1 DNA segment copy number increase was larger among illness affected groups than that in the healthy population with low-level duplication (72). In a study of 225 different types of human tumors, increased Glo1 copy number was discovered in 8% of tumors, with the highest prevalence of Glo1 amplification in breast cancer (22%), followed by sarcomas (17%) and non-small cell lung cancer (11%) (73). The correlation between Glo1 copy number increase assessed by qPCR and poor survival in gastric cancers has been ameliorated (74).

4.2 Glo2

Human Glo2 is another enzyme in the glyoxalase system. It is encoded by the hydroxyacylglutathione gene (HAGH[1]). Genetic polymorphisms of Glo2 are rare, with HAGH[2] being

the only the second phenotype expressed (75). It is a binuclear metalloenzyme with a Zn(II) site as the catalytically active site metal ion. By contrast, the Fe(II) site has no influence on the catalytic activity (70). However, the molecular structures of Glo2 share the same overall fold as Zn(II)-dependent metallo-β-lactamases (76). There are two isoforms of Glo2 depending on their localization in cellular compartments. This includes the mitochondrial form with a molecular mass of 33.8 kDa and a cytosolic form with a molecular mass of 29.2 kDa (77). Despite their differences, the two isoforms have identical isoelectric points of 8.3 (78).

Emerging evidence pointed out the novel independent role of this ancient enzyme from that of Glo1 in a possibly nonenzymatic manner in some malignant cells. In Cinzia et al.'s study, Glo2 was involved in the proapoptotic effects of Oleuropein in non-small-cell lung cancer A549 cells (79). Oleuropein led to an increase in mitochondrial Glo2 protein expression levels without enhancing the enzyme's activity. Conversely, Oleuropein did not affect expression or function of cytosolic Glo2. Through upregulation of mitochondrial Glo2, Oleuropein is able to induce apoptosis in A549 cells which is mediated by the superoxide anion and Akt signaling pathway. In addition, the proapoptotic effect of mGlo2 is related to the interaction with the Bax protein. Even though there is no distinction between the mitochondrial or cytosolic isoforms, this emerging independent role turns out to be opposite in prostate cancer cells, where an antiapoptotic nonenzymatic

role of Glo2 was identified (80). In prostate cancer cells, this ancient enzyme is able to stimulate cell proliferation and elude apoptosis in a mechanism dependent on androgen receptor and involving the p53-p21 axis (81).

5. BREAST CANCER

Breast cancer is the most common cancer in women worldwide with an estimated 2.09 million cases and 0.6 million deaths annually (82). It is a heterologous disease and categorized corresponding to the so-called intrinsic breast cancer subtypes employing the expression of estrogen receptor (ER), progesterone (PR) and human epidermal growth factor receptor 2 (HER2), together with the frequency of ki-67 (83, 84). Moreover, treatment strategy is designed based on the expression of receptors and ki-67 (5). The use of anti-endocrine therapy to downregulate ER signaling is the primary systemic therapy for ER-positive or PR-positive cases by receptor mediators such as tamoxifen. Patients with HER2-positve benefit from monoclonal antibodies directed against this EGF-receptor, such as trastuzumab and pertuzumab. For triple negative cases, there is no targeted therapy in routine clinical use, thus, most patients are treated with chemotherapy (6). However, this immunohistochemistry-based clinical classification is only a substitute for gene expression analysis and cannot identify all internal molecular characteristics (84).

To our knowledge, the first study giving a comprehensive picture of the role of Glo1 in breast cancer dates back to the 2001, when A Rulli et al. measured Glo1 specific activity in breast carcinoma and normal mammary gland tissue (85). Samples were drawn in the period from 1999 to 2000 of 20 women and Glo1 was significantly upregulated in human breast cancer cells and tissues, as shown by both spectrophotometrical assay and electrophoretic pattern compared with normal counterparts. A consistent enhanced of Glo1 expression was observed either at mRNA or protein level in human breast cancer tissues parallel with pair-matched normal tissue, providing evidence for a potential role of this enzyme in breast cancer (86–89). In addition, Glo1 promoted cell proliferation, invasion and migration and suppressed cell apoptosis. Hence, Glo1 overexpression correlated with aggressive clinicopathological features including lymph node metastasis, lymphovascular invasion, tumor grade and TNM stage and was an independent prognostic factor for clinical outcome of breast cancer patients. Specifically, patients with Glo1 overexpression had a shorter overall survival and recurrence-free survival than those with low Glo1 expression (88, 90). Moreover, knockdown of Glo1 suppressed invasion and migration and promoted apoptosis of breast cancer cells *in vitro* (88). These results suggest that Glo1 is significantly associated with tumorigenesis, metastasis, and poor prognosis, providing new impetus to the exploring the expression of Glo1. Additionally, gene expression data demonstrated that Glo-1 mRNA was regulated through a mechanism involving inflammation (NF-kB) and oxidative stress (NFE2L2) in malignant breast cells (91). In Guo et al.

study, Glo1 restraint treatment can hinder occurrence and development of breast cancer cells, adjusted by actuation of the MAPK signaling pathway and downregulation of Bcl-2 and MMP-9 (92). However, the intrinsic molecular biology and mechanisms of breast carcinogenesis remain to be further elucidated.

Therefore, Glo1 is involved in the regulation of tumorigenesis, proliferation, migration and survival in breast cancer (93). These data has supported the role of Glo1 as a potential target for anticancer drug development, which were indeed confirmed by some studies. Clinically, a major obstacle in the process of treating tumor lies in drug resistance. It has been reported in previous literature that chemotherapeutic resistance, including doxorubicin, was associated with upregulation of Glo1 (94). Recent studies on the mechanism of drug resistance of breast cancer have found that Glo1 inhibitors can reserve drug resistance of tumor cells. Davies et al. showed that the thiazolidinedione troglitazone downregulated Glo1 expression, leading to a regained sensitivity to doxorubicin. Furthermore, it is also reported that Glo1 abundance could predict the outcome of radiotherapy and overexpression of Glo1 was associated with a shorter relapse free survival after receiving radiotherapy (91). It is reported that more than 50% of all drugs used in tumor treatment contain either natural origin active principles or semisynthetic derivatives, thus, there is an urgent need to find new drugs from bioactive compounds (95). In a recent study, the influence of resveratrol, curcumin and piperine on Glo1 activity and expression was assessed in MCF-7 cell. The dose-dependent inhibitory effects of resveratrol, curcumin and piperine on Glo1 activity were observed after 24 hours of treatment. However, the expression of Glo1 could be reduced only by curcumin, due to the possible fact that resveratrol and piperine affect the activity of Glo1 in a posttranslational manner (96). Similar conclusions were also obtained to confirm the effect of curcumin on Glo1 (97, 98).

Moreover, distant metastasis would be present in 15% of patients with breast cancer, and contribute to approximately 90% of cancer-associated mortality (99). Thus, determining potential key regulators in the process of cancer metastasis seems to be increasingly important. According to a recent report, in patients with stage III−IV breast cancer, Glo1 and PKCλ may be cooperatively involved in cancer progression and patients with high Glo1 and PKCλ expression had worse prognosis (87). In addition, the Glo1 inhibitor, TLSC702, and the PKCλ inhibitor, aurothiomalate, may serve as novel pharmacological approaches to manage late−stage breast cancer through suppressing both cell viability and tumor−sphere formation in MDA−MB−157 and MDA−MB−468 human basal−like breast cancer cells. However, there is absence of *in vivo* studies using TLSC702 or aurothiomalate, further investigation of the inhibitors is needed in future.

It is worth noting that in the study of Marie-Julie Nokin et al., a tumor-suppressing role of Glo1 in breast cancer cells was identified for the first time (100, 101). Silencing of Glo1, bearing a higher level of MGO, promoted tumor growth and metastasis *in vivo* and Glo1-depleted breast cancer cells induced a

significant increase in pulmonary tumor burden. A similar role of Glo1 has also been validated in hepatocellular carcinoma and downregulation of Glo1 enhanced tumor growth (102). The mechanism was further revealed that metastasis was associated with the activation of MEK/ERK/SMAD1 cascade in breast cancer cells (101). Moreover, this study investigates therapeutic potential of MG scavengers, including carnosine and aminoguanidine, as promising target in the management of metastatic breast cancer.

In fact, these seemingly contradictory data might be explained by the effect exerted by MGO on cancer cells that is defined by low-dose stimulation and high-dose inhibition of tumor metastasis (103). Thus, it is necessary to determine the MGO concentrations when Glo1 inhibitor applied.

6. ENDOMETRIAL CANCER

Endometrial cancer is the most common gynecological malignancy in the United States, and its related mortality is on the rise (104). Surgical staging system including laparoscopic total hysterectomy, bilateral salpingo-oophorectomy, and sentinel lymph-node mapping, has been adopted. Most cases are diagnosed in the early stage of the disease, presenting with vaginal bleeding. Hence, the prognosis is good, with the overall five year survival rate being 90.88% for patients staged as IA using the FIGO 1988 surgical classification (105). However, challenges still remain, including increasing radical disparities in mortality (106).

6.5% of the patients suffered from endometrial cancer are younger than 45 years of age (107). Women of childbearing age prefer to preserve their fertility for future opportunities to give birth, rather than receive the standard surgical treatment of total hysterectomy with bilateral salpingo-oophorectomy, sentinel lymph node mapping and pelvic/para-aortic lymphadenectomy when necessary. Fertility preservation is suitable for young women with stage I, grade I adenocarcinoma. Thus, alternative treatments involving synthetic progestins, including medroxyprogesterone acetate (MPA), are the mainstays of such management. Unfortunately, about 30% of said alternatively treated cases, fail to respond to progestins initially. Although the response rate is approximately 70%, 57% of patients relapse and develop drug resistance (108). In brief, progestin resistance restricts the validity of progestin treatment. Zhang et al. reported that the expression of Glo1 in progestin-resistant Ishikawa cells was increased 2.4-fold higher than that in parental cells. This suggests that Glo1 is related to progestin resistance in endometrial cancer. Further, metformin, an insulin sensitizer, can downregulate Glo1 expression to enhance the response to MPA treatment by blocking PI3K-mTOR activation (109). In another study, metformin sensitizes progestin in endometrial cancer through downregulation of Ten-eleven translocation 1 (TET1), a dioxygenase responsible for transferring 5-methylcytosine into 5-hydroxymethylation and CpG islands enriched in the promoter region of Glo1 are possible target of TET1. Therefore, metformin enhances progestin sensitivity

underlying the potential mechanism of TET1/5hmC/GLOI signaling pathway (110). Therefore, the combination of metformin and MPA is likely an effective strategy for conservative treatments of endometrial cancer and accumulating evidence suggests that Glo1 is a potential target gene of metformin.

Traditionally, chemotherapy has been extensively used an adjuvant treatment for endometrial cancer. However, in this case, the initial reaction of malignant endometrial tumor cells to chemotherapy turns refractory over time, resulting in high rates of chemoresistance (111). There is an urgent need to address this issue. Considering that obesity and diabetes are risk factors for the incidence of endometrial cancer, it may be partly caused by metabolic disorders (112). Metformin, a well-tolerated biguanide drug, has been implicated in the treatment of various tumors, including endometrial cancer. According to research, compared with cisplatin and paclitaxel alone, as the first-line chemotherapeutics for endometrial cancer therapy, the administration of metformin strongly inhibits the proliferative activity of tumor cells (113). Further investigation of the possible molecular mechanism by which metformin enhances, chemotherapeutic drug-mediated cytotoxicity, revealed that increasing the dose of metformin reduces the expression of Glo1 protein. This indicates that metformin can enhance sensitivity to chemotherapeutic drugs in endometrial cancer by downregulating Glo1 expression. In fact, since overexpression is present in various cancers, aberrant expression of Glo1 is involved in drug resistance (85, 114). Thus, the expression pattern of Glo1 may play an important role in cancer proliferation.

Previous research has shown that the expression of Glo1 is upregulated in a variety of human malignancies, including melanoma, gastric cancer, pancreatic cancer, breast cancer, renal cancer, prostate cancer (5, 74, 80, 88, 115, 116). This result is similar to that of Sakamoto, who determined that Glo1 enzyme activity was elevated in all 38 human cancer cell lines compared to normal tissue samples (117). High expression of Glo1 is permissive for the survival of tumors with a relatively high flux of MGO formation. Furthermore, elevated Glo1 expression is associated with multidrug resistance in cancer chemotherapy (59). Davies et al. treated doxorubicin-resistant K562 leukemia cells with troglitazone, an insulin sensitizer, and drug resistance was reversed by downregulating the expression of Glo1 (114). The key to inhibiting Glo1 expression to reverse drug resistance lies in promoting cell apoptosis, and there are several potential mechanisms, as described below, although the exact mechanisms are not clear yet. Inhibiting Glo1 expression can result in MGO accumulation to cytotoxic levels that then cause cell death by apoptosis. Therefore, this mechanism is likely caused by increased intracellular MGO, as induced by antitumor agents. On the one hand, MGO has been proven to simulate the release of cytochrome C from mitochondria and subsequently induce apoptosis by modifying the mitochondrial permeability transition pore (118). In addition, nucleic acids and free amino groups in anti-apoptotic proteins can be modified by MGO, thus potentially leading to apoptosis. For example, MGO may enhance the anti-apoptotic activity of Hsp27 by inhibiting

the activation of caspase-3 and caspase-9 mediated by cytochrome c to protect cancer tumors from cell deaths (119–121). In this way, compared to cells with low endogenous MGO-modified Hsp27, lung cancer cells with high expression of MGO-modified Hsp27 are resistant to cisplatin-induced apoptosis (119). Similarly, MGO-modified Hsp27 has been found in melanoma, lung, and gastrointestinal tumors (119, 120). Accordingly, Glo1 inhibitors can induce the activation of p38 and JNK stress-activated kinases; which activates downstream caspases in Glo1-overexpressing tumor cells to induce apoptosis (117, 122). Godbout et al. found that the cisplatin-induced apoptosis of myeloma cells was promoted by MGO through activation of protein kinase Cσ (118). Although these results suggest that MGO plays an important role in inhibiting the expression of Glo1, the exact mechanism requires further exploration. According to the literature in the field of endometrial cancer, we found that metformin was an effective inhibitor of Glo1 that had antitumor activity, although the intrinsic mechanism needs to be explored further.

7. OVARIAN CANCER

Although the incidence of ovarian cancer is not as high as that of other cancers, such as endometrial cancer, it is the most lethal of the female reproductive tract malignancies in the United States (123). Owing to a lack of suitable screening methods, diagnosis is possible only at an advanced stage for most patients; however, at this stage, the tumor has usually spread to the peritoneal cavity and upper abdominal organs, leading to poor prognosis (124). The standard treatment for ovarian cancer focuses on cytoreductive surgery followed by postoperative adjuvant chemotherapy (125). At present, the five-year survival rate is approximately 47% even in countries with advanced medical technology such as the United States and Canada, mainly due to late diagnosis, recurrence, and chemoresistance (126).

Currently, the gold standard for diagnosis relies on pathological biopsy, and early screening methods are limited. Some existing biomarkers such as carbohydrate antigen 125, human epididymis protein 4, may be helpful in screening, but the wide application is hampered by their poor sensitivity or specificity. Thus, it is very necessary to identify novel biomarkers for early detection of ovarian cancer. Considering the fact that blockade of the RAGE-ligand pathway represents a novel target for some cancer therapy (127–130), the researchers have further investigated the role of RAGE in ovarian cancer development. Data showed that RAGE expression was upregulated in ovarian cancer tissue compared with matched normal tissue (131). Moreover, a significant relation between high RAGE expression levels and poor clinicopathological features, such as tumor size, depth of stromal invasion, lymphovascular invasion and stage of tumor was observed, suggesting an important role of RAGE in ovarian cancer progression. In the present study, the area under the curve value was 0.86 for RAGE, implying a relatively high sensitivity and specificity for the RAGE mRNA level to differentiate between malignant and non-malignant tissues. Thus, the overexpression of RAGE may be a potential biomarker for diagnosis of ovarian cancer. Consistent with our results, Poljicanin et al. also came to a similar conclusion (132).

In addition, most ovarian cancers originate from a single layer of surface epithelial cells (OSE), accounting for only a small proportion of the total ovarian mass (133). Apparently, normal OSE cells from women with a family history of ovarian cancer and breast cancer are different from women without phenotypic and/or genotypic family history. Smith Beckerman examined the proteomes of both SV-40-transformed FH-OSE cell lines and control OSE lines. Expression of several proteins appeared to be elevated in the FH-OSE cells, including Glo1, suggesting that high expression of Glo1 is related to the occurrence and progression of ovarian cancer (134). Although ovarian tumors at an early stage are highly curable (135), more than 70% of cases are not diagnosed until the tumor has progressed to advanced stages (136), reflecting the potential high morbidity and mortality caused by presentation with advanced-stage disease. Monica Brown Jones revealed a high degree of overexpression of Glo1 in invasive ovarian cancers compared with the low malignant potential ovarian tumors. Her work combined the technique of laser capture microdissection of epithelial tumor cells in human tissue specimens with two-dimensional gel electrophoresis (137). Results suggest that Glo1 may be a potential marker for early detection and therapeutic targets unique to the invasive phenotype.

The exact mechanisms of Glo1 in the ovarian cancer remain unknown and Glo1 may be used as a therapeutic target in the future. Thus, more investigations are encouraged to provide more reliable data.

8. CERVICAL CANCER

The cause of cervical cancer is clear, being mostly associated with the sexually transmitted persistent human papilloma virus infection. The key to intervention lies in primary and secondary prevention (138). Standard treatment after diagnosis consists of surgical resection and concurrent chemoradiation according to the stage of the tumor and clinicopathologic risk factors. Although the number of cervical cancer cases has decreased in developed countries in the past decade, its incidence has continued to rise rapidly in developing countries (139). According to the latest cancer statistics, cervical cancer is ranked fourth in terms of morbidity and is one of the main causes of death for women with malignant tumors, with approximately 604,000 new confirmed cases as well as 342,000 death cases worldwide in 2020 (140). Thus, cervical cancer still represents a major public health problem globally and there is an urgent need for improved therapeutic options to reduce the burden.

In recent years, more and more researchers have paid attention to phyto chemicals present in various plants, with properties being time tested usage and low toxicity. Hence, Raj Kumar et al. assessed pharmacological action of the inhibitor of

Nrf-2, Galangin, an active component of galangal, present in many traditional medicines. Previous reports have confirmed that Galangin contributes to health ranging from antioxidant effect to synergestics anticancer effects with other medicine (141, 142). In the present study, Galangin can modulate Nrf-2 levels to induce cell death and inhibit metastatic potential in human cervical cancer cell line (HeLa) cells *in vitro*. This occurs by downregulating the expression of Glo1 in concentration dependent manner and increasing the damage caused by MGO and oxidative stress (143). In fact, the cytotoxicity of Galangin has been proven in other cancer cell lines, such as human colon cancer cells, melanoma cells, and renal carcinoma cells (144–146). However, little research has been conducted on the role of glyoxalases in cervical cancer. More research is needed along these lines to inform future applications.

9. CONCLUDING REMARKS

Glyoxalases are often overexpressed in various tumor tissues and they play an important role in tumor proliferation, migration, survival, and drug resistance. In this review, we introduce the role of the glyoxalase system in breast cancer and gynecological cancer, including endometrial cancer, ovarian cancer and cervical cancer. The main function of the glyoxalase system is to metabolize MGO and other reactive acyclic a-oxoaldehyde metabolites, to maintain them at a low level to prevent cell and tissue dysfunction. In most cases, Glo1 overexpression correlated with aggressive clinicopathological features and poor prognosis. However, a tumor-suppressing

role of Glo1 has also been identified in breast cancer cells. Due to the possible effect exerted by MGO on cancer cells that is defined by low-dose stimulation and high-dose inhibition of tumor metastasis, it is necessary to determine the MGO concentrations when Glo1 inhibitor applied. These data demonstrated the potential of the glyoxalase system to be as a target for diagnosis and suggested that agents designed to regulate Glo1 may provide a promising method to cancer prevention and therapy. However, the intrinsic molecular biology and mechanisms of the glyoxalase system in breast cancer and gynecological cancer remain to be further elucidated. Therefore, further research is needed in this area.

AUTHOR CONTRIBUTIONS

FUNDING

REFERENCES

1. Verze P, Cai T, Lorenzetti S. The Role of the Prostate in Male Fertility, Health and Disease. *Nat Rev Urol* (2016) 13(7):379–86. doi: 10.1038/nrurol.2016.89

2. Cutruzzolà F, Giardina G, Marani M, Macone A, Paiardini A, Rinaldo S, et al. Glucose Metabolism in the Progression of Prostate Cancer. *Front Physiol* (2017) 8:97. doi: 10.3389/fphys.2017.00097

3. Ward PS, Thompson CB. Metabolic Reprogramming: A Cancer Hallmark Even Warburg did Not Anticipate. *Cancer Cell* (2012) 21(3):297–308. doi: 10.1016/j.ccr.2012.02.014

4. Phillips SA, Thornalley PJ. The Formation of Methylglyoxal From Triose Phosphates. Investigation Using a Specific Assay for Methylglyoxal. *Eur J Biochem* (1993) 212(1):101–5. doi: 10.1111/j.1432-1033.1993.tb17638.x

5. Yumnam S, Subedi L, Kim SY. Glyoxalase System in the Progression of Skin Aging and Skin Malignancies. *Int J Mol Sci* (2020) 22(1):310. doi: 10.3390/ijms22010310

6. McLellan AC, Thornalley PJ, Benn J, Sonksen PH. Glyoxalase System in Clinical Diabetes Mellitus and Correlation With Diabetic Complications. *Clin Sci (Lond)* (1994) 87(1):21–9. doi: 10.1042/cs0870021

7. Fan X, David RS, Zhang J, Ina N, Mathilde T, Lu J, et al. Anaerobic vs Aerobic Pathways of Carbonyl and Oxidant Stress in Human Lens and Skin During Aging and in Diabetes: A Comparative Analysis. *Free Radic Biol Med* (2010) 49(5):847–56. doi: 10.1016/j.freeradbiomed.2010.06.003

8. Agalou S, Ahmed N, Babaei-Jadidi R, Dawnay A, Thornalley PJ. Profound Mishandling of Protein Glycation Degradation Products in Uremia and Dialysis. *J Am Soc Nephrol* (2005) 16(5):1471–85. doi: 10.1681/ASN.2004080635

9. Thornalley PJ, Rabbani N. Glyoxalase in Tumourigenesis and Multidrug Resistance. *Semin Cell Dev Biol* (2011) 22(3):318–25. doi: 10.1016/j.semcdb.2011.02.006

10. Rabbani N, Thornalley PJ. Glyoxalase Centennial Conference: Introduction, History of Research on the Glyoxalase System and Future Prospects. *Biochem Soc Trans* (2014) 42(2):413–8. doi: 10.1042/BST20140014

11. Rabbani N, Xue M, Thornalley PJ. Dicarbonyls and Glyoxalase in Disease Mechanisms and Clinical Therapeutics. *Glycoconj J* (2016) 33(4):513–25. doi: 10.1007/s10719-016-9705-z

12. Richard JP. Mechanism for the Formation of Methylglyoxal From Triosephosphates. *Biochem Soc Trans* (1993) 21(2):549–53. doi: 10.1042/bst0210549

13. Pompliano DL, Peyman A, Knowles JR. Stabilization of a Reaction Intermediate as a Catalytic Device: Definition of the Functional Role of the Flexible Loop in Triosephosphate Isomerase. *Biochemistry* (1990) 29 (13):3186–94. doi: 10.1021/bi00465a005

14. Baynes JW, Thorpe SR. Glycoxidation and Lipoxidation in Atherogenesis. *Free Radic Biol Med* (2000) 28(12):1708–16. doi: 10.1016/S0891-5849(00)00228-8

15. Esterbauer H, Gebicki J, Puhl H, Jürgens G. The Role of Lipid Peroxidation and Antioxidants in Oxidative Modification of LDL. *Free Radic Biol Med* (1992) 13(4):341–90. doi: 10.1016/0891-5849(92)90181-F

16. Ray M, Ray S. Aminoacetone Oxidase From Goat Liver. Formation of Methylglyoxal From Aminoacetone. *J Biol Chem* (1987) 262(13):5974–7. doi: 10.1016/S0021-9258(18)45524-X

17. Reichard GAJr., Skutches CL, Hoeldtke RD, Owen OE. Acetone Metabolism in Humans During Diabetic Ketoacidosis. *Diabetes* (1986) 35(6):668–74. doi: 10.2337/diab.35.6.668

18. Chetyrkin S, Mathis M, Pedchenko V, Sanchez OA, Hayes WM, Hachey DL, et al. Glucose Autoxidation Induces Functional Damage to Proteins via Modification of Critical Arginine Residues. *Biochemistry* (2011) 50 (27):6102–12. doi: 10.1021/bi200757d

19. Giacco F, Brownlee M. Oxidative Stress and Diabetic Complications. *Circ Res* (2010) 107(9):1058–70. doi: 10.1161/CIRCRESAHA.110.223545

20. Veech RL, Raijman L, Dalziel K, Krebs HA. Disequilibrium in the Triose Phosphate Isomerase System in Rat Liver. *Biochem J* (1969) 115(4):837–42. doi: 10.1042/bj1150837

21. Nagao M, Fujita Y, Wakabayashi K, Nukaya H, Kosuge T, Sugimura T, et al. Mutagens in Coffee and Other Beverages. *Environ Health Perspect* (1986) 67:89–91. doi: 10.1289/ehp.866789

22. Wang J, Chang T. Methylglyoxal Content in Drinking Coffee as a Cytotoxic Factor. *J Food Sci* (2010) 75(6):H167–71. doi: 10.1111/j.1750-3841.2010.01658.x

23. Degen J, Vogel M, Richter D, Hellwig M, Henle T. Metabolic Transit of Dietary Methylglyoxal. *J Agric Food Chem* (2013) 61(43):10253–60. doi: 10.1021/jf304946p

24. Zhang S, Liang X, Zheng X, Huang H, Chen X, Wu K, et al. Glo1 Genetic Amplification as a Potential Therapeutic Target in Hepatocellular Carcinoma. *Int J Clin Exp Pathol* (2014) 7(5):2079–90.

25. Rabbani N, Thornalley PJ. Glyoxalase 1 Modulation in Obesity and Diabetes. *Antioxid Redox Signal* (2019) 30(3):354–74. doi: 10.1089/ars.2017.7424

26. Piperi C, Adamopoulos C, Papavassiliou AG. Potential of Glycative Stress Targeting for Cancer Prevention. *Cancer Lett* (2017) 390:153–9. doi: 10.1016/j.canlet.2017.01.020

27. Lee HM, Seo JH, Kwak MK, Kang SO. Methylglyoxal Upregulates Dictyostelium Discoideum Slug Migration by Triggering Glutathione Reductase and Methylglyoxal Reductase Activity. *Int J Biochem Cell Biol* (2017) 90:81–92. doi: 10.1016/j.biocel.2017.07.019

28. Baba SP, Barski OA, Ahmed Y, O'Toole TE, Conklin DJ, Bhatnagar A, et al. Reductive Metabolism of AGE Precursors: A Metabolic Route for Preventing AGE Accumulation in Cardiovascular Tissue. *Diabetes* (2009) 58(11):2486–97. doi: 10.2337/db09-0375

29. Larsen K, Aronsson AC, Marmstål E, Mannervik B. Immunological Comparison of Glyoxalase I From Yeast and Mammals and Quantitative Determination of the Enzyme in Human Tissues by Radioimmunoassay. *Comp Biochem Physiol B* (1985) 82(4):625–38. doi: 10.1016/0305-0491(85)90499-7

30. Nishimura C, Furue M, Ito T, Omori Y, Tanimoto T. Quantitative Determination of Human Aldose Reductase by Enzyme-Linked Immunosorbent Assay. Immunoassay of Human Aldose Reductase. *Biochem Pharmacol* (1993) 46(1):21–8. doi: 10.1016/0006-2952(93)90343-U

31. Thorpe SR, Baynes JW. Maillard Reaction Products in Tissue Proteins: New Products and New Perspectives. *Amino Acids* (2003) 25(3-4):275–81. doi: 10.1007/s00726-003-0017-9

32. Rabbani N, Xue M, Weickert MO, Thornalley PJ. Multiple Roles of Glyoxalase 1-Mediated Suppression of Methylglyoxal Glycation in Cancer Biology-Involvement in Tumour Suppression, Tumour Growth, Multidrug Resistance and Target for Chemotherapy. *Semin Cancer Biol* (2018) 49:83–93. doi: 10.1016/j.semcancer.2017.05.006

33. Thornalley PJ, Waris S, Fleming T, Santarius T, Larkin SJ, Winklhofer-Roob BM, et al. Imidazopurinones are Markers of Physiological Genomic Damage Linked to DNA Instability and Glyoxalase 1-Associated Tumour Multidrug Resistance. *Nucleic Acids Res* (2010) 38(16):5432–42. doi: 10.1093/nar/gkq306

34. Ahmed N, Argirov OK, Minhas HS, Cordeiro CAA, Thornalley PJ. Assay of Advanced Glycation Endproducts (AGEs): Surveying AGEs by Chromatographic Assay With Derivatization by 6-Aminoquinolyl-N-Hydroxysuccinimidyl-Carbamate and Application to Nepsilon-Carboxymethyl-Lysine- and Nepsilon-(1-Carboxyethyl)Lysine-Modified Albumin. *Biochem J* (2002) 364(Pt 1):1–14. doi: 10.1042/bj3640001

35. Ahmed N, Thornalley PJ. Chromatographic Assay of Glycation Adducts in Human Serum Albumin Glycated In Vitro by Derivatization With 6-Aminoquinolyl-N-Hydroxysuccinimidyl-Carbamate and Intrinsic Fluorescence. *Biochem J* (2002) 364(Pt 1):15–24. doi: 10.1042/bj3640015

36. Westwood ME, Thornalley PJ. Molecular Characteristics of Methylglyoxal-Modified Bovine and Human Serum Albumins. Comparison With Glucose-Derived Advanced Glycation Endproduct-Modified Serum Albumins. *J Protein Chem* (1995) 14(5):359–72. doi: 10.1007/BF01886793

37. Shipanova IN, Glomb MA, Nagaraj RH. Protein Modification by Methylglyoxal: Chemical Nature and Synthetic Mechanism of a Major Fluorescent Adduct. *Arch Biochem Biophys* (1997) 344(1):29–36. doi: 10.1006/abbi.1997.0195

38. Oya T, Hattori N, Mizuno Y, Miyata S, Maeda S, Osawa T, et al. Methylglyoxal Modification of Protein. Chemical and Immunochemical Characterization of Methylglyoxal-Arginine Adducts. *J Biol Chem* (1999) 274(26):18492–502. doi: 10.1074/jbc.274.26.18492

39. Ahmed MU, Frye EB, Degenhardt TP, Thorpe SR, Baynes JW. N-Epsilon-(Carboxyethyl)Lysine, a Product of the Chemical Modification of Proteins by Methylglyoxal, Increases With Age in Human Lens Proteins. *Biochem J* (1997) 324(Pt 2):565–70. doi: 10.1042/bj3240565

40. Lederer MO, Klaiber RG. Cross-Linking of Proteins by Maillard Processes: Characterization and Detection of Lysine-Arginine Cross-Links Derived From Glyoxal and Methylglyoxal. *Bioorg Med Chem* (1999) 7(11):2499–507. doi: 10.1016/S0968-0896(99)00212-6

41. Morcos M, Du X, Pfisterer F, Hutter H, Sayed AAR, Thornalley P, et al. Glyoxalase-1 Prevents Mitochondrial Protein Modification and Enhances Lifespan in Caenorhabditis Elegans. *Aging Cell* (2008) 7(2):260–9. doi: 10.1111/j.1474-9726.2008.00371.x

42. Yao D, Brownlee M. Hyperglycemia-Induced Reactive Oxygen Species Increase Expression of the Receptor for Advanced Glycation End Products (RAGE) and RAGE Ligands. *Diabetes* (2010) 59(1):249–55. doi: 10.2337/db09-0801

43. Chan WH, Wu HJ, Shiao NH. Apoptotic Signaling in Methylglyoxal-Treated Human Osteoblasts Involves Oxidative Stress, C-Jun N-Terminal Kinase, Caspase-3, and P21-Activated Kinase 2. *J Cell Biochem* (2007) 100(4):1056–69. doi: 10.1002/jcb.21114

44. Dobler D, Ahmed N, Song L, Eboigbodin KE, Thornalley PJ. Increased Dicarbonyl Metabolism in Endothelial Cells in Hyperglycemia Induces Anoikis and Impairs Angiogenesis by RGD and GFOGER Motif Modification. *Diabetes* (2006) 55(7):1961–9. doi: 10.2337/db05-1634

45. Taguchi A, Blood DC, Toro GD, Canet A, Lee DC, Qu W, et al. Blockade of RAGE-Amphoterin Signalling Suppresses Tumour Growth and Metastases. *Nature* (2000) 405(6784):354–60. doi: 10.1038/35012626

46. Loidl-Stahlhofen A, Spiteller G. Alpha-Hydroxyaldehydes, Products of Lipid Peroxidation. *Biochim Biophys Acta* (1994) 1211(2):156–60. doi: 10.1016/0005-2760(94)90264-X

47. Thornalley PJ, Langborg A, Minhas HS. Formation of Glyoxal, Methylglyoxal and 3-Deoxyglucosone in the Glycation of Proteins by Glucose. *Biochem J* (1999) 344 Pt 1(Pt 1):109–16. doi: 10.1042/bj3440109

48. Thornalley PJ. Protein and Nucleotide Damage by Glyoxal and Methylglyoxal in Physiological Systems–Role in Ageing and Disease. *Drug Metabol Drug Interact* (2008) 23(1-2):125–50. doi: 10.1515/DMDI.2008.23.1-2.125

49. Murata-Kamiya N, Kamiya H, Kaji H, Kasai H. Glyoxal, a Major Product of DNA Oxidation, Induces Mutations at G:C Sites on a Shuttle Vector Plasmid Replicated in Mammalian Cells. *Nucleic Acids Res* (1997) 25(10):1897–902. doi: 10.1093/nar/25.10.1897

50. Thornalley PJ. Glyoxalase I–structure, Function and a Critical Role in the Enzymatic Defence Against Glycation. *Biochem Soc Trans* (2003) 31(Pt 6):1343–8. doi: 10.1042/bst0311343

51. Thornalley PJ. The Glyoxalase System: New Developments Towards Functional Characterization of a Metabolic Pathway Fundamental to Biological Life. *Biochem J* (1990) 269(1):1–11. doi: 10.1042/bj2690001

52. Thornalley PJ. Pharmacology of Methylglyoxal: Formation, Modification of Proteins and Nucleic Acids, and Enzymatic Detoxification–a Role in Pathogenesis and Antiproliferative Chemotherapy. *Gen Pharmacol* (1996) 27(4):565–73. doi: 10.1016/0306-3623(95)02054-3

53. Brandt RB, Waters MG, Muron DJ, Bloch MH. The Glyoxalase System in Rat Blood. *Proc Soc Exp Biol Med* (1982) 169(4):463–9. doi: 10.3181/00379727-169-41376

54. Misra K, Banerjee AB, Ray S, Ray M. Glyoxalase III From Escherichia Coli: A Single Novel Enzyme for the Conversion of Methylglyoxal Into D-Lactate Without Reduced Glutathione. *Biochem J* (1995) 305(Pt 3):999–1003. doi: 10.1042/bj3050999

55. Lee JY, Song J, Kwon K, Jang S, Kim C, Baek K, et al. Human DJ-1 and its Homologs are Novel Glyoxalases. *Hum Mol Genet* (2012) 21(14):3215–25. doi: 10.1093/hmg/dds155

56. Richarme G, Abdallah J, Mathas N, Gautier V, Dairou J. Further Characterization of the Maillard Deglycase DJ-1 and its Prokaryotic Homologs, Deglycase 1/Hsp31, Deglycase 2/YhbO, and Deglycase 3/YajL. *Biochem Biophys Res Commun* (2018) 503(2):703–9. doi: 10.1016/j.bbrc.2018.06.064

57. Cameron AD, Olin B, Ridderström M, Mannervik B, Jones TA. Crystal Structure of Human Glyoxalase I–evidence for Gene Duplication and 3D Domain Swapping. *EMBO J* (1997) 16(12):3386–95. doi: 10.1093/emboj/16.12.3386

58. Han LP, Schimandle CM, Davison LM, Vander DL. Comparative Kinetics of Mg2+-, Mn2+-, Co2+-, and Ni2+-Activated Glyoxalase I. Evaluation of the Role of the Metal Ion. *Biochemistry* (1977) 16(25):5478–84. doi: 10.1021/bi00644a013

59. Sakamoto H, Mashima T, Kizaki A, Dan S, Hashimoto Y, Naito M, et al. Glyoxalase I is Involved in Resistance of Human Leukemia Cells to Antitumor Agent-Induced Apoptosis. *Blood* (2000) 95(10):3214–8. doi: 10.1182/blood.V95.10.3214

60. Rounds L, Nagle RB, Muranyi A, Jandova J, Gill S, Vela E, et al. Glyoxalase 1 Expression as a Novel Diagnostic Marker of High-Grade Prostatic Intraepithelial Neoplasia in Prostate Cancer. *Cancers (Basel)* (2021) 13 (14). doi: 10.3390/cancers13143608

61. Tripodis N, Mason R, Humphray SJ, Davies AF, Herberg JA, Trowsdale J, et al. Physical Map of Human 6p21.2-6p21.3: Region Flanking the Centromeric End of the Major Histocompatibility Complex. *Genome Res* (1998) 8(6):631–43. doi: 10.1101/gr.8.6.631

62. Bellahcène A, Nokin MJ, Castronovo V, Schalkwijk C. Methylglyoxal-Derived Stress: An Emerging Biological Factor Involved in the Onset and Progression of Cancer. *Semin Cancer Biol* (2018) 49:64–74. doi: 10.1016/j.semcancer.2017.05.010

63. Antognelli C, Palumbo I, Aristei C, Talesa VN. Glyoxalase I Inhibition Induces Apoptosis in Irradiated MCF-7 Cells via a Novel Mechanism Involving Hsp27, P53 and NF-κb. *Br J Cancer* (2014) 111(2):395–406. doi: 10.1038/bjc.2014.280

64. Xue M, Rabbani N, Momiji H, Imbasi P, Anwar MM, Kitteringham N, et al. Transcriptional Control of Glyoxalase 1 by Nrf2 Provides a Stress-Responsive Defence Against Dicarbonyl Glycation. *Biochem J* (2012) 443 (1):213–22. doi: 10.1042/BJ20111648

65. MacLeod AK, Mahon MM, Plummer SM, Higgins LG, Penning TM, Igarashi K, et al. Characterization of the Cancer Chemopreventive NRF2-Dependent Gene Battery in Human Keratinocytes: Demonstration That the KEAP1-NRF2 Pathway, and Not the BACH1-NRF2 Pathway, Controls Cytoprotection Against Electrophiles as Well as Redox-Cycling Compounds. *Carcinogenesis* (2009) 30(9):1571–80. doi: 10.1093/carcin/bgp176

66. Zhang M, Zhang C, Zhang L, Yang Q, Zhou S, Wen Q, et al. Nrf2 is a Potential Prognostic Marker and Promotes Proliferation and Invasion in Human Hepatocellular Carcinoma. *BMC Cancer* (2015) 15:531. doi: 10.1186/s12885-015-1541-1

67. Antognelli C, Moretti S, Frosini R, Puxeddu E, Sidoni A, Talesa VN, et al. Methylglyoxal Acts as a Tumor-Promoting Factor in Anaplastic Thyroid Cancer. *Cells* (2019) 8(6):547. doi: 10.3390/cells8060547

68. Nishimoto S, Koike S, Inoue N, Suzuki T, Ogasawara Y. Activation of Nrf2 Attenuates Carbonyl Stress Induced by Methylglyoxal in Human Neuroblastoma Cells: Increase in GSH Levels is a Critical Event for the Detoxification Mechanism. *Biochem Biophys Res Commun* (2017) 483 (2):874–9. doi: 10.1016/j.bbrc.2017.01.024

69. Liu GH, Qu J, Shen X. NF-Kappab/P65 Antagonizes Nrf2-ARE Pathway by Depriving CBP From Nrf2 and Facilitating Recruitment of HDAC3 to MafK. *Biochim Biophys Acta* (2008) 1783(5):713–27. doi: 10.1016/j.bbamcr.2008.01.002

70. Rabbani N, Xue M, Thornalley PJ. Activity, Regulation, Copy Number and Function in the Glyoxalase System. *Biochem Soc Trans* (2014) 42(2):419–24. doi: 10.1042/BST20140008

71. Redon R, Ishikawa S, Fitch KR, Feuk L, Perry GH, Andrews TD, et al. Global Variation in Copy Number in the Human Genome. *Nature* (2006) 444 (7118):444–54. doi: 10.1038/nature05329

72. Shafie A, Xue M, Thornalley PJ, Rabbani N. Copy Number Variation of Glyoxalase I. *Biochem Soc Trans* (2014) 42(2):500–3. doi: 10.1042/BST20140011

73. Santarius T, Bignell GR, Greenman CD, Widaa S, Chen L, Mahoney CL, et al. GLO1-A Novel Amplified Gene in Human Cancer. *Genes Chromosomes Cancer* (2010) 49(8):711–25. doi: 10.1002/gcc.20784

74. Hosoda F, Arai Y, Okada N, Shimizu H, Miyamoto M, Kitagawa N, et al. Integrated Genomic and Functional Analyses Reveal Glyoxalase I as a Novel Metabolic Oncogene in Human Gastric Cancer. *Oncogene* (2015) 34 (9):1196–206. doi: 10.1038/onc.2014.57

75. Thornalley PJ. The Glyoxalase System in Health and Disease. *Mol Aspects Med* (1993) 14(4):287–371. doi: 10.1016/0098-2997(93)90002-U

76. Daiyasu H, Osaka K, Ishino Y, Toh H. Expansion of the Zinc Metallo-Hydrolase Family of the Beta-Lactamase Fold. *FEBS Lett* (2001) 503(1):1–6. doi: 10.1016/s0014-5793(01)02686-2

77. Bito A, Haider M, Briza P, Strasser P, Breitenbach M. Heterologous Expression, Purification, and Kinetic Comparison of the Cytoplasmic and Mitochondrial Glyoxalase II Enzymes, Glo2p and Glo4p, From Saccharomyces Cerevisiae. *Protein Expr Purif* (1999) 17(3):456–64. doi: 10.1006/prep.1999.1151

78. Cordell PA, Futers TS, Grant PJ, Pease RJ. The Human Hydroxyacylglutathione Hydrolase (HAGH) Gene Encodes Both Cytosolic and Mitochondrial Forms of Glyoxalase II. *J Biol Chem* (2004) 279(27):28653–61. doi: 10.1074/jbc.M403470200

79. Antognelli C, Frosini R, Santolla MF, Peirce MJ, Talesa VN. Oleuropein-Induced Apoptosis Is Mediated by Mitochondrial Glyoxalase 2 in NSCLC A549 Cells: A Mechanistic Inside and a Possible Novel Nonenzymatic Role for an Ancient Enzyme. *Oxid Med Cell Longev* (2019) 2019:8576961. doi: 10.1155/2019/8576961

80. Antognelli C, Talesa VN. Glyoxalases in Urological Malignancies. *Int J Mol Sci* (2018) 19(2):415. doi: 10.3390/ijms19020415

81. Antognelli C, Ferri I, Bellezza G, Siccu P, Love HD, Talesa VN, et al. Glyoxalase 2 Drives Tumorigenesis in Human Prostate Cells in a Mechanism Involving Androgen Receptor and P53-P21 Axis. *Mol Carcinog* (2017) 56(9):2112–26. doi: 10.1002/mc.22668

82. Bray F, Ferlay J, Soerjomataram I, Siegel RL, Torre LA, Jemal A. Global Cancer Statistics 2018: GLOBOCAN Estimates of Incidence and Mortality Worldwide for 36 Cancers in 185 Countries. *CA Cancer J Clin* (2018) 68 (6):394–424. doi: 10.3322/caac.21492

83. Tse GM, Ma TK, Chu WC, Lam WW, Poon CS, Chan WC. Neuroendocrine Differentiation in Pure Type Mammary Mucinous Carcinoma is Associated With Favorable Histologic and Immunohistochemical Parameters. *Mod Pathol* (2004) 17(5):568–72. doi: 10.1038/modpathol.3800092

84. Rakha EA, Green AR. Molecular Classification of Breast Cancer: What the Pathologist Needs to Know. *Pathology* (2017) 49(2):111–9. doi: 10.1016/j.pathol.2016.10.012

85. Rulli A, Carli L, Romani R, Baroni T, Giovannini E, Rosi G, et al. Expression of Glyoxalase I and II in Normal and Breast Cancer Tissues. *Breast Cancer Res Treat* (2001) 66(1):67–72. doi: 10.1023/A:1010632919129

86. Yousefi T, Pasha AR, Kamrani G, Ebrahimzadeh A, Zahedian A, Tilaki KH, et al. Evaluation of Fructosamine 3-Kinase and Glyoxalase 1 Activity in Normal and Breast Cancer Tissues. *Biomedicine (Taipei)* (2021) 11(3):15–22. doi: 10.37796/2211-8039.1130

87. Motomura H, Ozaki A, Tamori S, Onaga C, Nozaki Y, Waki Y, et al. Glyoxalase 1 and Protein Kinase Cλ as Potential Therapeutic Targets for Late-Stage Breast Cancer. *Oncol Lett* (2021) 22(1):547. doi: 10.3892/ol.2021.12808

88. Peng HT, Chen J, Liu TY, Wu YQ, Lin XH, Lai YH, et al. Up-Regulation of the Tumor Promoter Glyoxalase-1 Indicates Poor Prognosis in Breast Cancer. *Int J Clin Exp Pathol* (2017) 10(11):10852–62.

89. Tamori S, Nozaki Y, Motomura H, Nakane H, Katayama R, Onaga C, et al. Glyoxalase 1 Gene is Highly Expressed in Basal-Like Human Breast Cancers and Contributes to Survival of ALDH1-Positive Breast Cancer Stem Cells. *Oncotarget* (2018) 9(92):36515–29. doi: 10.18632/oncotarget.26369

90. Fonseca-Sánchez MA, Cuevas SR, Hernández GM, Piña VB, Ocampo EA, Miranda AH, et al. Breast Cancer Proteomics Reveals a Positive Correlation Between Glyoxalase 1 Expression and High Tumor Grade. *Int J Oncol* (2012) 41(2):670–80. doi: 10.3892/ijo.2012.1478

91. Scheifele C, Zhu Q, Ignatov A, Kalinski T, Nass N. Glyoxalase 1 Expression Analysis by Immunohistochemistry in Breast Cancer. *Pathol Res Pract* (2020) 216(12):153257. doi: 10.1016/j.prp.2020.153257

92. Guo Y, Zhang Y, Yang X, Lu P, Yan X, Xiao F, et al. Effects of Methylglyoxal and Glyoxalase I Inhibition on Breast Cancer Cells Proliferation, Invasion, and Apoptosis Through Modulation of MAPKs, MMP9, and Bcl-2. *Cancer Biol Ther* (2016) 17(2):169–80. doi: 10.1080/15384047.2015.1121346

93. Hutschenreuther A, Bigl M, Hemdan NY, Debebe T, Gaunitz F, Birkenmeier G. Modulation of GLO1 Expression Affects Malignant Properties of Cells. *Int J Mol Sci* (2016) 17(12):2133. doi: 10.3390/ijms17122133

94. Davies GF, Roesler WJ, Juurlink BH, Harkness TA. Troglitazone Overcomes Doxorubicin-Resistance in Resistant K562 Leukemia Cells. *Leuk Lymphoma* (2005) 46(8):1199–206. doi: 10.1080/10428190500102555

95. Mann J. Natural Products in Cancer Chemotherapy: Past, Present and Future. *Nat Rev Cancer* (2002) 2(2):143–8. doi: 10.1038/nrc723

96. Schmidt B, Ferreira C, Passos CL, Silva JL, Fialho E. Resveratrol, Curcumin and Piperine Alter Human Glyoxalase 1 in MCF-7 Breast Cancer Cells. *Int J Mol Sci* (2020) 21(15):5244. doi: 10.3390/ijms21155244

97. Santel T, Pflug G, Hemdan NY, Schäfer A, Hollenbach M, Buchold M, et al. Curcumin Inhibits Glyoxalase 1: A Possible Link to its Anti-Inflammatory and Anti-Tumor Activity. *PloS One* (2008) 3(10):e3508. doi: 10.1371/journal.pone.0003508

98. Meiyanto E, Putri H, Larasati YA, Utomo RY, Jenie RI, Ikawati M, et al. Anti-Proliferative and Anti-Metastatic Potential of Curcumin Analogue, Pentagamavunon-1 (PGV-1), Toward Highly Metastatic Breast Cancer Cells in Correlation With ROS Generation. *Adv Pharm Bull* (2019) 9(3):445–52. doi: 10.15171/apb.2019.053

99. Weigelt B, Peterse JL, van 't Veer LJ. Breast Cancer Metastasis: Markers and Models. *Nat Rev Cancer* (2005) 5(8):591–602. doi: 10.1038/nrc1670

100. Nokin MJ, Durieux F, Peixoto P, Chiavarina B, Peulen O, Blomme A, et al. Methylglyoxal, a Glycolysis Side-Product, Induces Hsp90 Glycation and YAP-Mediated Tumor Growth and Metastasis. *Elife* (2016) 5:e19375. doi: 10.7554/eLife.19375

101. Nokin MJ, Bellier J, Durieux F, Peulen O, Rademaker G, Gabriel M, et al. Methylglyoxal, a Glycolysis Metabolite, Triggers Metastasis Through MEK/ERK/SMAD1 Pathway Activation in Breast Cancer. *Breast Cancer Res* (2019) 21(1):11. doi: 10.1186/s13058-018-1095-7

102. Zender L, Xue W, Zuber J, Semighini CP, Krasnitz A, Ma B, et al. An Oncogenomics-Based In Vivo RNAi Screen Identifies Tumor Suppressors in Liver Cancer. *Cell* (2008) 135(5):852–64. doi: 10.1016/j.cell.2008.09.061

103. Nokin MJ, Durieux F, Bellier J, Peulen O, Uchida K, Spiegel DA, et al. Hormetic Potential of Methylglyoxal, a Side-Product of Glycolysis, in Switching Tumours From Growth to Death. *Sci Rep* (2017) 7(1):11722. doi: 10.1038/s41598-017-12119-7

104. Henley SJ, Ward EM, Scott S, Ma J, Anderson RN, Firth AU, et al. Annual Report to the Nation on the Status of Cancer, Part I: National Cancer Statistics. *Cancer* (2020) 126(10):2225–49. doi: 10.1002/cncr.32802

105. Casey MJ, Summers GK, Crotzer D. Endometrial Cancer. In: *StatPearls*. Treasure Island (FL: StatPearls Publishing Copyright © 2021, StatPearls Publishing LLC (2021).

106. Lu KH, Broaddus RR. Endometrial Cancer. *N Engl J Med* (2020) 383 (21):2053–64. doi: 10.1056/NEJMra1514010

107. Taylan E, Oktay K. Fertility Preservation in Gynecologic Cancers. *Gynecol Oncol* (2019) 155(3):522–9. doi: 10.1016/j.ygyno.2019.09.012

108. Ushijima K, Yahata H, Yoshikawa H, Konishi I, Yasugi T, Saito T, et al. Multicenter Phase II Study of Fertility-Sparing Treatment With Medroxyprogesterone Acetate for Endometrial Carcinoma and Atypical Hyperplasia in Young Women. *J Clin Oncol* (2007) 25(19):2798–803. doi: 10.1200/JCO.2006.08.8344

109. Zhang Z, Dong L, Sui L, Yang Y, Liu X, Yu Y, et al. Metformin Reverses Progestin Resistance in Endometrial Cancer Cells by Downregulating GloI Expression. *Int J Gynecol Cancer* (2011) 21(2):213–21. doi: 10.1097/IGC.0b013e318207dac7

110. Jiang Y, Chen X, Wei Y, Feng Y, Zheng W, Zhang Z, et al. Metformin Sensitizes Endometrial Cancer Cells to Progestin by Targeting TET1 to Downregulate Glyoxalase I Expression. *BioMed Pharmacother* (2019) 113:108712. doi: 10.1016/j.biopha.2019.108712

111. Vasey PA. Resistance to Chemotherapy in Advanced Ovarian Cancer: Mechanisms and Current Strategies. *Br J Cancer* (2003) 89 Suppl 3(Suppl 3):S23–8. doi: 10.1038/sj.bjc.6601497

112. Saltzman BS, Doherty JA, Hill DA, Beresford SA, Voigt LF, Chen C, et al. Diabetes and Endometrial Cancer: An Evaluation of the Modifying Effects of Other Known Risk Factors. *Am J Epidemiol* (2008) 167(5):607–14. doi: 10.1093/aje/kwm333

113. Dong L, Zhou Q, Zhang Z, Zhu Y, Duan T, Feng Y. Metformin Sensitizes Endometrial Cancer Cells to Chemotherapy by Repressing Glyoxalase I Expression. *J Obstet Gynaecol Res* (2012) 38(8):1077–85. doi: 10.1111/j.1447-0756.2011.01839.x

114. Davies GF, Juurlink BH, Harkness TA. Troglitazone Reverses the Multiple Drug Resistance Phenotype in Cancer Cells. *Drug Des Devel Ther* (2009) 3:79–88. doi: 10.2147/dddt.s3314

115. Burdelski C, Shihada R, Hinsch A, Angerer A, Göbel C, Friedrich E, et al. High-Level Glyoxalase 1 (GLO1) Expression is Linked to Poor Prognosis in Prostate Cancer. *Prostate* (2017) 77(15):1528–38. doi: 10.1002/pros.23431

116. Wang Y, Kuramitsu Y, Ueno T, Suzuki N, Yoshino S, Iizuka N, et al. Glyoxalase I (GLO1) is Up-Regulated in Pancreatic Cancerous Tissues Compared With Related non-Cancerous Tissues. *Anticancer Res* (2012) 32 (8):3219–22.

117. Sakamoto H, Mashima T, Sato S, Hashimoto Y, Yamori T, Tsuruo T. Selective Activation of Apoptosis Program by S-P-Bromobenzylglutathione Cyclopentyl Diester in Glyoxalase I-Overexpressing Human Lung Cancer Cells. *Clin Cancer Res* (2001) 7(8):2513–8.

118. Godbout JP, Pesavento J, Hartman ME, Manson SR, Freund GC. Methylglyoxal Enhances Cisplatin-Induced Cytotoxicity by Activating Protein Kinase Cdelta. *J Biol Chem* (2002) 277(4):2554–61. doi: 10.1074/jbc.M100385200

119. van Heijst JW, Niessen HW, Musters RJ, van Hinsbergh VW, Hoekman K, Schalkwijk CG. Argpyrimidine-Modified Heat Shock Protein 27 in Human non-Small Cell Lung Cancer: A Possible Mechanism for Evasion of Apoptosis. *Cancer Lett* (2006) 241(2):309–19. doi: 10.1016/j.canlet.2005.10.042

120. Oya-Ito T, Naito Y, Takagi T, Handa O, Matsui H, Yamada M, et al. Heat-Shock Protein 27 (Hsp27) as a Target of Methylglyoxal in Gastrointestinal Cancer. *Biochim Biophys Acta* (2011) 1812(7):769–81. doi: 10.1016/j.bbadis.2011.03.017

121. Sakamoto H, Mashima T, Yamamoto K, Tsuruo T. Modulation of Heat-Shock Protein 27 (Hsp27) Anti-Apoptotic Activity by Methylglyoxal Modification. *J Biol Chem* (2002) 277(48):45770–5. doi: 10.1074/jbc.M207485200

122. Kuhla B, Lüth HJ, Haferburg D, Weick M, Reichenbach A, Arendt T, et al. Pathological Effects of Glyoxalase I Inhibition in SH-SY5Y Neuroblastoma Cells. *J Neurosci Res* (2006) 83(8):1591–600. doi: 10.1002/jnr.20838

123. Siegel RL, Miller KD, Jemal A. Cancer Statistics, 2020. *CA Cancer J Clin* (2020) 70(1):7–30. doi: 10.3322/caac.21590

124. Sharbatoghli M, Vafaei S, Es HA, Lari MA, Totonchi M, Madjd Z. Prediction of the Treatment Response in Ovarian Cancer: A ctDNA Approach. *J Ovarian Res* (2020) 13(1):124. doi: 10.1186/s13048-020-00729-1

125. Haunschild CE, Tewari KS. The Current Landscape of Molecular Profiling in the Treatment of Epithelial Ovarian Cancer. *Gynecol Oncol* (2021) 160 (1):333–45. doi: 10.1016/j.ygyno.2020.09.043

126. Lheureux S, Braunstein M, Oza AM. Epithelial Ovarian Cancer: Evolution of Management in the Era of Precision Medicine. *CA Cancer J Clin* (2019) 69 (4):280–304. doi: 10.3322/caac.21559

127. Nasser MW, Ahirwar DK, Ganju RK. RAGE: A Novel Target for Breast Cancer Growth and Metastasis. *Oncoscience* (2016) 3(2):52–3. doi: 10.18632/oncoscience.294

128. Wang D, Li T, Ye G, Shen Z, Hu Y, Mou T, et al. Overexpression of the Receptor for Advanced Glycation Endproducts (RAGE) is Associated With Poor Prognosis in Gastric Cancer. *PloS One* (2015) 10(4):e0122697. doi: 10.1371/journal.pone.0122697

129. Kuniyasu H, Chihara Y, Takahashi T. Co-Expression of Receptor for Advanced Glycation End Products and the Ligand Amphoterin Associates Closely With Metastasis of Colorectal Cancer. *Oncol Rep* (2003) 10(2):445–8. doi: 10.3892/or.10.2.445

130. Khorramdelazad H, Bagheri V, Hassanshahi G, Karami H, Moogooei M, Zeinali M, et al. S100A12 and RAGE Expression in Human Bladder Transitional Cell Carcinoma: A Role for the Ligand/RAGE Axis in Tumor Progression? *Asian Pac J Cancer Prev* (2015) 16(7):2725–9. doi: 10.7314/APJCP.2015.16.7.2725

131. Rahimi F, Karimi J, Goodarzi MT, Saidijam M, Khodadadi I, Razavi AN, et al. Overexpression of Receptor for Advanced Glycation End Products (RAGE) in Ovarian Cancer. *Cancer biomark* (2017) 18(1):61–8. doi: 10.3233/CBM-160674

132. Poljicanin A, Filipovic N, Pusic TV, Soljic V, Caric A, Babic MS, et al. Expression Pattern of RAGE and IGF-1 in the Human Fetal Ovary and Ovarian Serous Carcinoma. *Acta Histochem* (2015) 117(4-5):468–76. doi: 10.1016/j.acthis.2015.01.004

133. Auersperg N, Wong AS, Choi KC, KangSK , Leung PC. Ovarian Surface Epithelium: Biology, Endocrinology, and Pathology. *Endocr Rev* (2001) 22(2):255–88. doi: 10.1210/edrv.22.2.0422

134. Smith-Beckerman DM, Fung KW, Williams KE, Auersperg N, Godwin AK, Burlingame AL. Proteome Changes in Ovarian Epithelial Cells Derived From Women With BRCA1 Mutations and Family Histories of Cancer. *Mol Cell Proteomics* (2005) 4(2):156–68. doi: 10.1074/mcp.M400157-MCP200

135. Peres LC, Cushing-Haugen KL, Köbel M, Harris HR, Berchuck A, Rossing MA, et al. Invasive Epithelial Ovarian Cancer Survival by Histotype and Disease Stage. *J Natl Cancer Inst* (2019) 111(1):60–8. doi: 10.1093/jnci/djy071

136. Zeppernick F, Meinhold-Heerlein I. The New FIGO Staging System for Ovarian, Fallopian Tube, and Primary Peritoneal Cancer. *Arch Gynecol Obstet* (2014) 290(5):839–42. doi: 10.1007/s00404-014-3364-8

137. Jones MB, Krutzsch H, Shu H, Zhao Y, Liotta LA, Kohn EC, et al. Proteomic Analysis and Identification of New Biomarkers and Therapeutic Targets for Invasive Ovarian Cancer. *Proteomics* (2002) 2(1):76–84. doi: 10.1002/1615-9861(200201)2:1<76::AID-PROT76>3.0.CO;2-O

138. Pimple SA, Mishra GA. Global Strategies for Cervical Cancer Prevention and Screening. *Minerva Ginecol* (2019) 71(4):313–20. doi: 10.23736/S0026-4784.19.04397-1

139. Sriplung H, Singkham P, Iamsirithaworn S, Jiraphongsa C, Bilheem S. Success of a Cervical Cancer Screening Program: Trends in Incidence in Songkhla, Southern Thailand, 1989-2010, and Prediction of Future Incidences to 2030. *Asian Pac J Cancer Prev* (2014) 15(22):10003–8. doi: 10.7314/APJCP.2014.15.22.10003

140. Sung H, Ferlay J, Siegel RL, Laversanne M, Soerjomataram I, Jemal A, et al. Global Cancer Statistics 2020: GLOBOCAN Estimates of Incidence and Mortality Worldwide for 36 Cancers in 185 Countries. *CA Cancer J Clin* (2021) 71(3):209–49. doi: 10.3322/caac.21660

141. Heo MY, Sohn SJ, Au WW. Anti-Genotoxicity of Galangin as a Cancer Chemopreventive Agent Candidate. *Mutat Res* (2001) 488(2):135–50. doi: 10.1016/S1383-5742(01)00054-0

142. Tolomeo M, Grimaudo S, Cristina AD, Pipitone RM, Dusonchet L, Meli M, et al. Galangin Increases the Cytotoxic Activity of Imatinib Mesylate in Imatinib-Sensitive and Imatinib-Resistant Bcr-Abl Expressing Leukemia Cells. *Cancer Lett* (2008) 265(2):289–97. doi: 10.1016/j.canlet.2008.02.025

143. Kumar R, Tiku AB. Galangin Induces Cell Death by Modulating the Expression of Glyoxalase-1 and Nrf-2 in HeLa Cells. *Chem Biol Interact* (2018) 279:1–9. doi: 10.1016/j.cbi.2017.11.001

144. Ha TK, Kim ME, Yoon JH, Bae SJ, Yeom J, Lee JS. Galangin Induces Human Colon Cancer Cell Death via the Mitochondrial Dysfunction and Caspase-Dependent Pathway. *Exp Biol Med (Maywood)* (2013) 238(9):1047–54. doi: 10.1177/1535370213497882

145. Zhang W, Lan Y, Huang Q, Hua Z. Galangin induces B16F10 melanoma cell apoptosis via mitochondrial pathway and sustained activation of p38 MAPK. *Cytotechnology* (2013) 65(3):447–55. doi: 10.1007/s10616-012-9499-1

146. Cao J, Wang H, Chen F, Fang J, Xu A, Xi W, et al. Galangin Inhibits Cell Invasion by Suppressing the Epithelial-Mesenchymal Transition and Inducing Apoptosis in Renal Cell Carcinoma. *Mol Med Rep* (2016) 13(5):4238–44. doi: 10.3892/mmr.2016.5042

Frontiers in
Oncology

Advances knowledge of carcinogenesis and tumor progression for better treatment and management

The third most-cited oncology journal, which highlights research in carcinogenesis and tumor progression, bridging the gap between basic research and applications to imrpove diagnosis, therapeutics and management strategies.

Discover the latest Research Topics

See more →

frontiers | Research Topics